

Photo-Fragmentation of Lithium Atoms Studied with MOTReMi

DISSERTATION

ZUR ERLANGUNG DES DOKTORGRADES
DER NATURWISSENSCHAFTEN

VORGELEGT BEIM FACHBEREICH PHYSIK
DER JOHANN WOLFGANG GOETHE-UNIVERSITÄT
IN FRANKFURT AM MAIN

VON
Ganjun Zhu
AUS HUAINAN, V. R. CHINA

FRANKFURT AM MAIN, FEBRUARY 2010
(D30)

VOM FACHBEREICH PHYSIK DER
JOHANN WOLFGANG GOETHE-UNIVERSITÄT
ALS DISSERTATION ANGENOMMEN.

Dekan: Professor D.-H. Rischke

1. Gutachter: Prof. Dr. Reinhard Dörner
2. Gutachter: Priv.-Doz. Dr. Alexander Dorn

Datum der Disputation:

Abstract

Within this thesis, an experimental study of the photo double ionization (PDI) and the simultaneous ionization-excitation is performed for lithium in different initial states $\text{Li}(1s^22l)$ ($l = s, p$). The excess energy of the linearly polarized VUV-light is between 4 and 12 eV above the PDI-threshold.

Three forefront technologies are combined: a magneto-optical trap (MOT) for lithium generating an ultra-cold and, by means of optical pumping, a state-prepared target; a reaction microscope (ReMi), enabling the momentum resolved detection of all reaction fragments with high-resolution and the free-electron laser in Hamburg (FLASH), providing an unprecedented brilliant photon beam at favourable time structure to access small cross sections.

Close to threshold the total as well as differential PDI cross sections are observed to critically depend on the excitation level and the symmetry of the initial state. For the excited state $\text{Li}(1s^22p)$ the PDI dynamics strongly depends on the alignment of the $2p$ -orbital with respect to the VUV-light polarization and, thus, from the population of the magnetic substates ($m_p = 0, \pm 1$). This alignment sensitivity decreases for increasing excess energy and is completely absent for ionization-excitation. Time-dependent close-coupling calculations are able to reproduce the experimental total cross sections with deviations of at most 30%. All the experimental observations can be consistently understood in terms of the long range electron correlation among the continuum electrons which gives rise to their preferential back-to-back emission. This alignment effect, which is observed here for the first time, allows controlling the PDI dynamics through a purely geometrical modification of the target initial state without changing its internal energy.

Zusammenfassung

In dieser Arbeit wurde die Photo-Doppelionisation (PDI) und die simultane Ionisation und Anregung von Lithium für verschiedene Anfangszustände $\text{Li}(1s^22l)$ ($l = s, p$) untersucht. Die Überschussenergie des linear polarisierten VUV-Lichts oberhalb der PDI-Schwelle lag zwischen 4 und 12 eV.

Drei neuartige Technologien wurden kombiniert: eine magnetooptische Falle (MOT) zur Erzeugung eines kalten und durch optisches Pumpen in ausgewählten Zuständen präparierten Targets; ein Reaktionsmikroskop (ReMi), das die Messung der Impulse aller Ionisationsprodukte ermöglicht; und der Freie-Elektronen Laser in Hamburg (FLASH), der einen Photonenstrahl mit beispielloser Brillanz bei günstiger Zeitstruktur zur Messung kleiner Wirkungsquerschnitte zur Verfügung stellt.

Nahe der Schwelle zeigen sowohl totale als auch differentielle PDI-Wirkungsquerschnitte eine starke Abhängigkeit vom Anregungsniveau und von der Symmetrie des Anfangszustands. Für den angeregten Zustand $\text{Li}(1s^22p)$ hängt die PDI-Dynamik stark von der Ausrichtung des $2p$ -Orbitals relativ zur Polarisation der VUV-Strahlung und damit von der

Besetzung der magnetischen Unterzustände ($m_p = 0, \pm 1$) ab. Diese Alignment-Abhängigkeit verringert sich für zunehmende Überschussenergie und fehlt bei der simultanen Ionisation und Anregung völlig. ‘Time-dependent close-coupling’ Rechnungen können die integralen Wirkungsquerschnitte bei Abweichungen von maximal 30% reproduzieren. Alle experimentellen Beobachtungen können mittels der Elektronenkorrelation über große Entfernungen, also der langreichweitigen Coulombwechselwirkung, erklärt werden. Diese dominiert die PDI-Dynamik nahe der Schwelle und führt zur bevorzugten Emission der Elektronen in entgegengesetzte Richtungen. Die hier erstmals beobachtete Ausrichtungsabhängigkeit der PDI erlaubt die Kontrolle der Doppelionisationsdynamik durch eine rein geometrische Modifikation des Anfangszustands bei fester innerer Energie.

Contents

1	Introduction and Motivation	1
2	Theory on Photoionization	9
2.1	Basics of Photo-Fragmentation Process	9
2.1.1	Mechanisms of Photo Double Ionization	10
2.1.2	Photoionization plus Excitation	14
2.1.3	Dependence of PDI Dynamics on the Quantum Numbers of the State $\{L M S \pi\}$	16
2.1.4	Fragmentation Influenced by Valence Electron Configuration	22
2.1.5	Wannier Threshold Law	25
2.2	Brief Introduction of the Calculation Methods	26
3	Principle of Laser Cooling and Trapping	33
3.1	Doppler Cooling	33
3.2	Magneto-Optical Trapping	36
3.3	Principle of Zeeman Slowing	40
3.4	Spectroscopic Properties of Lithium	42
4	An Elementary Introduction to the Free Electron Laser	45
4.1	Working Principle of FEL	45
4.1.1	The Way to Lasing for FEL — SASE principle	46
4.1.2	Operation of Low-Gain and High-Gain FEL	47
4.2	Free Electron Laser in Hamburg Facility	49
5	Experiment Setup — MOTReMi	53
5.1	Reaction Microscope	53
5.1.1	Spectrometer	55

CONTENTS

5.1.2	Momenta Reconstruction	62
5.1.3	Detector Systems	66
5.2	Magneto-Optical Trap	68
5.2.1	MOT-Coils in Anti-Helmholtz Configuration	69
5.2.2	Laser System for Cooling and Optical Pumping	70
5.2.3	Trap Loading System	80
5.3	Integration of a Reaction Microscope with a Magneto-Optical Trap	83
5.4	Experiment Control Devices	87
5.4.1	Adwin Gold DA System	87
5.4.2	LabView User Interface	88
5.5	Data Acquisition Units	88
6	Data Processing and Event Identification	91
6.1	General Classification of Photoionization Reactions	91
6.2	Recorded Raw Spectrum — Description, Clarification and Modification	95
6.3	Determination of Excited State Fraction	102
6.4	Measurement of Magnetic Sublevel Populations	103
7	Experimental Results	113
7.1	Photo Double Ionization	113
7.1.1	$(\gamma, 2e)$ on $\text{Li}\{L M_L S \pi\}$ at $E_\gamma = 85$ eV	114
7.1.2	$(\gamma, 2e)$ on $\text{Li}\{L M_L S \pi\}$ at $E_\gamma = 91$ eV	119
7.2	Single Ionization plus Simultaneous Excitation	122
7.2.1	$(\gamma, e + e^b)$ on $\text{Li}\{L M_L S \pi\}$ at $E_\gamma = 85$ eV	123
7.2.2	$(\gamma, e + e^b)$ on $\text{Li}\{L M_L S \pi\}$ at $E_\gamma = 91$ eV	127
7.3	Comparison and Conclusion	129
8	Summary and Outlook	135
A	Atomic Units	139
B	Polarization Gradient Cooling Method	141
C	TDCS Calculation for Li DPI Based on Parity	145
C.1	Even parity state - $\text{Li}(1s^2 2s^2 S^e)$	145
C.2	Odd parity state - $\text{Li}(1s^2 2p^2 P^o)$	146

D	C++ Code Segments in Data Analysis Program Agat32root	149
D.1	Agat32root Code for Cartesian Coordinate Transformation:	149
D.2	Agat32root Code for ToF /position Signal Correction:	149
E	Rotations and Wigner D-Functions	151
E.1	Rotation Operator and Euler Angles	151
E.2	Definition of D-Function	151
F	Single-Particle Coordinates and Jacobi Coordinates	153
G	Deutsche Kurzfassung der Dissertation: Untersuchungen zur Photodoppelionisation von Lithium mit MOTRIMS	155
G.1	Einleitung	155
G.2	Das Experiment	157
G.3	Ergebnisse	159
G.4	Zusammenfassung	164
	Bibliography	165

CONTENTS

Chapter 1

Introduction and Motivation

Since the first observation by Hertz in 1887 [Her87] and the interpretation by Einstein in 1905 [Ein05] the investigation of photoionization has followed a continuous development. In particular with the advent of modern light sources as synchrotron radiation sources, photoionization became an important tool not only in physics to probe the inherent structure and dynamics of atoms, molecules and solids but also in chemistry and biology.

While the one-electron-transition in bound systems, as a result of the absorption of a single light quantum (the photon), is the most simple process, there are other fundamental processes of interest as the non-linear multi-photon absorption or multiple-electron transitions. Although the former reaction was discussed theoretically already in 1931 by Maria Göppert-Mayer [Goep31] within her Ph.D thesis ‘Über Elementarakte mit zwei Quantensprüngen’, the experimental observation became possible only thirty years later with the development of lasers. Starting with the pioneer experiment by Kaiser and Garret [Kai61] in 1961, who demonstrated the production of optical harmonics via the method of two-photon absorption and fluorescence emission in the Eu^{2+} endowed CaF_2 crystal, various fundamental non-linear processes have been verified experimentally promoting our understanding of light-matter interaction: the first multiphoton ionization (MPI) observation by Voronov and Delone [Vor66]; the discovery of above threshold ionization (ATI), using the advent of pulsed, high intensity laser sources [Ago79]; the verification of the ponderomotive effects [Bor79, Ago87]; the distinguishing of the MPI mechanisms, non-resonant multiphoton ionization (NRMPI) and resonance-enhanced multiphoton ionization (REMPI) [Mor76, Sch98b]; and the non-sequential double ionization process (NSDI), which gives rise to a prominent ‘knee’ structure in the laser-intensity dependent ion yield [Fit92, Kon93, Wal94a], *etc.*.

On the other side, single-photon induced multi-electron transitions where more than one electron is ionized or excited, have been an important topic in atomic and molecular physics research due to their prototype character to explore electron-electron correlation. At low photon energies it is generally argued that only one electron absorbs the photon subsequently interacting with the second electron and promoting it to an excited state or the continuum. Most of the discussion has been focused on the photo double ionization (PDI) of the helium atom which is the simplest two-electron-single-photon process.

In this respect important milestone experiments were: the first kinematically complete measurement of helium photo double ionization [Sch93]; the confirmation of the combined effect of post-collision interactions (PCI) and interference in indirect PDI [Rio01]; the identification of PDI mechanisms at a high excess energy [Kna02a]; the complete photo-fragmentation of the D_2 molecule [Web04], involving a Coulomb explosion of the molecule; the discovery of strong electron correlation effects in double-excitation resonant states of rare gases [Mad63]; the demonstration of the intensity inversion between main and satellite lines in atomic photoionization [Cub07].

Accompanying the experimental studies of photo-ionization of atoms and molecules various theoretical approaches have been developed to describe real few-body time-dependent quantum systems. For example, the many-body perturbation theory (MBPT) has been applied to both single-photon double ionization [Ist02] and two-photon complete break-up of He [Nik01]. The double screened Coulomb method has been used to calculate total and single energy differential cross sections for He [Pro93, Pon95, Pon96]. The convergent close-coupling (CCC) method has successfully calculated total as well as single and triple differential cross sections for helium [Khe98a, Khe00b]. Recently the hyperspherical R -matrix method has had great success in calculating single differential and triple differential cross sections for helium for a wide range of electron energy sharings [Mal99, Mal00, Sel02]. It should be noted here, that despite all the difficulties to find an adequate theoretical description within the framework of quantum mechanics, many of the processes and fragmentation channels can be cast into appealingly intuitive and simple mechanistic pictures, which greatly facilitate their identification and the interpretation of experimental data.

As result of these developments for the benchmarking helium target a remarkable agreement has been achieved between non-perturbative theoretical approaches and experimental observations for a wide range of incident photon energies and energy sharings between the outgoing electrons. Therefore, it seems that the photo double ionization of the ground state of helium may be regarded as a well understood problem from both the theoretical and experimental viewpoints.

Being a three-electron system, the element of lithium represents the next step in complexity after helium. The photoionization of Li is of topical interest not only because experimental ionization data of this target is sparse compared to the amount of data available for He, but rather due to the following more profound reasons:

Firstly, the loosely bound outer electron and deeply bound closed inner shell make lithium a qualitatively completely different target as compared to the extensively studied noble gases [Bri00, Bol04, Ava05]. The first ionization potential IP_{Li} is just 5.39 eV, while the second one IP_{Li^+} is about 75.64 eV [NIS09]. As a consequence, for reactions with lower energy transfer where only the outer electron is involved lithium constitutes an effective atomic hydrogen like target, where the inner electrons only give rise to a modification of the pure $1/R$ - Coulomb potential. Thus, lithium becomes an ideal target for reactions where a simple target description is advantageous.

Secondly, lithium contains one additional bound electron with respect to helium. The complete fragmentation of lithium, thus, represents a pure four-body system which in its full complexity still is a highly challenging problem for theorists and experimentalists.

The exact description of the triple ionization of Li (as well as the double ionization of Li by electron impact) involving three free electrons today is beyond the capability of even advanced computation methods which are able to handle only up to two continuum electrons [Res99, Bra02]. Therefore, lithium is a benchmark atomic system for the further development of theory towards many-body Coulomb systems. An interesting aspect of this research is the recent discussion of the role of the initial state structure in threshold phenomena. Until recently it was well accepted that multi-electron ejection close to threshold evolves via highly symmetric emission configurations independent of the initial state [Kla76]. Two-electron emission shows the well known Wannier-configuration where the electrons recede back-to-back with equal energies. Three electron emission was assumed to proceed via symmetric emission in a common plane with 120° relative angle. Only recently, the generality of this behaviour was questioned by surprising theoretical results for triple photoionization (TPI) of Li. These predict a nonsymmetric, *T*-shaped final configuration of the emerging electrons at threshold [Emm08] due to the double shell structure of the Li ground state. Despite these exciting assertions, no higher differential TPI experiments have been reported, to the best of our knowledge, exploring the initial-state dependence of this process. On the other side, for three electron emission after ionization of equivalent electrons, as it is the case for electron impact double ionization of helium symmetric emission is predicted theoretically [Mal97, Goet06, Emm08] as well as observed experimentally [Ren08].

Thirdly, lithium atoms can be prepared easily by means of optical pumping and, therefore, multiple-ionization starting from different excited and/or spatially anisotropic initial states can be investigated. While respective experiments do not exist so far there are theoretical calculations comparing DPI for the He($1s^2\ ^1S$) ground state to the He($1s2s\ ^1,3S$) excited states at high energies [Ten94] as well as close to threshold [Har98, Khe00a, Col03]. Significant differences in the total cross sections, their excess energy dependence, and their electron angular distributions were predicted essentially based on the symmetry of the two-electron wavefunction and selection rules. The present work concentrates on photo-double ionization of lithium with threshold energy of $E_\gamma > 81.03\text{ eV}$. Here, the significant difference between the electron-binding energies for the K- and L-shell results in vastly different photo-absorption cross sections being more than one order of magnitude higher for absorption in the inner-shell compared to the outer-shell. Therefore, differently from ionizing two equivalent electrons as, e.g., in helium it is possible to differentiate between the electron which absorbed the primary photon and the one which was ejected by means of correlation. Thus, as will be elucidated in more detail below preparation of the valence electron allows to modify and control the electron-electron interaction without changing the primary photoabsorption process, thereby giving new insight into electron correlation. As was shown theoretically the two-shell structure also allows to distinguish different multiple ionization mechanisms [Khe01, Pat01] and to investigate the influence of exchange on the ejection process [Har98].

In order to get insight into the underlying dynamic mechanisms and to critically test theories, highly differential experimental data are indispensable. For two-electron emission kinematically complete measurements delivering fully differential cross sections have been feasible since the first and pioneering ($e, 2e$) experiment for electron impact single

ionization of atoms by Ehrhardt *et al.* in 1969 [Ehr69]. This was realized by the coincident detection of both final state electrons with two electrostatic spectrometers. For double or triple-ionization studies, the small combined solid angle of the several spectrometers required for the multi-particle coincidence detection and the small cross sections for multiple-ionization¹ sets serious challenges to the experimentalists. Therefore, new electron spectrometers with improved detection efficiency have been developed. These may provide extended collection solid angles so that a range of ejection angles is viewed simultaneously, or the simultaneous detection of a range of electron energies, or indeed they may do both. Of the first category are toroidal analysers [Hue94, Red97] and multiple analyzer platforms [Bly99], time of flight spectrometers [Weh95] belong to the second type, and charged particle projection techniques [Doer98, Hue00] belong to the third.

Nevertheless, it should be noticed that, for most of the methods listed above, the phase space acceptance was rather small due to technical restrictions, covering a selected fraction only. In this respect the more recently developed multi-particle imaging spectrometers as the cold target recoil ion momentum spectrometer (COLTRIMS) [Mer95] and the ‘reaction microscope’ (ReMi), developed by Ullrich and Moshhammer in 1994 [Mos94], mark a decisive improvement and basically overcome most of the previous limitations by employing projection techniques. They combine a recoil-ion spectrometer and an electron spectrometer covering a solid angle of 4π for low energetic target fragments by applying appropriate guiding fields. In order to obtain sufficient momentum resolution a localised and cold (in the sub- K range) atomic or molecular target is required which is normally provided by means of a supersonic gas jet.

The field has also benefited by the development of synchrotron radiation sources and VUV monochromators as the source of tunable VUV radiation with high flux, narrow spectral spread and various polarization modes (elliptic, linear and circular). In recent years, a number of free electron laser (FEL) facilities — the fourth generation photon source, have come into operation [FEL09]. The high intensities available, the unique temporal structure with a pulse width in the few 10-fs range along with a continuously tuneable frequency at narrow bandwidth enables, for the first time, to explore non-linear processes in the VUV regime with ultimate precision. A prominent example is the two-photon double-ionization of helium where first experiments exist [Rud08].

Since a cold target sample of the element studied here, lithium, cannot be provided via the ‘conventional’ method of the supersonic gas jet, a conceptually different technique, magneto-optical trapping (MOT) is used [Din92, Sch96, Mar98]. Dating back to 1975, the idea of ‘laser cooling’, an active slowing method applied to neutral atoms through a radiation pressure force, was proposed by Hänsch and Schawlow [Haen75]. During the last three decades this principle rejuvenated atomic physics and lead to substantial progress in experiments and theory of cold gases. A series of experiments demonstrated that by a counter-propagating laser beam, a thermal atomic beam can be slowed down to rest essentially [Bal79, Phi82, Ert85, Zhu91]. After the first successful demonstration of trapping atoms (in momentum space) in a three-dimensional optical molasses by Chu

¹Taking Li atom for example, the double ionization cross section $\sigma_{Li^{2+}}$ is about 10^{-21} cm^2 5 eV above threshold, and the triple ionization cross section $\sigma_{Li^{3+}}$ is at the level of 10^{-24} cm^2 [Col04].

et al. [Chu86], Raab *et al.* realized the spatial confinement via a hybrid trap (magneto-optical trap, MOT), which generated a position-dependent trapping force [Raa87]. This type of trap can accumulate up to 10^{10} atoms at temperatures of typically $100 \mu\text{K}$. In 1997, S. Chu, W. D. Phillips and C. Cohen-Tannoudji were awarded the nobel prize in physics “for development of methods to cool and trap atoms with laser light”. The so-called magneto-optical trap technique soon became a standard method to produce cold atom or molecule ensembles and, thus, lead to a wide range of applications in atomic physics and quantum optics. Examples are the creation of degenerate quantum gases [And95, Dav95, DeM99, Tru01, Don02, Joc03], the development of frequency standards (atomic clocks) driven by new precision spectroscopy methods [Kas89, Gib93, Cla95], the flourishing of the field of quantum information [Kuz03, Cho05, Yua08], the study of ultracold collisions [Nap94, Wal94b, Wei99] and even the precision experiments for testing the Standard Model (SM) [Beh09].

The magneto-optical trap also found applications in scattering experiments, as a superior tool for the target preparation, which provides a properly characterized target ensemble, in terms of its sufficient atom number, favorable density, negligible initial kinetic energy and well defined quantum state. Furthermore, it also has the option of manipulating the trapped atoms, *e.g.*, by laser excitation and optical alignment. A number of fragmentation experiments based on laser cooled target atoms have been performed to obtain absolute ionization cross sections by fluorescence imaging or time-of-flight spectroscopy, such as for electron impact ionization (Rb [Sch96, Kee00], Cs [Mac02, Luk05], Li [Hua02, Hua03] and metastable He [Uhl05]) and for photoionization as well (Rb [Din92], Cs [Mar98], Mg [Mad02] and metastable Ne [Cla06]).

Exploiting its main benefit, the intrinsically low temperature, a magneto-optical trap was combined with a recoil ion momentum spectrometer, resulting in a new concept known as ‘magneto-optical trap recoil-ion momentum spectroscopy’ (MOTRIMS). With respect to the promoted technique of COLTRIMS (COLd Target Recoil Ion Momentum Spectroscopy), MOTRIMS enhanced the recoil-ion momentum resolution to a higher level via reducing the mean thermal energy of the target further². Therefore, it would offer a detailed insight view into the dynamics of a strongly driven electron in the vicinity of its parent core, *e.g.*, studying photoionization processes near threshold, and detecting very small scattering angles in charge-transfer collisions as well. In years 1997 and 2000, Wolf and Helm performed pioneering experiments on multi-photon ionization of rubidium, a striking energy resolution of $1 \mu\text{eV}$ was achieved with the magneto-optically trapped atoms of $300 \mu\text{K}$ [Wol97, Wol00]. In the last ten years, the field of dynamics studies with alkaline metal MOTs was booming, dozens of ion-atom collision experiments have been performed, and most of them concentrated on the themes of charge transfer, electron capture reactions [Poe01, Tur01, Fle01] and single ionization processes [Kno06] or phenomena containing both capture and ionization [Kno05, Zap05].

It should be pointed out that a kinematically complete experiment requires the momentum resolved detection of $N-1$ particles where N is the number of continuum particles

²A minimum initial kinetic energy near 10neV in a Cs-MOTRIMS was reported by Coutinho *et al.* [Cou04].

in the final state. Thus, for charge transfer and single photoionization processes (whose initial state is well known and final state only contains two free particles) the sole detection of the recoil-ion is sufficient to determine the kinematics complete. Respective studies for processes giving rise to more free electrons, e.g., multiple ionization, are possible only if the detection of emitted electrons is permitted additionally. Therefore, the implementation of an electron spectrometer, as a decisive step forward with respect to the MOTRIMS concept, results in a more powerful and versatile apparatus —‘MOTReMi’, which is actually a combination of a magneto-optical trap and a reaction microscope.

The experimental realization of a MOTReMi is part of the work presented in this thesis. Aiming for a scientific apparatus for kinematically complete experiments, which enables the coincident detection of all charged collision fragments (ions and ejected electrons), which uses state-prepared ultra-cold atoms, and is capable to accept all kinds of projectiles (electrons, ions and photons), several technical obstacles need to be overcome.

The most challenging task is to integrate the magneto-optical trap into the reaction microscope. Both are in conflict with their requirements concerning the magnetic field: a gradient magnetic field is necessary to generate position-dependent trapping forces to cool and confine a MOT target spatially, while a homogeneous and stable extraction field is demanded for mapping and reconstructing momenta of ionized electrons. As a solution, a field switch operation mode, has been realized to circumvent this dilemma. Once a sufficient number of atoms are accumulated in the MOT, a short trapping field-free window is open for the reaction and data acquisition, followed by switching-on the MOT field and a recapture and/or reload process till the next projectile shot arrives.

To enhance the resolution of both the longitudinal and the transversal ion momentum, a modification on the ion spectrometer side has been made, fulfilling a ‘time- and position-focusing’ configuration. Together with the limited mean thermal energy of MOT targets, a momentum resolution of the recoil ion $\Delta p_{ion} = 0.05$ a.u. (in total for three dimensions, $\Delta p = \sqrt{(\Delta p_x)^2 + (\Delta p_y)^2 + (\Delta p_z)^2}$) has been achieved, which is a leading world record of COLTRIMS. Thus, it is comparable with the momentum resolution $\Delta p_e = 0.02$ a.u. achieved at the electron spectrometer side simultaneously.

Another essential task was to build up a powerful and reliable laser system for the MOT. Four different laser setups have been designed and applied to generate a Li-MOT. Finally, a diode laser system based arrangement led to a steady ultra-cold target ensemble with a density of $10^{10}/cm^3$ at a minimum temperature of about $400 \mu K$. In addition, our laser scheme in practice offers the intriguing possibility of further manipulation of the trapped atoms and the preparation of specific target states, such as excited states and the population of specific angular momentum states by optical pumping.

After successful commissioning, a series of photoionization experiments were performed on the lithium target, including the theme of this thesis, a campaign where the whole experimental setup was transported to the Free Electron Laser in Hamburg (FLASH) at DESY in order to perform a PDI study using the FLASH VUV photon source. Other measurements concerned lithium single ionization by multi-photon absorption and strong field ionization in infrared femtosecond laser pulses [Ste07, Sch08].

To realize the control of the threshold dynamics in photo double ionization of Li, which

involves two active electrons, an innovative experimental concept has been applied, which manipulates the electrons correlation via initial state preparation. To explore the threshold phenomena, ionization reactions have been studied at photon energies of both $E_\gamma = 85$ eV and $E_\gamma = 91$ eV. The photoionization plus simultaneous excitation (PIE) phenomena have also been studied within our experimental frame.

This thesis is structured as follows: Chapter 2 gives an introduction on the phenomena of multiple photoionization and related processes encountered in the above-threshold ionization regime, as well as the intuitive pictures of double ionization mechanisms. Additionally, a selection of theoretical treatments is presented. Chapter 3 reviews the principles of laser cooling and trapping of neutral atoms, and the method of loading the trap. The properties of lithium specific to laser cooling are also presented for completeness. Chapter 4 presents a general background of the free electron laser, the breakthrough technology in photon science, and the properties of FLASH (Free electron LASer in Hamburg) facility, which was used in our study. Chapter 5 deals with the experimental setup, giving detailed information about the numerous different components. Apart from the heavy attention paid to the combination of magneto-optical trap and reaction microscope, the newest enhancements and modifications of the MOTReMi apparatus, *e.g.*, 3D-Focusing (time and position) and dual-frequency MOPA (master-oscillator-power-amplifier) scheme, are stressed out particularly. The following Chapter 6 is dedicated to the methods of data analysis, including modifications on the raw data, classification of reaction channels, and determination of atomic state populations. Chapter 7 finally gives an overview of the experimental results, which focuses on PDI of lithium atoms and the PIE processes as well. Conclusions on the threshold dynamic and kinematic mechanisms are drawn. In the end, this thesis closes with a summary and gives an outlook on future perspectives for experiments with this unique research tool.

Chapter 2

Theory on Photoionization

The multiple ionization of light atoms (or small molecules) induced by absorption of a single photon is the most fundamental few-body reaction in atomic and molecular physics. This process is of fundamental and high topical interest since it is mediated exclusively by internal target correlation, *i.e.*, the interactions of the atomic or molecular constituents before and after the very instant of photo-absorption. However, this dynamic correlation can also be revealed in other ways, for example, by electron impact ionization. The $(\gamma, 2e)$ process is preferred to the $(e, 2e)$ or $(e, 3e)$ one, as an easier system to treat theoretically and to interpret experimentally. Especially for the photon in vacuum ultraviolet (VUV) range, the essence of advantages comes from the ‘beauty of photon’: the weak interaction with the atom, the known energy, angular momentum and parity transfer (with the light polarization known), the negligible momentum transfer, the chargeless state of the photon and its annihilation after the interaction.

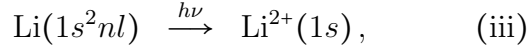
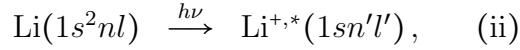
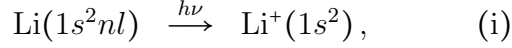
Our experiment aiming at photo double ionization (PDI) was performed by combining MOTRIMS and the intense FEL radiation at FLASH. To assist in the experimental search for interesting correlation effects related with PDI of lithium, we briefly present some theoretical background introduction here, with several available calculation methods included as well, which could reproduce these phenomena of lithium photoionization mathematically.

2.1 Basics of Photo-Fragmentation Process

As an atom or molecule absorbs a light quantum, a wide range of phenomena may happen, depending on the binding energy and symmetry of the target. Among such photon induced reactions are processes like ionization or excitation, *etc.*, where one or several bound electrons change their quantum-state, and hence the electron-correlation based internal-collision can be viewed as a dynamical few-body problem.

In the case of the lithium atomic target, if the incident photon’s energy is just above the ‘lowest’ double ionization threshold, in which one of the two $1s$ electrons (standing as inner shell electron, IS) and the valence electron (standing as outer shell electron, OS)

are involved, an insight into dynamical electron-electron correlation is provided. In total, three different reaction paths can be opened:



where nl and $n'l'$ indicate the initial and final states of the valence electron. The OS single ionization (i), IS single ionization with simultaneous OS excitation (ii) (including the special case in which $n = n'$, $l = l'$, meaning it degenerates to the pure IS single ionization) and double ionization (iii) of lithium are listed, respectively.

Especially, the lithium PDI process with an IS- and an OS-electron involved is of interest in the study of the three-body continuum Coulomb system. Generally, this reaction can be decomposed into two phases: firstly, the IS electron obtains the energy transferred by a photon and gets ionized; secondly, an induced ejection happens to the OS electron subsequently or instantly [Car81, Ish91, Khe01, Pat01, Sch02]. Regarded as an effective three-body process, these type of PDI mechanisms are dictated by the electron-electron correlation.

The photoionization plus simultaneous excitation process (PIE) also represents a different three-body problem with the OS electron staying bound in the final state. Actually, in this kind of reaction two active electrons participate, and no doubt, their correlation through the electron-electron interaction plays a non-negligible role. An argument about the spatial overlap of the initial and final state wave functions gives a qualitative explanation on this spectacular dynamic process [Zho99, Che00, Cub07].

However, in both cases, a fully quantum mechanical description remains as a challenging task, which concerns the three particles in a final state interacting by the long-range Coulomb force.

2.1.1 Mechanisms of Photo Double Ionization

Since the pioneering works by Carlson [Car67], Byron and Joachain [Byr67] both in 1967, it is generally accepted that mainly two different mechanisms, ‘shake-off’ and ‘two-step-one’ (also referred as knock-out), contribute to a two-electron emission following absorption of a single photon. The strengths of the different mechanisms leading to two-electron transitions vary as a function of the photon energy, while it is difficult to separate the processes explicitly. However, they are distinct with respect to their quantum nature: shake-off is a purely quantum mechanical phenomenon while two-step-one dynamics occurs classically as well as quantum mechanically. In addition, another mechanism named ‘photon sharing’ [Ten94] is also proposed to be the third contribution to the PDI process.

Shake-off Mechanism

Fig. (2.1) gives an intuitive picture describing the dynamic process of shake-off mechanism, and shake-up process as well (more precisely, for the case of ionization with simultaneous

excitation). When a photon interacts with an atom, it usually does so by means of the photoelectric effect in which all the energy is converted into the ejection of a single electron. However, if the emitted electron obtains substantial kinetic energy, and is removed from one of the inner shells (in particular for K shell) of the atom suddenly, there is an instant change in the atomic potential, which is induced by the change of effective charge and experienced by the outer shell electrons. If the outer shell electron (normally the valence electron) can not follow the potential evolution, it can relax to an unoccupied state of the remaining ion (excitation) with a certain probability, this phenomenon is referred to as shake-up (SU); or just fall into the continuum directly (ionization), which is termed as shake-off (SO).

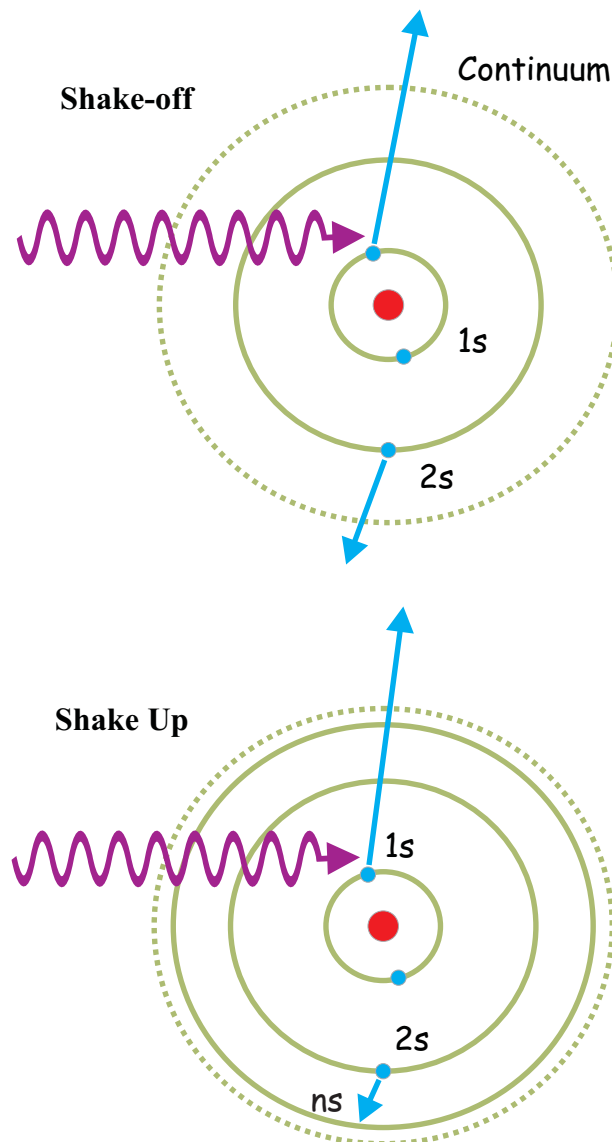


Figure 2.1: Shake-off/Shake-up mechanism

It is clear that the shake-off mechanism requires a certain excess energy above the ionization threshold which enables the first ejected electron to leave the atom quickly enough

to produce a sudden change of the atomic field. For this reason one would not expect this mechanism to be dominant near the double ionization threshold. In contrast, when the excess energy is large, one can neglect the interaction of the fast ejected electron (leaving the atom rather instantly) with the ion and the whole yield of the PDI process would be due to ‘shake-off’.

Two-step-1 Mechanism

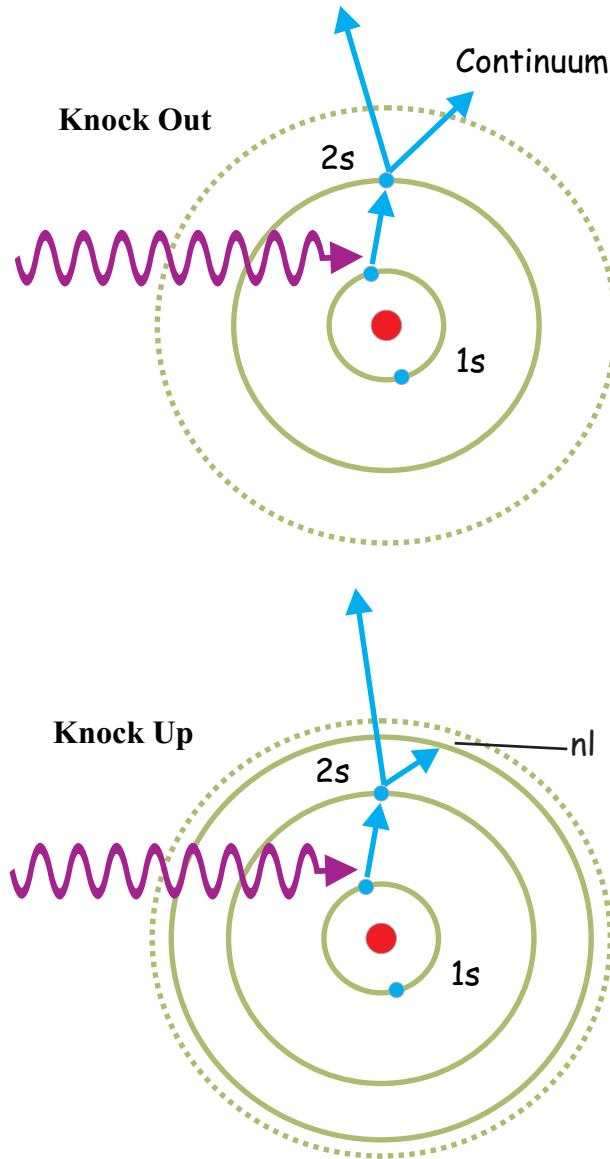


Figure 2.2: Two-step-1 (Knock-out/Knock-up) mechanism

As illustrated in Fig. (2.2) (upper), if a projectile photon just supplies kinetic energy close to the double ionization threshold, the first photoelectron ionized will not escape abruptly, which allows the outer shell electrons follow the field change adiabatically, thus, weakening the ‘shake’ channel. However, the low kinetic energy of the ejected electron ‘on the way out’ favors a strong interaction with the remaining bound electrons, leading to an $(e, 2e)$ -

like reaction in which a secondary electron is knocked out. Due to the dynamic features of this PDI mechanism, the model is often termed as ‘TS1’ (Two-Step-1: two-step with one projectile interaction). Since the ejection of the second electron resembles electron impact ionization, and because the primary electron absorbing the photon (the projectile) is initially localized inside the atom near the nucleus, this inter-electron-collision corresponds to a ‘half-collision model’ [Pat01]. The contribution of the TS1 mechanism is not only limited to the PDI process, but also favors the PIE reaction, in which the secondary electron is excited via the internal collision. Intuitively, the contribution by TS1 decreases as the photon energy increases, since the higher the excess energy carried by the primary electron the weaker the inter-electron-interaction it endures.

Compared with the ‘shake’ mechanism, the ‘two step’ mechanism channel, however, is more complicated because it depends delicately on correlation effects between atomic electrons. Physically, this sensitivity is very intriguing, since it might enable the distinction between the two mechanisms possible, via manipulating the target’s electron correlation.

Photon Sharing Mechanism

In both SO and TS1 mechanisms, the large net momentum carried away by electrons must originate from a hard collision with the nucleus, because the photon can impart energy to the electrons, but not momentum (with the retardation neglected throughout). However, if two electrons partake of one photon, they would leave in a Coulomb explosion manner, without exchanging as much momentum with the nucleus as in TS1 and SO. Actually, nearly no net momentum needs to be exchanged with the nucleus if the two electrons partition the photon energy equally. This PDI mechanism is often referred to as photon sharing (PS) [Ten94].

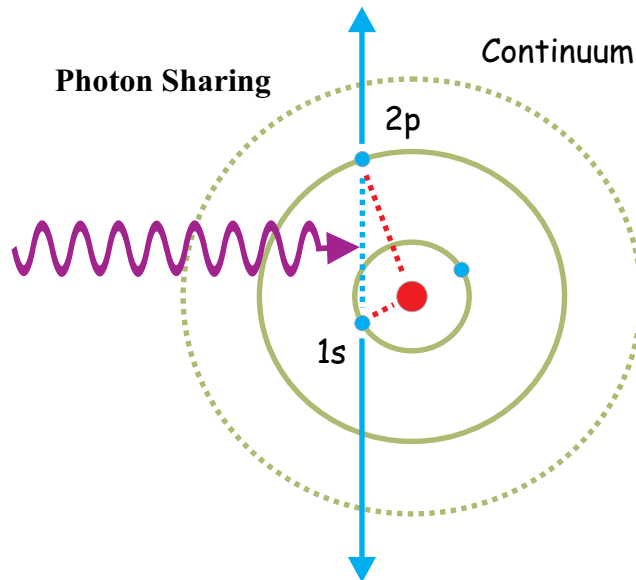


Figure 2.3: Photon sharing mechanism

If the electric dipole (in the center-of-mass coordinate of two charged particles) does

not accelerate, photon sharing is somewhat inhibited due to the missing of radiation absorption. Consequently, two electrons can absorb radiation either under an external force, *e.g.*, an extra driving field which induces a dipole motion, or in the presence of a third body (usually the nucleus), as displayed in Fig. (2.3); while an isolated electron-positron pair can absorb radiation naturally. It should be pointed out that, in the ‘third body’ consideration, the photon can be shared by the electrons only if they are close to each other and to the nucleus. When these two electrons constitute a spin-triplet state, photon sharing is suppressed because of the Pauli exclusion principle; even when the ‘initial state’ is spin singlet, the two electrons can not emerge with exactly equal and opposite momenta, a rule which follows from inversion symmetry [Ten94].

After having presented all three possible DPI mechanisms, we summarize and emphasize that: in shake-off, the screening of the nucleus by one of the electrons plays a crucial role, but the correlation between the electrons plays no role; on the other hand, correlation in the final continuum state plays a crucial role in TS1; while the correlation in the initial bound state plays a crucial role in photon sharing. Therefore, due to the difference of dynamics, the different mechanisms would leave their mark on the exhibited angular distribution and energy partition of the ejected electrons: the very low energy secondary electrons with an isotropic manner in emission pattern are mostly emitted via the shake-off process; while a higher energy transfer requires a hard binary collision and leads to an angle of 90° between the electrons, which is one signature of the TS1 mechanism; the photon sharing channel would present the two outgoing electrons with nearly equal and opposite momenta. However, in principle the PDI amplitude is a superposition of all contributing amplitudes. Thus, the momentum distribution of the two ionized electrons exhibits a coherent behavior, entangling the characteristic emission patterns of every mechanism.

2.1.2 Photoionization plus Excitation

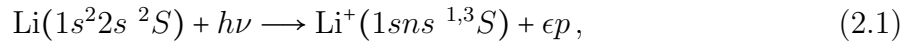
Besides photo double ionization (PDI), the photo single ionization plus simultaneous excitation (PIE) of atoms can also happen after absorbing a photon with an energy above the threshold for double ionization, exhibiting another aspect of the dynamic process with two active electrons involved. This kind of photoionization process, leading to satellites produced by inner-shell photoionization, is another manifestation of electron correlation, and thus it is strictly forbidden in the ‘one-electron’ model of the atom [Abe76].

Photoionization of an atom from the initial state into the continuum leaves the core-ionized residual ion in its lowest energy state, corresponding to the so-called main line in the photoelectron spectrum (the electronic configurations of the initial atomic state and of the final ionic state are the same, except for the ejected electron) or in a state of higher energy, corresponding to the correlation satellite lines, accompanying with an alteration on the principal quantum number n or orbital quantum number l (or both) of a second electron. The nature of the mechanisms responsible for the characteristics of the correlation satellites differs essentially, depending upon the behavior of the orbital quantum number l of the ‘second’ electron during the transition.

Case $\Delta l = 0$

The satellites in which the excited electron conserves its angular momentum during PIE have been interpreted well by the shake theory [Car68], which entitle them ‘shake-up’ (SU) satellites consequently. Like the ‘shake-off’ depiction for PDI, instead of jumping into continuum, the second electron collapses to an orbital with a relative higher principal quantum number than the initial state, which results from monopole relaxation of the system following the ionization of an inner shell electron. Fig. (2.1) (bottom) presents ‘shake-up’ transition for Li atom from the ground state $2s$, as an example elucidating such a PIE mechanism.

Photoionization of one $1s$ electron in Li gives rise to the $(1sns \ ^1,^3S)$ SU satellites, which is written as



with $n > 2$. The intensity is proportional to the matrix element $\langle \epsilon p | D | 1s \rangle \langle ns | 1s \rangle$, where the first term accounts for the single photoionization and the second term describes the satellite excitation. Consequently, the branching ratio between the satellite and main line reads $|\langle ns | 2s \rangle|^2 / |\langle 2s | 2s \rangle|^2$.

As the primary photoelectron leaves the atom more and more quickly, the satellite transition intensity approaches a constant value asymptotically, with a fixed ratio to the main line intensity. However, for low photoelectron kinetic energies, the remaining electrons have enough time to adjust adiabatically to the gradually changing screening potential of the nuclear charge. Therefore, the readjustment is the most effective for low photoelectron kinetic energies, leading to the decrease of satellite intensity towards the ionization threshold.

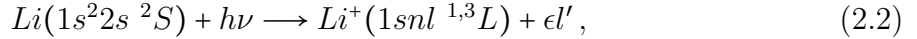
Case $\Delta l \neq 0$

Transitions with the excited electron’s orbital number changed, which are classified as a second category of satellites, imply an exchange of angular momentum between the residual ionic core and the outgoing photoelectron. Comparable with TS1 in PDI, these satellites results from a ‘soft collision’ between one of the bound electrons in the ion with the ejected photoelectron on its way out [Cha71, Cha75b, Car77]. This mechanism is shown in Fig. (2.2) (bottom), where Li in the $2s$ ground state is chosen as the target for PIE.

This type of collisional process has been termed also as inelastic scattering [Cha71], internal electron scattering [Cha75b], continuum-continuum configuration interaction [Mar76a], direct knock-out [Amu93], or interchannel coupling [Man76], as well as the improper name ‘conjugate shake-up’ satellites [Wui74, Gel74], with an intent to keep an analogy with the ‘shake-up’ satellites. We abandon the misleading term in describing the PIE satellites, since it just refers to certain overlap integrals in the satellites intensity calculations via the Hartree-Fock approximation in history, and may confuse the nature of the real mechanism. We choose the name interchannel coupling (IC) satellites in the following. Intuitively, the intensity of IC satellites should increase towards threshold, which is confirmed by all theoretical predictions. It should be noted, however, that this ‘soft collision’ mechanism can also populate the SU satellite states in a same manner. As a consequence, it is difficult to

identify the mechanisms contributed to PIE in the case of no angular momentum exchange $\Delta l = 0$, solely based on the photon-energy dependence of their transition amplitudes near the ionization threshold. Though, the variation of the intensities of the satellite lines, as a function of photon energy, is still valuable information to assign the origin of various correlation satellites.

Photoionization of one $1s$ electron in Li gives rise to the $(1snl\ ^{1,3}L, l \geq 1)$ IC satellites:



with $n > 2$ and $l' = l + 1$ or $l' = l - 1$.

2.1.3 Dependence of PDI Dynamics on the Quantum Numbers of the State $\{L M S \pi\}$

Indeed, the main object of the studies on photo-double-ionization is to understand the correlated motion of the electrons emerging from the nucleus, *i.e.* how energy, momentum and angular momentum are shared. Routinely, a triple-differential cross section (TDCS, expressed as $d^3\sigma/d\Omega_1 d\Omega_2 dE_2$, where $d\Omega_{1,2}$ denote the emission solid angles of the two outgoing electrons and dE_2 is usually the energy of an ejected electron) is used to describe the three-particle final state in a kinematically complete way, with the remaining four degrees of freedom fixed by momentum and energy conservation, and the dipole approximation. The structure of the TDCS is strongly influenced by the symmetry of the final state in terms of $\{L M S \pi\}$, a complete set of total orbital, spin and parity, particularly utilizing the fact that photon absorption transmits a single unit of angular momentum to the atom, while, the individual orbital angular momenta of the two electrons are not good quantum numbers. For an atomic bound system with low and intermediate nuclear charge Z , the LS coupling scheme is valid as a good approximation, which implies that the spin-orbit interaction can be treated as a ‘small’ perturbation, and the total orbital angular momentum L and total spin S are approximately good quantum numbers individually. The projection M of the angular momentum L and the parity π are additional quantum numbers of the bound atomic system.

Pioneered by Huetz and coworkers [Hue91, Sel87], a mathematical approach of the transition matrix element and cross section by expanding in terms of angular functions has been developed. We describe this approach in the following.

Parametrization of the Transition Matrix Element

Within the LS coupling scheme we consider the matrix element for transition \hat{T} of a pair of electrons from an initial state $|L_i M_i S_i \pi_i\rangle$ to a final state characterized by $|\vec{k}_1, \vec{k}_2\rangle$. The general matrix element T_M reads:

$$T_M = \langle \vec{k}_1, \vec{k}_2 | \hat{T} | L_i M_i S_i \pi_i \rangle .$$

For PDI, within the dipole approximation we substitute the arbitrary transition operator \hat{T} with $\vec{e} \cdot \vec{D}$, where $\vec{D} = (\nabla_{ra} + \nabla_{rb})$ is the dipole operator in velocity form for two electrons;

due to the spin conservation in the transition, spin S is not specified, thus, the matrix element becomes

$$T_M = \langle \vec{k}_1, \vec{k}_2 | \vec{e} \cdot \vec{D} | L_i M_i \rangle = \sum_{LM\ell_1\ell_2} \langle \vec{k}_1, \vec{k}_2 | \ell_1 \ell_2 LM \rangle \langle k_1 k_2 \ell_1 \ell_2 LM | \vec{e} \cdot \vec{D} | L_i M_i \rangle. \quad (2.3)$$

By decomposing the bipolar harmonics in terms of complete products of Racah tensors C_m^ℓ , and by expanding the scalar product in terms of spherical components, the final result is derived as the compact form

$$T_M = \sum_{L\ell_1\ell_2} [L_i]^{-1/2} \langle \ell_1 \ell_2 L \| D^1 \| L_i \rangle [e^1 \otimes C^L(\vec{k}_1 \vec{k}_2, \ell_1 \ell_2)]_{M_i}^{L_i}, \quad (2.4)$$

where the reduced matrix element is a function of k_1 , k_2 , and thereby the emission energies. Hence the angular dependence has been separated, at a cost of introducing an infinite sum over the angular momenta $\ell_1 \ell_2$.

However, the bipolar harmonics of rank L can be expanded in simpler harmonics where, for arbitrary $\ell_1 \ell_2$, the ranks of the spherical harmonics involved cannot exceed the value L , *i.e.*

$$C^L(\ell_1 \ell_2) = \sum_{\lambda=\lambda_P}^L a_\lambda(\ell_1 \ell_2 L, \cos \theta_{12}) C^L(\lambda, L + \lambda_P - \lambda), \quad (2.5)$$

where $\lambda_P = 0, 1$ according to whether $\ell_1 + \ell_2 - L$ is even or odd. The angle θ_{12} is simply the (body-fixed) angle between the vectors \vec{k}_1 and \vec{k}_2 , which depends on the electron-electron correlation [Man96].

Parametrization of the Cross Section

The cross section should similarly be expressible in terms of bipolar harmonics. As the differential cross section is proportional to the modulus square of the transition matrix element, it follows from Eq. (2.4):

$$d\sigma(\vec{k}_1 \vec{k}_2) \propto \sum_{L\ell_1\ell_2\ell'_1\ell'_2} [L_i]^{-1} \langle L_i \| D^1 \| \ell'_1 \ell'_2 L \rangle \langle \ell_1 \ell_2 L \| D^1 \| L_i \rangle \cdot [e^1 \otimes C^L(\vec{k}_1 \vec{k}_2, \ell'_1 \ell'_2)]_{M_i}^{L_i} [(e^1)^* \otimes C^L(\vec{k}_1 \vec{k}_2, \ell_1 \ell_2)]_{M_i}^{L_i} \quad (2.6)$$

where irrelevant arguments have been omitted for brevity. Indeed, it can even be extended to a more general case, in which an arbitrary number of electrons are involved. It can be rearranged in a transparent form, through the separation of the polarization properties of light, and the generalized Clebsch-Gordan series [Mal97]

$$d\sigma(\vec{k}_1 \vec{k}_2) \propto \sum_{K=0}^2 \sum_{L_1 L_2}^{\infty} \sum_{\ell_1 \ell_2 \ell'_1 \ell'_2}^{\infty} B_K(k_1 k_2 \ell_1 \ell_2 \ell'_1 \ell'_2) C^K(L_1 L_2, \vec{k}_1 \vec{k}_2) T^K, \quad (2.7)$$

where the $T^K = [e^1 \otimes (e^1)^*]^K$ is the separated light polarization tensor. However, in view of the large number of coherent summations, such an expansion is of little use in fitting to experimental data with the aim of extracting coefficients B_k . An alternative parametrization of the cross section was derived [Man96], in which the vector quantities

involved appeared directly, rather than tensorial sets C^K and T^K composed of these vectors. Using the set \vec{k}_a, \vec{k}_b of momenta, the TDCS can be written as

$$d\sigma(\vec{k}_a \vec{k}_b) \propto \sigma_0 + \xi \sigma_1 \hat{k} \cdot (\vec{k}_a \times \vec{k}_b) + \sigma_2 \{3\text{Re}((\vec{e} \cdot \vec{k}_a)(\vec{e}^* \cdot \vec{k}_b)) - \vec{k}_a \cdot \vec{k}_b\} \\ + \sigma_2^{(1)}(3|\vec{e} \cdot \vec{k}_a|^2 - 1) + \sigma_2^{(2)}(3|\vec{e} \cdot \vec{k}_b|^2 - 1), \quad (2.8)$$

where ξ is the degree of circular polarization (Stokes parameter) and \hat{k} the direction of photon propagation. The coefficients σ_i are functions of k_a , k_b and θ_{ab} , which can be related to the coefficients B_K of the expression (check [Man96] for details).

Selection Rules

For certain momentum configurations, the right hand side of Eq. (2.3) may become null: either, the matrix element $\langle k_1 k_2 \ell_1 \ell_2 LM | \vec{e} \cdot \vec{D} | L_i M_i \rangle$ vanishes, depending on the symmetry of the initial state and the nature of the dipole operator \hat{D} ; or, the bipolar harmonic $\langle \vec{k}_1, \vec{k}_2 | \ell_1 \ell_2 LM \rangle$ becomes zero for particular directions of the momenta $\vec{k}_{1,2}$. This leads to selection rules derived for all possible two-electron final states [Mau95].

The nine distinguishable momentum configurations to be discussed in the following are:

- (A) both \hat{k}_1, \hat{k}_2 are perpendicular to some quantization axis z ;
- (B) $\vec{k}_1 = \pm \vec{k}_2$ ‘parallel/antiparallel emission’;
- (C) $\vec{k}_1 = -\vec{k}_2$ ‘back-to-back’ with equal energies;
- (D) $\vec{k}_1 = \vec{k}_2$ ‘co-direction’ with equal energies;
- (E) $k_1 = k_2$ ‘equal kinetic energy sharing’;
- (F) $k_1 = k_2$ and $\theta_1 = \pi - \theta_2$;
- (G) $k_1 = k_2$ and $\theta_1 = \theta_2$;
- (H) $k_1 = k_2$ and $\theta_1 = \pi - \theta_2$ and $\phi_1 = \phi_2$;
- (I) $k_1 = k_2$ and $\theta_1 = \pi - \theta_2$ and $|\phi_2 - \phi_1| = 180^\circ$.

where the angles θ_i and ϕ_i ($i=1,2$) are the polar and the azimuth angle of the electron momenta \vec{k}_1 and \vec{k}_2 with respect to some quantization axis z (normally the light polarization axis).

In an electric dipole (E1) transition, only a very restricted number of states are populated after the absorption of a single photon. Since the photon carries one unit of angular momentum, the parity of the system π changes from even to odd, or vice versa; and the total orbital angular momentum L is changed to $(L - l)$, L , $(L + 1)$ at most; while the total spin S is conserved. With a further assumption that the light is linearly polarized, the projection M of the angular momentum L gets unaffected, due to the transition rule $\Delta M = 0$. For these possible states of the atomic system, the selection rules which are connected to some specific emission patterns can easily be applied.

Tab. (2.1) gives an overview of the applicability of selection rules A-I for a few final states up to $L = 3$, which are possibly reached after a PDI transition. Apparently in this list, for the $^1S^e$ ($M_S = 0$) and $^1D^e$ ($M_D = 0$) symmetry configurations, none of the specific selection rules applies, which suggests a high freedom in these two-electron emissions. Therefore, at threshold the two electrons are expected to escape from the ion in opposite directions prevalently, due to their mutual repulsion, as considered by Wannier theory.

Now, with all selection rules at hand we study their implications on PDI of lithium.

Table 2.1: Selection rules that apply for the given final states are denoted by crosses. Especially, selection rule B is divided into two groups, B1 for states with $M \neq 0$ and B2 for $M = 0$ terms.

State		Selection rule									
		A	B1	B2	C	D	E	F	G	H	I
$1S^e$	$M = 0$										
$3S^e$	$M = 0$				×	×	×	×	×		×
$1P^e$	$M = 0$			×			×				
	$M = \pm 1$		×	×			×			×	
$3P^e$	$M = 0$			×	×	×				×	×
	$M = \pm 1$		×	×	×	×					
$1P^o$	$M=0$	×			×			×		×	
	$M = \pm 1$		×		×						×
$3P^o$	$M = 0$	×				×			×		×
	$M = \pm 1$		×			×				×	
$1D^e$	$M = 0$										
	$M = \pm 1$		×							×	×
	$M = \pm 2$		×								
$3D^e$	$M = 0$				×	×		×	×	×	×
	$M = \pm 1$		×		×	×					
	$M = \pm 2$		×		×	×				×	×
$1D^o$	$M = 0$	×		×	×					×	
	$M = \pm 1$		×	×	×						×
	$M = \pm 2$		×	×	×					×	
$3D^o$	$M = 0$	×		×		×					×
	$M = \pm 1$		×	×		×				×	
	$M = \pm 2$		×	×		×					×
$1F^e$	$M = 0$			×							
	$M = \pm 1, \pm 3$		×	×						×	×
	$M = \pm 2$		×	×							
$3F^e$	$M = 0$			×	×	×				×	×
	$M = \pm 1, \pm 3$		×	×	×	×					
	$M = \pm 2$		×	×	×	×				×	×
$1F^o$	$M = 0$	×			×			×		×	
	$M = \pm 1, \pm 3$		×		×						×
	$M = \pm 2$		×		×					×	
$3F^o$	$M = 0$	×				×			×		×
	$M = \pm 1, \pm 3$		×			×				×	
	$M = \pm 2$		×			×					×

Firstly, let us take the PDI process of lithium in the ground state $|1s^2 2s\rangle$ with symmetry of $^2S^e$ via a linearly polarized light for example, the dominated final state of two free electrons therefore is $^1P^o (M_P = 0)$, here the polarization axis is chosen as quantization axis. With $M_P = 0$ and π odd it can easily be seen that selection rule A applies. Because of $\pi + S = 1$, selection rule C applies as well, ‘back-to-back’ emission of the two electrons with equal energies $\vec{k}_1 = -\vec{k}_2$ is therefore forbidden. This is a drastic restriction on the cross section especially close to threshold where electron correlation favours this configuration. However, it should be noticed that this zero cross section according to selection rule C is not an isolated zero in momentum space. Since $\pi + S = 1$ and $\pi + L = 2$, selection rule F applies, and therefore it is embedded in a cone of zeros $\theta_1 = \pi - \theta_2$ around the polarization axis (see Figure 1. (a) of [Mau95]). Selection rule H applies as well, but the corresponding configuration is part of selection rule F.

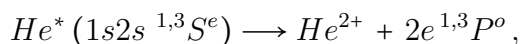
Secondly, we choose the double photoionization from the first excited state of lithium in $^2P^o (M_P = \pm 1)$ as another example. The two electrons in the continuum are projected to the final state $^1D^e (M_D = \pm 1)$ principally. Though in this case the selection rule C is no longer valid, due to the condition $\pi + S = 0$, the selection rule B1 applies because of $M_D \neq 0$, which indeed holds for any sharing of the energy, thus including the geometries concerned by selection rule C (emission along the quantization axis), leading to the same assertion as for the $^1P^o (M_P = 0)$ final state that ‘back to back’ emission of the two electrons with equal energies is largely suppressed also. Since $\pi + S + M_D$ is odd, the selection rule H for $M_L \neq 0$ with further restriction applies, so does selection rule I as well for $S + M_D = \pm 1$, corresponding to additional cones of zero cross section.

Finally we should keep in mind that selection D applies in any case, purely due to the Pauli exclusion principle in an interacting two-electron system.

Spin Orientations of Electrons in the PDI Process

During the PDI of a n -electron ($n \geq 3$) system, the spin orientations of two emitted electrons are possibly configured as ‘Singlet’ ($2S + 1 = 1$) and ‘Triplet’ ($2S + 1 = 3$), which contribute with different strength in the dynamic process, due to the different binding energy E_b in the ‘intermediate stage’ (in a general form $A \rightarrow A^+(^1,^3L) + e + E_b$). Here, the PDI of a lithium atom in ground state is chosen as the example. The ionization diagrams for the singlet and triplet configurations are shown in Fig. (2.4), where it is assumed that the PDI process not too far above threshold can be thought of as a two-step process, according to Samson’s argument [Sam90].

As can be seen in Fig. (2.4) (A), the $\text{Li}^{2+}(1s^2 S) + 2e(^3P)$ final state can be generated after ionization of the $\text{Li}^+(1s2s^1 S)$ singly ionized state without a ‘spin flip’, while the $\text{Li}^{2+}(1s^2 S) + 2e(^1P)$ final state can be created through the $\text{Li}^+(1s2s^3 S)$ state, as shown in Fig. (2.4) (B). The binding energy for $\text{Li}^+(1s2s^3 S)$ is 64.41 eV and the binding energy for $\text{Li}^+(1s2s^1 S)$ is 66.31 eV, which directly leads to the fact that the $\text{Li}^+(1s2s^3 S)$ intermediate state has a larger cross section than the $\text{Li}^+(1s2s^1 S)$ [Fer87, Lan91]. Furthermore, as inspired by the calculations for metastable $\text{He}(1s2s)$ [Har98, Khe00a]



which consistently show that the 1S state has a PDI probability about ten times higher

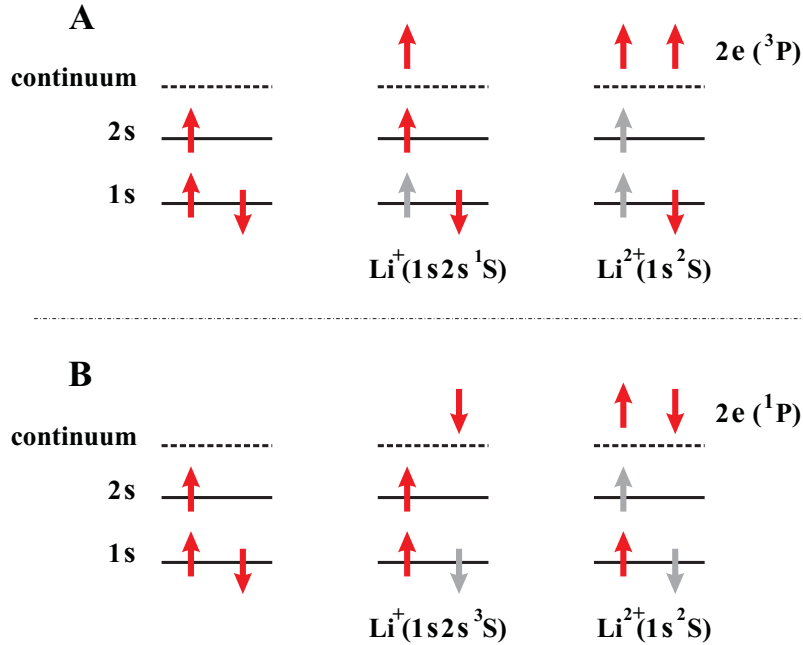


Figure 2.4: Schematic diagram of possible spin configurations after single- and double- photoionization of lithium from the ground state. The red and gray arrows represent the spin orientations of electrons and vacancies, respectively.

than the 3S state in the region 5 eV to 10 eV above threshold. In analogy we expect that in the case of Li PDI reaction, the two fragmented electrons would end up in the $2e(^1P)$ state other than in the $2e(^3P)$ state, or in another words, the two escaping electrons are more likely to have an antiparallel spin orientation rather than a parallel situation.

This assertion has been approved by the observation by Wehlitz et al. [Weh02], comparing the double- to single-photoionization ratios of lithium $\sigma(Li^{2+})/\sigma(Li^+)$ (in the energy range from 81 to 110 eV) with those of helium in ground- and metastable-state.

However, the above discussion based on the simple model with a precursor of TS1 mechanism, is only valid close to the threshold, while at higher photon energies, TS1 is not the dominant process anymore (the ratios for PDI and electron-impact ionization show discrepancies in the high-energy limit, the electron-impact cross section will go to zero, but the PDI ratio will reach a nonzero value due to SO) [Sam90], which limits the applicability of the model to an energy region where the TS1 mechanism is still dominant.

It should also be noted that, lithium has a second $1s$ electron, which is assumed to provide just a screening effect and can be regarded as an inert core in the normal approximative treatment. In fact, the additional $1s$ electron will affect the overall strength of interaction as a third body; furthermore, it manifests itself in a different energy dependence, thus it affects the contribution of the different (energy-dependent) PDI mechanisms (SO, TS1, PS).

2.1.4 Fragmentation Influenced by Valence Electron Configuration

In PDI of many-electron atoms, the fragmented electrons may arise from different shells (one electron comes from an inner shell, one electron belongs to an outer shell). Depending on the photon energy, one is confronted with not only the direct ejection of both electrons, but also the sequential ejection, although in principle these two competing processes cannot be separated. In sequential PDI, one electron from an inner shell is ejected after photoabsorption, which immediately induces the formation of a well-defined intermediate resonant state with a characteristic lifetime; a subsequent decay of this state would result in an additional Auger electron in the continuum. The interaction of the primary electron with the resonant state and the Auger electron leads to so-called post-collision interaction (PCI) effects. This fragmentation mechanism is influenced by the valence electron configuration, which mediates the electron correlation involved in the PDI transition. This study has become an important sub-field of PDI, particularly where the direct and sequential processes cannot be separated.

To elucidate the PCI effect, the calculated single differential cross sections (SDCS) for PDI of atomic helium at four different excess photon energies from different initial state $\text{He}(1s2s^1S)$, $\text{He}(1s2s^3S)$ [Col03], are presented in Fig. (2.5) respectively, compared with the similar SDCS calculations for $\text{He}(1s^2^1S)$ [Col02a], in which the two emitted electrons originally stay in the same orbital. For comparison, we plot the single differential cross section against the normalized ejected energy (equal to ejected energy/excess energy). The magnitudes of the single differential cross sections reflect the total integral cross section at each excess photon energy. In the convention used here, the area under the single differential cross-section curve from 0 to E equals the total integral cross section.

By inspection of Fig. (2.5), the most striking difference found is that the SDCS from the $(1s2s^1S)$ and $(1s2s^3S)$ states exhibit the characteristic U-shape structure with much higher curvature than similar cross sections for the $(1s^2^1S)$ state, which are rather flat, even at an excess photon energy of 60 eV. In fact, this more U-shaped nature reveals the electron correlation during and after photoionization, since now the two ejected electrons are ionized from different shells and so they are less likely to be ejected with similar energies. Further on, for the $(1s2s^3S)$ state, the cross sections are drastically U-shaped, even at the lowest photon energies considered. While, at the higher energies, the possibility of equal energy sharing between the electrons (where the normalized ejected energy = 0.5) is nearly zero. This is due to the large electron-electron repulsion present between two electrons in the same spin state, and with equal outgoing energies [Col03]. Another theoretical work by Teng and Shakeshaft [Ten94], which considered much higher photon energies, also confirmed the statement that for double photoionization from the 3S state, the electrons are most likely to come out at very unequal energy sharings. While in contrast, for $1s^2$ case (or PDI of electrons from the same shell, in general), ejection at equal energies is almost as probable as at the unequal case in the moderate photon energy range.

The importance of electron correlations was also investigated by comparing the multi-electron transitions, so-called satellites lines, and the direct process, so-called main lines.

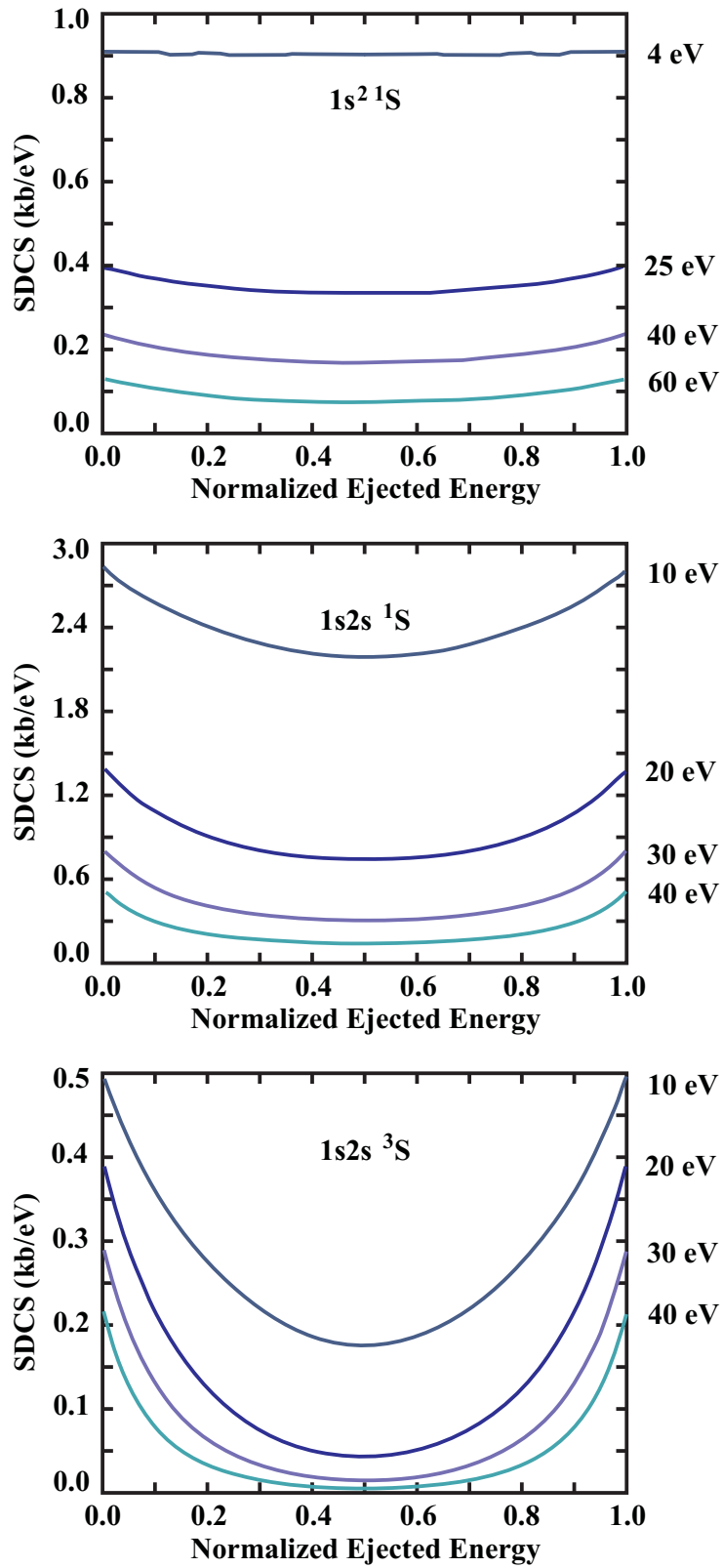


Figure 2.5: Single differential cross sections in units of kb/eV for He($1s^2\ ^1S$), He($1s2s\ ^1S$) and He($1s2s\ ^3S$) at various excess photon energies as indicated ($1.0\text{ kb} = 1.0 \times 10^{-21}\text{ cm}^2$). The cross section plots are such that the normalized ejected energy = ejected energy / excess energy.

The relative intensity of the satellites increases with the level of initial excitation of the Li atom [Zho99, Fel92, Cub07].

In studies of simultaneous ionization plus excitation, such ‘valence electron mediated electron correlation’ demonstrates its importance, in comparisons of the intensities between the multi-electron processes, so-called satellites lines, and the direct process, so-called main lines, where the relative intensity of the satellites varies depending on the initial orbital $n\ell$ of the outer shell electron, and increases for rising level of initial excitation of the Li atom.

Table 2.2: Branching ratios of the $(n+1)\ell$ shake-up relative to the $n\ell$ main line intensities for photoionization at $h\nu = 120\text{ eV}$ from the Li ($1s^2 2s^2 S$) ground state and the $2p$, $3s$, and $3p$ excited states. Only the intensity of the respective 3S and 3P lines are given.

Initial state	2s	2p	3s	3p
Experiment	0.25	0.64(3)	1.8(2)	5.2(5)
Theory	0.25	0.65	...	5.24

Inspired by theoretical predictions using the R-matrix method [Zho99, Che00], an experimental study on PIE of Li atom [Cub07] with the valence electron prepared in different states ($2s$, $2p$, $3s$ and $3p$) gives a good example, investigating intensity inversion between main and satellite lines in atomic photoionization. Tab. (2.2) lists the branching ratios of interest ($(n+1)\ell$ shake-up line over $n\ell$ main line), where the measured data are consistent with the R-matrix calculation very well. These results show an increasing trend with the level of initial excitation of the Li atom in general. The shake-up process already dominates for states with an $n = 3$ valence electron and the satellites become stronger than the main lines. Even more appealing, the shake-up products increase dramatically as the valence orbital changes from ns to np .

These strong effects can be explained by the spatial overlap of the initial and final state wave functions. The change of the atomic potential when going from the neutral atom to the ion results in a change of the wave function. This effect is especially large for outer levels carrying an angular momentum, as the difference in perceived central charge is maximal there. A simple model using the formula for the mean radii of hydrogen-like systems shows the proximity of the atomic $3p$ orbital with a radius of $12.1 a_0$ and the ionic $4p$ with $11.3 a_0$, in contrast to a value of $6.1 a_0$ for the radius of the ionic $3p$. So the $3p$ wave function of the neutral laser-excited atom is much closer to the $4p$ than to the $3p$ wave function in the ion, giving rise to the dominance of the satellite lines. This finding is similar to the situation observed upon resonant inner shell excitation [Aks88, Mey91], where shake-up processes dominate the resonant Auger decay.

The energy dependence of the branching ratio between the shake-up satellites (SU) and the main photo lines (ML) shows a decrease of the satellite intensity when the photon energy approaches the Li^+ ($1s np$) ionization threshold, as shown in Fig. (2.6). This tendency is well known, and could be understood in a simple picture: this effect arises from the fact

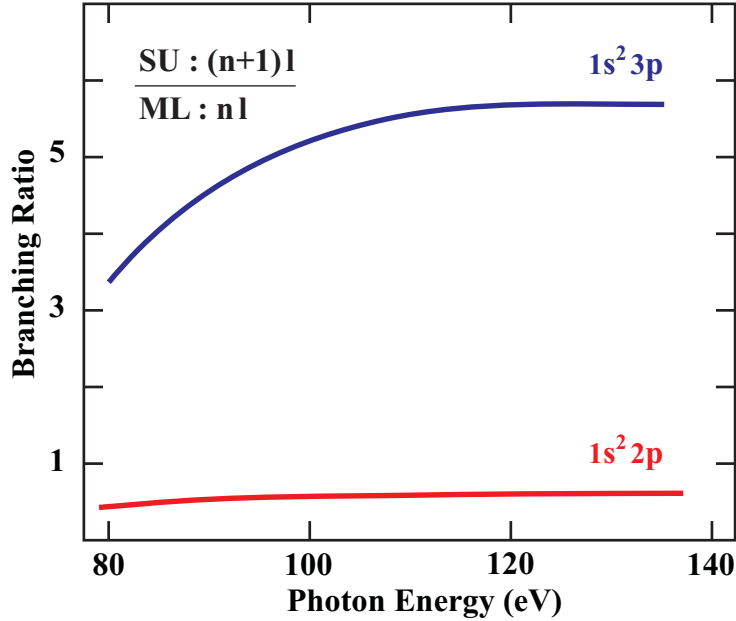


Figure 2.6: Branching ratio between the $(n + 1)\ell$ shake-up satellites and the $n\ell$ main photo lines after photoionization from the $\text{Li}^* (1s^2 2p^2 P_{3/2})$ and $\text{Li}^* (1s^2 3p^2 P_{3/2})$ excited states. Curves are produced by R-matrix calculations [Zho99].

that only far above threshold the overlap between the neutral and the ionic wave functions can be considered as constant, which is the so-called sudden approximation. Closer to threshold, the interaction between the outgoing electron and the remaining core has to be taken into account causing a more adiabatic relaxation and thereby a higher main line intensity [Bec90].

2.1.5 Wannier Threshold Law

One aspect of the general three-body continuum Coulomb system that is of interest in physics is the threshold law for three-body problem. Due to the feature that long-range forces are present, such problem in atomic physics has particular subtleties as all three partners are charged.

Originally, the threshold law for multi-electron escaping processes was derived by Wannier especially for the ‘electron impact induced ionization’ [Wan53, Wan55]. It is actually a classical approach under the assumption of ‘small excess energy’ $E_{exc} = E_0 - IP \rightarrow 0$, which circumvented the complicated quantum-mechanical description for the ionization process. Essentially, such treatment gives predictions without the knowledge of the detailed ejection mechanism at hand. The deduced cross section for the fragmentation of atoms rises with a power law $\sigma \propto E_{exc}^\alpha$, where $\alpha \approx 1$ for photo double ionization of atoms. The exponent α depends on the number of final state electrons and the charge of the ion. In a crude description by neglecting the electron-electron correlation of the out-going electrons, it scales as $\alpha \approx (n - 1)$. While considering the effects of electron correlation

additionally, a general expression for including the charge Z of the residual ion can be derived [Kla81].

The original treatment by Wannier only dealt with one particular set of the quantum numbers $\{L S \pi\}$ of the pair, namely $^1S^e$, though there were already indications that the threshold law was largely independent of these parameters. A sophisticated description with L and S values extended to the whole basis were done by [Rot72, Kla76, Gre82a].

Besides the threshold law (the exponent in the relation), the Wannier threshold theory also provides information on the allocation of residual energy between all fragments, the angular distribution of escaping electrons, and the correlations between their spins.

Taking PDI as example, actually no matter which mechanism (TS1, SO, or PS) does participate in the dynamic process, it takes place in the ‘so-called’ reaction zone at small distances from the nucleus. As the escaped electrons enter the classical ‘Coulomb zone’ far away from the ‘break-up area’, a post-collision correlation between charged particles emerges due to the Coulomb force. Thus the emission pattern is not only guided by symmetry and the angular momentum conservation, but also determined by the long range electron interaction, which becomes more and more important as the excess energy decreases, just due to the fact that the less kinetic energy the fragments have, the longer interaction would be experienced. Albeit, as a widely accepted knowledge, Wannier theories give the prediction that, at threshold the emission pattern is completely determined by stable configurations in the Coulomb zone, e.g., for the double ionization the two electrons have to recede back-to-back with equal energies ($r_1 = r_2$, $\vartheta_{12} = 180^\circ$). From zero at threshold, the double ionization cross section rises, depending on the growing phase space in the vicinity of this configuration, as the excess energy rises. Within this model, the electron emission pattern especially at the threshold region does not rely on the details of the dynamics within the reaction zone or the initial configuration of the bound electron pair any more. However, in the treatments of promoted versions on the Wannier theory (including semi-classical and quantum mechanical extensions) [Sta82, Gre82a], the influence of the symmetry of the emitted two-electron wave function may exhibit nodes or antinodes at the Wannier configuration and therefore the symmetries are classified in ‘unfavoured’ and ‘favoured’ respectively.

2.2 Brief Introduction of the Calculation Methods

Due to the development of bright light synchrotrons and free electron lasers, correlated photoionization processes in two-electron atomic systems have received extensive theoretical attention. To keep pace with the rapid experimental advances, several numerical approaches relying on spectacularly powerful computer systems have been developed. Apart from the many-body perturbation theory (MBPT), which has been fruitfully applied to a diverse number of photoionization calculations [Cha68, Car77, Ish91, Nik01, Ist02], there are also several non-perturbative time-independent or time-dependent methods proposed for exploring the correlated double ionization of few-body quantum systems, such as the convergent close coupling method [Khe96, Khe98c, Khe00b], the R-matrix Floquet theory [Har98, Ky98, Mal00], and the time-dependent closing coupling [Pin98a, Col02a, Col02b]

calculations on a numerical lattice. Especially for all measurements made on helium to date, all these nonperturbative approaches have demonstrated excellent agreement with each other and with experimental results for a wide range of incident photon energies and energy sharings between the outgoing electrons.

In this section, a short summary of the most popular methods for handling double photoionization will be presented briefly.

Convergent Close Coupling

The convergent close coupling (CCC) method was introduced to the theory of atomic and molecular scattering by Bray and Stelbovics [Bra92]. It is based on the close coupling (CC) and momentum-space coupled channels formalisms, in which the coupled equations are solved without approximation through a large number of discrete and continuum channels over the target space. The eigenstate of the system (target plus projectile) is constructed by diagonalizing the target Hamiltonian using the orthogonal square-integrable (L^2) basis. The completeness of such a basis is obtained as its size is increased. The nature of the basis (i.e. square-integrability) ensures that the states corresponding to negative energy converge pointwisely to the exact state with increasing basis size, while those with positive energy discretize the target continuum [Fur95].

Within the L^2 basis set, the solution of the coupled Lippmann-Schwinger integral equations are then obtained and the physical observables of interest can be deduced directly from the resulting K - and T -matrix elements. All information regarding the collision processes such as elastic and inelastic collisions, ionization and ionization with excitation can be obtained from a single simultaneous calculation. The CCC method is without approximation, since the convergence is achieved by increasing the size of basis functions included in the calculation. This technique also ensures that the pseudo-resonances associated with the positive energies in the asymptotic continuum states can be treated efficiently.

There have been numerous CCC applications on the photoionization with excitation (PIE) and double-photoionization (PDI). For example, the calculation of the double-to-single photoionization cross-section ratio R for helium at photon energies from the double ionization threshold to 400 eV [Khe96] was achieved and was found in accordance with the available experimental data [Doer96a]. The satisfactory agreement among all three forms of the electromagnetic operator (length, velocity and acceleration form) applied in the calculation of the ratio R [Khe98b] was demonstrated, which was crucially determined by the description of the ground state correlation. Furthermore, an *ab initio* calculation on the fully resolved triply-differential cross section (TDCS) of the helium ground state [Khe98a] was performed, which provided detailed information regarding the probability of observing two photoelectrons with completely determined kinematics.

Box: CCC Formalism

We use the following multichannel expansion for the final-state wave function of the two-

electron system:

$$\left\langle \Psi_j^{(-)}(k_b) \right| = \left\langle k_b^{(-)} j \right| + \sum_i \sum \int d^3 k \frac{\left\langle k_b^{(-)} j \middle| T \middle| i k^{(+)} \right\rangle \left\langle k^{(+)} i \right|}{E - \epsilon_k - \epsilon_i + i0}, \quad (2.9)$$

with boundary conditions corresponding to an outgoing wave in a given channel $\left\langle k_b^{(-)} j \right|$ and incoming waves in all other channels $|i k^{(+)}\rangle$. Here, $E = k_b^2/2 + \epsilon_j$ is the final-state energy. The channel wave function $\left\langle k_b^{(-)} j \right|$ is the product of a one-electron orbital $\bar{\phi}_j$ with energy ϵ_j , obtained by diagonalizing the target Hamiltonian in a Laguerre basis, and an outgoing distorted Coulomb wave $\chi^{(-)}(k_b)$ with energy ϵ_k . The asymptotic charge seen by the Coulomb wave function is $Z - 1$, where Z is the charge of the nucleus. The half off-shell T matrix in Eq. (2.9) is the solution of the corresponding Lippmann-Schwinger integral equation [Bra94]:

$$\left\langle k^{(+)} i \middle| T \middle| j k_b^{(-)} \right\rangle = \left\langle k^{(+)} i \middle| V \middle| j k_b^{(-)} \right\rangle + \sum_{i'} \sum \int d^3 k' \times \frac{\left\langle k^{(+)} i \middle| V \middle| i' k'^{(-)} \right\rangle \left\langle k'^{(-)} i' \middle| T \middle| j k_b^{(-)} \right\rangle}{E - \epsilon_{k'} - \epsilon_{i'} + i0}. \quad (2.10)$$

The photoionization cross section corresponding to a particular bound electron state j is given, as a function of the photon energy ω , by the formula [Amu90]

$$\sigma_j(\omega) = \frac{4\pi^2}{\omega c} \sum_{m_j} \int d^3 k_b \left| \left\langle \Psi_j^{(-)}(k_b) \middle| \mathcal{D} \middle| \Psi_0 \right\rangle \right|^2 \delta(\omega - E + E_0), \quad (2.11)$$

where $c \approx 137$ is the speed of light in atomic units. The dipole electromagnetic operator \mathcal{D} can be written in one of the following forms commonly known as length, velocity, and acceleration form [Amu90]:

$$\begin{aligned} \mathcal{D}^r &= \omega(z_1 + z_2), \\ \mathcal{D}^\nabla &= \nabla_{z_1} + \nabla_{z_2}, \\ \mathcal{D}^{\dot{v}} &= \frac{Z}{\omega} \left(\frac{z_1}{r_1^3} + \frac{z_2}{r_2^3} \right), \end{aligned} \quad (2.12)$$

with the z axis chosen along the polarization vector of the photon. The dipole matrix element with the CCC final-state wave function of Eq. (2.9) can be calculated as

$$\left\langle \Psi_j^{(-)}(k_b) \middle| \mathcal{D} \middle| \Psi_0 \right\rangle = \left\langle k_b^{(-)} j \middle| \mathcal{D} \middle| \Psi_0 \right\rangle + \sum_i \sum \int d^3 k \frac{\left\langle k_b^{(-)} j \middle| T \middle| i k^{(+)} \right\rangle \left\langle k^{(+)} i \middle| \mathcal{D} \middle| \Psi_0 \right\rangle}{E - \epsilon_k - \epsilon_i + i0}. \quad (2.13)$$

After some angular momentum algebra, the first-order dipole matrix element $\left\langle k^{(+)} i \middle| \mathcal{D} \middle| \Psi_0 \right\rangle$ breaks down into one-electron radial integrals and angular coefficients.

We separate the contribution from the final channels $\left\langle k_b^{(-)} j \right|$ into single and double ionization according to the energy ϵ_j , which is positive for the doubly-ionized channels and negative for the singly-ionized channels. We also ensure that for the negative-energy

state cross sections, contributions to the ionization plus excitation cross sections are multiplied by the projection of the state onto the true target discrete subspace as is done for electron-impact ionization [Bra93].

R-matrix Floquet Theory

The R-matrix method has been mainly applied to electronic and photonic excitation and ionization of outer atomic electrons, but has also been borrowed to analyze the various shake-up processes due to inner-shell $1s$ ionization of small atoms like Li and Be [Lis90, Ky92, Ky98].

By considering the close-coupling (CC) approximation, the complete wave function is taken to be

$$\Psi^{SL\pi} = \mathcal{A} \sum_{i=1}^{N^F} c_i \phi_i(S_i L_i; x_1, \dots, x_N, x_{N+1}) F(k_i l_i; r_{N+1}) r_{N+1}^{-1} + \sum_{j=1}^{N^B} d_j \Phi_j^{SL\pi}, \quad (2.14)$$

where the $(N+1)$ -electron functions $\Phi_j^{SL\pi}$ are configuration state functions built entirely from the bound orbitals. The functions ϕ_i are constructed by coupling the angular and spin functions of the additional electron with the wave functions $\Phi_j^{S_i L_i}$ of the target terms that are included in the close-coupling (CC) expansion. In the equation, $F(k_i l_i; r_{N+1})$ is the radial function of the additional electron, \mathcal{A} is the anti-symmetrization operator $\mathcal{A} = (N+1)^{-1/2} \sum_{n=1}^{N+1} (-1)^n$, and the coefficients c_i and d_j are determined by diagonalizing the $(N+1)$ -electron Hamiltonian. In the first term, the summation runs over all free channels N^F obtained by adding a collision-type electron with appropriate quantum numbers to the (frozen) target states, whereas the second sum includes all $(N+1)$ -electron bound channels N^B (the ‘bound states’) that can be made up from the target configurations plus another target orbital. The latter sum includes at least those configurations that have to compensate for orthogonality constraints imposed on the radial solution F and allows for the addition of correlation functions.

Here we discuss the calculation of the target state functions $\Phi_j^{S_i L_i}$. They are represented by configuration-interaction (CI) expansions of the form

$$\Phi_j^{S_i L_i} = \sum_{j=1}^M a_j \psi_j^{S_i L_i}, \quad (2.15)$$

where the configuration state functions (CSFs) ψ_j are constructed from one-electron orbitals of the form

$$\frac{1}{r} P_{nl}(r) Y_l^{ml}(\theta, \phi) \chi_{m_s}(\sigma), \quad (2.16)$$

with the orbital angular momenta coupled to form a total L_i and the spin quantum numbers are coupled to form a many-electron spin S_i .

The target states in these calculations have been determined using the code CIV3 [Hib75], in which the radial functions $P_{nl}(r)$ are expressed in a Slater-type analytic form:

$$P_{nl}(r) = \sum_{j=1}^k c_{jnl} r^{I_{jnl}} \exp(-\xi_{jnl} r), \quad (2.17)$$

and the orthonormality condition is satisfied for any $P_{nl}(r)$,

$$\int_0^\infty P_{nl}P_{n'l}(r)dr = \delta_{nn'}, \quad (2.18)$$

which uniquely determines the coefficients C_{jnl} in Eq.(2.17) so that (since the integers I_{jnl} are fixed) only the ξ_{jnl} are treated as variational parameters.

With the R-Matrix code thus constructed (radial function set), a number of parameters can be calculated, i.e. total and partial photoionization cross sections, branching ratios, asymmetry parameters (β), and energy positions of the resonances.

Box: R-Matrix

A value a of the radial variable r is chosen to be such that the functions χ_i , and Φ_j are small for $r \geq a$. We refer to $r \leq a$ as the inner region and $r \geq a$ as the outer region. A first step is to obtain solutions which satisfy a fixed condition on the boundary at $r = a$. These solutions, $\Psi = \psi_n$, exist for a discrete set of energies, $E = \epsilon_n$, and contain radial functions $F_i(r) = f_{in}(r)$. Different choices of the boundary condition can be made but in all of the work of the Opacity Project [Sea87, Ber87], the choice is taken to be

$$\left. \frac{df_{in}(r)}{dr} \right|_{r=a} = 0. \quad (2.19)$$

The functions ψ_n , are normalized to

$$\langle \psi_n | \psi_{n'} \rangle_I = \delta_{nn'}, \quad (2.20)$$

where the integrals in the matrix elements $\langle \psi_n | \psi_{n'} \rangle_I$ are evaluated in the inner region. For any value of E , the complete wave function Ψ_E , constructed with the radial functions $F_{iE}(r)$, can be expanded as

$$\Psi_E = \sum_n \psi_n A_{nE}, \quad (2.21)$$

and it can be shown [Bur71] that

$$A_{nE} = (\epsilon_n - E)^{-1} \sum_i f_{in}(a) F'_{iE}(a), \quad (2.22)$$

where $F'_{iE}(a)$ is taken to be such that Ψ_E satisfies the required normalization and boundary conditions. Substituting Eq. (2.22) in Eq. (2.21), it may be shown that

$$F_{iE}(a) = \sum_{i'} R_{ii'}(E) F'_{i'E}(a), \quad (2.23)$$

where $R_{ii'}(E)$ denotes the elements of the R matrix:

$$R_{ii'}(E) = \sum_n f_{in}(a) (\epsilon_n - E)^{-1} f_{i'n}(a). \quad (2.24)$$

Time-dependent Closing Coupling

Inspired by the statement by Bottcher [Bot85], stating that the time evolution of a wave function localized in space obviates the need to care about the asymptotic form of the wave

function in coordinate space or its singularities in momentum space, a time-dependent close-coupling method is developed to study the correlated photoionization process, i.e. two electron outgoing within the long-range Coulomb field of a third body. This larger set of coupled partial differential equations may then be time propagated on a lattice to yield accurate cross sections for a variety of correlated photoionization processes in two-electron atomic systems.

The time-dependent wave function for any two-electron atomic system may be divided into two parts:

$$\Psi(\vec{r}_1, \vec{r}_2, t) = \phi_0(\vec{r}_1, \vec{r}_2)e^{-iE_0t} + \psi(\vec{r}_1, \vec{r}_2, t), \quad (2.25)$$

where ϕ_0 is the exact eigenfunction and E_0 is the exact eigenenergy of the time-independent atomic Hamiltonian. Substituting into the time-dependent Schrödinger equation, a simpler form can be derived in the weak-field perturbative limit:

$$i\frac{\partial\psi(\vec{r}_1, \vec{r}_2, t)}{\partial t} = H_{atom}\psi(\vec{r}_1, \vec{r}_2, t) + H_{rad}\phi_0(\vec{r}_1, \vec{r}_2)e^{-iE_0t}, \quad (2.26)$$

where H_{rad} is the Hamiltonian for interaction with a time-dependent radiation field. The second term on the right-hand side acts as a source for the time evolution of $\psi(\vec{r}_1, \vec{r}_2, t)$ from zero at time $t = 0$ to some final value at time $t = T$.

Utilizing a standard procedure found in time-independent scattering theory [Tem62, She94], for a given LS symmetry, the eigenfunction $\phi_0(\vec{r}_1, \vec{r}_2)$ (ground or low-lying excited states) is found by an expansion in coupled spherical harmonics and subsequent relaxation of the time-dependent Schrödinger equation – containing only the nonrelativistic Hamiltonian H_{atom} – in imaginary time.

The time-dependent wave function $\psi(\vec{r}_1, \vec{r}_2, t)$ for a given LS symmetry is also expanded in coupled spherical harmonics and the resulting set of time-dependent close-coupled partial differential equations (see below) are solved on a numerical lattice with a mesh spacing Δr and time propagated for certain number of field periods $n \cdot \frac{2\pi}{\omega}$, depending on the excess photon energy

$$i\frac{\partial P_{\ell_1\ell_2}^{LS}(r_1, r_2, t)}{\partial t} = T_{\ell_1\ell_2}(r_1, r_2)P_{\ell_1\ell_2}^{LS}(r_1, r_2, t) + \sum_{\ell'_1\ell'_2} V_{\ell_1\ell_2, \ell'_1\ell'_2}^L(r_1, r_2)P_{\ell'_1\ell'_2}^{LS}(r_1, r_2, t) + \sum_{\ell''_1\ell''_2} W_{\ell_1\ell_2, \ell''_1\ell''_2}^{LL_0}(r_1, r_2, t)P_{\ell''_1\ell''_2}^{L_0S}(r_1, r_2, t)e^{-iE_0t}. \quad (2.27)$$

Here, the $P_{\ell_1\ell_2}^{LS}(r_1, r_2, t)$ are the radial wave functions, the $T_{\ell_1\ell_2}(r_1, r_2)$ is the kinetic energy operators, $V_{\ell_1\ell_2, \ell'_1\ell'_2}^L(r_1, r_2)$ is the Coulomb interaction operator, and the expression $W_{\ell_1\ell_2, \ell''_1\ell''_2}^{LL_0}(r_1, r_2, t)$ denotes the radiation field operator [Pin98a, Pin98b].

After calculation of the two-electron eigenfunction for the initial atom and the one-electron eigenfunctions for the final ion, the time-dependent close-coupled equations found in Eq. (2.27) are propagated in real time for the appropriate LS symmetry and the initial condition $P_{\ell_1\ell_2}^{LS}(r_1, r_2, t = 0) = 0$. An explicit ‘staggered leapfrog’ approximation [Pre92] is used for time propagation.

The cross section for photoionization with excitation to a bound state $n\ell m$ is given by

$$\sigma_{n\ell m}^{LS} = \frac{\omega}{I} \frac{\partial \wp_{n\ell m}^{LS}}{\partial t}, \quad (2.28)$$

where I is the intensity of the radiation field, and $\wp_{n\ell m}^{LS}$ is the probability for simultaneous ionization plus excitation.

$$\begin{aligned} \wp_{n\ell m}^{LS} = & \int d\vec{r}_1 \left| \left\langle \psi^{LS}(\vec{r}_1, \vec{r}_2, T) \middle| \chi_{n\ell m}(\vec{r}_2) \right\rangle \right|^2 \\ & - \sum_{n'\ell'm'} \left| \left\langle \psi^{LS}(\vec{r}_1, \vec{r}_2, T) \middle| \chi_{n'\ell'm'}(\vec{r}_1) \chi_{n\ell m}(\vec{r}_2) \right\rangle \right|^2 \\ & + \int d\vec{r}_2 \left| \left\langle \psi^{LS}(\vec{r}_1, \vec{r}_2, T) \middle| \chi_{n\ell m}(\vec{r}_1) \right\rangle \right|^2 \\ & - \sum_{n'\ell'm'} \left| \left\langle \psi^{LS}(\vec{r}_1, \vec{r}_2, T) \middle| \chi_{n\ell m}(\vec{r}_1) \chi_{n'\ell'm'}(\vec{r}_2) \right\rangle \right|^2. \end{aligned} \quad (2.29)$$

The cross section for double photoionization is given by

$$\sigma_{dion}^{LS} = \frac{\omega}{I} \frac{\partial \wp_{dion}^{LS}}{\partial t}, \quad (2.30)$$

while the probability for double ionization reads:

$$\begin{aligned} \wp_{dion}^{LS} = & \left\langle \psi^{LS}(\vec{r}_1, \vec{r}_2, T) \middle| \psi^{LS}(\vec{r}_1, \vec{r}_2, T) \right\rangle - \sum_{n\ell m} \wp_{n\ell m}^{LS} \\ & - \sum_{n\ell m} \sum_{n'\ell'm'} \left| \left\langle \psi^{LS}(\vec{r}_1, \vec{r}_2, T) \middle| \chi_{n'\ell'm'}(\vec{r}_1) \chi_{n\ell m}(\vec{r}_2) \right\rangle \right|^2. \end{aligned} \quad (2.31)$$

Chapter 3

Principle of Laser Cooling and Trapping

In this chapter we will talk about the concept of cooling and trapping, which is exploited to prepare the ultra-cold alkali atom target for dynamic fragmentation study via the device of the magneto-optical trap (MOT).

The laser cooling mechanism is based on the fact that a photon carries momentum, and that this momentum can be transferred to the atom via absorption and emission of the photon. As a result the atom will change its momentum, and as a consequence can be cooled [Haen75, Win75]. Combining this basic idea with magnetic field, a MOT is structured to manipulate and cool atoms down to temperatures not reachable with conventional techniques.

The frame of this theoretical introduction part will be organized like this: First of all, a brief introduction to Doppler cooling is given, with the concept of atom-light interaction included; further on, the working principle of the MOT is explained (which is a standard tool to trap and examine atomic samples), so are the dynamic properties of the MOT discussed as well; then, the atom loading method — Zeeman slowing is introduced; in the end, the specific properties of ^7Li related to laser cooling are presented, also. It should be mentioned that the MOT could realize the cooling and trapping the atoms in position space, while in fact, the mechanism of Doppler cooling works only in momentum space.

Three good and comprehensive review papers on the development of laser cooling and trapping were presented by Steven Chu, Claude Cohen-Tannoudji and William D. Phillips in their Nobel Lectures in 1997 [Chu98, Coh98, Phi98]. For descriptions of this topic in more detail, it is referred to books [Met99, Pet02].

3.1 Doppler Cooling

When atoms are irradiated by light, they experience strong forces and accelerations, which can be used to have them cooled and trapped, as an application. Via undergoing a velocity dependent radiation pressure force, the kinetic energy of moving atoms is diminished. This

so-called Doppler cooling technique, which was first proposed by Hänsch and Schawlow in 1975 [Haen75], was named after the Doppler effect, due to the velocity dependent property.

Radiation Pressure Force

Considering the one dimensional case, a two level atom, with a resonant absorption frequency ω_A , mass m and a velocity v , encounters a laser beam, with a frequency ω_L and thus a wavevector $k_L = \omega_L/c$ (c is the speed of light). If immersed in light fields, the atom may absorb and emit photons. Every photon carries a momentum $\Delta p = \hbar k$ and hence transfers in each absorption process a momentum $\hbar k$ in direction of the light beam to the atom. The characteristic of the re-emitted photons from the atom is a dipole type, which is symmetric in inversion and, therefore, the momentum transfer is null on an average. The velocity change of the atom and the frequency difference of the re-emitted photon after a resonant absorption read:

$$v_R = \frac{\hbar k}{m}, \quad \Delta\omega = kv + \frac{\hbar k^2}{2m} \quad (3.1)$$

here v_R dedicates the recoil velocity (the velocity change an atom experiences when it absorbs a single photon) and kv means the Doppler shift ($kv = \omega_L v/c$). The second term in the second formula of Eq. (3.1) denotes recoil shift, and is equal to the kinetic energy in frequency units.

The difference between the optical transition frequency and the radiation frequency is denoted as detuning of the laser $\delta = \omega_A - \omega_L$ (it will play an important role for laser cooling). However the effective detuning should take the Doppler shift $\delta_{Dopp} = kv$ into account, $\delta_{eff} = \delta - kv$. As a result of the upper considerations, an atom will receive/sustain a so-called radiation pressure force:

$$F = \hbar k \frac{\Gamma}{2} \frac{I/I_S}{1 + I/I_S + [2(\delta - kv)/\Gamma]^2} \quad (3.2)$$

where I is the intensity of the laser, I_S is the saturation intensity. Eq. (3.2) is just the product of the photon momentum $\hbar k$ times the scattering rate. The scattering rate describes the atom's ability to absorb and re-emit spontaneously a photon. The force saturates for large intensities and a laser detuning of $\delta = kv$ to $F = \hbar k \Gamma/2$; also it depends on the linewidth of the atomic transition Γ .

Doppler Cooling and Optical Molasses

If we expand this example to two counter propagating laser beams, the net force applied on the atom becomes:

$$F = \hbar k \frac{\Gamma}{2} \left\{ \frac{I/I_S}{1 + I/I_S + [2(\delta - kv)/\Gamma]^2} - \frac{I/I_S}{1 + I/I_S + [2(\delta + kv)/\Gamma]^2} \right\} \quad (3.3)$$

This force for $\delta = -\Gamma$ at a laser intensity $I = 2I_S$ is illustrated in Fig. (3.1), as well as the components F^+ and F^- generated by one arm beam. In the limit of small velocities v and

I/I_S , the expression is simplified as:

$$F(v) = 2\hbar k^2 \frac{(2I/I_S)(2\delta/\Gamma)v}{[1 + (2\delta/\Gamma)^2]^2} = -\alpha v \quad (3.4)$$

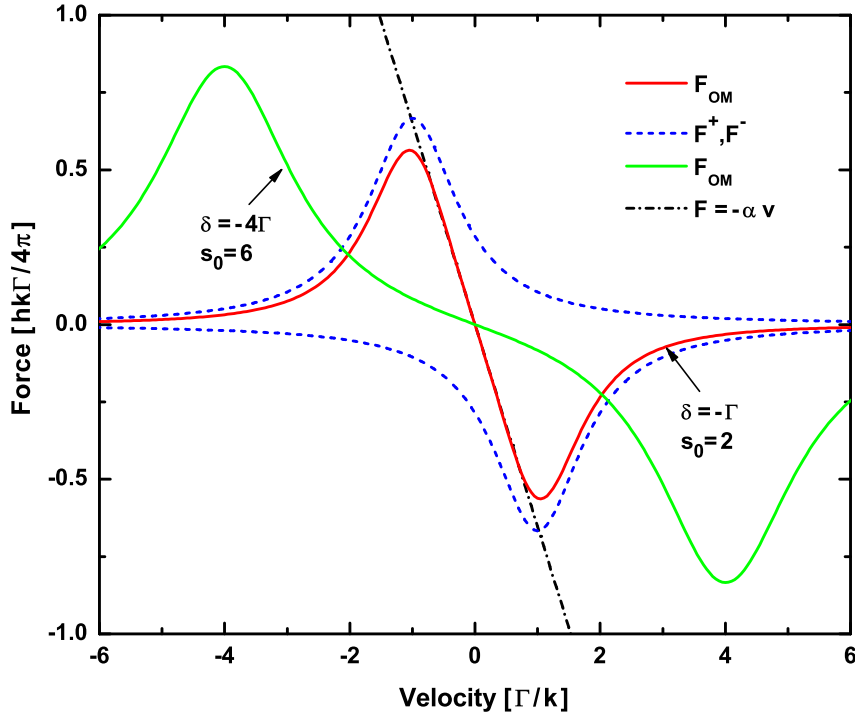


Figure 3.1: Velocity dependent force F in a one-dimensional optical molasses. The red curve shows the total force F_{OM} as the sum of the single beam forces F^+ , F^- (dashed blue lines), calculated for a detuning $\delta = -\Gamma$ and an intensity saturation condition of $s_0 = I/I_S = 2$, and the black dash-dot line is the linear approximation for small velocities. Additionally, a situation for a large detuning of 4Γ and higher saturation of $s_0 = 6$ is depicted by the green curve.

For $\delta < 0$, the force can be associated with a friction force as it is proportional to the velocity v and in the opposite direction of v . The physics behind can be understood intuitively: Due to the Doppler effect, a red-detuned laser beam, which counter-propagates the atomic motion, is shifted closer to resonance in the rest frame of the atoms; in spite of that, the laser beam that propagates in the same direction as the atom is shifted further away from resonance. In consequence, the atom always absorbs more photons from the beam that is opposing its motion and therefore is decelerated. Because of this analogous friction force, atoms could be cooled down by irradiating them with red-shifted laser light $\delta < 0$.

Up to now only the one-dimension case of Doppler cooling is considered. However, this model can easily be developed to a three dimensions situation with three pairs of cooling beams, orthogonal to each other. This case is routinely called optical molasses [Let89], because of the viscous nature of the damping force.

Doppler Limit

Now an important question emerges: what is the lowest temperature reachable with this method? By now, we only discuss the damping force F , resulting from a time average of many absorption and emission processes. Nevertheless, the contribution from the discrete amount of momentum transfer on spontaneous emission would cause a fluctuation of the force, finally tend to heat the atom. In fact, when an atom approaches zero velocity, it becomes equally likely that it absorbs a photon of any of the two laser beams. In this situation, the random nature of the absorption and emission processes induces the atom to undergo a random walk, with a step size of $\hbar k$, which defines the lowest reachable temperature. From a random walk treatment, we get a total momentum diffusion of:

$$2D_{spont} = \langle \dot{p} \rangle = 2\hbar^2 k^2 \frac{\Gamma}{2} \frac{I/I_S}{1 + (2\delta/\Gamma)^2} \quad (3.5)$$

The heating resulting from this is the increase in kinetic energy $p^2/2m$:

$$\langle \dot{E}_{heat} \rangle = \frac{\langle \dot{p}^2 \rangle}{2m} = \frac{D}{m} - \langle \dot{E}_{cool} \rangle = \alpha \langle v^2 \rangle \quad (3.6)$$

In an equilibrium state the cooling and heating rate are equal. By using $(dE/dt)_{cool} + (dE/dt)_{heat} = 0$ and the above equations one is able to determine a root mean square velocity for the atomic samples :

$$k_B T = \frac{D}{\alpha} = \frac{\hbar\Gamma}{4} \left(\frac{\Gamma}{2\delta} + \frac{2\delta}{\Gamma} \right) \quad (3.7)$$

The temperature minimizes for $\delta = -\Gamma/2$, and leads us to

$$k_B T_{Dopp} = \hbar\Gamma/2 \quad (3.8)$$

Here T_{Dopp} is the so-called Doppler cooling limit or Doppler Temperature. It is only depends on the natural linewidth of the cooling transition Γ . For alkali metals this is typically in the order of some hundred μK . In the special case of ${}^7\text{Li}$ it is $T_{Dopp} = 142 \mu\text{K}$ for lithium. This gives a mean velocity for Lithium atoms of 0.39 m/s.

However, such a limit of Doppler Temperature prediction is not unviolatable, in deed [Let88]. It is possible to break through this critical point, by employing another specific cooling mechanism [Dal89], which is depicted in Appendix B.

3.2 Magneto-Optical Trapping

Based on the upper discussion, we know the possibility to cool atoms in momentum space with light forces; but to trap them in position space, an additional inhomogeneous

magnetic field is superposed on the light field to generate a position dependent force, confining the atoms at a localized position in real space [Raa87, Lin92]. This hybrid configuration named Magneto-optical trap (MOT) or Zeeman assisted radiation pressure trap (ZARPT) has the properties of both position-dependence and velocity-selection, which make it as a robust device to manipulate and store neutral atoms.

MOT Operation Principle

The working principle of MOT (in a one-dimensional model) is illustrated in Fig. (3.2).

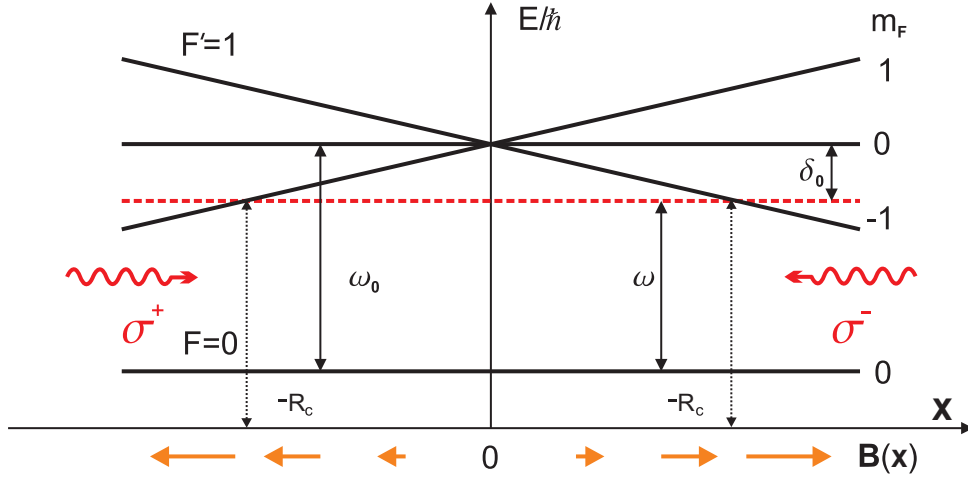


Figure 3.2: A simple one-dimensional model demonstrates the magneto-optical trap principle, showing the energy splitting due to the Zeeman effect and the corresponding polarizations.

A magnetic field with gradient $B(x) = B_0 \cdot x$ is employed (normally a quadrupole field generated by a pair of anti-Helmholtz coils, etc), where the magnitude is proportional to the distance from the center and the direction reverses at the trap center, therefore, the atoms at different position are selected-detuned from resonance differently, due to a space dependent Zeeman splitting $\Delta E = -\mu_B \cdot g_F \cdot m_F \cdot B(x)$. By setting the trapping beams (red-detuned) as circular polarized light σ^+/σ^- properly, the space dependence of the Zeeman splitting is transferred to a space dependent conservative force that effects in an addition to the dissipative cooling force a relaxation of the atoms to the field minimum. That is, for escaping atoms in an effective capture range, the further and the faster they way out, the more radiation pressure force they encounter, which push them back to the origin. The force now reads:

$$F = F_{\sigma^+} + F_{\sigma^-} = \frac{\hbar k \Gamma}{2} \left[\frac{I/I_s}{1 + 4 \left(\frac{\delta - kv - \mu B(x)/\hbar}{\Gamma} \right)^2} - \frac{I/I_s}{1 + 4 \left(\frac{\delta + kv + \mu B(x)/\hbar}{\Gamma} \right)^2} \right] \quad (3.9)$$

$$\mu = \mu_B (g_e m_e - g_g m_g)$$

where m_e and m_g are the magnetic quantum numbers of the ground state $|g\rangle$ and $|e\rangle$, and g_e , g_g are the corresponding Landè factors. If these conditions $|kv| \ll \Gamma$, $|kv| \ll |\delta|$ and

$|\mu B(x)|/\hbar \ll \Gamma$, $|\mu B(x)|/\hbar \ll |\delta|$ are holded, Eq. (3.9) could be expressed as:

$$F(v, x) = F(v) + F(x) = 4\hbar k \frac{I}{I_S} \frac{2\delta/\Gamma}{[1 + (2\delta/\Gamma)^2]^2} (kv + \beta x) \quad (3.10)$$

with $\beta = \mu B_0/\hbar$. It indicates the atoms in a MOT behavior like a damped harmonic oscillator about the origin $\ddot{x} + \gamma\dot{x} + \omega^2 x = 0$

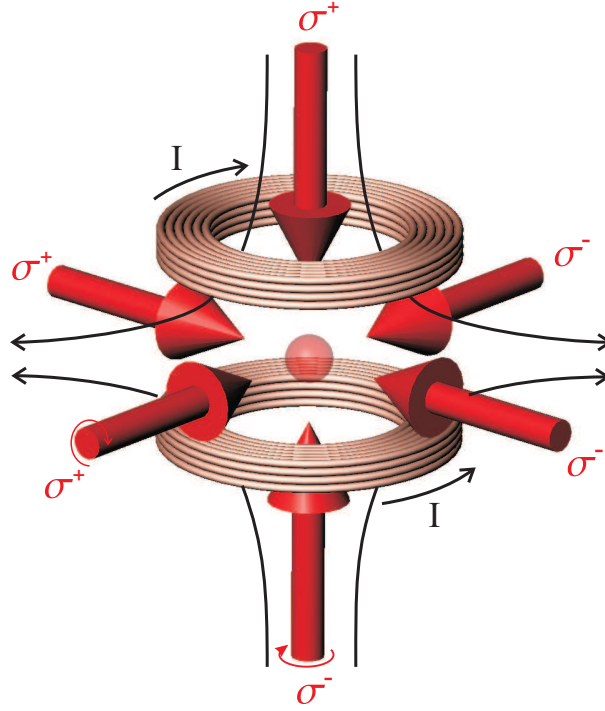


Figure 3.3: A schematic overview showing a three-dimensional magneto-optical trap configuration: A pair of anti-Helmholtz coils supplies a spherical quadrupole magnetic field; six red-detuned, circular-polarized laser beams provide the trapping force.

In the experimental realization of a MOT in three dimensions, two coils in anti-Helmholtz configuration are employed to generate the needed magnetic field customarily. In each spatial direction, two counter-propagating laser beams with the rightly chosen polarization are implemented to cool and trap atoms. Fig. (3.3) gives a schematic overview of a three-dimensional MOT operation, as a realistic illustration.

Dynamic Behavior of a MOT

A complete theoretical description (in three dimensions) of the dynamics of a MOT is difficult, because many dynamic process, like scattering, sub Doppler cooling, multi-photon effect *etc.*, should all be considered, not only with the mechanism of Doppler cooling included. However an alternative treatment is commonly used, dividing all the process within a MOT into distinct atom number regions [Tow95].

Considering a MOT operating in a dynamic equilibrium, there exists a competition between the MOT capture rate and various loss channels. The temporal evolution of the

trapped atomic ensemble in the number space can be described in terms of a rate equation [Wal94b]:

$$\frac{dN}{dt} = L - \alpha N - \beta \int dV n(r)^2, \quad (3.11)$$

where N is the trapped atom number, $n(r)$ means the density of the atomic ensemble, and L is the loading rate in units of atoms/s, while α , β denote the coefficients of loss rate:

α Describes the channel of ‘one-body loss’, which is essentially dominated by the background collisions. By the transferred kinetic energy from hot background atoms and molecules via scattering, trapped atoms can be heated up to escape the trap.

$$\alpha = n_0 \cdot \sigma \cdot \bar{v} \quad (3.12)$$

where n_0 is the background gas density, σ is the scattering cross-section and \bar{v} is the velocity of background atoms. Obviously this loss rate α is independent of the MOT density, and in fact, α defines the lifetime τ_{MOT} of the trap population by the inverse proportion relation $\alpha = 1/\tau_{MOT}$.

β Describes the contribution of binary inelastic collisions between the trapped atoms, which is also referred to ‘two-body loss’. This loss has two channels: Radiative Escape (RE) and Fine-structure Changing Collision (FSC), with the essence that, during the collision process, internal energy loss is converted to kinetic energy and at least one collision participator acquires enough energy to be ejected from the trap [Jul91]. It should be noted that this type of loss depends on the trapped atom density. At atom densities encountered in MOTs ($10^9 - 10^{11}$ atoms/cm³) the two-body loss rate is usually small compared to the one-body loss rate.

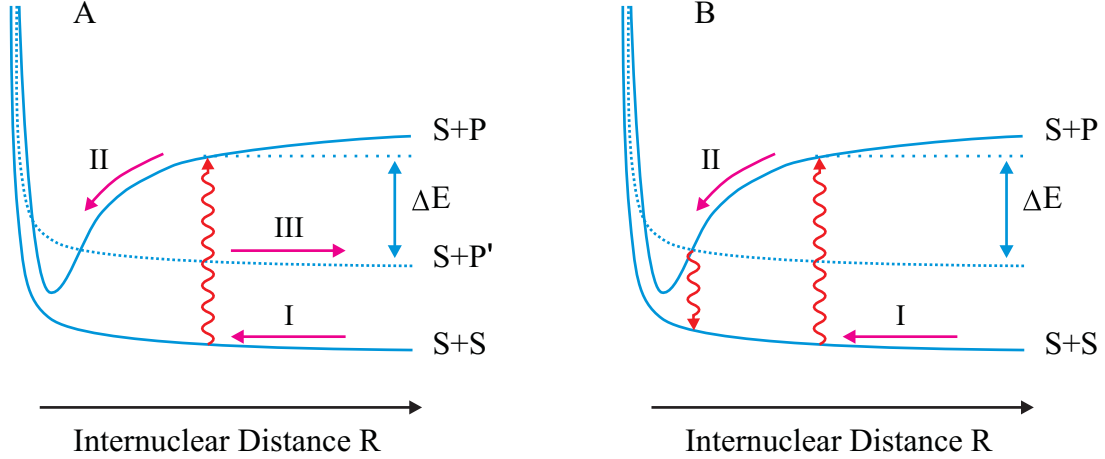


Figure 3.4: Two types of trap loss processes induced by the binary inelastic collision between trapped atoms. A: Fine-structure Changing Collision (FSC); B: Radiative Escape (RE).

By neglecting the term of two-body loss $\beta \int dV n(r)^2$ due to the low MOT density, and through solving Eq. (3.11), the form for the atom number evolution specially is derived as

$$N(t) = \frac{L}{\alpha} [1 - \exp(-\alpha t)] = N_{max} [1 - \exp(-t/\tau)] \quad (3.13)$$

by which the atom number shows a asymptotical growth to its steady state atom number N_{max} .

It contains such information that, to achieve capturing a large amount of atoms, not only a high loading rate is indispensable, but also the small loss rate plays an important role, which requires an excellent vacuum environment in the UHV-range ($p < 10^9$ mbar).

Fine-structure changing collisions

In the fine-structure change mechanism, the atoms that were excited at R0 to an S+P state move down the attractive potential. In this phase it can happen, that the atoms in the S+P molecular fine-structure state cross an potential that has a different S+P' asymptote. At this point the atom can be coupled to the S+P state and a population transfer takes place. When the atom move apart afterwards, they gain kinetic energy, which is give by the difference of the laser photon energy and the lower fine-structure state S+P', (see picture left). Typically this energy exceeds the trap depth and the atoms hence are able to leave the trap.

Radiative Escape

In the radiative escape process the colliding atoms are also excited to an attractive potential and accelerated towards each other. In contrast to FC, this acceleration is interrupted by a spontaneous decay of the excited molecular state back to the ground molecular state. The gain in kinetic energy of the atoms is then given by the relative kinetic energy, which the atoms get due to the acceleration phase in the excited state. If the atoms get close enough to each other during acceleration, it is possible that the gain in energy is such big that the atoms may escape from the trap.

3.3 Principle of Zeeman Slowing

In order to build up a MOT, a sufficient flux of atoms with a velocity below the criterion for MOT capture is a prerequisite. Among various methods to slow an atomic beam, the technique of the Zeeman slower [Phi82, Lis99, Ded04] gains applause most, since it shows competitive advantages, such as good efficiency and easy handling, other than chirping [Ert85], broadband cooling [Hof88, Zhu91], *etc.* With the knowledge of the radiation pressure force mentioned above, a counter-propagating laser is employed to slow down a large fraction of atoms obtained from a collimated oven. Taking into account the maximum possible deceleration and considering the encountered Doppler shift in the slowing procedure, a spatially varying magnetic field is applied along the beam trajectory, which keeps the atoms in resonance with the counter-propagating photon beam via the Zeeman effect at any point.

Moving atoms see the frequency of a light wave shifted due to the Doppler effect, leading

to a velocity-dependent detuning δ in the moving frame of the atom

$$\delta = \delta_0 + kv, \quad (3.14)$$

with the laser detuning

$$\delta_0 = \omega_{laser} - \omega_0,$$

where ω_0 is the rest frequency of the atomic transition. For counter-propagating beams, where v has a positive sign, the laser is red-detuned to fulfill the ‘on resonance’ condition $\delta = 0$. The maximum acceleration conveyed to the atom is

$$a_{max} = \frac{\hbar k \Gamma}{m 2}, \quad (3.15)$$

where Γ is the natural linewidth. Once its velocity is reduced, associated with the change of Doppler shift, the laser with ω_{laser} will fall out of the resonance regime; therefore, the deceleration spontaneous force on the atom will diminish unless the frequency detuning is reduced, or the laser intensity is increased. The method of Zeeman slowing gives a solution by imposing a velocity-determined magnetic field B externally, inducing a varying Zeeman energy, which compensates the Doppler shift of the moving atom. Hence, the detuning relation for δ is

$$\delta = \delta_0 + kv - \Delta\mu B/\hbar = 0 \quad (3.16)$$

here $\Delta\mu B/\hbar$ denotes the contribution of Zeeman effect δ_Z .

Conventionally, there are three main types of Zeeman slowers, termed and characterized according to its magnetic field profile, in consequence, the choice on detuning δ_0 of the slowing laser is different from one another.

Decreasing field magnetic slower: The magnetic field strength $|B(x)|$ has its maximum value at the beginning of the deceleration path, compensating for the Doppler shift of the fastest atoms. And the slowing laser has to be shifted from the resonance for atoms at rest, to the red a bit.

Increasing field magnetic slower: The magnetic field is zero at the beginning, where the deceleration happens, and reaches its maximum value at the end of the slowing path. Apparently, a large red detuning of the slower beam is needed to balance the Doppler shift of the fastest slowable atoms according to $\delta_0 + kv_0 = 0$.

Spin-flip slower: This configuration combines the decreasing and increasing magnetic field slowing. The atom’s trajectories start in a decreasing field, which crosses the zero of the magnetic field along the slowing distance and reverses its direction to rise again to a maximum value. The position of the zero crossing is determined by the chosen laser detuning $\delta_0 = -kv(z)$. It should be pointed out that the magnetic momenta of the atoms keep their orientation, as crossing the zero field region; indeed, they are just reversed (‘flipped’) with respect to the magnetic field’s direction.

Beside the cooling beam, the repumping component also plays its role in the Zeeman slower. At magnetic fields where two different Zeeman levels cross each other, the states are degenerated in energy. This may result in atom loss, since atoms can decay to another state manifold out of the closed two-state system coupled by the cooling light. One

solution to overcome this problem is adding a repumping frequency into the slower beam, which pumps atoms back.

An important feature of the Zeeman slower lies in the evolution of the velocity distribution: a large fraction of atoms are bunched into the same slow velocity group irrespective of their initial velocity, because of the resonance condition for slower atoms fulfilled at the slower's terminal. The compression of the velocity distribution in phase space distinguishes the slowing process from cooling. It should be emphasized that the dissipative nature of the spontaneous force makes the treatment using a 'conservative potential' impossible.

3.4 Spectroscopic Properties of Lithium

In Sec. 3.1, the principles of laser cooling have been elucidated by means of a model two-level system. In an effective and efficient laser cooling realization, a closed transition circle (loop) is a mandatory requisition. If the excited atoms spontaneously decay to another state other than the initial starting level, e.g. the ground state, and get accumulated in this so-called dark state, the cooling mechanism, which is a sustained procedure of thousands cycles, would be interrupted. Thus, at least one more pumping laser is needed to keep atoms from sneaking out of the cooling cycle.

For the alkali metals, this situation is generally realized. Fig. (3.5) displays atomic energy levels relevant to laser cooling of ${}^7\text{Li}$ atoms. The D2-component ($2^2S_{1/2} - 2^2P_{3/2}$) of the prominent D-line is employed as cooling transition, which is the common choice for alkali atoms cooling. In principle, the D1-line ($2^2S_{1/2} - 2^2P_{1/2}$) could be utilized as cooling line as well, however, its line strength is reduced by half compared with the line strength of the D2-transition. The wavelength of this transition is 671 nm, which is in the red visible region.

The radiative lifetime of the D-line transition is $\tau = 27.10$ ns [McA96, Vol96], corresponding to a natural linewidth of $1/(2\pi\tau) = 5.87$ MHz. Due to the interaction of the nuclear magnetic moment with the electronic magnetic moment, both the ground $2^2S_{1/2}$ and the excited state $2^2P_{3/2}$ show a characteristic hyperfine structure splitting, with the hyperfine structure constant a_{HFS} of the state $2^2S_{1/2}$ of 401.76 MHz, and the constant a_{HFS} of the state $2^2P_{3/2}$ of -3.05 MHz.

The chosen cooling scheme is illustrated in Fig. (3.5): Starting from the atomic sublevel ($2^2S_{1/2}, F = 2$), ${}^7\text{Li}$ atoms get excited, driven by a so-called Cooler laser at the strong transition ($2^2S_{1/2}, F = 2 - 2^2P_{3/2}, F' = 3$). Governed by the selection rule for electric dipole (E1) transitions, the target state ($2^2P_{3/2}, F' = 3$) could only decay to the initial state ($2^2S_{1/2}, F = 2$), thus a cycling transition for laser cooling is guaranteed. However, the hyperfine splitting of the ($2^2P_{3/2}$) is relatively small, and all four hyperfine sublevels are spaced within a frequency interval of 18.33 MHz in total, which is about three times of the natural linewidth 5.87 MHz approximately. Thus, not only the $F' = 3$ state, but the dipole transition allowed $F' = 1, 2$ states can be populated, due to an off-resonant excitation. In a consequence, atoms can go to the other ground state ($2^2S_{1/2}, F = 1$), which is the dark state for cooling transition ($2^2S_{1/2}, F = 2 - 2^2P_{3/2}, F' = 3$) actually.

As result, this unresolved hyperfine structure induces a strong coupling between the two ground states, turning the D2-line of ${}^7\text{Li}$ into a three-level Λ configuration essentially. In case of all ${}^7\text{Li}$ atoms being depleted from the cooling transition cycle via the Raman scattering process (from ground state of $F = 2$ to the $F = 1$), leading to the atom escape from the trap. The transition line ($2^2S_{1/2}, F = 1 \rightarrow 2^2P_{3/2}, F' = 2$) is utilized as ‘Repumper’ beam, kicking the sneaked-out atoms back to the cooling course. Indeed, Repumper not only serves as an auxiliary transition, remedying the trap loss, but also contributes an additional cooling force.

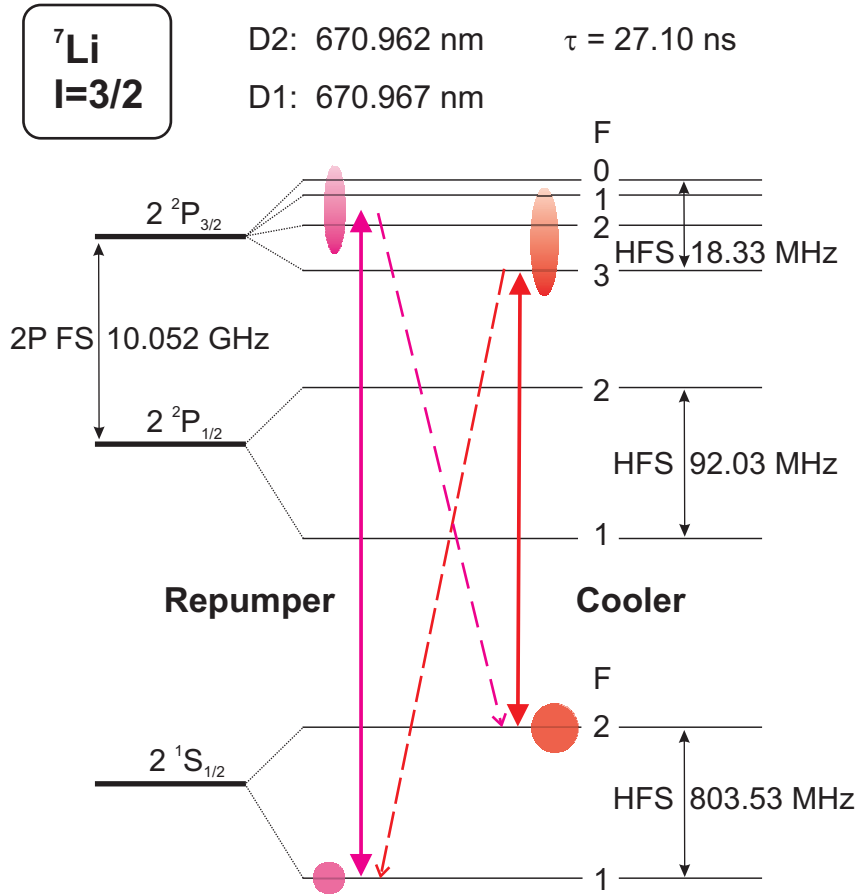


Figure 3.5: Schematic of the atomic levels of ${}^7\text{Li}$ relevant to laser cooling: The full lines indicate the ‘closed transitions’ of the cooler and repumper laser, dashed lines the decay channels to the other ground state. HFS: Hyperfine Splitting; FS: Fine structure Splitting.

Since the hyperfine sublevels of ${}^7\text{Li}$ in the $2^2P_{3/2}$ excited state are very close, and the branching ratio to the undesired state is rather high, the repumper beam must be fairly intense, leading to an approximate 1 : 1 power ratio between two different color lasers (while, in the case of ${}^{87}\text{Rb}$, the repumper only consumes a little fraction of the total cooling power, due to a rather large hyperfine splitting of 496 MHz). Therefore, for ${}^7\text{Li}$, the distinction between ‘cooler’ and ‘repumper’ is somehow ambiguous, both contribute with rather equal scattering forces.

Table 3.1: Spectroscopic properties of ${}^7\text{Li}$ relevant to laser cooling.

Quantity	Symbol	Value
Wavelength Vacuum D2($2^2S_{1/2}-2^2P_{1/2}$)	λ_{vac}	670.9767 nm
Wavelength Vacuum D1($2^2S_{1/2}-2^2P_{3/2}$)	λ_{vac}	670.9616 nm
Wavelength Air D2($2^2S_{1/2}-2^2P_{1/2}$)	λ_{air}	670.7764 nm
Wavelength Air D1($2^2S_{1/2}-2^2P_{3/2}$)	λ_{air}	670.7915 nm
Frequency D2	ν	446.8102 THz
Photon Energy D2	$\hbar\omega$	1.84786 eV
Lifetime 2^2P	τ	27.10 ns
Natural Linewidth 2^2P	Γ	5.873 MHz
		$36.90 \cdot 10^6 \text{ s}^{-1}$
Saturation Intensity D2	I_s	2.54 mW/cm ²
Hyperfine Structure Constant $2^2S_{1/2}$	a_{HFS}	401.76 MHz
Hyperfine Structure Constant $2^2P_{3/2}$	a_{HFS}	-3.05 MHz

Chapter 4

An Elementary Introduction to the Free Electron Laser

First proposed by Madey [Mad71] in early 1970's, then followed by tremendous endeavor from both theoretical and experimental sides (see review papers and books of [Rob89, Las90, Bra90, Dat95]), the free electron laser (FEL) explores the boundaries of light source with amazing characteristics, such as ultra-fast, ultra-brilliant, etc. Different from conventional lasers, FEL uses a bunched relativistic electron beam as the lasing medium rather than a gas or a solid. Based on the Self-Amplified Spontaneous Emission (SASE) principle, the combination of an unbounded electron (also defined as free electron) source and magnetic undulators produces a bremsstrahlung-induced coherent photon beam, which covers wavelengths from infrared to ultraviolet and is nudging into the soft X-ray regime and beyond [Poo92, Fel05]. In this chapter, an elementary introduction to the operating principles and main characteristics of the employed Free Electron Laser in Hamburg (FLASH) facility are presented.

4.1 Working Principle of FEL

Although the original explanation by Madey and the pilot Stanford FEL demonstrations [Eli76, Dea77] tend to treat the FEL as a quantum device, a completely classical description [Col77] of the FEL mechanism is technically feasible and widely accepted. At the heart of FEL lies the SASE principle (Self-Amplified Spontaneous Emission), which counts for the amazing features of the state-of-the-art photon machine. Via experiencing a periodic magnetic field, the high speed electron beam would spontaneously emit photons on its slalom course; in certain circumstances, the spontaneous emission can be converted into the much stronger stimulated emission, in particular in the presence of the emitted field itself.

4.1.1 The Way to Lasing for FEL — SASE principle

The operation principle of a FEL is illustrated in Fig. (4.1). Being accelerated to relativistic speed, a bunch of electrons is forwarded through the key component of an FEL facility — an undulator [Mot51], which is an array of dipole magnets with alternating poles' configuration. Because of the periodical and transversal magnetic field applied on the moving electrons, they wiggle sinusoidally under the Lorentz force, which leads to the spontaneous emission of bremsstrahlung photons; instantly, emitted photons form an additional electro-magnetic field, which interacts with the co-propagating electrons on the waggling way through the present static magnetic field: the electrons that are in phase with the transverse pulsating field are dragged as it passes by, while out-of-phase electrons get boosted. Gradually, the electron cloud is packed into microbunches that are overtaken by exactly one photon wavelength for each wiggle. As a consequence, all the electrons of the microbunches, just like a point macroparticle, radiate collectively, producing an extremely short, coherent and intense photon pulse; in contrast, at conventional wigglers electrons radiate independently. The separation between the forwarded electron flux and the co-propagating FEL photon beam is accomplished by a magnetic deflector at the export of undulator array. Routinely, two methods are employed to tune the wavelength of emitted light: either adjusting the energy of the electron beam, or changing the magnetic field strength of the undulators.

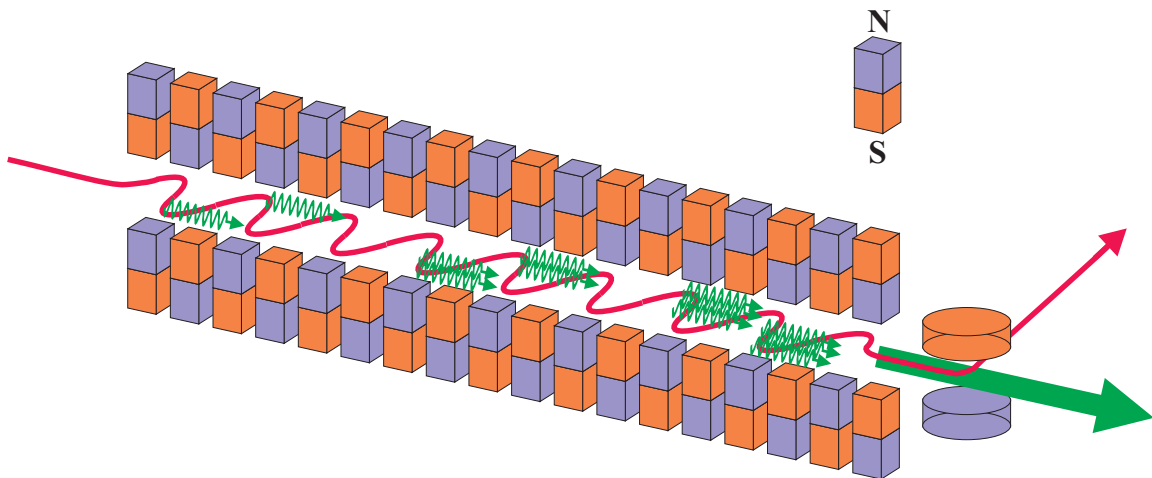


Figure 4.1: Schematic representation of the kernel process of the free electron laser (FEL) operation — undulator radiation.

Though entitled with the acronym LASER, the FEL differs from conventional lasers: a conventional laser consists of three basic components, a laser medium, an energy pump, and an optical resonator; while, a FEL merges the active laser medium and the energy pump as one, taken place by the relativistic electron beam.

For a conventional laser, stimulated emission directly relates to the population in excited state, resulting in the laser power is proportional to the particle number of this lasing medium; while, in a FEL many electrons radiate coherently, the radiation power then grows quadratically with the number of these particles.

Wavelength of undulator radiation

The wavelength of undulator radiation in the forward direction reads:

$$\lambda_\ell = \frac{\lambda_u}{2\gamma^2} \left(1 + \frac{K^2}{2} \right)$$

where λ_u is called the undulator period (the distance between two identical poles), the quantity K is the termed undulator parameter,

$$K = \frac{eB_0\lambda_u}{2\pi m_0 c};$$

and γ is the Lorentz factor, the ratio between moving mass m and rest mass m_0 , which is equivalent to the ratio between total energy W and rest energy W_0 :

$$\gamma = \frac{m}{m_0} = \frac{W}{W_0}$$

Obviously, λ_ℓ is determined by the electron's total energy W , peak magnetic field B_0 in the undulator, and by the undulator period λ_u .

4.1.2 Operation of Low-Gain and High-Gain FEL

When electrons slalom through an interaction region accompanied by a light wave, a transfer of energy between electrons and the light field happens just along the dimension, where the velocity component of the electrons motion is consistent with the transverse electric field of the light. Specifically, the electron-wave coupling goes linearly with the electric field strength of the electro-magnetic wave, and the FEL gain is proportional to the number of photons in the light wave. Hence it is well justified to speak of light amplification by stimulated emission of radiation concerning the free-electron laser. It should be noted that the function of the undulator magnet field is only to induce a transverse motion component, allowing the upper dynamic process to occur, not to supply extra energy to participate this interaction.

For a FEL operating at infrared and optical wavelengths, a high output power could be obtained by installing a short undulator magnet at an electron storage ring or a recirculating linear accelerator, in which a train of relativistic electron bunches makes many revolutions, with an additional optical resonator equipped externally, as illustrated in Fig. (4.2) (A). Therefore, the confined electron bunches keep cycling through the undulator, amplify the seeded light mode or the selected eigenmode of the cavity from the spontaneous undulator radiation. The gain of such FEL lasing mechanism is very low (a few percent upon each turn), that is how the terminology of 'low-gain FEL' gets introduced; however, an output in the order of gigawatts still could be achieved if electron beam makes an abundant turns.

But this technique is just valid unless the wavelength is decreased below 100 nm, because

of fabrication limitations of optical components in the Extreme Ultraviolet (XUV) regime. Nevertheless, the essence of SASE mechanism gives the solution to achieve a high gain for FEL running at XUV and X-ray wavelength range. In reality, the kernel undulator passage extends to a much longer distance, maximizing the number of electrons radiating coherently. The key step is modulating the electron concentration, which enables the collective radiation form a point-macroparticle-like electron bunch. In practice, it is unfeasible to compress electrons of 10^9 into such a tiny space whose diameter is far smaller than the light wavelength, especially for the X-ray regime.

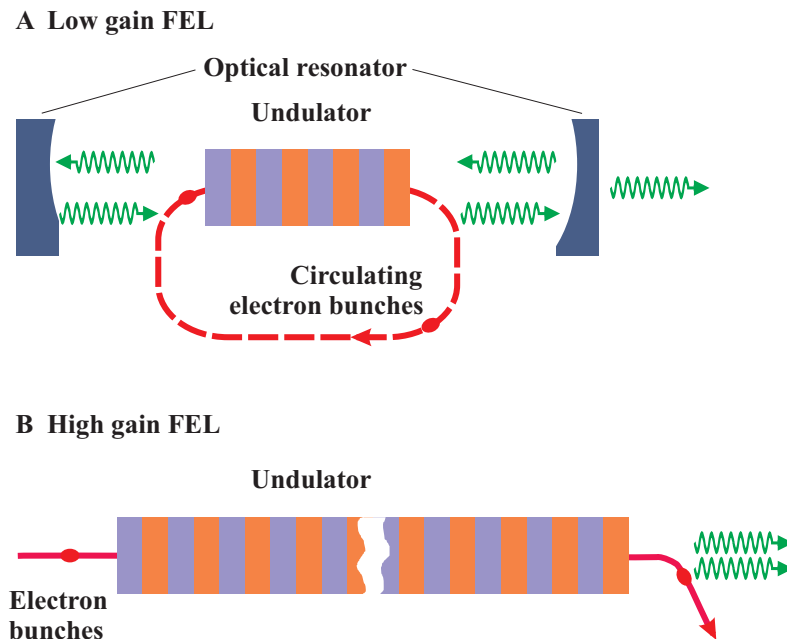


Figure 4.2: Two different schemes for amplifying FEL output: A. For visible or infrared light an optical resonator can be used. A gain of a few percent for each passage of a short undulator magnet is sufficient to achieve laser saturation within many round trips through the undulator, referred as a ‘low gain FEL’; B. In the ultraviolet and X-ray region one can apply the mechanism of self-amplified spontaneous emission where the laser gain is achieved in a single passage of a very long undulator, cited as a ‘high gain FEL’.

To overcome this obstacle, a trick the so-called microbunching is proposed: instead of being concentrated as a whole, the electrons are allocated in slices that are shorter than the wavelength. The physics lies in that the slalom trajectories of electrons that transfer energy to the light wave experience larger amplitudes than the case that electrons gain energy from the light wave; hence, a lightwave-dependent modulation of the electrons’ longitudinal velocity is induced. Once the electrons are microbunched, the coherent radiation gets enhanced; on the other hand, the enhanced radiation packs these microbunches further; thus as a consequence, the radiation power exhibits an exponential growth as a function of the length of the undulator. This remarkable feature gives this FEL mechanism the name ‘high-gain FEL’.

In the first section of the undulator, the FEL power remains constant; still, a certain distance is needed to establish the exponential growth, therefore, this FEL mechanism is characterized by a much longer magnet undulator, shown in Fig. (4.2) (B); the amplification process ceases once all available electrons are converted into microbunches.

4.2 Free Electron Laser in Hamburg Facility

Nowadays, the FEL development has reached the stage where a number of user facilities are already in operation or very near to completion, among which the Free-Electron Laser in Hamburg (FLASH), embedded in Deutsches Elektronen-Synchrotron (DESY) laboratory, is the first free-electron laser worldwide to produce femtosecond pulses in soft X-ray regime. The 260-meter-long pilot facility of FLASH, equipped with a 27-meter undulator passage, keeps a world record by producing the most brilliant femtosecond pulses ever of EUV radiation with wavelengths down to 13.1 nm.

The schematic view of the FLASH facility is shown in Fig. (4.3). Initially, the electron bunches are produced in a laser-driven photoinjector, and the bunch charge is 0.5 to 1 nC; then they are accelerated to 1 GeV maximally by a linac which consists of five accelerator modules containing eight superconducting cavities each; in between the acceleration stages, the electron bunches are longitudinally compressed by bunch compressor devices at intermediate energies of 125 MeV and 370 MeV typically, leading to a peak current's enhancement up to 1000 A from initially 50 A. Therefore, all the three requirements on the drive beam of an X-ray FEL — high peak current, very low emittance and very small energy spread are fulfilled. The FEL radiation is generated in a 27-m-long undulator system composed of six magnets of 4.5 m length each. In the end, a dipole magnet deflects the electron beam into a dump, while the FEL radiation propagates to the experimental hall. In order to make efficient use of the FEL radiation, presently, the FEL light is delivered to one of five experimental stations via steering one or two plane mirrors implanted in the photon beam transport system.

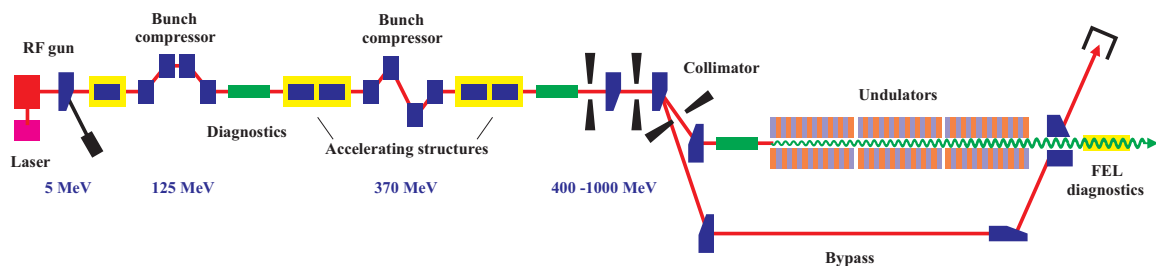


Figure 4.3: Schematic view of the FLASH facility. The beam is accelerated to a maximum energy of 1 GeV in six accelerator modules, each containing eight superconducting cavities. Two magnetic chicanes are installed for longitudinal bunch compression. A collimator removes the beam halo which might cause radiation damage in the permanent magnets of the undulator.

FLASH radiation produces photons with wavelength ranging from the extreme ultraviolet

down to soft X-rays. Together with the unprecedented properties of high brilliance (one billion times more intense than conventional devices) and small time resolution scaled as femtosecond, the FLASH demonstrates itself to be a sophisticated single-shot machine suitable in the dynamic probing and the structure resolving at the molecule and atom level. As a novel tool in photon science, FLASH shows incredible potential applications in atomic and molecular physics, solid physics, biology and medicine research, plasma, *etc.*, and also opens windows into unknown territories. Even more, the FLASH facility supplies itself as the prototype machine in the advanced photonic light source study and development.

Table 4.1: Performance of the FEL radiation @ FLASH (2005-2007).

Wavelength range of the fundamental	13 - 47 nm (from fall 2007: 6.5 nm)
Higher harmonics	3rd 4.6 nm 5th 2.7 nm 7th 1.9 nm
Average pulse energy	up to 100 μ J
Peak pulse energy	170 μ J
Peak power	5 GW
Average power	100 mW
Pulse duration	10-50 fs
Repetition rate	5 Hz
Spectral width	0.5 - 1 %
Peak brilliance	$10^{29} - 10^{30}$ [photons/(smrad ² mm ² 0.1%BW)]

With a world-wide collaboration, FLASH has gained great success and raised the international attention and interest. In 2013, the European XFEL facility (under construction) will deliver hard X-ray pulses with better time resolution and higher peak brilliance than other X-ray sources, so will several FELs for hard X-rays, *e.g.* the SLAC in California *etc.*, be ready in the near future.

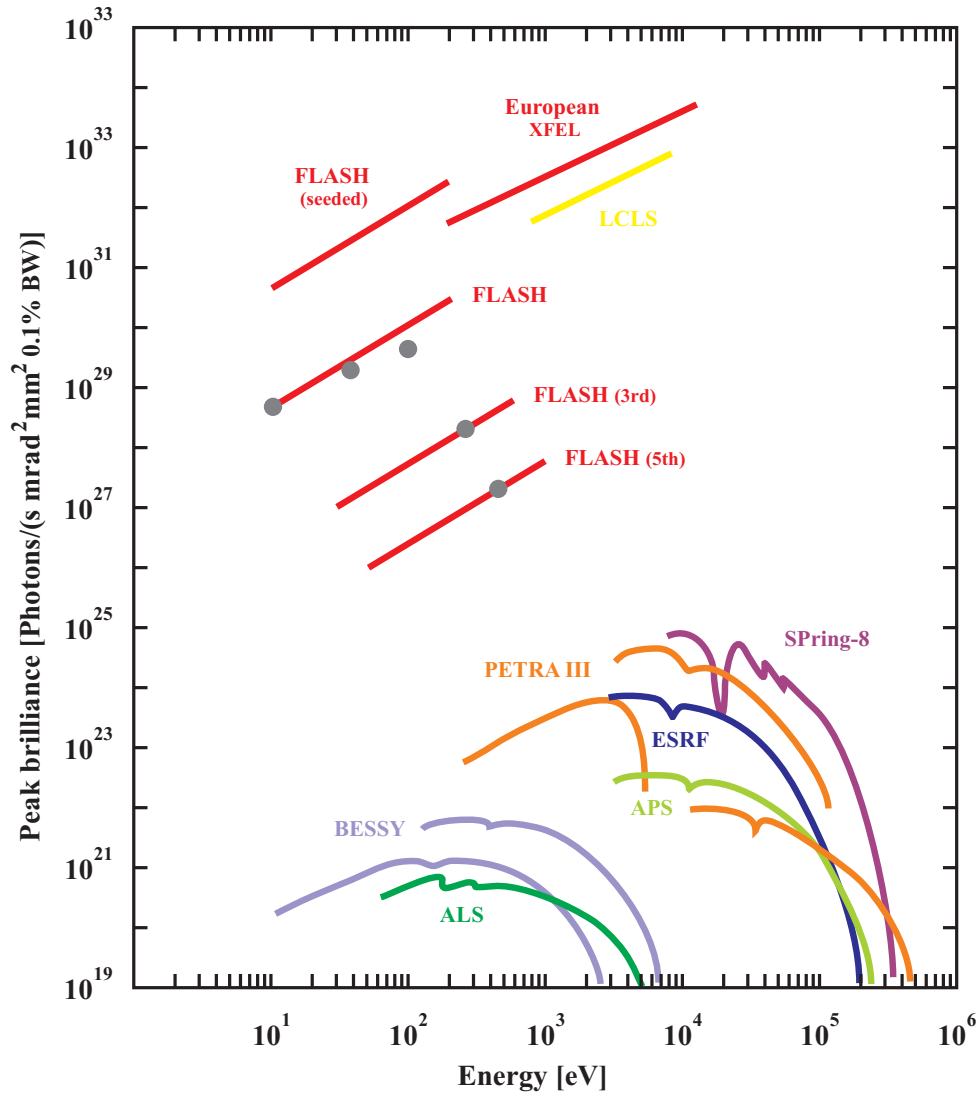


Figure 4.4: Peak brilliance of FLASH and future FELs — XFEL at DESY, and LCLS (USA), compared with selected 3rd generation synchrotron radiation sources: ALS (USA), APS (USA), BESSY (Germany), ESRF (France), SPring-8 (Japan) and PETRA III at DESY, denoted by different colors. Grey dots in plot are used for measured values.

Chapter 5

Experiment Setup — MOTReMi

This chapter describes the experimental realization of the MOTReMi apparatus used to measure fully differential cross sections for ionization of a laser-cooled lithium target. Firstly, Sec. 5.1 introduces the imaging technique of the reaction microscope (ReMi), which was originally invented and developed by J. Ullrich and R. Moshhammer [Mos94, Mos96, Ull03a]. Secondly, Sec. 5.2 presents the technical details of the magneto-optical trap (MOT), including laser cooling and optical pumping system. Thirdly, Sec. 5.3 briefly discusses the experimental implications arising from the combination between a MOT and a ReMi. The following, Sec. 5.4 and Sec. 5.5 sketch out the experiment control devices and the data acquisition units respectively.

It should be emphasized that our MOTReMi setup, compared to conventional ReMis, not only has the target species extended and the momentum resolution improved, but also allows a wide range of projectiles to be used, *e.g.*, electrons, ion beams, ultra-fast laser pulses, synchrotron radiation and FEL radiation sources, can be employed to our MOTReMi environment, therefore, a large number of different experiments can be performed, investigating a wide range of quantum dynamics phenomena. However, several systematic difficulties are encountered in designing such an ambitious scientific apparatus, especially in merging the two state-of-the-art experimental techniques so-called ReMi and MOT. The modifications implemented, the performance achieved as well as the alternate solution proposed with this new apparatus are presented in detail within this chapter.

5.1 Reaction Microscope

As often referred to as the ‘bubble chamber’ of atomic physics, the Reaction Microscope allows the kinematically complete measurements on the fragmentation of atoms and molecules by particle impact, *i.e.*, the final state momenta of all the charged fragments emerging from a breakup process are determined coincidentally by time- and position-sensitive detection equipment.

Via recording the full momentum vector of every reaction product, the full kinematics of the process can be reconstructed. However, for a total number of N particles in the final

state (including the projectile), and provided precise knowledge of the initial momenta of the collision partners, a set of $N - 1$ measured final momenta allows the determination of all kinematic parameters of the reaction by means of momentum conservation

$$p_P^i + p_R^i = p_P^f + p_R^f + \sum p_{ej}^f + \sum p_{\gamma l}^f. \quad (5.1)$$

Here, p_P^i and p_P^f indicate the initial (pre-collision) the final (post-collision) momentum of the projectile, while p_R^i , p_R^f mean the initial and final momenta of the target atom and recoil-ion, respectively. p_{ej}^f are the momenta of the ejected electrons and $p_{\gamma l}^f$ are the ones of eventually produced photons. To simplify the analysis and interpretation of data, p_R^i is set to zero since normally the atom target is prepared in a well defined initial momentum state. The momenta carried and transferred by photons can be omitted from the momentum balance, because usually they are negligibly small compared to the ionic and electronic momenta (even in multiphoton ionization); while in the consideration of the energy balance, the photons have to be taken into account.

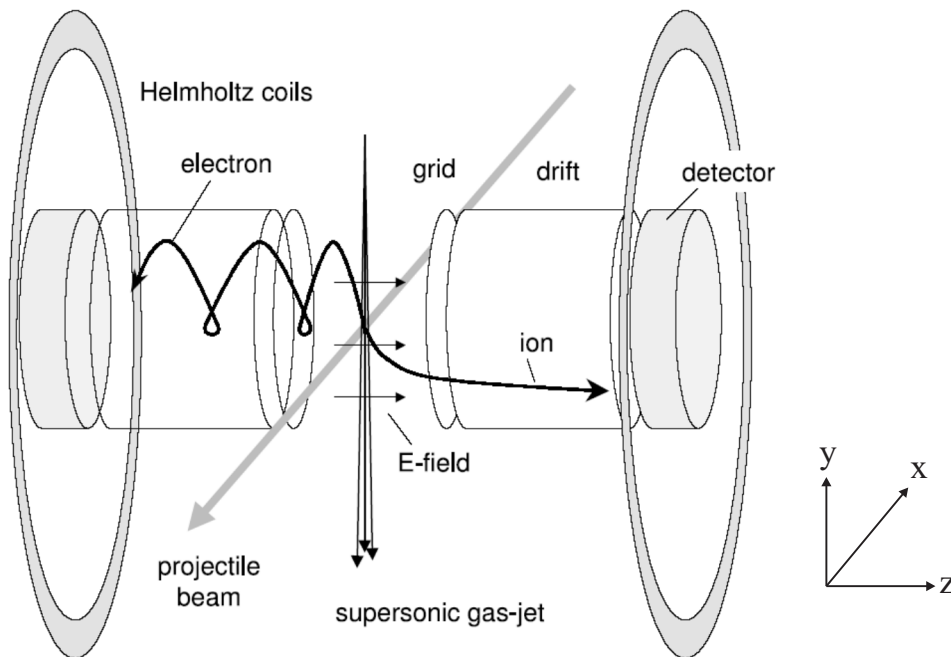


Figure 5.1: Schematic of a ‘classic’ reaction microscope, as used in ion-atom or ion-electron collisions. Ions and electrons produced by collisions with the projectile beam are guided towards position sensitive detectors by homogeneous electric and magnetic fields. The supersonic jet provides an internally cold target.

As illustrated in Fig. (5.1), a reaction microscope is essentially a combination of a recoil-ion spectrometer and an electron spectrometer, both equipped with the capability to measure the momentum vectors of charged particles. Born in the collision process, the recoil-ions and the electrons are guided onto time- and position-sensitive detectors in opposite directions, by means of a weak electric field. For the slow and low energetic

recoil ion a homogeneous electric field of a few V/cm is sufficient, while the fast and high energetic electrons are additionally radially confined by a homogeneous magnetic field of a few Gauss, parallel to the electric field. By knowledge of the external fields, the final state momentum vector (p_x, p_y, p_z) of a particle emerging from the collision can be derived from the impact position on the detector and the time of flight (x, y, t) . Assuming that a sufficient number of events was recorded, this corresponds to a direct mapping of the squared final state momentum wave-function of the collision system and therefore provides the possibility to evaluate Fully Differential Cross Sections (FDCS).

The concept of imaging spectrometers has several advantages compared to traditional experimental techniques: First of all, an acceptance for all target fragments of 4π can be achieved by adjusting the extraction fields properly, *i.e.*, there is no selectivity in energy or direction; and the whole final state phase space of the reaction is covered at once, together with the multi-hit ability of the detector systems, even multiple ionization events can be registered kinematically complete. While conventional electron spectrometers have typical detection solid angles of $\frac{\Omega}{4\pi} \approx 10^{-3}$. In a coincidence experiment, two detectors are necessarily employed, where one of them is scanned over the angle with respect to the other to cover the different collision geometries. In this case, a reaction microscope brings about an increase in the detected phase space by a factor of 10^6 .

Furthermore, the recoil-ion spectrometer identifies the species and charge state of the ion by its time-of-flight, thus allowing purification of the data from events stemming from ionization of residual gas atoms or when an electron was not detected. However, the experimentalist has to take care, that on average no more than one atom is ionized within one projectile shot. Multiple events can aggravate the identification of correlated electrons from the same source atom or even render it impossible.

For more insight into the technique of this scientific instrument the reader is referred to several review articles published in the last decade [Ull97, Doer00, Ull03a] and a book, which deals with this topic [Ull03b].

5.1.1 Spectrometer

The spectrometer units are designed to resolve all three momentum components (p_x, p_y, p_z) of ions and electrons produced after the fragmentation with a solid angle of 4π . First, a homogeneous electric field projects the charged particles onto position sensitive detectors; ions and electrons are dragged into opposite directions due to their different charge sign. After the charged particles have been accelerated over distance a , they pass through another distance d which is a field free drift region. Considering that the electrons have much higher energy and velocity than the ions, only a small fraction of them could be mapped onto the detector directly, under the weak extraction field only. This problem is resolved by imposing a homogeneous magnetic field parallel to the electric field, which is generated by a pair of coils in Helmholtz configuration. Now the electrons trajectories are confined within the spectrometer volume due to field-induced cyclotron motion. Therefore, a 4π -acceptance for electron detection is enabled, at cost of a slightly complicated recalculation of the initial momenta.

Spectrometer Design Chart

The technical design of our spectrometer is shown in Fig. (5.2), which is divided into two units (one for ions and one for electrons), each is composed by an acceleration region and a drift region.

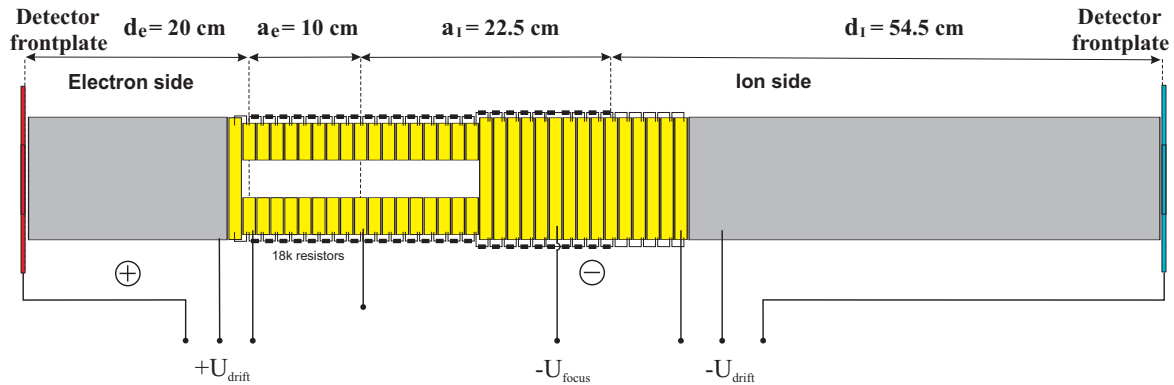


Figure 5.2: Schematic of the spectrometer with the capability of time- and position-focusing. The electrical connections are also displayed. The electrode in charge of for the 3D-focusing is supplied with an independent voltage.

At the electron spectrometer unit, an acceleration distance of $a_e = 10$ cm plus a drift distance of $d_e = 20$ cm (matching the time-focusing condition [Wil55]), which is much shorter compared with the ion's part. However, this electron spectrometer is sufficient in length to resolve the electron kinetic momenta.

In the ion part, the acceleration length is $a_I = 22.5$ cm and the drift length is $d_I = 54.5$ cm, observably, the normal configuration condition $d = 2a$ is not fulfilled here, due to the implemented time- and position-focusing (3D-focusing) requirement (which will be explained in detail in the following part). Compared with the former design (see a group thesis [Ste07]), the ion side has a longer extracting pass now, with the goal to enhance the recoil ions' momenta resolution.

The accelerating field is provided through an array of single *AlMg3* electrodes, coated with gold, isolated by ceramic spacers. Via a resistor voltage divider chain each electrode is supplied with its appropriate potential, with maximum tolerance of 10^{-4} of the absolute value. The drift tubes are unitary metal tubes, which are set to the same voltage as the ends of the acceleration region.

Adapted to the MCP detectors employed, the spectrometer has an inner free diameter of 83 mm, thus the whole detector area (diameter of 80 mm) can be used for data acquisition. An additional disc ring with a 30 mm diameter aperture was implemented in between the 'lens' and the source volume, to avoid a field penetration into the interaction region by the high voltage at the 3D-focusing segment.

During the measurements, normally the acceleration E-field was kept between $E_{el} = 0.4 - 0.8$ V/cm, which is rather low for Reaction Microscopes. Hence, the setup gets very sensitive to stray fields caused by charged isolators, and ripples on supply voltages.

For that reason several low-pass filters had to be inserted between electrodes and power supplies, annihilating the voltage fluctuation's influence on the spectra conveniently. By contrast, it was not feasible to get rid of certain stray fields forcing the ions to hit the detector a bit off the center.

For photoionization experiments, where the reaction zone is rather small, benefited by the strong focusing of projectile laser beams, the 3D-focusing method becomes unnecessary. Thus, the focusing lens electrode can be set in such a way that the whole E-field for accelerating ions is homogeneous, which enables the reconstruction of the initial momentum for recoil ions in a routine procedure (depicted in the next Subsection 5.1.2).

Time and Position Focusing

In the experimental reality, the registered electrons and ions do not originate from a point like interaction zone, but from an extended source volume determined by the overlap of the projectile beam with the target, introducing an additional uncertainty into the initial momentum calculation. This drawback can be partly compensated, if we arrange the spectrometer geometry such that the acceleration region and the drift region fulfill the length condition $d = 2a$. Then the arrival time depends only on the initial momentum in the longitudinal direction and is in first order independent on the z -position where the fragmentation occurs. This condition is called time focusing, also known as Wiley-McLaren configuration [Wil55]. In this configuration, the extension of the interaction volume along the spectrometer axis doesn't affect the resolution of longitudinal momentum anymore.

However the time focusing configuration still leaves another effect unsolved, which is caused by different starting positions transversal to the extraction direction: the extension of the reaction regime along the transversal dimension reduces the resolution for the registered transversal momenta. To fully overcome this problem, a method named position focusing [Mer96, Doer97] can be applied. Since this kind of field configuration has properties such that it maps particles with the same velocity vector but different starting points onto the same spot on the detector, while at the same time the information on longitudinal momentum is preserved, it is also called 3D-focusing. To realize such a 3D-focusing spectrometer, an additional electrostatic Einzellens was inserted into the acceleration part of the ion spectrometer (one of the electrodes on the ion side was isolated from the others and supplied with one separate voltage source), and in the mean while, the length of the drift tube was also modified to match the 'focusing condition':

$$d = 2(a_1 + a_2 + a_L) \cdot \left(1 + \sqrt{\frac{a_1 + a_2 + a_L}{a_1}} - \sqrt{\frac{2a_1 + a_L}{a_1 + a_L}} \right) \quad (5.2)$$

with

$$a_L = \frac{U_L}{E}$$

where the effective acceleration path is divided into three different segments now: a_1 , acceleration zone before the lens; a_2 , acceleration zone after the lens; and a_L , the imaginary third zone, which is defined by the voltage U_L applied on the focus lens and the acceleration electric field E .

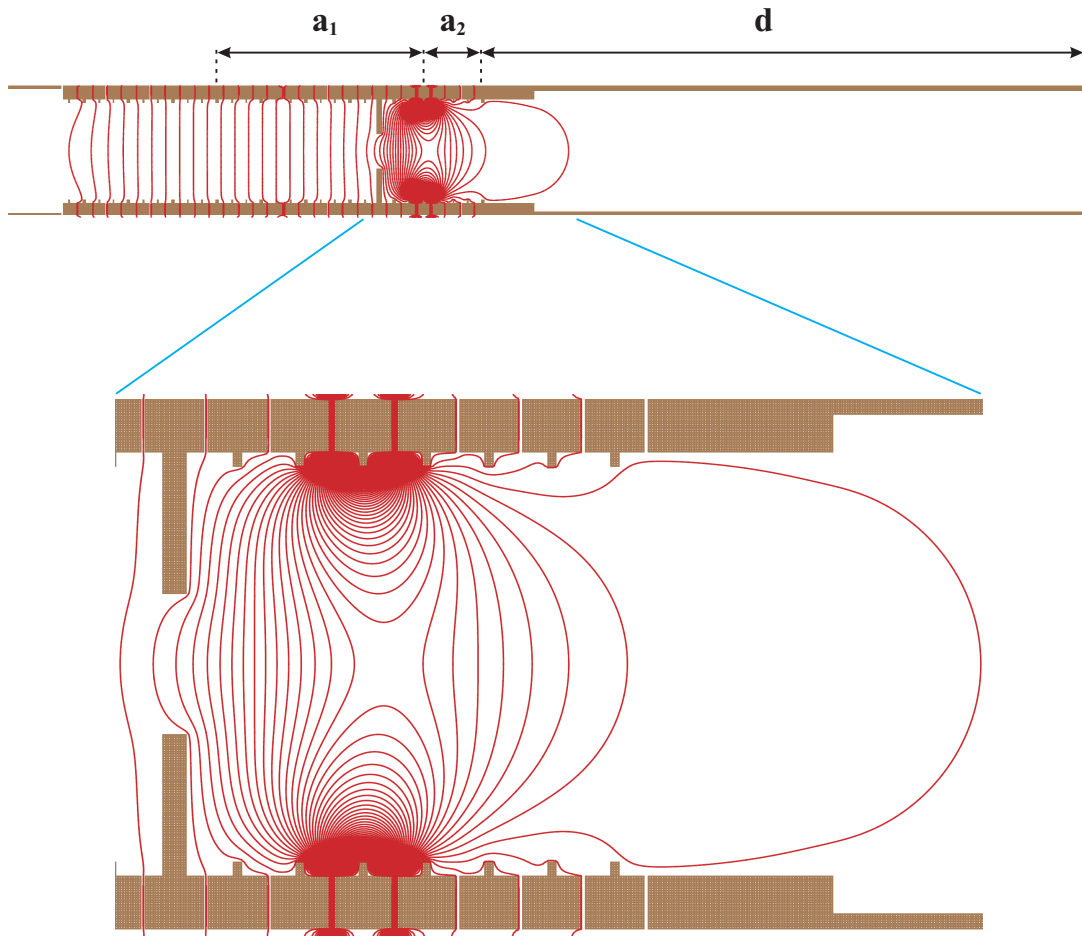


Figure 5.3: Electric potential inside the spectrometer, simulated by **SIMION3D 7.0**. Upper picture shows the whole potential array for recoil ion and electron both, where the extracting fields shows homogeneity, so dose drifting parts as well, while the 3D-focusing zone exhibits a character of field jump. The electric field at electrodes adjacent to the focus lens is displayed in detail at the bottom graph.

The position dependent electric field has been simulated numerically with the program **SIMION3D 7.0**, displayed in Fig. (5.3). In this way, optimum field arrangements for extracting and 3D-focusing have been found for various experimental requirements.

Several factors have to be considered in such a spectrometer design:

First, the ‘lens’ should be installed as far away as possible from the target, in order not to destroy the homogeneous extracting field at the collision zone. This is also a compulsory for the electron spectrometer part, since the ejected electrons may have large initial energy and fly towards the ion detector (who will be reflected by the extracting field and registered by electron detector also): If the electrons enter the focusing zone at the ion side, their trajectory will be distorted, leading to ambiguities in the reconstruction of the electron’s initial impetus. On the other hand, the distance between the reaction zone and the focusing area should not be too long, since the trajectories of the recoil ions may

expand too much, thus reducing the effectiveness of 3D-focus and increasing distortions to the imaging properties in addition;

Second, the length ratio of a_1/a_2 should be chosen appropriately, which depends on the a_L also, resulting a perfect time- and position-focusing within a compact space;

Third, inside the ion spectrometer one additional ring aperture with an inner diameter of 30 mm (in our case) is added just behind the position which the fastest ionized electron to be recorded can reach, to shield the homogeneous acceleration region from the lens potential and help to shape an efficient focusing field.

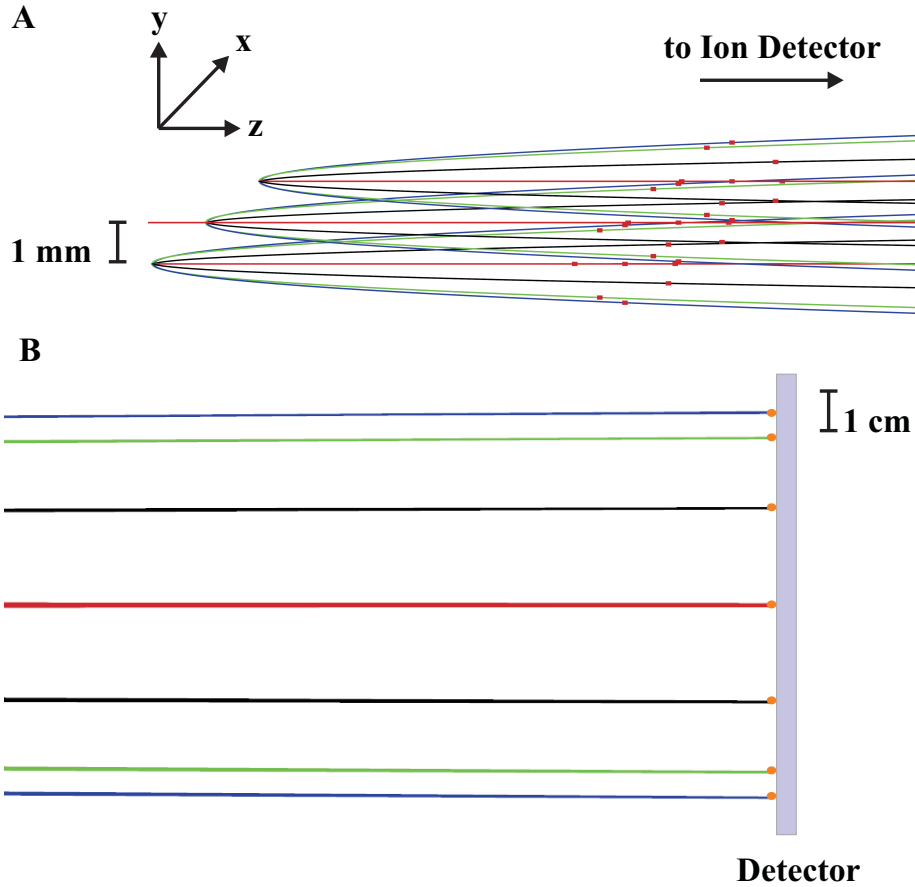


Figure 5.4: Simulated recoil Li^+ trajectories, all the parameters for trajectory simulation are referred to in the text. A: close to the interaction region. Three source points, varying by $(\Delta Y, \Delta Z) = (-1, -1), (0, 0), (1, 1)$ mm to the origin, are chosen to represent the ion spread in space. The trajectories of recoil ions with different emission angles are indicated by different colors. Here, the marker in red denotes the ions position after $4 \mu\text{s}$ flight. B: at the phase of register. After a 740 mm' s flight, ions with same kinetic momentum but different starting point converge at the detector, after a successful time and position focusing. The marker for different trajectory on the detector indicates a convergence in both spatial and ToF domain ($\delta_R \leq 0.07$ mm and $\delta_{ToF} \leq 1$ ns).

The recoil ions' trajectories, shown in Fig. (5.4), have also been simulated numerically with the program **SIMION3D 7.0**, providing reference parameters to adjust the electric potential in order to optimize the 3D-focusing effect.

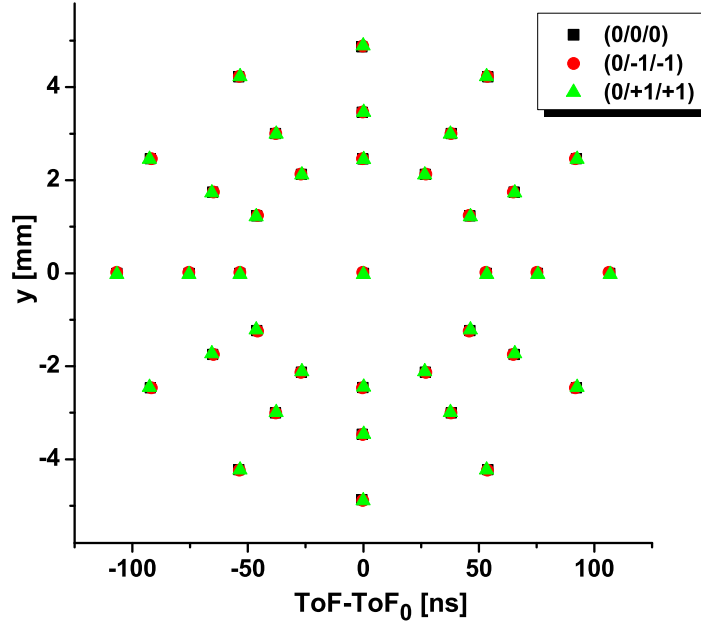


Figure 5.5: Simulation result of final momentum distribution, for given momentum distribution (see text) with varying locations (0/0/0), (0/-1/-1), (0/+1/+1).

A simulation of the recoil ion momentum distribution is shown in Fig. (5.5). Due to the limited MOT size (a maximal diameter of 2 mm), the ions starting point may vary by ± 1 mm with respect to the origin. Assuming that the kinetic energy of the recoiling Li^+ is 2 meV (ionization excess energy of 25.8 eV), with a corresponding momentum of about 1.38 a.u. in atomic units. The extracting electric field is 2 V/cm, while the voltage for the 3D-focusing lens is set to -150 V. After passing through the spectrometer region of a 740 mm, ions are registered by the detector. The focusing effect for time and position fulfills the experimental requirements: a deviation in time-of-flight of $\delta_{ToF} \leq 1$ ns has been achieved, while the time-of-flight distribution Δ_{ToF} is stretched up to about 200 ns; the position uncertainty for ions from different fragmentation sites δ_R is reduced from 2 mm to a maximal value of 0.07 mm, while the total position pattern is expanded to a larger disc with a diameter of $2R = 9.8$ mm. Thus, a better momentum resolution (especially in the transverse dimension) is obtained, resulting from the 3D-focusing technique. In addition, recoil Li^+ kinetic energies of 0.5 meV and 1 meV are also put into the simulation, to check the focusing effect. In Fig. (5.5), the regular pattern shows the final momentum distribution of ions with different initial momentum. From big to small radii, the different circles are for 2 meV, 1 meV and 0.5 meV, each point around the circle indicates a different emission angle with respect to the x axis (0° , $\pm 30^\circ$, $\pm 60^\circ$, $\pm 90^\circ$, $\pm 120^\circ$, $\pm 150^\circ$ and 180°).

The three different symbols denote ions from site (0/0/0), (0/-1/-1), (0/+1/+1), showing a good convergence in space.

With **SIMION3D 7.0**, not only the field profile and ions' trajectories can be simulated in order to optimize the 3D-focus effect, but the momentum calibration of fragments as well, which is helpful in the ion momentum reconstruction, since the trajectories are altered by the focusing electric field, thus adding difficulties in deducing the initial kinetic momenta. While in practice, an accurate momentum calibration on recoil ion is established with the knowledge of physical process at hand, e.g., a well-known momentum gap in the spectrum (exhibiting a strip or shell structure) as a criterion, or a coincidentally measured electron spectrum as a precise reference.

Magnetic Extraction Field

To obtain a spectrometer acceptance also for fragmented electrons up to 4π solid angle, an additional magnetic extraction field is in required to confine the electronic motion to a cyclotron orbit. A routine treatment is to install a pair of large size coils encompassing the whole experimental apparatus, and approximately fulfilling the Helmholtz-condition $r = D$, where r is the coil radius and D is the mutual distance, thus a homogeneous magnetic field is established within the spectrometer region.

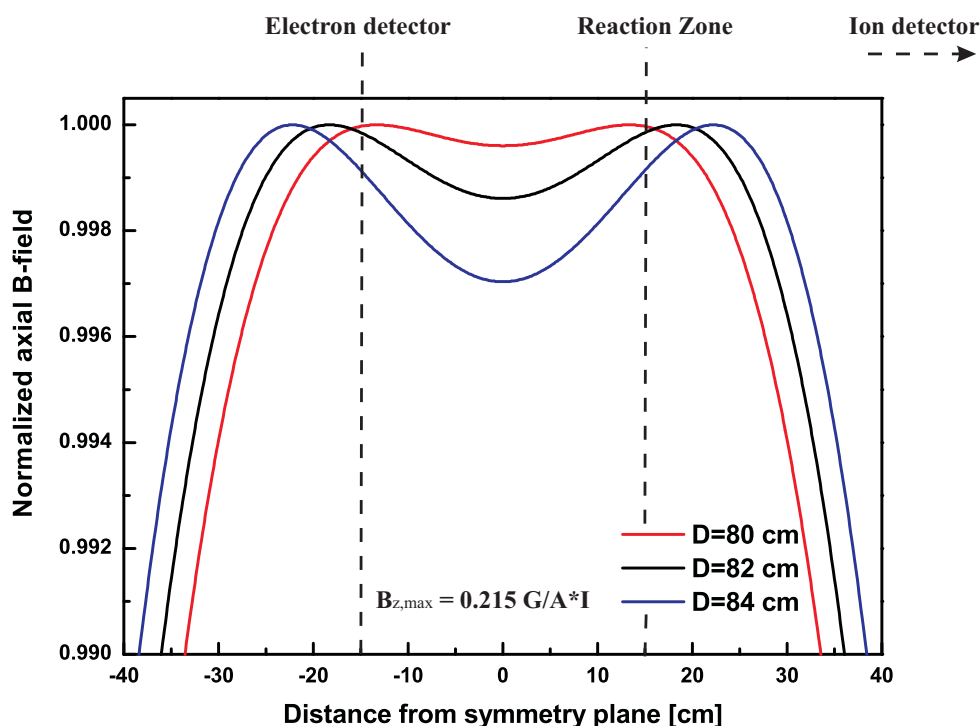


Figure 5.6: Calculated axial magnetic field B_x of the Helmholtz-coils for different coil spacing D (here D is the distance between the inner faces of the coils). Each curve is normalized to its maximum value. The position configuration for the vintage electron extraction is also marked, for installation instruction.

These coils are wound with water-cooled copper tube to 24 turns, and the maximum

current is 50 A. The coils have an inner diameter of 156 cm and are asymmetrically mounted to the interaction region along the spectrometer's longitudinal axis z , with a mutual distance of about 80 cm. Since the electron's trajectory has more critical demand on the field homogeneity than the ion's, the coils could be placed a little bit further apart and slightly center-shifted toward the electron detector.

The calculated axial magnetic field B_z for different coil spacing D , is plotted in Fig. (5.6), showing that the magnetic homogeneity critically depends on D . However, a deviation of less than 0.5% of the maximum value throughout the whole electron spectrometer volume is easily maintained. One measurement on the relation between running current I and the generated magnetic field B_z with a fixed spacing $D = 80$ cm is performed, confirming our calculation of B_z .

Concerning the initial kinetic energy of the liberated electrons under our experimental conditions, the extraction field was chosen to be a few Gauss. As a consequence, an extra magnetic field should be employed to compensate the influence of the earth magnetic field, which is about a half Gauss. The solution is rather simple but reliable, with two more pairs of additional Helmholtz-coils made of ribbon cable added along the x - and y -transversal directions, indicated in Fig. (5.1) [Sch08]. Furthermore, the implementation of ribbon cable coils also offer the function of trimming the zero crossing of the MOT magnetic field, resulting in a precisely adjustment of MOT position.

5.1.2 Momenta Reconstruction

The trajectories of the charged particles carry the kinetic information imprinted by the dynamic fragmentation process. All the information is contained in the time-of-flight signal and the position signal once the collision products get recorded by detectors. Therefore, knowing the external extracting field exactly, the initial momenta of fragments can be reconstructed precisely via a classical mechanics analysis. Based on the axial symmetry of the spectrometer, it is convenient to express the momentum vectors of the electrons and ions in cylindrical coordinates. In standard notation, p_{\parallel} denotes the longitudinal momentum along the spectrometer axis z , and $p_{\perp} = \sqrt{p_x^2 + p_y^2}$ is the transversal or radial momentum. Besides the two momenta (p_{\parallel}, p_{\perp}) description, also the coordinates (p_{total}, φ) are used to derive the full three dimensional information from the experimental data. Here $p_{tot} = \sqrt{p_{\parallel}^2 + p_{\perp}^2}$ is the total momentum, and $\varphi = \arccos(p_{\parallel}/p_{total})$ is the angle between the total momentum and the longitudinal momentum.

Reconstruction of Ion Momenta

The trajectories of the ions (with charge q and mass M) along longitudinal axis is easy to calculate within the frame of Newton's laws of motion, leading to the expression of the time-of-flight between the starting point and the detectors,

$$t_{\pm}(E_{\parallel}) = f \cdot \sqrt{M} \cdot \left(\frac{2a}{\sqrt{E_{\parallel} + qU} \pm \sqrt{E_{\parallel}}} + \frac{d}{\sqrt{E_{\parallel} + qU}} \right). \quad (5.3)$$

As shown in the equation, the motion of the particle is divided into two parts: the first

term corresponds to the acceleration by a constant electric field $E = U/a$ through a length of a ; the second term describes a drift with a constant velocity along a distance of d until it reaches the detector; here the '+' sign has to be used for ions emitted in direction of acceleration and the '-' sign is used for those emitted in opposite direction. The pre-factor is $f = 719.7 \sqrt{\text{eV}/\text{amu}} \cdot \text{ns}/\text{cm}$ if the units are chosen like these: the time-of-flight in ns, the length of both the acceleration a and the drift region d in cm, the mass M in amu, and qU in eV, as well as the longitudinal component of the initial kinetic energy E_{\parallel} .

By replacing E_{\parallel} with $p_{\parallel} = \sqrt{2ME_{\parallel}}$ within the upper formula, a numerical solution of the longitudinal momentum p_{\parallel} can be derived from the measured time-of-flight with an approximate assumption applied to Eq. (5.3). In the case of $qU \gg E_{\parallel}$ for ions, the energy gained during acceleration is much larger than the initial longitudinal energy, a linear approximation of Eq. (5.3) around the point $t_0 = t_{\pm}(E_{\parallel} = 0)$ can be justified, which leads to the relation

$$p_{\parallel} = 8.042 \times 10^{-3} \frac{\text{cm a.u.}}{\text{eV ns}} \cdot \frac{q \cdot U \cdot \Delta t}{a}, \quad (5.4)$$

where $\Delta t = t_{\pm}(E_{\parallel}) - t_0$. The actual value of t_0 has to be determined carefully in a calibration procedure. It should be pointed out that this derivation of the longitudinal momentum is also applicable for fragmented electrons.

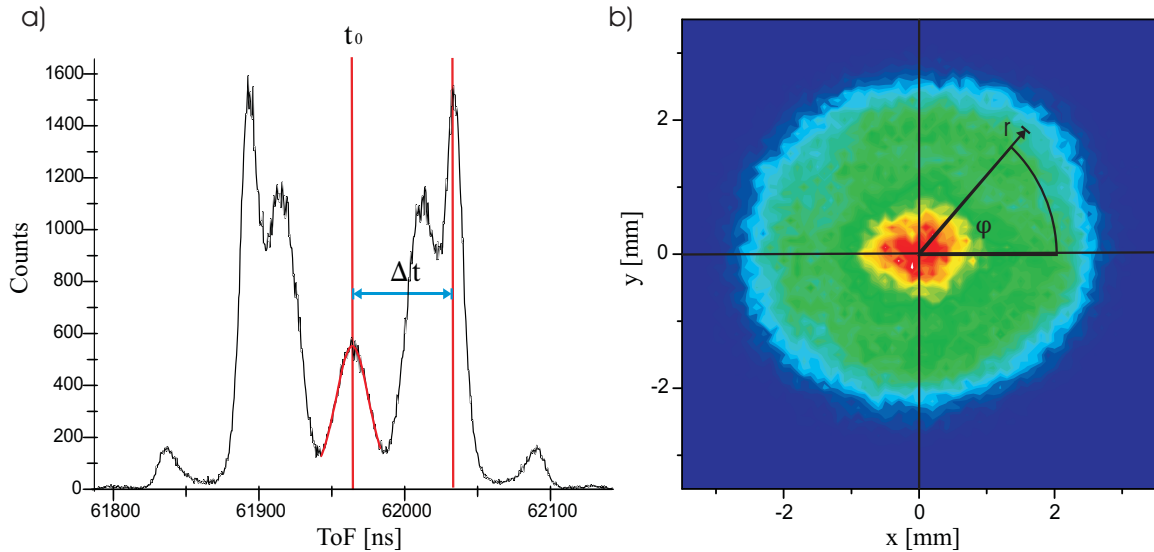


Figure 5.7: Exemplary time- and position-spectrum for momenta reconstruction. Left: Time-of-flight spectrum of recoil ions, from which the longitudinal momentum p_{\parallel} is extracted with the time difference Δt , with respect to the center of the time-of-flight t_0 , which is calibrated as the zero initial momentum $p_{\parallel} = 0$. Right: Normalized position spectrum of the ions (in color), with the radial vector indicated, which carries the information on the transverse momentum. The azimuth angle of the recoil ions ϕ is also displayed here.

The transversal component of the recoil ion's trajectory can be regarded as a uniform linear motion; therefore the ion's transverse momentum can be deduced directly, once the

transversal displacement and time-of-flight are measured.

However, under the condition of $qU \gg E_{\parallel}$, a simple form of the transversal displacement is derived,

$$r := \sqrt{(x_{ion} - x_0)^2 + (y_{ion} - y_0)^2} = (2a + d) \cdot \sqrt{\frac{E_{\perp}}{qU}}, \quad (5.5)$$

where (x_{ion}, y_{ion}) is the arrival position on the detector, a reference point (x_0, y_0) denotes the spot at which an ion with zero initial momentum gets registered. The transverse momentum in a.u. is then given by:

$$p_{\perp} = 11.6 \frac{\text{a.u.}}{\sqrt{\text{amu eV}}} \cdot \frac{r}{2a + d} \cdot \sqrt{qU \cdot M}. \quad (5.6)$$

The reference point (x_0, y_0) is uniquely defined by the centre of the spatial distribution of the events on the detector, due to the cylindrical symmetry of the reaction with respect to the projectile or polarization axis. Besides the transverse momentum, also the emission angle in the xy -plane can be calculated by $\varphi = \arctan 2(y_{ion} - y_0, x_{ion} - x_0)$.

Reconstruction of Electron Momenta

Now we switch to the reconstruction of the electron momentum, which is more difficult, because the electron's trajectory is more complicated under the superposition of magnetic and electric fields.

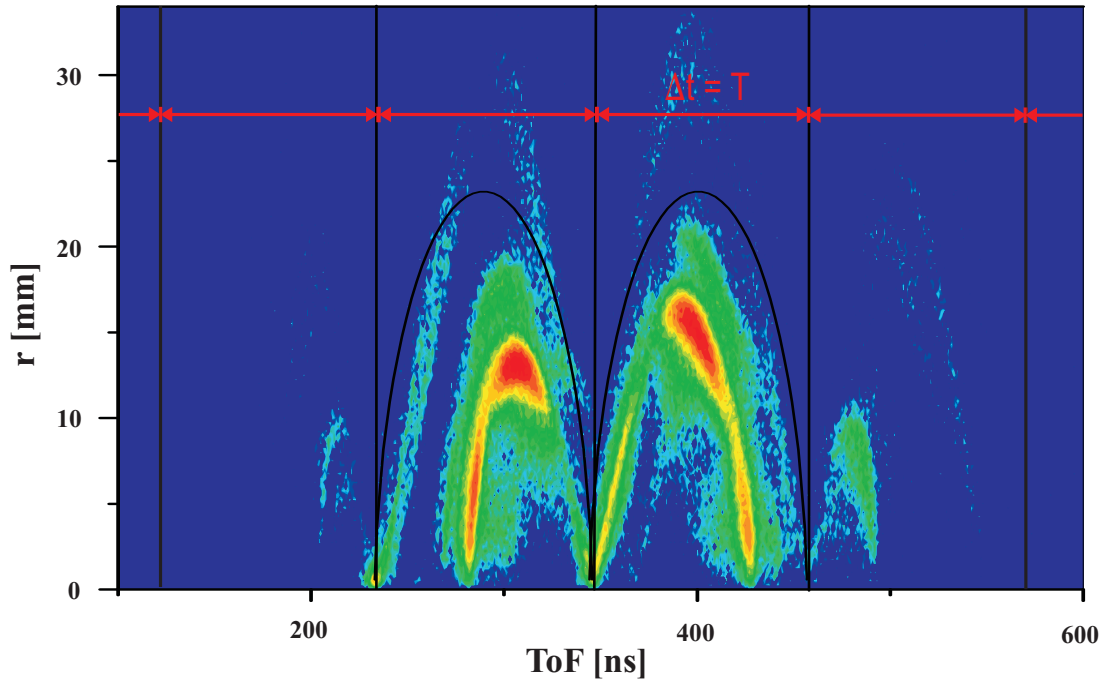


Figure 5.8: The detected radial range of electron trajectories as a function of the time-of-flight, exhibiting a characteristic wiggly structure.

The longitudinal momentum of the electrons is not influenced by the magnetic extraction field, meaning that Eq. (5.4) is still valid. Due to the small mass of the electron, the initial

kinetic energies of the particles is now on the same order of magnitude as the acceleration potential qU . Therefore condition $qU \gg E_{\parallel}$ is not fulfilled anymore. Hence, either the nonlinear Eq. (5.3) has to be solved, e.g. by the Newton method [Bro01], or the inverse function [Sch98a] has to be approximated. However, the absolute zero point of the time-of-flight $t_e = 0$ is needed for both approaches. This can be identified with the help of the electron cyclotron motion, where the time of circulation is determined by the magnetic field B . The cyclotron frequency is

$$\omega = \frac{2\pi}{T} = \frac{qB}{m}. \quad (5.7)$$

An electron emerging from the spectrometer axis will always come back to it after one full revolution, which generates a ‘wiggle’ structure in the Radius-over-ToF-spectra Fig. (5.8). Since the time $t_e = 0$ has to be in a wiggle, and a particle that hits at $t = t_{e,0} + nT$ with $n \in 2N$ will also be in a wiggle, the absolute zero point of the electron time-of-flight is figured out through a linear extrapolation of the wiggles obtained toward $t = 0$. In addition, the distance between the wiggles, which dedicates the cyclotron period time T actually, can be extracted to inspect the magnetic field strength in the inside the chamber.

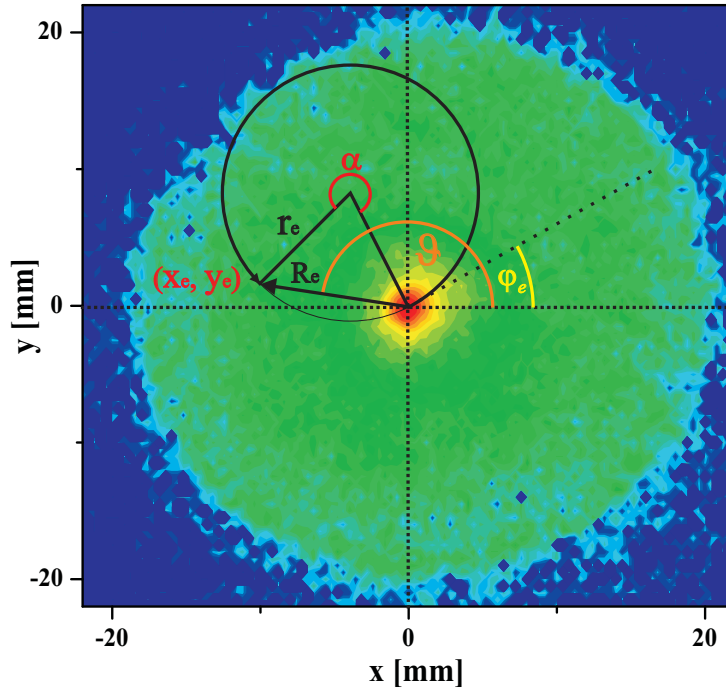


Figure 5.9: Electron position spectrum E for the reconstruction of transversal momentum p_{\perp} .

The derivation of the electron’s transversal momentum depends on another attribute belonging to the cyclotron motion of electron in magnetic field, which reads:

$$r = p_{\perp}/qB, \quad (5.8)$$

thus the judgment of the radius r of the cyclotron motion becomes the key point. Illustrated in Fig. (5.9), the electron hits the final arrival position (x_e, y_e) after passing through $\omega \cdot t / 2\pi$ turns in the magnetic field, whose trajectory depends on the initial azimuthal angle φ_e also. The centre of the xy -coordinate system is defined by the origin of the electron trajectories which lies on the spectrometer axis. The relation between the radius r_e and the distance R_e of the hitting position from the detector center reads

$$r_e = \frac{R_e}{2|\sin(\omega t/2)|}. \quad (5.9)$$

In the end, the transverse momentum gets such an expression of

$$p_\perp = \frac{1}{2} \cdot \frac{eR_e B}{|\sin(\omega t/2)|}. \quad (5.10)$$

And the azimuthal angle during the emission φ_e is related to angle ϑ in the detector plane by

$$\varphi_e = \vartheta - \omega t/2 \quad (5.11)$$

derived from simple geometrical considerations.

It should be pointed out, that the resolution strongly depends on the time-of-flight, such that the momentum resolution gets worse approaching a wiggle, where R_e is small and the denominator in Eq. (5.9) approaches zero. Actually, all information on the momentum of the electrons arriving in a wiggle collapses. However, in practice two methods are available to bypass this limitation: either, one can vary the magnetic field, focusing the electrons at different times; or, the time-of-flight is altered by simply changing the electric extraction voltage. In both cases two spectra are recorded, which have to be merged in order to get the full picture.

5.1.3 Detector Systems

The full kinetic momenta of fragments are recorded by time- and position-sensitive detectors, which are the combination of a pair of micro channel plates (MCP) and a delay-line anode.

A MCP is a device for particle detection by secondary electron multiplication. It has one planar cellular structure via fusing few-micron-diameter glass tubes together, both faces are metalized to provide parallel electrical connections to all channels. Applying a potential difference of 10^3 V between the faces, each channel becomes an independent electron multiplier with a gain of about 10^4 . Usually two MCPs are stacked in Chevron-configuration to enhance the net gain further. When a charged particle impinges on the MCP, a cloud of secondary electrons is produced, then accelerated towards the position sensitive anodes, normally delay-line anodes, and wedge-and-strip anodes [Mar81] as well.

The different trajectories and different registration manners between the recoil ion and the electrons, as mentioned earlier, give the difference requirements on the delay-line anodes: a two-pairs-wire wound at an angle of 90° is used to detect ions; while a three-pairs-wire

wound at an angle of 60° (so-called delay-line Hexanode) acts as an electron detector, with the multi-hit capability significantly enhanced.

First a commonly used delay-line Quadraanode is picked out to demonstrate the working principle of a position encoding anode, afterward, more information related to the deadtime-free Hexanode will be presented in detail.

The arrival time of an impinging particle is extracted from the MCP as the arrive time t_0 ; the subsequently induced electron cloud is picked up by the positively biased wire and produces a charge pulse, that travels along the wire in both directions. The position measurement is reduced to a time measurement: assuming that the signals with an effective velocity v_{eff} (concerning the centroid averaging effect) propagates along each coordinate, the registered timing signal at each end of the delay-line is marked as t_l and t_r , respectively, the position coordinate in one layer shows a proportional relation with and the arriving time difference :

$$x = v_{eff} \cdot ((t_l - t_0) - (t_r - t_0)) = v_{eff} \cdot (t_l - t_r) \quad (5.12)$$

The second layer, wound orthogonal to the first one, provides the second coordinate y . In practice, a pair of wires is used (the signal- and the reference wire), to suppress ambient electro-magnetic noise picked up by the anode wire. The signal wire is biased with a more positive potential in order to collect the main fraction of the charge. The achievable resolution depends on the timing resolution, which is about 0.5 ns with the present setup which would correspond to a resolution of about 0.5 mm.

By adding the arrival times of the signals on both ends of the wire a constant value the so called time-sum is derived, dependent on the anode size and the cable length only

$$t_{sum} = (t_l - t_0) + (t_r - t_0) = const \quad (5.13)$$

During analysis, ‘good’ events are filtered from noise by examining the time sum for each detected particle. Furthermore the time-sum can be utilized to reconstruct events, if for example the time signal of one end of the wire is not detected.

Hexanode Detector

This position encoding detector allows registration of several electron hits arriving within a time interval of a few nanoseconds as encountered in double or multiple ionization. Since information about particle impact at times and positions very close to each other may get lost due to the deadtime, in the so-called Hexanode delay-line a third layer of wire collects redundant position information. The deadtime, originated in the numb period of the time to digital converter (TDC) and the ability of the constant fraction discriminator (CFD) to separate two subsequent signals, is around $\Delta t_d = 10$ ns in practice. Thus, the signals from the delay-lines get lost when they overlap at the readout electronics. The deadtime regions of a standard delay-line Quadraanode and Hexanode are compared in Fig.(5.10), which are dependent on the position difference (Δx , Δy) of the first and second hit, relative to the arrival time difference Δt . Obviously the Hexanode wins over the Quadraanode by the performance in electron detection.

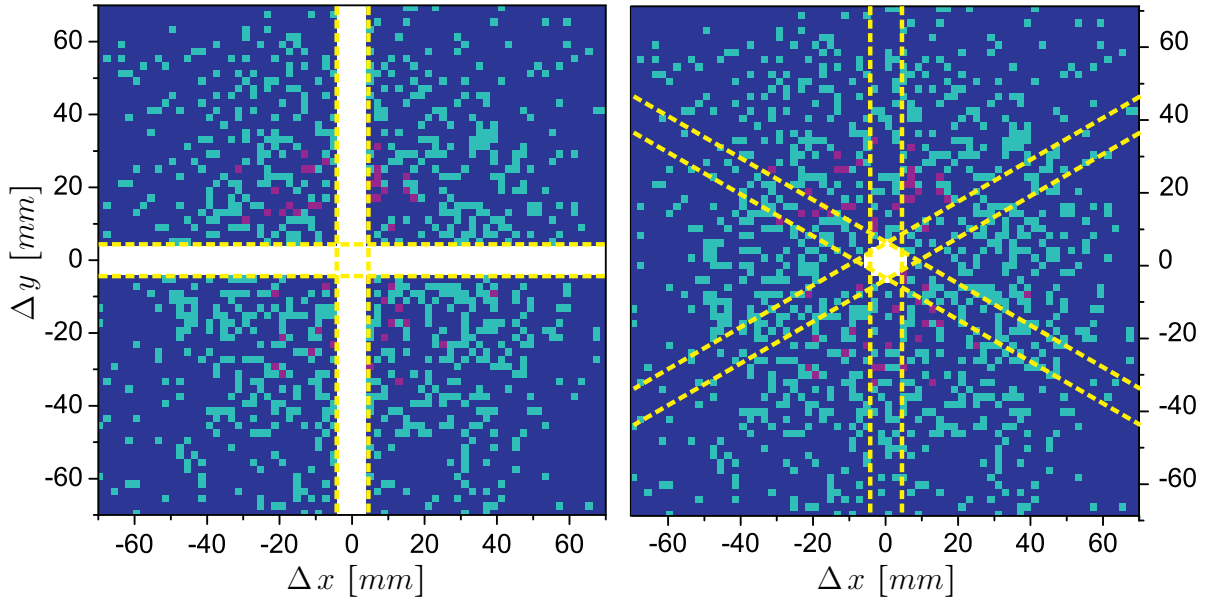


Figure 5.10: Deadtime region (indicated by blank area) resulting for the second hit arriving within 10 ns after the first hit. A comparison is made between a 'conventional' Quadraanode using two layers of delay lines (left) and a novel Hexanode consisting of three layers (right), plotted in the position difference of the first and second hit.

As the Hexanode provides three wire layers u , v , w with a mutual angle of 60° , to restore a Cartesian coordinates (X, Y) the following transformations have to be applied:

$$\begin{aligned}
 X_{uw} &= u \\
 Y_{uw} &= \frac{1}{\sqrt{3}}(u - 2v) \\
 X_{uv} &= u \\
 Y_{uv} &= -\frac{1}{\sqrt{3}}(u + 2w) \\
 X_{vw} &= v - w \\
 Y_{vw} &= -\frac{1}{\sqrt{3}}(v + w)
 \end{aligned} \tag{5.14}$$

5.2 Magneto-Optical Trap

Now we focus on another key component of the MOTReMi apparatus — the magneto-optical trap (MOT), which prepares the cold atomic target and holds the ensemble fixed in space also. This implementation of target preparing, other than the routinely used supersonic jet technique, shows significant advantages: firstly, a minimum temperature of about $400 \mu\text{K}$ can be reached via the active laser cooling method, breaking the supersonic jet's temperature limitation at mK level; secondly, atoms are three-dimensionally cooled and spatially localized, while the jet target maintains a superimposed drift veloc-

ity; thirdly, sophisticated manipulations of the target, *e.g.* excited state selection, valence electron orbit alignment, spin-polarized target preparation, all can be realized. In this section, a systematic browse on the MOT setup is exhibited, with the cooling machine mainly decomposed into three parts: the MOT coils (trapping magnetic field), the laser system and the atomic beam source/Zeman slower. The respective theoretical description is given in Chap. 3. More construction details on the present MOT setup are found in [Ste07].

5.2.1 MOT-Coils in Anti-Helmholtz Configuration

Aiming at magneto-optical trapping of alkali atoms, we employ a pair of coils in anti-Helmholtz configuration, which generate a heterogeneous magnetic field with a gradient in three dimensions. The build-in MOT coils should fulfill the following specifications:

- High field gradients along the coils' symmetry axis should be realized;
- The field switching times have to be kept as short as possible;
- The eddy currents (induced by rapidly varying of the magnetic field) in the adjacent conducting components, *e.g.*, the vacuum chamber, the spectrometer and the supporting frames, ought to be annihilated as fast as possible;
- The cooling scheme should effectively remove the heat generated by coils current in an ultra high vacuum (UHV) environment.

The coils are manufactured of round copper tube (with a 5 mm outer diameter and inner one of 3 mm), conducting both electric current and cooling water. After 4×6 turns winding (along the axial dimension 4 times and the radial direction 6 rounds), a coil package with an inner diameter of 12 cm and an outer diameter of 19.5 cm is formed. As the electrical insulation material, 0.125 mm-thick Kapton-HN foil is selected to wrap the copper wire and to cover the coil holder's contact surface. The coil assembly is then mounted to the coil holder attached to a CF200-flange, and soldered to a nonmagnetic copper tube vacuum feedthrough, which guides the electric current and cooling water in and out.

According to the anti-Helmholtz configuration's condition $r = D$, two coils are placed apart by 10.4 cm. To reduce the induced eddy currents during magnetic field switching, several efforts are taken: a slit is introduced in the plane coil holder to avoid a big electric circuit; ceramic spacers are inserted into three braces out of four of the coil holder, to interrupt the forming of electric loops also.

Based on the upper selected design, the MOT coils can produce a magnetic field gradient of 0.282 G/cm · A along the axial direction and 0.141 G/cm · A in the radial plane. Fig. (5.11) gives the calculated axial field gradient, where each turn of the coil has been approximated by a circular current loop. A maximum operation current of 70 A is tolerated in continuous duty. The coils have an Ohmic resistance of $R = 44 \text{ m}\Omega$ and an inductance of $L = 75 \mu\text{H}$.

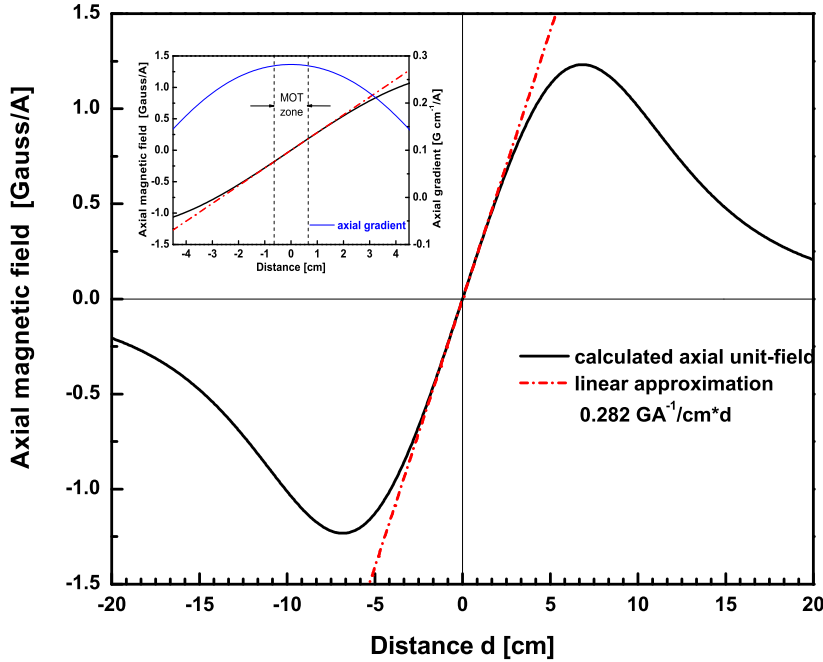


Figure 5.11: Calculated axial field (at a unit current of 1 A as a demonstration) of the MOT coils (in anti-Helmholtz configuration). Within the MOT zone, the magnetic field gradient is constant, shown by an inner plot (upper-left).

In experiments for ionization of laser-cooled Li atoms, the MOT coils are operated in a switched mode. This scheme will be discussed in Sec. 5.3.

5.2.2 Laser System for Cooling and Optical Pumping

As the principles on laser cooling and trapping have been being explained in Chap. 3, so have the spectroscopic properties of Lithium (especially the $D2$ transition line $|2^2S_{1/2}\rangle \rightarrow |2^2P_{3/2}\rangle$) been introduced, in referring to Fig. (3.5). Hence, we acquire the optical specifications on cooling and trapping laser system:

Six duochromatic beams, in the counter propagation configuration along three dimensions, serve as the MOT beams, where the so-called ‘cooler’ frequency component drives the transition $|2^2S_{1/2}, F = 2\rangle \rightarrow |2^2P_{3/2}, F' = 3\rangle$ and the ‘repumper’ is responsible for the $|2^2S_{1/2}, F = 1\rangle \rightarrow |2^2P_{3/2}, F' = 0, 1, 2\rangle$ line. The total light power in the order of 100 mW is shared by the two frequency components, both red-detuned by a few linewidths (-5 MHz to -20 MHz), which is sufficient to saturate the atomic transition;

One beam which serves as the atom bumper — Zeeman slower beam, contains two frequencies which drive the same transition as the MOT beams but are far off resonance in

red (-200 MHz to -280 MHz);

The laser linewidth should be considerably narrower than the natural linewidth of the cycling transition. In lithium, a laser linewidth less than 1 MHz is necessary, considering the natural linewidth of 5.9 MHz on the lithium $D2$ transition. Additionally, in order to obtain the long term stability of MOT operation, the center frequency drift of the running laser should be kept below 2 MHz/24 hour;

The power ratio between cooler and repumper should be well balanced, to ensure an efficient repumping process, bringing atoms back into ‘cooling cycle’ instantaneously and exhaustive. For Li^7 atoms, a proportion of 1:1 is needed.

All these requirements can be fulfilled by a tunable dye laser or Ti:Sa laser, however the delicate manipulation and the immoderate cost kept us seeking another choice. The single-mode diode laser based on T. Hänsch’s littrow configuration delivers high-power, tunable spectroscopic lasers, covering a large near infrared wavelength range, are widely used in cooling alkali atoms (Li, Rb, Cs). Nowadays, maximum 500 mW output diodes are even available at the rubidium D-lines (at 780 nm, 795 nm). However, at the wavelength of lithium (671 nm), the commercial available diodes can only supply power up to 30 mW. This limitation on lasing power could be circumvented by employing the method of ‘injection-lock’ via a master-slave configuration, or just introducing one amplifier.

Within the last few years, three different methods based on different laser systems have been tested to achieve a Li-MOT in our laboratory. Since lots of technical details have been presented in several group theses [Spi05, Ste07], here only a brief overview is given:

Injection-Locking Method using Broad Area Laser

The injection-locking is a frequency phenomenon can be observed in numerous physical systems, particularly often associated with laser oscillators. When a pair of master oscillator and slave laser is coupled together, the free running resonator (Slave) is disturbed by the frequency stabilized oscillator (Master) operating at a neighboring frequency; above the threshold of sufficient coupling, the slave laser will take over the spectral characteristics of the master laser, meaning the essential spontaneous lasing is superseded by stimulated emission processes, whereas its eigenmodes are completely suppressed.

A low-cost semiconductor device, broad area lasers (BAL), is selected as the slave resonator, which has a much wider active layer ($200\ \mu\text{m}$) than conventional diodes (giving the BAL also the name broad emitter diode), and largely enhances the power amplification capacity [Gol88, Paw00, Shv00]. Several drawbacks torture the implementation of laser cooling due to the lasing medium’s highly asymmetric dimensions: several spatial and spectral modes are simultaneously tolerated within the Fabry-Perot-type laser cavity, resulting in a power competition between all permitted modes covering a wide spectral bandwidth about 2 nm; its beam profile in far-field is terribly poor and far from Gaussian. The long term stability of BAL injection-locking suffers from the mode-drifting and mode-hopping within the non-linear medium. Additionally, non-linear effects such as self-focusing and filamentation, caused by random fluctuations in current density and light intensity, deteriorate the beam quality further.

To achieve a predominant gain on the wanted seeding mode, a good ‘mode-matching’ is

prerequisite [Pra98], where in experimental arrangement a ‘cylindrical lens plus collimator’ combination is used to trim the injected beam. Different ‘mode-matching’ schemes have been proposed, *e.g.*, small/large angle injection, a single longitudinal-/transverse- mode selection, but in manipulation the suitable one depends on the fabricated BAL chip’s eigen-specification.

Two-Mode Operation of a Dye Laser System

Because of the inconvenience in the BAL injection-locking implementation, we switched to a dye laser system **Coherent CR-599-21** with a linear resonator, which produces 300 mW power with a Gaussian profile, matching the requirement of laser cooling.

It is widespread textbook knowledge that it is challenging to achieve a single-mode operation using a linear resonator due to the spatial hole burning phenomenon of the inversion in dye medium [Dua90, Men07]. The physics behind could be simply stated as: In a lasing active medium, a standing wave of frequency ν_1 , which has an inhomogeneous spatial distribution of its electric field strength, may ‘burn up’ the population inversion at the antinodes of the standing wave, inevitably resulting in a stronger saturation of the gain for that lasing mode than for other competing modes, while leave the part near the nodes unchanged. However there may exist another standing wave with frequency ν_2 , whose antinodes coincide with the nodes of the ν_1 one in the active medium, leading to the favorable ‘burn up’ for ν_2 lasing at different spots. This effect can be used to construct a dual-frequency laser source, in order to excite both hyperfine levels of the Li ground state.

For the realization of two-mode lasing at 671 nm, with an 803 MHz frequency difference, the resonator length L is selected as 55.24 cm; and the nearest reflection mirror to the jet is set at a distance D of 9.21 cm, just satisfying the relation:

$$\Delta\nu = |\nu_1 - \nu_2| = \left(m + \frac{1}{2}\right) \cdot c/2D \quad (5.15)$$

where c is the velocity of light; $m = 0, 1, 2, \dots$ [Her75, Bal85]. Indeed, the two frequencies will interact with different groups of the dye molecules; therefore the phenomenon of spatial hole burning of the inversion further weakens the competition between two frequencies. In this way, the lasing efficiency gets enhanced, thus a total output of 400 mW with two modes is delivered, higher than the yield of single-mode operation condition.

It should be pointed out that, the dual-wavelength scheme based on the spatial hole burning requires a linear resonator, where propagate standing waves; and can not be applied to a normal ring dye laser with traveling waves [Mar76b, Sch77].

To stabilize the selected frequencies, FM-lock techniques for long- and short-term stabilization are implemented for the dye laser [Ste07]. A spectroscopy setup as a reference is built up externally to determine the MOT-transition and to modify the laser frequency. Since the dye laser lacks the possibility of central frequency scanning, a magnet coil wrapping the spectroscopy cell is used to modulate the transition signal alternately, via varying the Zeeman shift of the resonance. Then a dispersive error signal generated by electronic devices is feed to the external scan input of the dye laser. Once the dye laser is tuned to the Li D_2 transition lines, this lock-in method does function effectively for hours. In

parallel, the internally equipped Fabry-Perot interferometer (an inner lock-in loop based on the cavity's transmission maximum), enables the **COHERENT CR-599-21** the capability of short-term frequency stabilization, which can not be provided by the low-speed external lock-in detector.

In general, this two-mode dye laser demonstrates significant advantages: the unique 'one laser' device delivers an intrinsic dual-frequency composition output, fulfilling the cooling and repumping requirement automatically, which enlists less optics elements, and thus largely reduces the optical losses; a narrow bandwidth laser with power up to 400 mW can be achieved; a simple but effective means of FM-lock scheme guarantees the dye laser's frequency stabilization for more than 6 hours. Nevertheless, this MOT laser system still has several drawbacks, e.g., the capability of central frequency detuning is absent; the frequency difference between the two modes is difficult to modify; and the power proportion of each mode is not well controlled. Even more critically, the dye laser performance is heavily influenced by irregular small air bubbles within the dye jet which change the effective cavity length, resulting in a fluctuation in lasing power and wavelength, or in a big bubble case, an induced mode-hop which interrupts the mode-lock process. Such a quasibistable system is of limited application in a dexterous and long-term MOT manipulation.

Tapered Amplifier and Master-Oscillator-Power-Amplifier Scheme

The output power of conventional semiconductor lasers is limited by the transverse and lateral dimensions of the narrow-striped optical waveguiding structure, which is necessary to maintain a single spatial mode. A strategy of enlarging the gain volume, by introducing a tapered flared region, succeeded in enhancing brightness by an order of magnitude.

The structure of a tapered amplifier (TA) is depicted in Fig. (5.12). The active gain medium is the tapered region (red area) through electrically pumping. As it propagates from the narrow entrance to the wide end, the optical beam grows and expands laterally due to diffraction, thus the intensity at the output facet is kept below the threshold value for catastrophic optical mirror damage (COMD). This device can serve as either an amplifier [Wal92] or a laser [Kin93], depending upon the coating way on the input and output facet.

The configuration of a master-oscillator-power-amplifier (MOPA) [Yaz91, Kor91, Wel92], an integration of a distributed-Bragg-reflector (DBR) laser with a TA device, is customarily used to boost laser brightness in the near infrared regime. In our setup, a **DL 100** single-mode diode laser @ 671 nm is coupled to a **TA-0670-0500-6** chip (both from **TOP-TICA Photonics AG**) with both facets antireflection coated. The built-in single-mode waveguide operates as a preamplifier which curtails the needed seeding power, and as a mode filter which selects out the transversal TEM₀₀-mode only. By injecting a saturation power of 13 mW, an output of 550 mW maximal is achieved in a single nearly diffraction-limited lobe. This MOPA system wins over the other laser pumping schemes, by unique features, as a more efficient light amplification yield, a more modest requirement (beam profile, power) on the injected seed, and a more robust stability and reproducibility.

Through an optical isolator (retrieved-light protection), a 400 mW laser power is extracted to an AOM-based optical system for further frequency modulation. In the initial scheme,

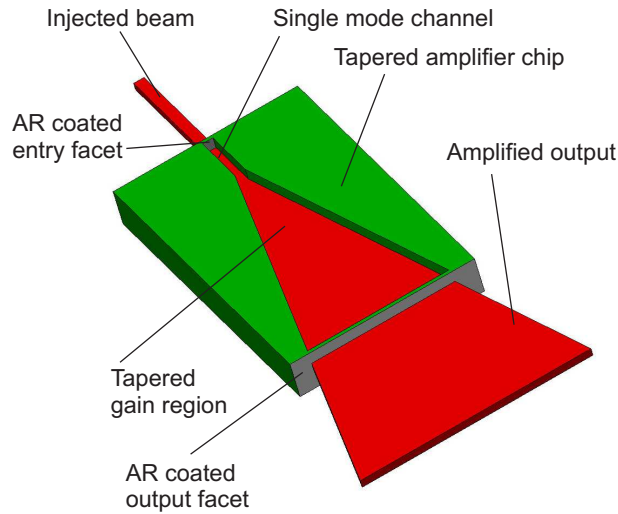


Figure 5.12: TA chips

the laser frequency was locked to the ‘crossover’ resonance line, which sits in the middle of the $|2^2S_{1/2}, F = 2\rangle - |2^2P_{3/2}, F' = 3\rangle$ and $|2^2S_{1/2}, F = 1\rangle - |2^2P_{3/2}, F' = 2\rangle$ transition lines. The amplified beam was split into two beams with equal intensity, shifted to the cooler and repumper frequency through two ‘double-pass acousto-optic modulator’ systems [Don05], and superimposed again as the MOT beam. A third AOM is responsible for the slower beam generation, introducing another 200 MHz redshift to each frequency. In all frequency modulation units, a passive ‘cat’s-eye retroreflector’ optics is employed to preserve the cooling beam path while detuning the frequency [Sny75]. In the end, three MOT beams with 50 mW each, and a slower beam of 20 mW are obtained.

For more details on the TA semiconductor lasing source, please refer to a comprehensive tutorial review paper by J. N. Walpole [Wal96].

Present Laser Setup

Till now, all the optics setups mentioned above are free-space-propagating configurations. Because of safety and security reasons for the FLASH measurement, the laser beams were guided through optical fibers into the experiment; Furthermore, due to the space requirement, the transportation and installation, a compact, robust and powerful arrangement is a mandatory.

The whole laser-setup used for the measurements presently which is illustrated in Fig. (5.13), fits a $150 \times 90 \text{ cm}^2$ optical table. Diode laser 1 is FM-locked by means of Doppler-free spectroscopy through a lithium-vapor cell. Diode laser 2 is then overlapped with Diode laser 1 using a polarization beam splitter (PBS). One arm output is used for a beating-lock loop, which stabilizes laser 2 referring to laser 1 with a frequency difference of 803 MHz. The other arm is coupled into the **TA 100** amplifier. Both frequency components are amplified simultaneously, and the output spectrum is almost identical to the seeding beam, excepted for additionally induced frequency sidebands. The power ratio of the two components is freely adjustable by varying the intensity ratio of the two injected modes [Fer99]. AOMs are employed to detune frequencies and switch beams: the +1 order beam after

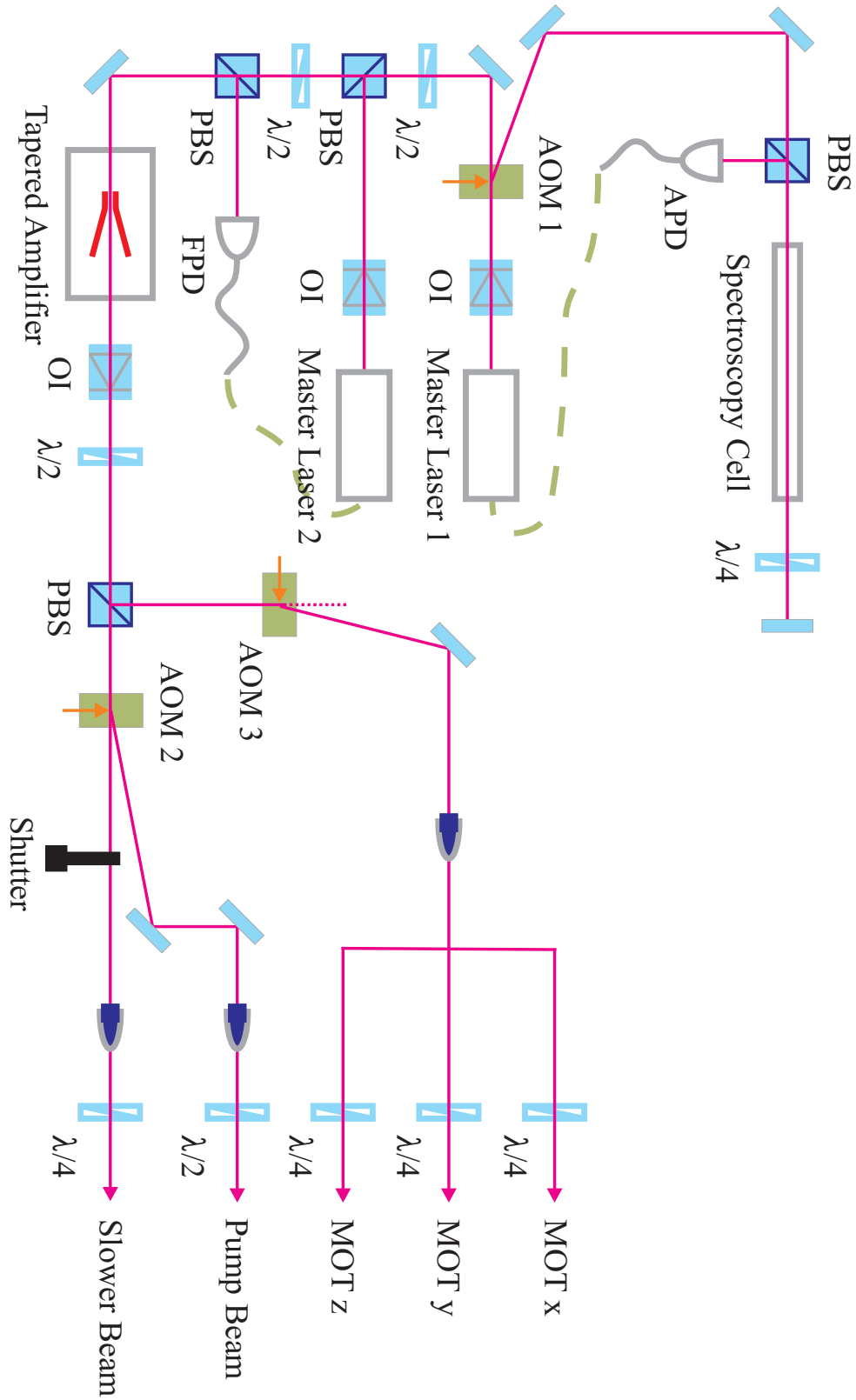


Figure 5.13: Schematic drawing of the laser setup

AOM 1 is used for absorption spectroscopy, and locked at the Lithium $D2$ transition line $|2^2S_{1/2}, F = 2\rangle - |2^2P_{3/2}, F' = 3\rangle$, leading to that both master lasers are red-shifted by 200 MHz with respect to the cooling and repumping resonance lines; then the amplified duo-frequency beam is blue-shifted by 190 MHz through AOM 2, serving as the MOT beam with 10 MHz redshift, while the 0th order fraction after AOM 2 acts as the slower beam with 200 MHz detuning; one additional AOM 3 @ $RF = 200$ MHz is implanted in the slower beam's path, grabs the laser power as the MOT loading process is finished, pumping the Lithium target to the excited state $|2p\rangle$ on resonance. The MOT beams and pumping light are electro-optical switched by AOM 2 and AOM 3 individually, within 200 ns; while the slower light is switched by one home-built mechanical shutter within 1 ms. A set of polarization-maintaining (PM) fibers from **OZ optics** is used to transport the laser beams to our MOTRIMS apparatus: a coupling efficiency up to 58% has been reached for the PM fiber patchcords, which deliver the Slower and pumping beam separately; a PM fiber based beam splitter is employed to divide the MOT beam into three equal portions with 50% power loss, and to guide them to the main chamber in x, y, z directions. Collimation tubes with a quarter wave plate installed are mounted at the PM fiber end couplers, trimming laser beams on demand. Via overlapping the 25 mm diameter trapping beams precisely, a steady lithium MOT with a density of $10^{10}/\text{cm}^3$ is generated under a saturation parameter of $s_0 = 97$. With the 4 mm diameter optical pumping beam, a $|2p\rangle$ excitation fraction up to 45% has been reached during the photofragmentation @ FLASH experiment.

Scheme of Frequency Stabilization

In realizing atom cooling and trapping, it is necessary to stabilize the laser frequencies to atomic transitions. A free running laser, without stabilization, will never stay at a specific frequency. Even small environmental effects, such as temperature change or noise, could lead to a frequency drift as the laser is not actively stabilized.

Here, we briefly introduce the frequency-lock methods employed in the present laser scheme.

First of all, in order to stabilize the laser at a specific frequency, the frequency of the laser should be known precisely. The Doppler-Free Saturation (DFS) spectroscopy method is recommended, and routinely used for frequency measurement. One very good and comprehensive introduction is given in 'Laser Spectroscopy' by W. Demtröder [Dem91].

Frequency Modulation Lock

The modulation of the diode lasers injection current produces both amplitude modulation (AM) and frequency modulation (FM), according to the unique aspects of semiconductor diode lasers. In many cases of atomic transitions the frequency modulation is the dominant effect, because the atomic linewidth corresponds to a small fractional change in frequency. Thus it provides us the particular application to lock the laser frequency, so-called FM-Lock [Cas82, Bjo83, Dre83].

The circuit drawing of a general FM-Lock loop is shown in Fig. (5.14).

The DFS spectroscopy signal recorded by an avalanche photodiode (APD) is fed to a Pound-Drever detector, which generates a so-called Pound-Drever error signal (the first

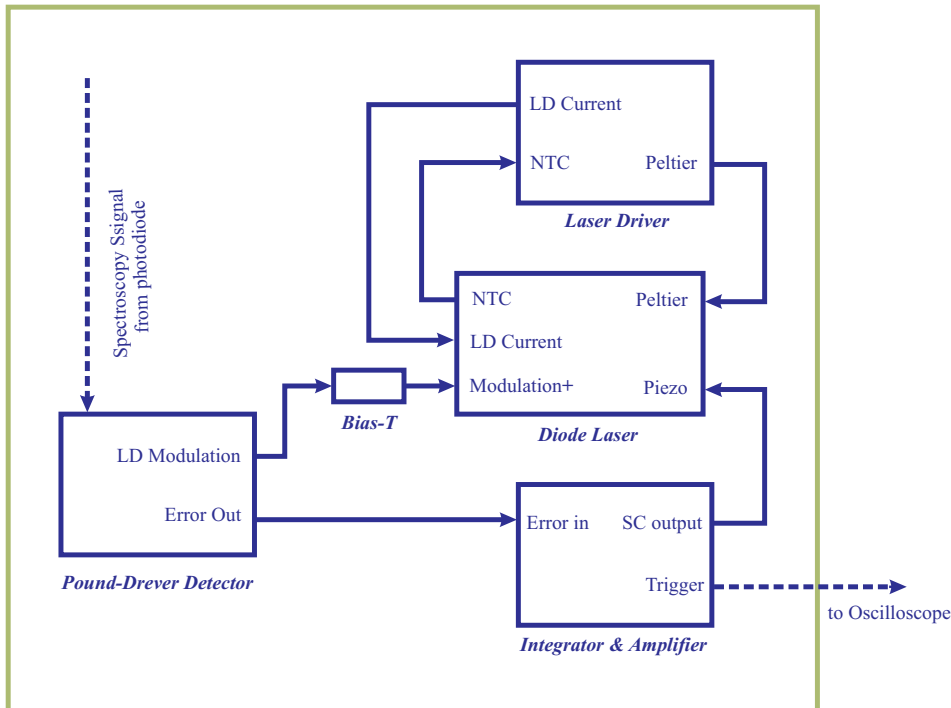


Figure 5.14: FM Lock Chart

derivative of the atomic absorption line). This error signal is transferred to an ‘integrator & amplifier’ unit, consisting of a proportional-integral-derivative element (PID) and a high voltage amplifier, which regulates the amplitude and offset of the error signal. Afterwards, the well-adjusted feedback signal is delivered to the piezo crystal, which moves the optical grating inside diode laser. Thus, the electronic feedback effects the length of the external cavity, and so the laser frequency. When the laser is right on an atomic transition, the error signal is zero and the cavity length is unchanged. If the laser drifts, the error signal is different from zero and as a result, the cavity length is changed. When the phase of the error signal is adjusted correctly, the change of the cavity length brings the laser back to the desired atomic transition.

In principle, the error signal can also be used to modulate the laser diode current, which modifies the laser frequency much faster than the ‘grating stabilizing’ method via controlling the laser external cavity. However, the regulation bandwidth of the error signal for such a frequency modulation option is much higher than the one for ‘external cavity manipulation’, which challenges the lock-in amplifier. To prevent the current overrun while modulation, an element of Bias-T is necessarily employed, and one additional attenuator (Mini-circuits) is needed normally.

Fig. (5.15) displays the error signal (in red) derived from the absorption spectroscopy signal of atomic Li^7 isotope (in blue) in a FM-lock scheme.

In producing a MOT, the modulation of the cavity length via a feedback on the piezo (controlling the optical grating) is sufficient.

Frequency Offset Lock

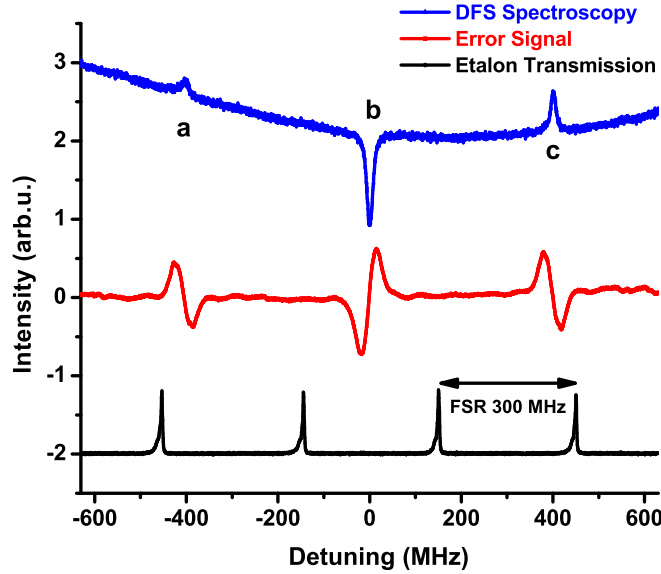


Figure 5.15: FM Lock Signal, and each transition line (dip) is labeled out, so is the crossover. The transmission etalon signal serves as a frequency marker.

In the last paragraphs, we have discussed one method (FM-Lock) to stabilize our laser to one specific atomic transition. In experimental realization of MOT, at least two laser frequencies need to be stabilized (with respect to each other). One is driving the $|2^2S_{1/2}, F = 2\rangle - |2^2P_{3/2}, F' = 3\rangle$ transition, referred as ‘cooler’, the other is exciting the $|2^2S_{1/2}, F = 1\rangle - |2^2P_{3/2}, F' = 2\rangle$ one, referred as ‘repumper’. Aiming at loading atoms faster and trapping more efficiently, these two driving frequencies need to be detuned independently depending on the applied trapping magnetic field.

To fulfill these requirements, one possible solution is to apply the FM-locking method on the two lasers independently. We either lock both lasers onto the same narrow Lamb dip (crossover for example) and employ additional AOM devices to shift the frequency to the two different transition lines, respectively, at the cost of losing laser power; or just lock them onto the two separate D2 transition lines directly, which loses the flexibility of frequency detuning, unfortunately.

The technique of Frequency Offset Lock (FO-Lock) [Sch99] enables us to overcome the dilemma of normal FM-Lock. Since the FO-Lock method employs a frequency beating signal, usually it is also referred to as Beating Lock (B-Lock).

The FO-Lock loop composition from electronic elements (Mini-circuits) is shown in Fig. (5.14).

A fast photodiode (FPD) is employed to measure the beating signal of the overlapped beams from one FM-locked laser 1 (stabilized as frequency reference ν_1) and one free running laser 2 (with centered frequency ν_2). The converted electronic signal flows through a high-pass filter, which bans low frequency noise and selects the wanted component

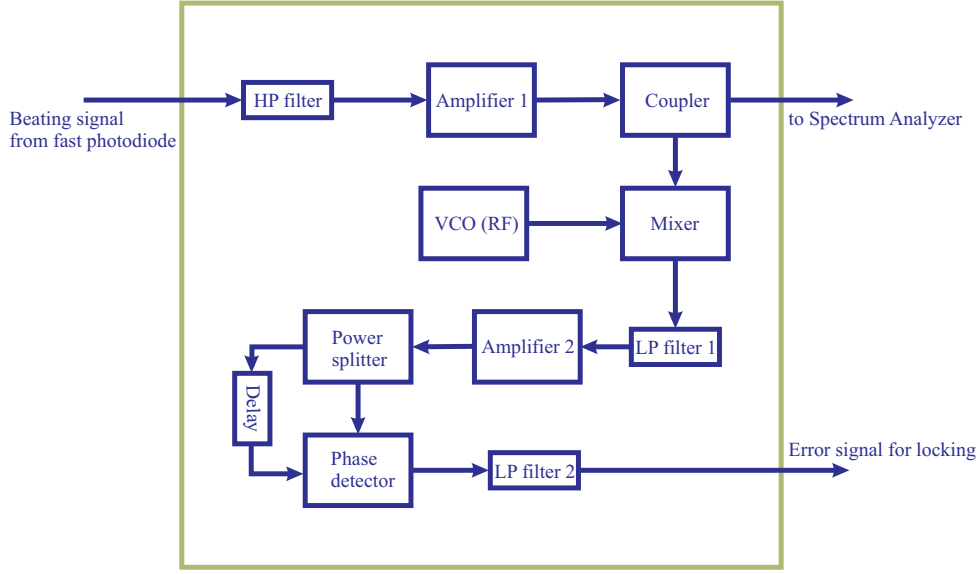


Figure 5.16: FO Lock Chart

$\Delta\nu = \nu_1 - \nu_2$ (the beating component $\nu_1 + \nu_2$ is not within the detection range). A high gain amplifier intensifies this signal if necessary. A coupler picks up a small portion of the beating signal, serving as a monitor ‘leak out’ to a spectrum analyzer (or a fast oscilloscope); while most of the power goes through the following mixer, where it is mixed with a reference radio frequency (RF) ν_{RF} produced by a Voltage Control Oscillator (VCO) or a Wave Generator. A low-pass filter afterwards blocks the high frequency component of the mixing output $\Delta\nu + \nu_{RF}$ and selects the low frequency component $|\Delta\nu - \nu_{RF}|$. This signal is amplified by another low noise amplifier, and then is divided into two equal parts by a power splitter. One is delayed by a few meters long coax cable (e.g. BNC), then both parts are recombined and compared on a phase detector. The resulting output voltage U of the phase detector varies as $\cos \Phi$, where the phase shift Φ introduced by the cable is given by

$$\Phi = 2\pi(\Delta\nu - \nu_{RF})\tau = 2\pi(\Delta\nu - \nu_{RF})\frac{nL}{c} \quad (5.16)$$

where n is the refractive index dependent on the dielectric properties of the cable, L is the length of the cable.

The output signal U of the phase detector as a function of the frequency difference between reference and the beating signal is shown in Fig. (5.17), where the beat frequency is scanned by detuning the frequency of one of the lasers. The envelope of the cosine curve reflects the limited bandwidth of the phase detector. The so-produced voltage U as an error signal, is fed to the diode laser via the ‘integrator & amplifier’ (the unit for locking signal modulation). Thus the laser can be locked via choosing a zero crossing in the error signal curve.

As shown in Fig. (5.17), there are several zero crossings, spaced by $1/\tau \approx 80$ MHz, which can be utilized to stabilize the laser frequency. The locking point can be tuned either by

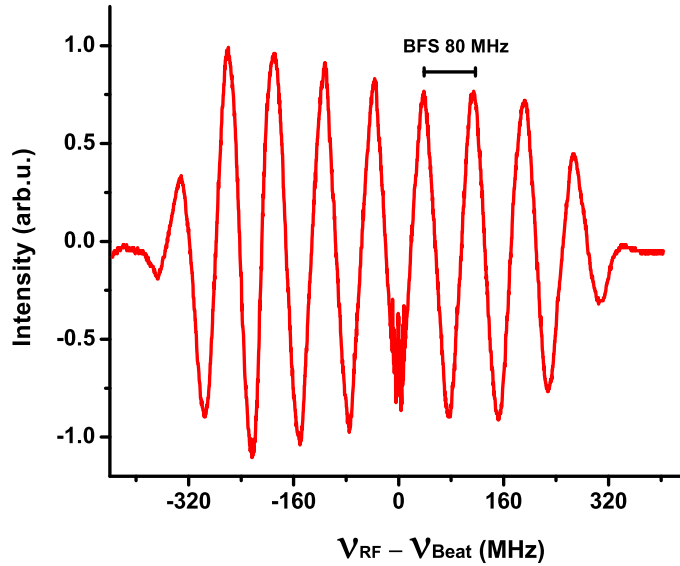


Figure 5.17: Beating Signal

adjusting the offset of error signal, or by simply varying the reference frequency ν_{RF} . The frequency resolution is determined by the slope of the error signal at the locking point. A longer delay line enhances the resolution, but reduces the capture range. Due to the capability of the phase detector, which can not detect a frequency difference less than 25 MHz, a blind zone is inevitable, as seen in the figure. Thus, in practice, a setting of $|\Delta\nu - \nu_{RF}| \approx 50$ MHz is chosen for FO-Lock.

It should be pointed out that, in FO-Lock operation, two cases of beating signal would appear within a large frequency scan area, one is called ‘down beating’, corresponding to $\nu_1 - \nu_2 > 0$, and the other is call ‘up beating’, corresponding to $\nu_1 - \nu_2 < 0$, which are hardly distinguished. However, with the help of simultaneously recorded atomic absorption spectroscopy, they are easily recognized, which is illustrated by Fig. (5.18).

In conclusion, this compact laser system provides a stable and reliable MOT-operation virtually ‘at the push of a button’. The enrolled duo-frequency seeding MOPA scheme supplies us a powerful and flexible realization of laser cooling. It also shows the robust property in a way of ‘ready to go and to play’ campaign.

5.2.3 Trap Loading System

An oven - Zeeman slower system is used to deliver a dilute gas flow of Lithium to the magneto-optical trapping region. Equipped with a mechanic shutter, this atom source unit provides an atom flux at trappable velocities either in a continuous manner or in an intermittent one with a millisecond switch.

Zeeman Slower

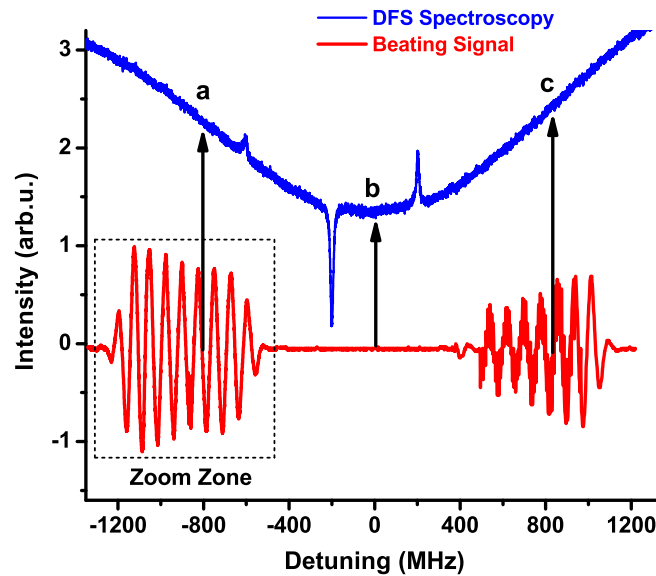


Figure 5.18: FO Lock Signal

The schematic of Fig. (5.19) presents the mechanical structure of present Zeeman slower device, which was constructed in a diploma thesis [Spi05]. A decreasing field geometry consisting of nine 40 mm long coil sections in a sequence is chosen, forming a deceleration length of 35 cm, which make it a rather compact construction. A 25×1 mm copper tube with 2 mm cooling sink serves as the beam path, also as the frame where coils are wound; it is integrated in the vacuum system via welded-on CF40 flanges, with one end attached to MOT main chamber, and the other connected with oven unit.

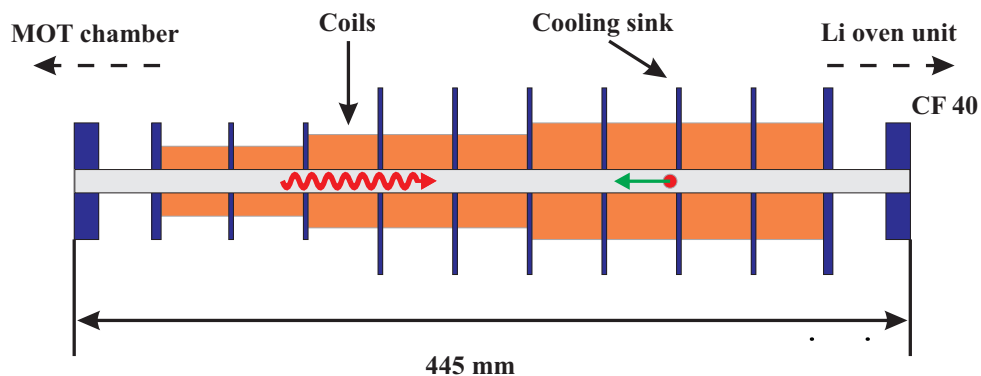


Figure 5.19: Schematic of Zeeman slower

To match the decreasing field geometry, where the maximum absolute value of the magnetic field strength $B(z)$ locates at the beginning of the Zeeman slower, the slowing laser has to be red-detuned in resonance with atoms of criterion velocity at the outlet.

This Zeeman slower was designed to slow the thermal Lithium with initial velocity up to 800 m/s. The design parameters have achieved a constant deceleration of $a = \eta a_{max}$, where the η is the assumed safety factor, accounting for an eventual low saturation of the transition and inevitable deviations of the magnetic field gradient from the ideal profile, and the value of η equals to 0.5 here; the a_{max} is the maximum acceleration conveyed to the atom, which can be derived from Eq. (3.2) and reads

$$a_{max} = \frac{\hbar k \Gamma}{m \cdot 2} \quad (5.17)$$

The measured magnetic field produced by the Zeeman slower is displayed in Fig. (5.20), together with the magnetic field, produced by each individual coil segment along the slower axis.

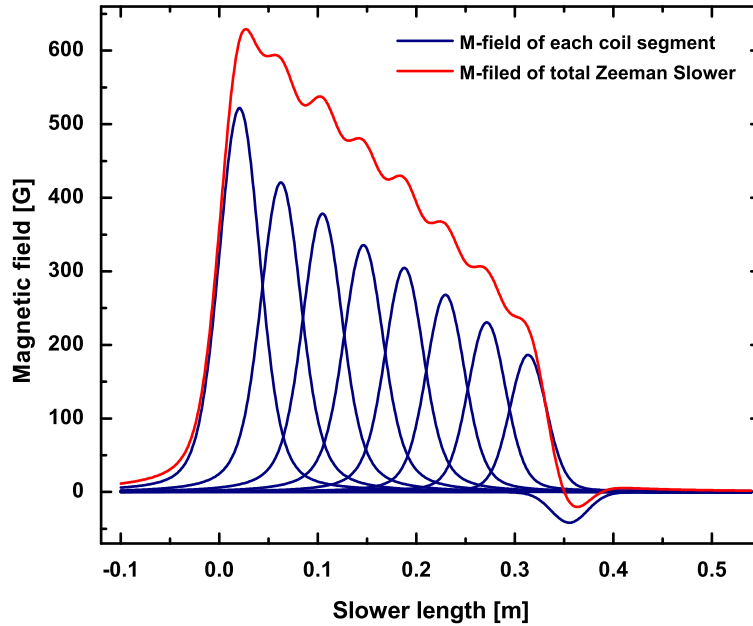


Figure 5.20: The magnetic field behavior (measured) of Zeeman slower: the individual sub M-field by each coil segment is plotted in blue, the superposed M-field is indicated by the red curve. Every sub M-field is generated properly to compose a smooth decreasing field configuration, by modulating each running current separately.

Thermal Lithium Source

In the laser cooling procedure, alkali atoms in the gas phase originally are produced in an effusive oven. By heating alkali metals beyond the melting points, an equilibrium vapour pressure is established within the oven reservoir; as a consequence, gas atoms are pushed through a small nozzle, into the Zeeman slower section for further manipulation.

The temperature-dependent vapour pressure of alkali metals is expressed as [Nes63]:

$$\log p_v[\text{Torr}](T[\text{K}]) = \log A - B/T + CT + D \log T \quad (5.18)$$

In the case of lithium, the coefficients are:

$$\begin{aligned} A &= 10.3454 \\ B &= 8345.574 \\ C &= -0.0000884 \\ D &= -0.68106 \end{aligned}$$

A resistively heated oven with maximum achieved temperatures of 800°C is employed as the Lithium reservoir. The material of molybdenum is chosen to manufacture the oven, with its chemical resistivity, low thermal expansion coefficient and low magnetic permeability considered.

In MOT operation, the oven is heated to a moderate temperature between 350°C and 400°C, by a tantalum wire (0.5 mm) covered with alumina insulators. Although, in the first run an operation at 550°C is needed to break the oxides crust covering the lithium block. The nozzle part should be hotter than the oven body by 50°C, to prevent the lithium atoms from depositing in the nozzle (an aperture of 1 mm diameter).

Intermediate Stage

A CF40 cube chamber of $7 \times 7 \times 7 \text{ cm}^3$ connects the slower and oven parts, with an extension of a CF40 four-way cross. As an intermediate stage, this part is equipped with several components, enabling multi functions: a viewport for optical inspection, e.g. to check the alignment of the slower laser; a rotary feedthrough, steering the lithium beam shutter installed inside; a VARIAN V-70 turbo pump and ion gauge, which maintains and monitors the vacuum of the oven chamber. Connected to the fore-vacuum of $1.3 \times 10^{-3} \text{ mbar}$, the 681/s turbo pump creates a high vacuum of 10^{-6} mbar in the oven section, which is a hazard to the UHV circumstance in MOTRIMS operation. Thus a differential pumping tube (146 mm long, and 6 mm in inner diameter) is installed within the slower tube, starting from the cube chamber, to avoid the degradation of the main chamber UHV. In practice a pressure ratio of $p_1/p_2 = 10^4$ can be maintained, with a 5001/s pumping speed of main chamber pumps system estimated conservatively.

5.3 Integration of a Reaction Microscope with a Magneto-Optical Trap

The most prominent and pernicious incompatibility in merging of a magneto-optical trap and a reaction microscope lies in the conflict of the mandatory stipulations on magnetic fields: the electric and magnetic fields in a reaction microscope need to be homogeneous to guide and resolve the fragmentation trajectories, while a MOT operates in a strong gradient magnetic field congenitally. Thus, a ‘switching mode operation’ is adopted, with the MOT magnetic field being turned off within the time of data-acquisition periodically.

In this section, we briefly present the mechanical design on the merging of setups and the field switching mode.

Mechanical Arrangement of a MOTReMi

Fig. (5.21) shows the schematic drawing of the integrated MOTRIMS apparatus, which was employed for the ‘double photoionization of laser cooled lithium’ at FLASH. The detection part of reaction microscope has less modifications, compared with its conventional scheme; while the MOT part has received more adjustments.

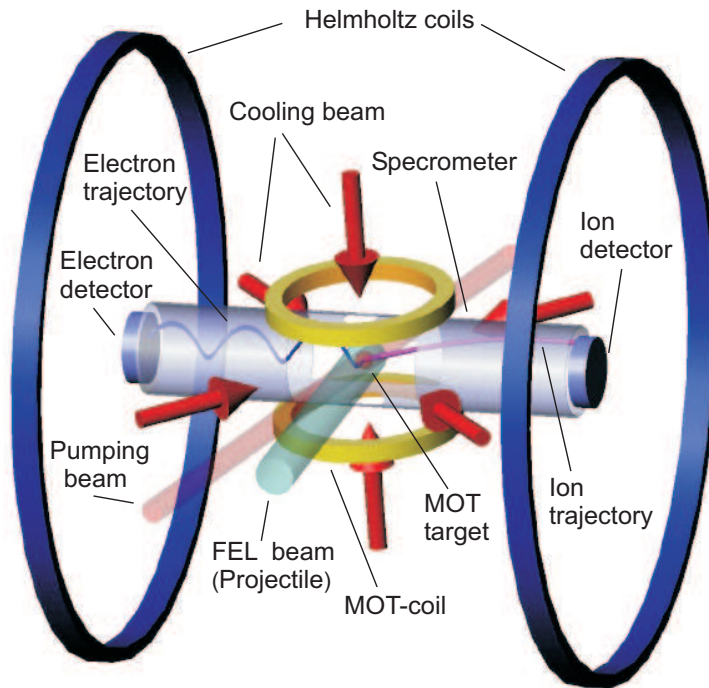


Figure 5.21: Schematic of the MOTRIMS, displaying the essential components of the Reaction Microscope (in blue) and MOT (in yellow). Here, the FEL photon source acts as projectile beam. PSD: Position sensitive detector.

The anti-Helmholtz coils are placed inside the vacuum-chamber, separated by 10.4 cm, with a distance just accommodating the spectrometer within. It is based on two considerations: first, coils in a small size enable a fast switching; secondly, external coils make the main vacuum chamber a huge conductor for eddy currents induced by switching, which should be abstained.

The geometric size used here determines the transversal momentum resolution of ReMi possibly achieved, by confining the fragmentation trajectory in the transversal plane and by defining the detector’s active area. In practice, well-chosen extracting electric and magnetic fields are applied, which allow to fully exploit the spectrometer volume. Therefore the employed 80 mm MCP detector determines the space of the spectrometer and the size of MOT coils, aiming at a compact construction.

To minimize the induced eddy currents in ‘switching mode’ operation, all inner metal

parts, e.g. electrodes for extracting field, coil holders and binding units, are designed to avoid loop circuits, by either introducing slits or inserting electric insulation spacers.

Given that the operation of a MOT requires laser beams accessing the interaction region from six directions, a rectangular opening of $30 \times 200 \text{ mm}^2$ is formed in the horizontal plane of the central electrodes; additionally a round hole is cut at the top and bottom of the spectrometer. These apertures in the spectrometer also serve as accesses to the target region for projectiles, probe beams, diagnostic means, and for loading atoms into trap as well.

To enclose the kernel part of the MOTReMi (MOT coils, spectrometer electrodes and support structure *etc.*), a spherical chamber with a diameter of 40.5 cm is employed as the main experimental vacuum chamber. For an overview of the experimental chamber, please refer to [Ste07].

During experiment, the gradient of the MOT-field in the radial direction has a typical value in the order of 10 Gauss/cm, while the homogeneous field confining the cyclotron motion of electrons is about 5 Gauss. This superimposed magnetic field leads a MOT displacement by a few mm, due to the shift of the zero point of the MOT magnetic field. However, a simple way of increasing the trapping field gradient can undermine this detrimental effect for the MOT operation.

Field Switching Operation

A coincident measurement of electrons and ions in a fragmentation process has a critical demand on the extracting fields. A three-dimensional gradient MOT field spoils the electrons' trajectories, making the reconstruction of the initial kinetic momenta nearly impossible; while this magnetic field has less influence on the ion part, but a displacement and deformation of an ion spot still add difficulties to the reconstruction of the ions' trajectories.

As proposed early in a series of papers [Tur01, Kno03, Kno05], a field-switch procedure is applied to our MOTRIMS operation, where a MOT-field-free condition is created during the data acquisition period.

In designing such a timing cycle, two key points should be considered: firstly, the off-time of the MOT magnetic field should be long enough to eliminate the residual components of the MOT field and the stray fields generated by eddy currents; secondly, the cold atom ensemble should survive during the field switch sequence, due to the fact that target atoms would escape the trap zone at the speed of a few m/s, once the trapping forces withdraw. Therefore, artifices of atom recapture and reload are applied to compensate the atom loss. Furthermore, all the cooling beams should be turned off as the trap field ramps down; otherwise, the atoms would drift away due to the unbalanced radiation forces under the persistent extracting magnetic field.

A sophisticated timing scheme specially designed for photoionization experiment @ FLASH (the FEL pulse train contains 30 pulses, each with a duration of about 30 fs and separated by an interval of $5 \mu\text{s}$ approximately, and the pulse train repetition rate is 5 Hz), is illustrated in Fig. (5.22), which is compromised between momentum resolution, count rate and experimental possibilities.

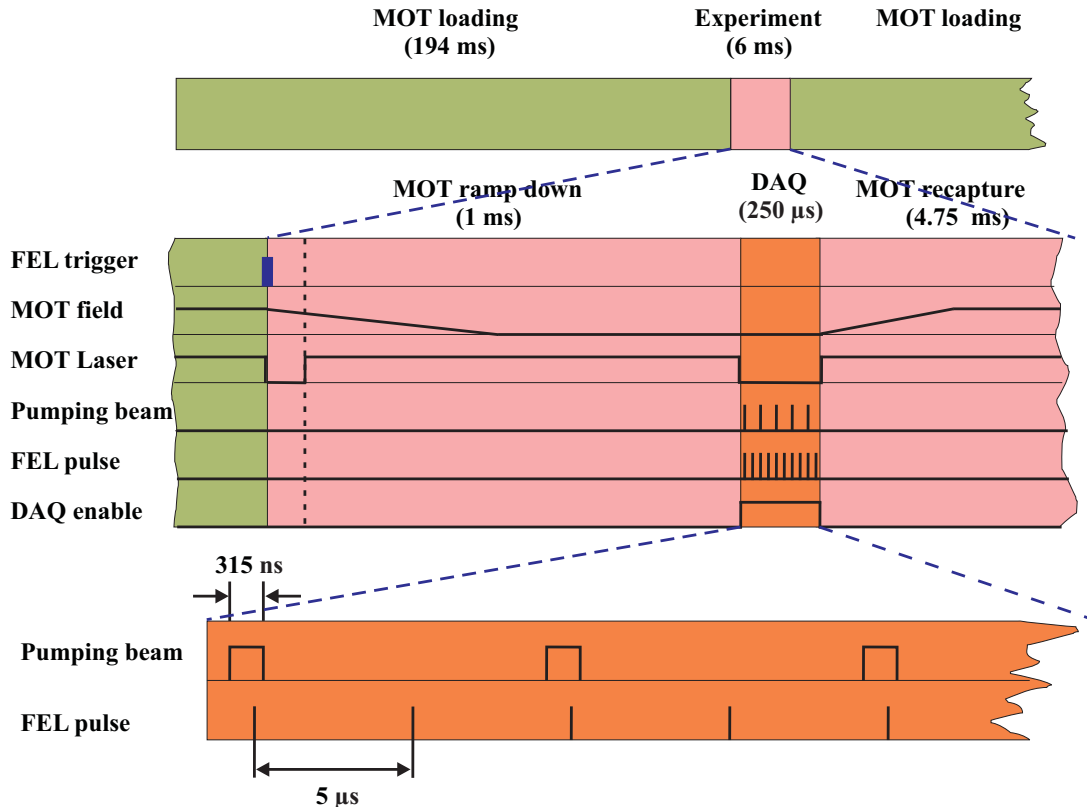


Figure 5.22: Duty cycle

Once a MOT with sufficient atoms is formed, the loading procedure is ceased by blocking off the atom beam and slower laser, subsequent to this, MOT-fields ramps down within $400 \mu\text{s}$ (however, a thorough vanishment of trap field needs a duration of a few ms, due to the induced eddy current), and in the mean time the cooling laser beams are shut off. The data acquisition time is set to $250 \mu\text{s}$, which is capable of handling the photoionization result from all FEL shots. A train of laser pulses @ the D2 resonance transition ($|2^2S_{1/2}\rangle \rightarrow |2^2P_{3/2}\rangle$) are employed to prepare the initial state of lithium target on demand: corresponding to the FEL pulse of odd order, a pumping beam with 315 ns is shot on the Li cloud; while, for the ionization event generated by the FEL pulse of even order, no pumping beam is applied, leaving the Li target in its ground state initially. In case of that the atom ensemble is depleted, the MOT-field is ramped up and the cooling beams are turned on again, immediately after the photoionization fragments get extracted and detected, to recapture and reload the Li atoms. Then, another measurement cycle follows. To synchronize with the VUV photon pulses, the electronic signal delivered from the FLASH facility is employed to trigger the whole experimental cycle.

As noticed in the schematic of the applied timing sequence, in the experimental phase of ‘field ramp down’, MOT beams are re-permitted after a $200 \mu\text{s}$ shut down, as an option for holding atoms, due to the absence of the extracting magnetic field.

The debut of MOTReMi not only shows talent performance in combining the merits of two ‘art-of-the-state’ apparatuses, but also exhibits a unique achievement in resolving the

momentum spectroscopy, with the ever finest resolutions (on the order of $\Delta p = 0.01$ a.u.) in all three dimensions. Furthermore, as a novel tool, it would have a strong impact to AMO science with the multi-projectile compatible stunt.

However the ‘switching mode operation’ has the drawback of a reduced count rate, due to the switch caused ‘dead time’ in data acquisition, and in a resolution degradation suffered by the ballistician expansion of atom target. Thus, a revolutionary proposal with an auxiliary dipole trap (a pure optical trap) would solve this dilemma annoyed by conflicting operation fields once for all, based on the fact that operation of a far red-detuned dipole trap is not disturbed by any weak magnetic fields. Through transferring atom from a dynamic MOT to a passive dipole trap in situ, continuous manipulations and data acquisition in a ‘field-free’ circumstance are permitted till that all targets are depleted. In addition, compared with a standard MOT, the feats of a dipole trap, *e.g.* smaller volume limited by a tight focus and less thermal perturbation manaced by a well-defined trap depth, would enhance the momentum resolution further.

5.4 Experiment Control Devices

In experimental realizing the sophisticated ‘mode of operation’, a LabView/ADwin system controls an elaborate timetable on successive execution phases swiftly and precisely. A user-friendly interface embedded in a PC enables ‘on-line’ accesses to conduct the experiment within a ‘real-time’ frame, ramping the MOT gradient magnetic field, gating the atom source for trap loading, switching laser beams for cooling and pumping individually, synchronizing duty cycles with the projectiles of FEL pulses and triggering the data acquisition as well.

5.4.1 Adwin Gold DA System

The gadget of Adwin-Gold, which is a member of Adwin DA system family, provides a real-time solution precisely to applications demanding extremely short reaction times. Equipped with a microprocessor, the real-time system operates and reacts within a defined period of time as short as $1\mu s$, exactly and predictably. The consistent interface concept, via a straight-forward connection (databases Network connectivity via Ethernet / TCP/IP) between the ADwin device and a PC, makes it a comfortable and independent environment for the programming of real-time processes. As a clearly structured, parallel job scheduling platform, it is capable of controlling several external devices via analog and digital channels: 2x8 analog input/output channels, with an operation voltage range between $-10V$ and $+10V$; 32 bidirectional digital channels (DIO) working with TTL logic levels, half of which are configured as inputs and the rest as outputs.

5.4.2 LabView User Interface

A visual programming language of LabVIEW by National Instruments sits in the heart of the user interface of MOTRIMS, managing instrument control and data acquisition.

The program used for the FLASH measurement is one modification of the original version for the multiphoton ionization measurements [Ste07]. The single loop is divided into merely three proceeded steps, which governs the subsequent experimental phase exclusively: MOT loading/reloading, Fields switching-off, target manipulation/data acquisition. The parameters of different steps, e.g. the switching times, the output states and voltages are configurable from the front panel.

In the near future, a more dexterous and flexible program in a uniform layout will be developed to fulfill different tasks' needs, enabling experimental sequences with an arbitrary number of steps/loops and the generation of waveforms at the analog outputs.

5.5 Data Acquisition Units

Once the ToF and position information for photoionization fragments is converted into electronic signal by the delay-line anodes and the MCPs, respectively, a task-dependent data processing begins.

First of all, the resulting signal pulses need to be amplified. The operation on output from the MCPs is rather straightforward. A device of **ORTEC FTA820A** (bandwidth of 350 MHz) is employed, as the external fast amplifier. While the processing of the delay-line signals requires a little more effort: since the position timing pulse is derived by a comparison of the 'signal-wire' and the parallel wound 'reference wire', a circuit box should be inserted between the position-sensitive detector and the fast amplifier, giving the voltage difference as the output. To improve detectors' readout, the distance of signal transmission (via cables) should be kept as short as possible. Therefore, a specially designed electronic 'readout' box is mounted on the detector flange directly, with a resistor-chain voltage divider implemented, which allocates the right voltage to the individual detector elements (MCPs, delay-line anodes, *etc.*). Being amplified, the electronic signals are fed into the constant fraction discriminator (CFD) (**ORTEC 835**), where the TTL signal is converted into a standard NIM-pulse.

For conventional experiments (multi photoionization, electron impact, *etc.*), a routine data acquisition system identifies the so-produced signal first, which performs a logic algorithm to pick out the physical events of interest, using the Time-to-digital Converter (TDC) and Analog-to-digital (ADC) cards as the kernel elements, and logic gates as well. A rack unit of Computer Automated Measurement and Control (CAMAC), which accommodates TDCs and ADCs, is responsible for data transfer, communicating with the measurement PC via an ISA-bus.

However, this data acquisition system has a few fatal drawbacks, which reduce the sampling efficiency. The data acquisition procedure, *i.e.* TDC and ADC read out by the computer, is time-consuming, which generates a so-called 'dead time' (in the order of few

hundred μs). If extra events arrive within this period, they can not be recognized and get lost. This is due to that the ISA-bus only has a bandwidth of 8 MHz, limiting the data communication between the CAMAC-crate and the data storage PC.

At FLASH, the repetition rate of measurement is extremely high due to the structure of FEL photon pluses — 30 pulses in sequence with a time interval (mini-bunch distance) of $5 \mu s$. Therefore, a different scheme of data acquisition has been used, avoiding data loss.

The Acqiris high-speed digitizers (**Agilent U1064A**) sits in the heat of the data acquisition system, which samples the received electronic signal with high fidelity. The measured the voltage (slope) and arriving information for individual signals are extracted by an integrated software, *i.e.* Agat32root. Here each signal is identified according to its specified registration date, for further event selection and data analysis via algorithms.

During measurement at FLASH, two pieces of **271 DC** cards were utilized as the Acqiris unit, supplying 8 channels. And each channel has an acquisition memory of 128 kSamples, together with the chosen sampling distance of 2 ns, a maximum continuous measurement duration of $256 \mu s$ is achieved, while the available TDC (**LeCroy 3377**) only allows a maximum continuous recording period of $32 \mu s$.

For more information on Acqiris based data acquisition, please refer to several theses [Kur07, Fou08].

Chapter 6

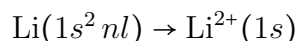
Data Processing and Event Identification

In this chapter, we will discuss the methods applied for data analysis, under the topics of reaction channels identification, raw data modifications, and target initial states determinations, which include the measurements on excitation fraction and the M -substate population.

6.1 General Classification of Photoionization Reactions

Experimental Method and Conditions

The focused experiment is performed for the PDI reaction



induced by linearly polarized light, *i.e.* photoionization of one inner shell electron and the valence electron which is either in the $2s$ ground state or in the $2p$ excited state prepared and aligned by optical pumping, as illustrated in Fig. (6.1).

Differently from ionizing two equivalent electrons as, *e.g.*, in helium, here, the primary photon is most likely absorbed by a $1s$ -electron, while direct photoionization of the outer electron is suppressed by a factor 4×10^{-2} and 1.3×10^{-3} for the $2s$ and $2p$ initial states, respectively. Photoionization of the $1s$ -electron by radiation with linear polarization E along the z -axis results in a \cos^2 -electron emission (indicated by the red lobes), which should not be influenced by the presence of the electron in valence shell (represented by the blue lobes). The ejection (or excitation in PIE process) of the second electron takes place by the ‘two step’ or ‘shake’ mechanisms as elucidated before.

The experiment schematic for FLASH measurement is indicated in Fig. (6.2). Our MOT based Li target contained about 10^7 atoms in a volume of 0.5 mm diameter at a temperature of roughly 1 mK, indicated by the red dot. The FLASH photon beam illuminated

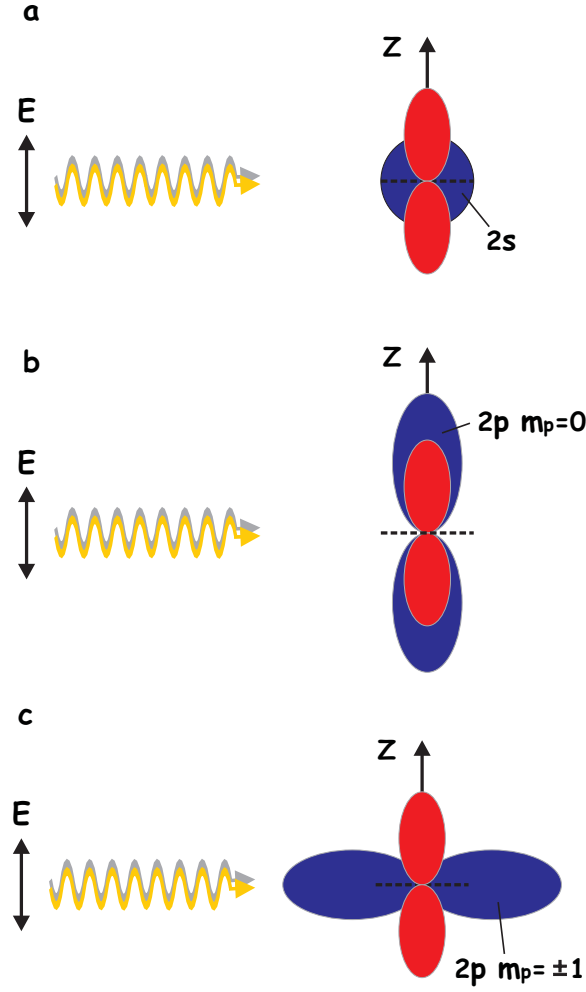


Figure 6.1: Schematics of the PDI process. Lithium targets are initially prepared in different state nlm_l . The quantization z -axis is defined by \mathbf{E} , the polarization of FEL. Blue lobe shows the valence orbital, indicating different spatial alignment; and red lobe represents the dipole emission pattern of the ionized $1s$ electron.

the target at a pulse train repetition rate of 5 Hz along the blue arrow, whose polarization was linear as shown by \mathbf{E}_{FEL} . FLASH pulse train consisted of 30 pulses separated by $5\ \mu\text{s}$, each with a duration of about 30 fs and containing up to 10^{13} photons. Another synchronized laser pulse train (driving the $|2^2S_{1/2}\rangle \rightarrow |2^2P_{3/2}\rangle$ transition) supplied the excitation and alignment function as demand. The ions were extracted by a homogenous electric field and projected onto a time and 2D position sensitive detector. The MOT unit was running in a switching mode for optimal momentum resolution, as displayed by Fig. (5.22): the MOT was switched off about 1 ms before each FLASH pulse train, followed by a MOT field-free period of $250\ \mu\text{s}$ required for data acquisition (DAQ).

Here, we emphasize the special care taken for state preparation of the target atoms in

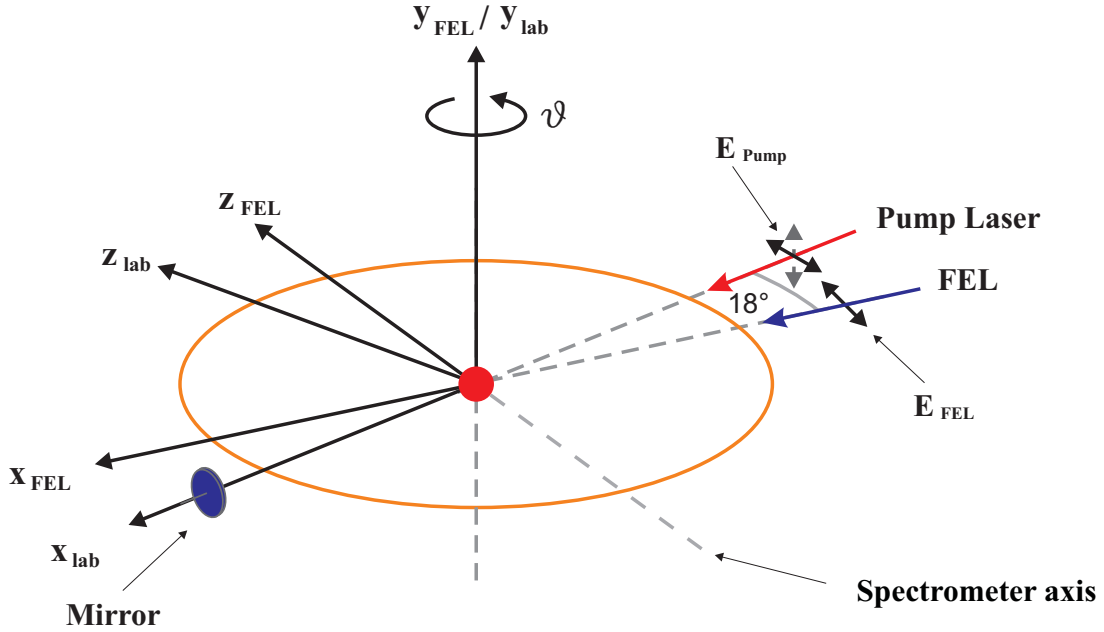


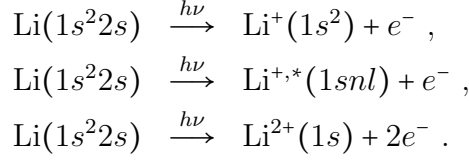
Figure 6.2: Experimental arrangement for photoionization study @ FLASH. The beam directions of the VUV radiation and near infrared pump laser are indicated by the blue and red arrows, and their polarizations are displayed individually. Here, the laboratory frame for determining the alignment parameter \mathcal{A}_{20} is specially labeled out, which is connected with the FEL coordinate system via a rotation operation around the y_{lab} -axis.

the $\text{Li}|2p\rangle$ excited state by applying a dedicated linearly polarized optical pumping laser pulse. It started about 300 ns before each other FLASH pulse. Thus, the influence of target excitation on the photoionization process could be directly observed for identical experimental conditions, since within a pulse train of 30 pulses, during 15 pulses a fraction of target atoms was excited while during the other 15 pulses a pure ground state target was used. The fraction of excited atoms in $2p$ state can be determined from the decrease of the photoline intensity arising from direct ionization of the valence electron [Naj08]. Furthermore, the degree of target alignment of the laser excited state was determined by measuring the degree of polarization of the emitted fluorescence radiation, which allowed to derive the magnetic sub-state populations. The fraction of excited atoms was determined to be $46 \pm 1\%$ and the magnetic sublevel populations in the l basis were obtained as: $P(m_p = 0) = 0.50$ and $P(m_p = \pm 1) = 0.25$ in the parallel-case (\parallel) where the optical pumping laser polarization is aligned along VUV-polarization, the quantization axis for photoionization; while $P(m_p = 0) = 0.20$ and $P(m_p = \pm 1) = 0.40$ in the perpendicular-case (\perp) populations. Detailed treatment will be discussed later in Sec. 6.3 and Sec. 6.4.

Reaction Channels

Consider the lithium atom initially in ground state $|1s^2 2s\rangle$, for incident photon with 85 eV or 91 eV, which is above the double-ionization threshold of 81 eV (which concerns one of the two $1s$ electrons and the valence $2s$ electron), possible photoreactions are listed as

below:



where single photoionization of $2s$ electron only, single photoionization of $1s$ electron

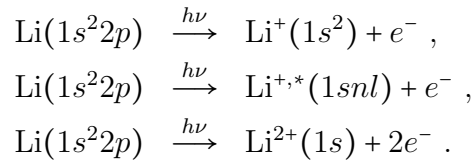
Table 6.1: Energy(/momentum) diagram for ionization of lithium from the ground state ($1s^2 2s \ ^2S$), where for individual final state, the corresponding electronic configuration, the ionization energy E_I and the excess energy E_{Exc} (in SI unit) and the recoil ion momentum p_R (in atomic unit) at a photon energy of $E_\gamma = 84.932/91.176$ eV (wavelength $\lambda = 14.6/13.6$ nm) are listed.

Initial state		Final state		E_I (eV)	E_{Exc} (eV)	p_R (a.u.)
Configuration	Term	Configuration	Term			
Li($1s^2 2s$)	2S	Li($1s^2$)	1S	5.392	79.540/85.785	2.418/2.511
		Li($1s 2s$)	3S	64.413	20.519/26.764	1.228/1.402
		Li($1s 2s$)	1S	66.314	18.617/24.862	1.170/1.352
		Li($1s 2p$)	3P	66.672	18.259/24.504	1.158/1.342
		Li($1s 2p$)	1P	67.608	17.324/23.568	1.128/1.316
		Li($1s 3s$)	3S	74.173	10.759/17.004	0.889/1.118
		Li($1s 3s$)	1S	74.671	10.260/16.505	0.868/1.101
		Li($1s 3p$)	3P	74.761	10.171/16.416	0.865/1.098
		Li($1s 3d$)	3D	74.977	9.955/16.200	0.855/1.091
		Li($1s 3d$)	1D	74.981	9.951/16.196	0.855/1.091
		Li($1s 3p$)	1P	75.040	9.891/16.136	0.853/1.089
		Li($1s 4s$)	3S	77.300	7.631/13.876	0.749/1.010
		Li($1s 4s$)	1S	77.501	7.431/13.676	0.739/1.002
		Li($1s 4p$)	3P	77.536	7.395/13.640	0.737/1.001
		Li($1s 4d$)	3D	77.627	7.305/13.550	0.733/0.998
		Li($1s 4d$)	1D	77.629	7.303/13.548	0.733/0.998
		Li($1s 4f$)	3F	77.630	7.301/13.546	0.732/0.998
		Li($1s 4f$)	1F	77.630	7.301/13.546	0.732/0.998
		Li($1s 4p$)	1P	77.653	7.278/13.523	0.731/0.997
				\vdots	\vdots	\vdots
		Li($1s$)	2S	81.032	3.900/10.145	—

(including $1s$ single ionization plus simultaneous $2s$ electron excitation) and double photoionization are shown separately. In the second equation, the final orbit of the valence electron is indicated by the principal quantum number $n \geq 2$ and the angular quantum number $l = 1, 2, \dots$. If $l = 0$, which the angular momentum of the valence electron maintains the same during the simultaneous excitation, the process is entitled as ‘shake-up’; while for $l \neq 0$, which encounters an angular momentum exchange between the excited electron and the outgoing ionized one, the process is then termed ‘interchannel coupling’ (IC) [Che00]. Especially, the $(1s2s)$ case just means the pure single photoionization of $1s$ electron.

Starting from ground state $\text{Li}|1s^22s\rangle$, the Tab. (6.1) gives the calculated values of ionization potentials (E_I) according to the different final states $\text{Li}|1snl\rangle$ ($n = 1, 2, \dots; l = 0, 1, \dots$) listed, and different excess energies in the units of eV and a.u., with respect the photon energy of 85 eV and 91 eV respectively.

Analogously, for the initial state of $\text{Li}|1s^22p\rangle$, the first excited state, a same treatment is carried out, *i.e.* the reaction channels are describes as below, and the related energy diagram is presented in Tab. (6.2).



6.2 Recorded Raw Spectrum — Description, Clarification and Modification

An object-oriented program of ROOT written in C++ language takes care of the Data acquisition and data analysis for our experiment. After the general signal processing, depicted in Sec. 5.5, the time-of-flight (ToF) and position signals of the recoil lithium ions are obtained.

Fig. (6.3) shows the raw ToF spectrum with strong Li^+ -lines and weak Li^{2+} -lines. Due to the experimental procedure, half of the photolines (in even order) correspond to photoionization of the $\text{Li}|1s^22s\rangle$ ground state, while the rest (in odd order) originate from the $\text{Li}|1s^22p\rangle$ excited initial state.

By summing up the lines which belong to the same reaction channel, the ToF spectrum displayed in Fig. (6.4) is obtained, where the time basis is extended to two times of the ‘mini-bunch distance’ deliberately. Thus within one graph all the photoionization events could be displayed separately and completely. However, it should be kept in mind, that the true ToF_{Li^+} is around 5.8×10^4 ns and $\text{ToF}_{\text{Li}^{2+}}$ center is 4.1×10^4 ns.

Fig. (6.5) (left) shows the raw position signal of Li^+ , which is not centered and even far from round in shape obviously, since the recoil ions’ trajectories get shifted and distorted during the measurement by some unclear external bias electric fields. Therefore, we apply a Cartesian coordinate transformation (translation, rotation & rescaling) to restore the

position signal, for detail treatment in program ‘Agat32root’, please refer to Appendix D. A reshaped position spectrum is shown in Fig. (6.5) (right).

With the recorded ToF and position signals of the recoil ions, we could derive the initial momentum in three dimensions by applying the momentum reconstruction method explained in Subsection 5.1.2. Fig. (6.7) (upper row) shows the two-dimensional plots of the Li^+ momenta, which do not show the expected circular structure around the origin.

Table 6.2: Energy(/momentum) diagram for ionization of lithium from the first excited state ($1s^2 2p \ ^2P$), where for individual final state, the corresponding electronic configuration, the ionization energy E_I , the excess energy E_{Exc} (in SI unit) and the recoil ion momentum p_R (in atomic unit) at a photon energy of $E_\gamma = 84.932/91.176$ eV (wavelength $\lambda = 14.6/13.6$ nm) are listed.

Initial state		Final state		E_I (eV)	E_{Exc} (eV)	p_R (a.u.)
Configuration	Term	Configuration	Term			
Li($1s^2 2p$)	2P	Li($1s^2$)	1S	3.544	81.388/87.633	2.445/2.537
		Li($1s2s$)	3S	62.565	22.367/28.612	1.282/1.450
		Li($1s2s$)	1S	64.467	20.465/26.710	1.226/1.401
		Li($1s2p$)	3P	64.824	20.107/26.352	1.216/1.392
		Li($1s2p$)	1P	65.760	19.171/25.416	1.187/1.367
		Li($1s3s$)	3S	72.325	12.607/18.852	0.962/1.177
		Li($1s3s$)	1S	72.824	12.108/18.353	0.943/1.161
		Li($1s3p$)	3P	72.913	12.018/18.263	0.940/1.158
		Li($1s3d$)	3D	73.129	11.802/18.047	0.931/1.152
		Li($1s3d$)	1D	73.133	11.799/18.044	0.931/1.151
		Li($1s3p$)	1P	73.192	11.739/17.984	0.929/1.150
		Li($1s4s$)	3S	75.452	9.479/15.724	0.835/1.075
		Li($1s4s$)	1S	75.653	9.279/15.524	0.826/1.068
		Li($1s4p$)	3P	75.689	9.243/15.488	0.824/1.067
		Li($1s4d$)	3D	75.779	9.153/15.398	0.820/1.064
		Li($1s4d$)	1D	75.781	9.151/15.396	0.820/1.064
		Li($1s4f$)	3F	75.782	9.149/15.394	0.820/1.064
		Li($1s4f$)	1F	75.783	9.149/15.394	0.820/1.064
		Li($1s4p$)	1P	75.806	9.126/15.371	0.819/1.063
				⋮	⋮	⋮
		Li($1s$)	2S	79.184	5.748/11.993	—

This is mainly due to inaccuracies in the mechanical assembly of the momentum spectrometer. In the right situation, as illustrated in Fig. (6.6) (a), the detector plane is orthogonal to the axis of the extracting E-field. Thus, recoil ions with a same longitudinal momentum p_{\parallel} , and a same absolute value of transversal momentum but different direction, keep the same ToF and end up in a circle at the position sensitive detector. However, in an improper assembly geometry, as shown in Fig. (6.6) (b), the detector plane is tilted with reference to the ‘orthogonal alignment’, therefore distortion in both the position and the timing signal is inevitable: the recorded position pattern becomes stretched, while the ToF deviates according to the registered position also.

Therefore, modifications on ToF & position signals are needed to correct this kind of distortion, which read:

$$T = T_0 + [C_{X1} \cdot \Delta X + C_{X2} \cdot (\Delta X)^2] + [C_{Y1} \cdot \Delta Y + C_{Y2} \cdot (\Delta Y)^2] \quad (6.1)$$

and

$$\begin{aligned} X &= X_0 + [C_{T0} + C_{T1} \cdot \Delta T + C_{T2} \cdot (\Delta T)^2] \\ Y &= Y_0 + [C'_{T0} + C'_{T1} \cdot \Delta T + C'_{T2} \cdot (\Delta T)^2] \end{aligned} \quad (6.2)$$

where T_0 , X_0 and Y_0 denote the first hand information on ToF and position, and the modified T , X and Y are obtained by performing a ToF- or position-dependent correction

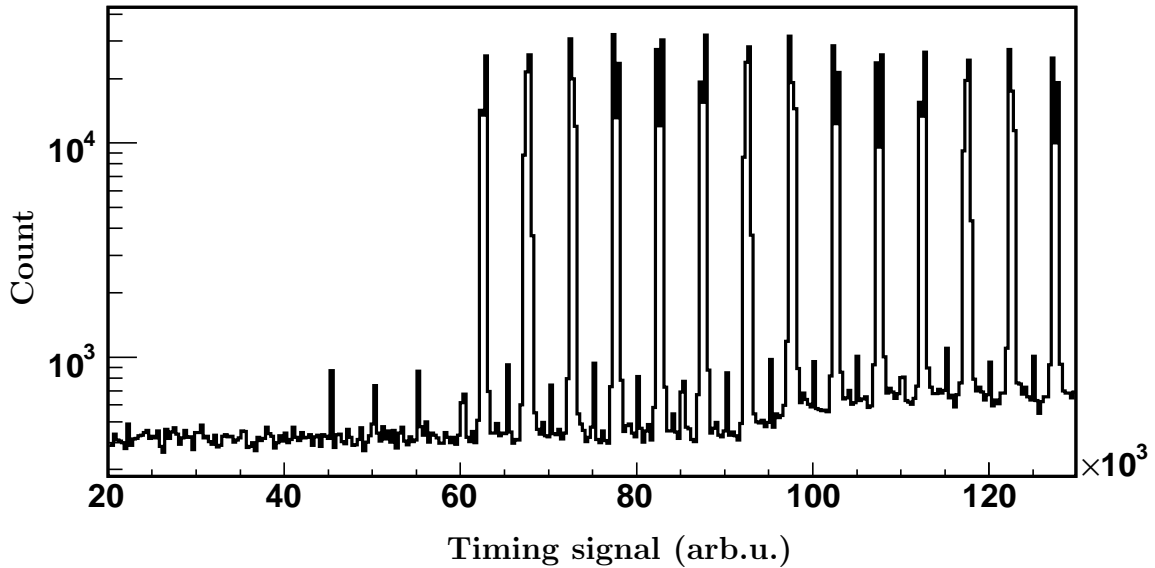


Figure 6.3: Time signal (unsorted) for recorded recoil ions, presenting a FLASH pulses like structure (the regularly spacing between peaks in the same level of amplitude represents the ‘mini-bunch distance’ of a FLASH pulse train), where high-amplitude peaks are for Li^+ , and low-amplitude peaks are for Li^{2+} . It should be noted that the time basis (abscissa) here does not behav the information of ToF in reality.

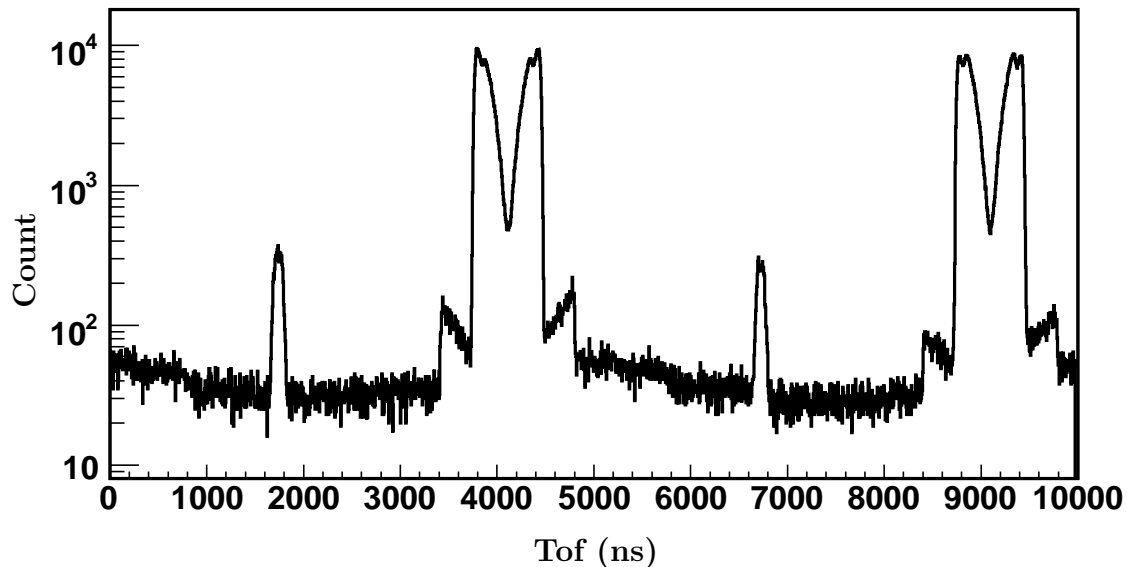


Figure 6.4: Time-of-flight (ToF) of Li photoionization (sorted) plotted as ‘4-in-1’ deliberately. The two small peaks correspond to the double ionization events, where the first one indicates an initial state of Li(2*s*) and second one denotes an initial state of Li(2*p*). While, two big peaks correspond for the single ionization events from the target in Li(2*p*) (first) and Li(2*s*) (second) respectively.

separately. The coefficient set $C_{X/Y}$ are used to correct the distorted ToF signal, while coefficient set C_T are used to correct the distorted position signal. ΔT , ΔX and ΔY are the ToF and position displacements with respect to the spectra centers. The code in C++ program language on ‘removing signal distortion’ can be found in Appendix D.

Fig. (6.7) (bottom row) shows the corrected two-dimensional plots of the Li⁺ momenta, which are distortion-free now.

To check the quality of the ToF and position corrections, two more testing diagrams are used. Fig. (6.8) (left) displays the ion signal intensity versus the recoil ion’s total momentum and versus the azimuthal emission angle ϕ with respect to the z -axis (defined by the FEL polarization axis). Since the ion emission is axially symmetric with respect to this axis, parallel strips with ϕ -independent are expected and observed for appropriate corrections. Fig. (6.8) (right) show the same data versus the polar emission angle θ with respect to the z -axis. For dipole emission, characteristic $\cos^2 \theta$ intensity distributions are expected, peaking at 0° and 180° and diminishing at 90°. Here the ϕ and θ angles are defined as:

$$\begin{aligned}\phi &= \text{atan2}(p_y/p_x) \\ \theta &= \text{acos}(p_z/p_{total})\end{aligned}\tag{6.3}$$

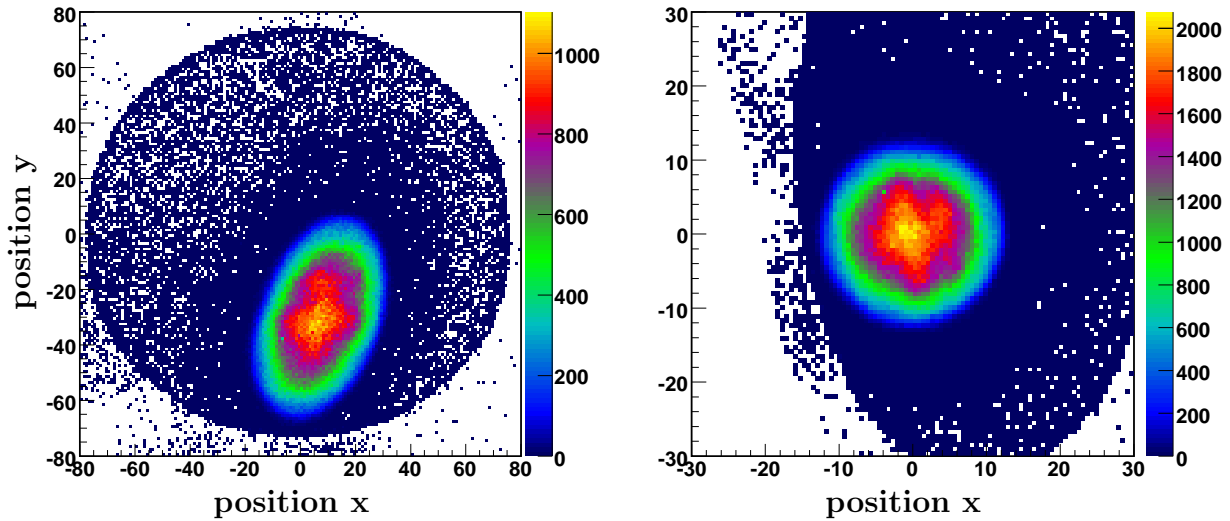


Figure 6.5: Left: Raw position signal of Li^+ , which is shifted and distorted; Right: Corrected position signal of Li^+ after a physical treatment in Cartesian coordinate, which is rather round and symmetric with respect to the new origin in the plot.

All the modifications performed for Li^+ spectrum are applied to Li^{2+} spectrum also, with the same procedure and technique in general.

One two-dimensional (ToF and position) recoil ion spectrum is shown in Fig. (6.9), with all the ionic charge states included. As indicated in the graph, the small isolated fraction denotes doubly charged lithium ions. While, the large and multiple shell structure part results from single ionization. The width of the rings is determined by the linewidth of the FLASH photon source, the momentum resolution of MOTRIMS machine, and the

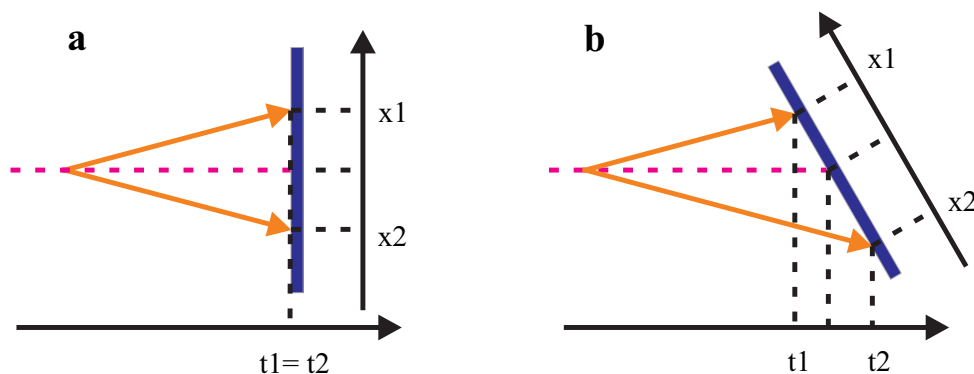


Figure 6.6: Schematics for illustrating the influence of the mechanical assembly on the recorded ToF & position signals. Draft a: the right geometry, generating signals without distortion; draft b, the improper one, introducing artificial effects to the spectrum.

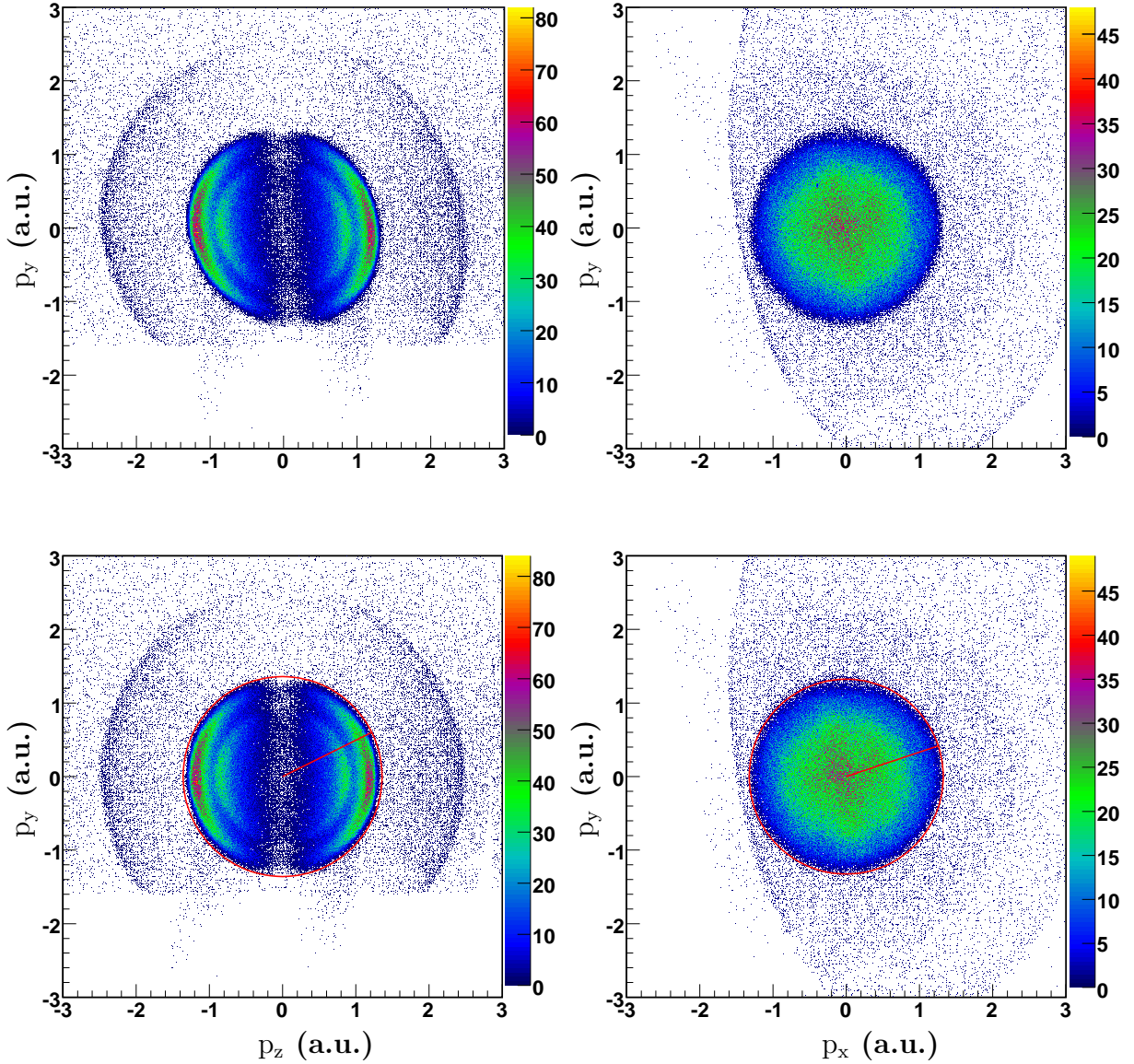


Figure 6.7: Uncorrected (upper row) and corrected (bottom row) two-dimensional momentum plots of recoil ions Li^+ . Plots in the left column are for p_y *v.s.* p_z , where one dimension p_x is derived from the position signal and the other dimension $p_z = p_t$ (along the longitudinal axis) is reconstructed from the ToF information; while plots in the right column are for p_y *v.s.* p_x , where only transversal momenta are preserved.

ionization energy separation of each PIE transition channel, all together. Here three circular shells are visible with a double lobe angular distribution aligned along the VUV polarization characteristic for dipole transitions, which represent the clear separation of final state groups (going from large to small radii) of $1s^2$, $1s2l$ and $1snl$ ($n \geq 3$), corresponding to ionization of valence electron, single-ionization of one of the two inner shell

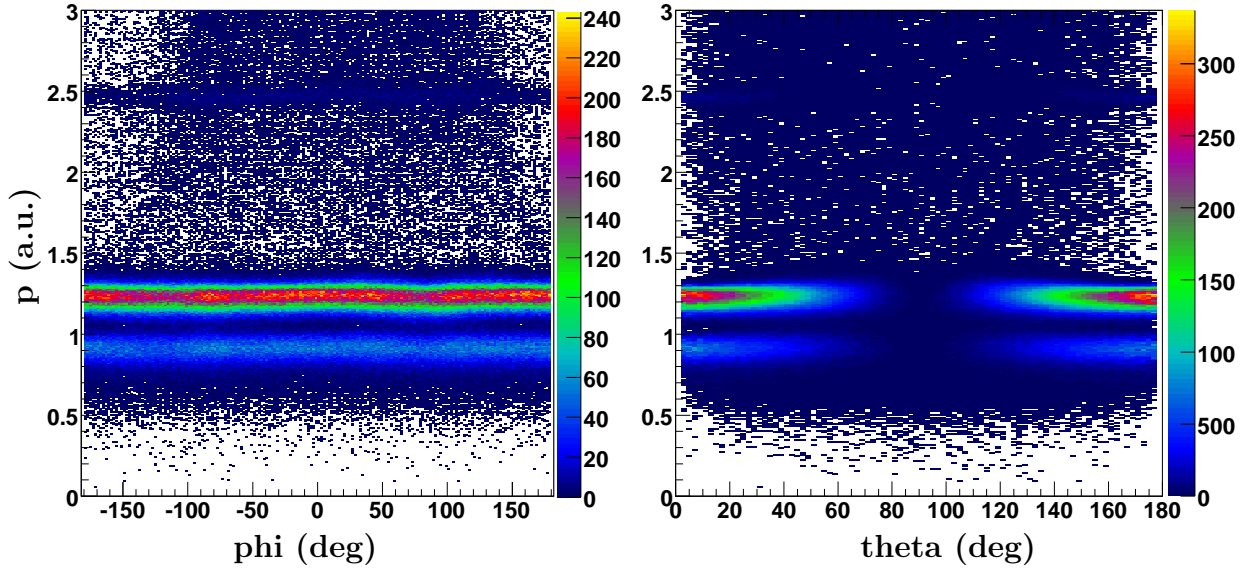


Figure 6.8: Auxiliary diagrams as criterions for momentum modification. Left: total momentum p_{total} versus the emission angle of ϕ . Right: total momentum p_{total} versus the emission angle of θ .

electrons and single-ionization of inner shell electron with simultaneous excitation of the valence electron to an orbital with higher principal quantum number n , respectively.

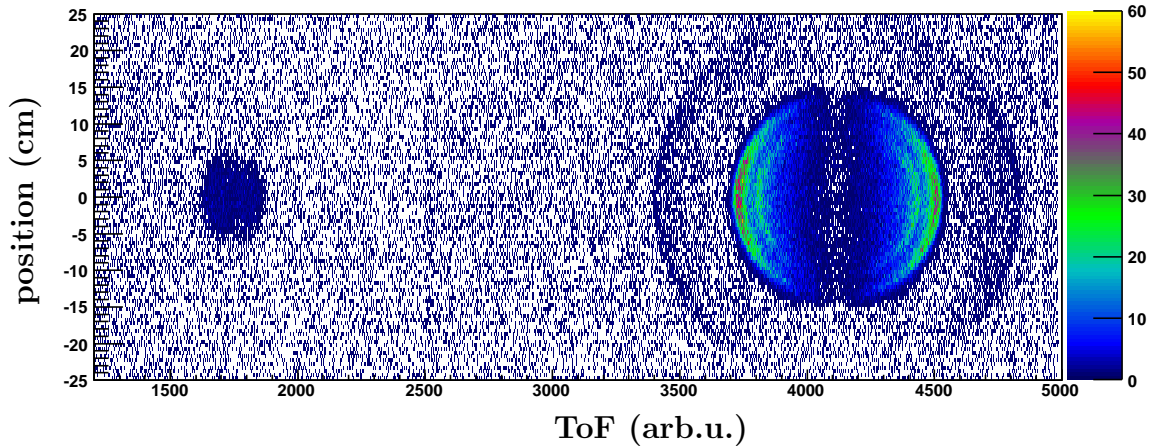


Figure 6.9: A 2D plot of recoil ions, including the doubly charged Li^{2+} (the small disc in the left) and the singly charged Li^+ (the large shell structure in the right). For the Li^+ pattern, three visible circles refer to $1s^2$, $1s2l$ and $1snl$ ($n \geq 3$) from outer to inner part, which are results of the ionization of the valence electron ($2s$ or $2p$), inner shell electron ($1s$) only, and simultaneous inner shell ionization plus valence electron excitation, respectively.

6.3 Determination of Excited State Fraction

As mentioned above, the initial state preparation was realized via applying a dedicated optical pumping laser pulse starting before each other FLASH pulse with linear polarization and on resonance of the transition $|2^2S_{1/2}\rangle \rightarrow |2^2P_{3/2}\rangle$. We noticed that, for the single photoionization of valence electron directly,



under the same experimental conditions, the $\text{Li}^+(1s^2)$ yield was dramatically affected by its initial orbit. As shown by Fig. (6.10), this process is by a factor of 27 weaker from the $2p$ state compared to from the $2s$ state at the incident photon energy of 85 eV, such that the decrease of $\text{Li}^+(1s^2)$ ion intensity reflects the excited state fraction.

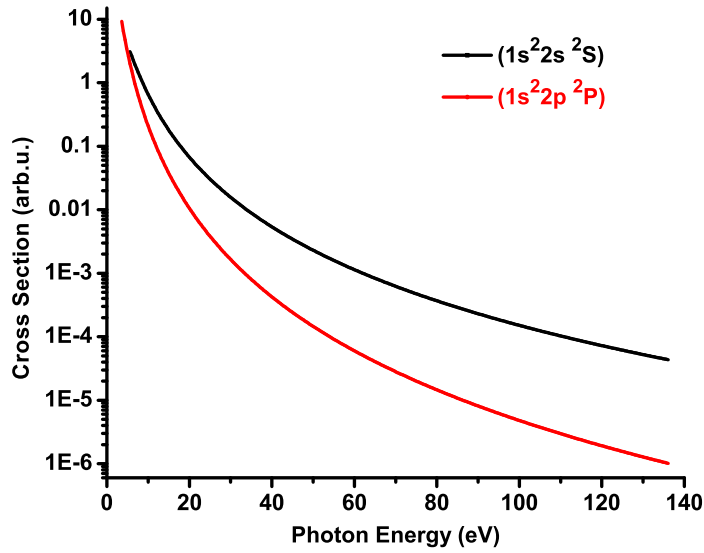


Figure 6.10: Theoretical calculation on the total cross section for the transition of $\text{Li}(1s^22l) + \gamma \rightarrow \text{Li}^+(1s^2) + e$ at different photon energy (from 0 eV to 140 eV), where $l = 0$ (black curve) for photoionization of $2s$ valence electron and $l = 1$ for photoionization of $2p$ electron (red curve) respectively.

Assume the lithium number N in both ‘pumping’ and ‘without pumping’ cases are the same, thus the yield A of $\text{Li}^+(1s^2)$ in two situations reads:

$$\begin{aligned} \text{laser off: } A &= N \cdot (\sigma_{2s} \cdot F_{2s}^1 + \sigma_{2p} \cdot F_{2p}^0) \\ \text{laser on: } A' &= N \cdot (\sigma_{2s} \cdot F_{2s}' + \sigma_{2p} \cdot F_{2p}') \end{aligned} \quad (6.5)$$

with

$$F_{2s}' + F_{2p}' = 1$$

where the σ_{2s}, σ_{2p} are the total cross sections of photoionization of lithium $2s$ and $2p$ valence electron; F numbers are the fractions for individual atomic states. Thus, with the knowledge of σ_{2s}, σ_{2p} in hand, and by comparing the measurements of $\text{Li}^+(1s^2)$ yields, we could determine the $2p$ fraction with the formula:

$$F'_{2p} = \frac{(1 - A'/A)}{(1 - \sigma_{2p}/\sigma_{2s})} \quad (6.6)$$

where the $\text{Li}^+(1s^2)$ yields could be obtained by integrating the intensity of the corresponding photolines as indicated in Fig. (6.11).

Special care has been taken into the fraction determination of the $2p$ excited state, and most of the effort has been concentrated on the ‘background subtraction’.

The procedure of true $\text{Li}^+(1s^2)$ counts determination was executed in steps: firstly, the Li^+ events of different data sets were displayed in a one-dimensional plot as a function of the total recoil ion’s momentum, after the careful modifications on the Li^+ spectrum mentioned above; secondly, segments of the pure background adjacent to the single-ionization of valence electron peak $\text{Li}^+(1s^2)$ were picked out as the basis data, to which a polynomial fitting (with up to the 3rd order) was made to reproduce the background variation; an integration over the raw counts confined by physically selected boundaries was performed, so was the integration over the simulated background curve in the same momentum region; finally, the events of interest were obtained, following a direct background subtraction from the primitive data.

It should be emphasized that this procedure of fraction determination plays a decisive role in the data analysis of our FLASH measurements, since the extraction of pure $\text{Li}(2p)$ data relies on the accurate subtraction of the ground state contribution from the experimental data. The systematic and statistical error of the results for the $\text{Li}(2p)$ initial state mostly come from the employed method of fraction determination. This is due to the poor statistics of the $\text{Li}^+(1s^2)$ signal and the relatively large background.

As depicted in Fig. (6.12), in determining the yield of $\text{Li}^+(1snl)$ for ionization of Li in both the ground state and the first excited state, the same method has been employed, as in the procedure of $\text{Li}^+(1s^2)$ estimate before: summing all raw $\text{Li}^+(1snl)$ events up and integrating the fitting curve for background determination, followed by a direct subtraction.

6.4 Measurement of Magnetic Sublevel Populations

After spectral identification of the individual atomic states of the target, the fluorescence spectroscopy method can be utilized to provide access to the optical alignment and/or orientation as well. In fact, the alignment \mathcal{A}_{20} and therefore the population of the magnetic substates of the laser-excited atom can be determined either via the angular distribution of the fluorescence [Men98] or by analyzing its linear polarization [OKe04]. In contrast, the orientation \mathcal{A}_{10} is accessible only by measuring the degree of circular polarization of the fluorescence [OKe04].

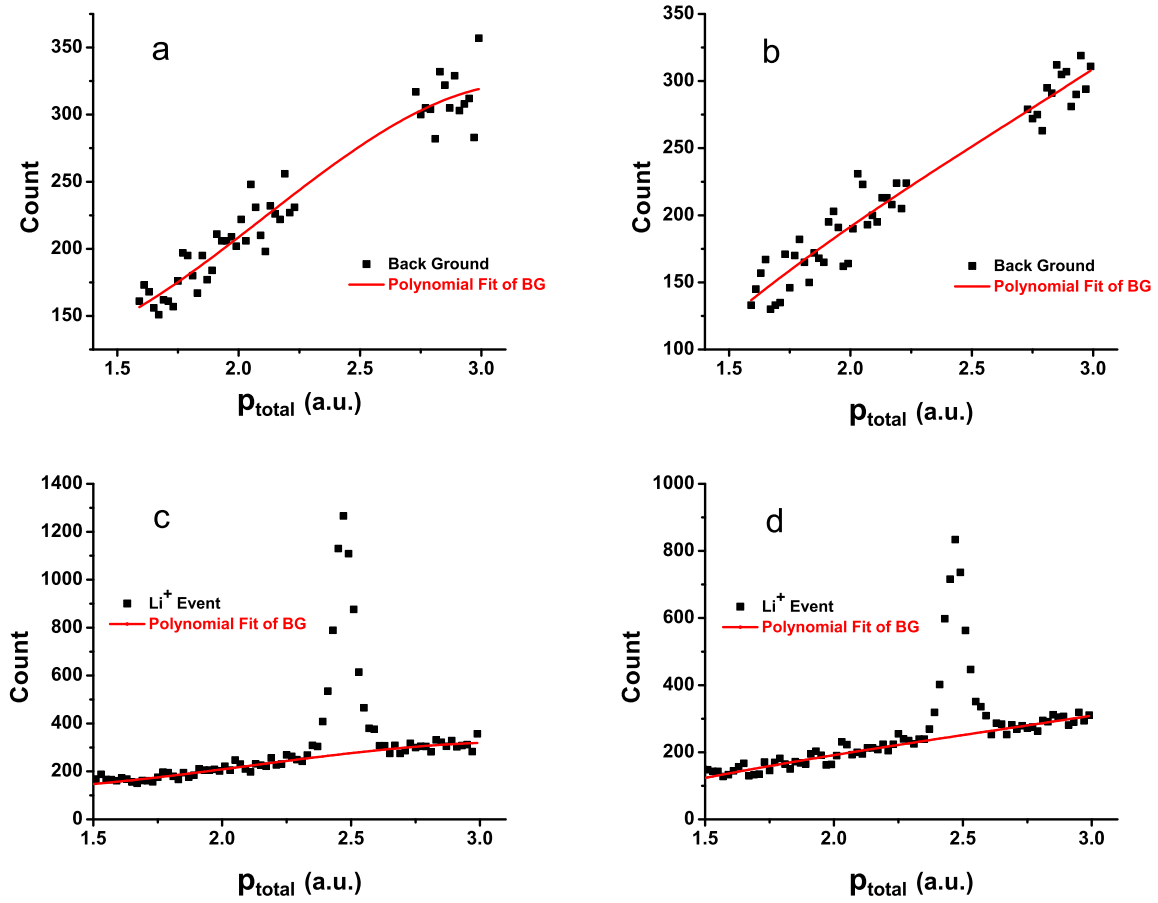


Figure 6.11: Fitting on background for $\text{Li}^+(1s^2)$ yield determination. Plot a: based on the chosen background segments, a polynomial fit (up to the third order) has been made to retrieve the background tendency as a function of the recoil ion's momentum, in a momentum region where $\text{Li}^+(1s^2)$ from the ionization of $\text{Li}(1s^22s)$ ground state emerges. Plot c: both the recoil $\text{Li}^+(1s^2)$ events (with background not subtracted) and the polynomial fit on background are presented, as a function of the recoil ion's momentum. Applying integral on both the interested recoil ion plot and the background fitting curve via choosing same physical boundary, following by a subtraction of these integrations, we could obtain the true $\text{Li}^+(1s^2)$ yield. Plot b and d are specially for the ionization of $\text{Li}(1s^22p)$ excited state to estimate $\text{Li}^+(1s^2)$ counts, which resemble Plot a and c.

Fluorescence Analysis

Consider the angular distribution of photons emitted in a de-excitation process (e.g. $\text{Li}(2p) \rightarrow \text{Li}(2s) + \gamma$ in our case):

$$A^*(\alpha\mathbf{J}) \longrightarrow A(\alpha_f\mathbf{J}_f) + \gamma \quad (6.7)$$

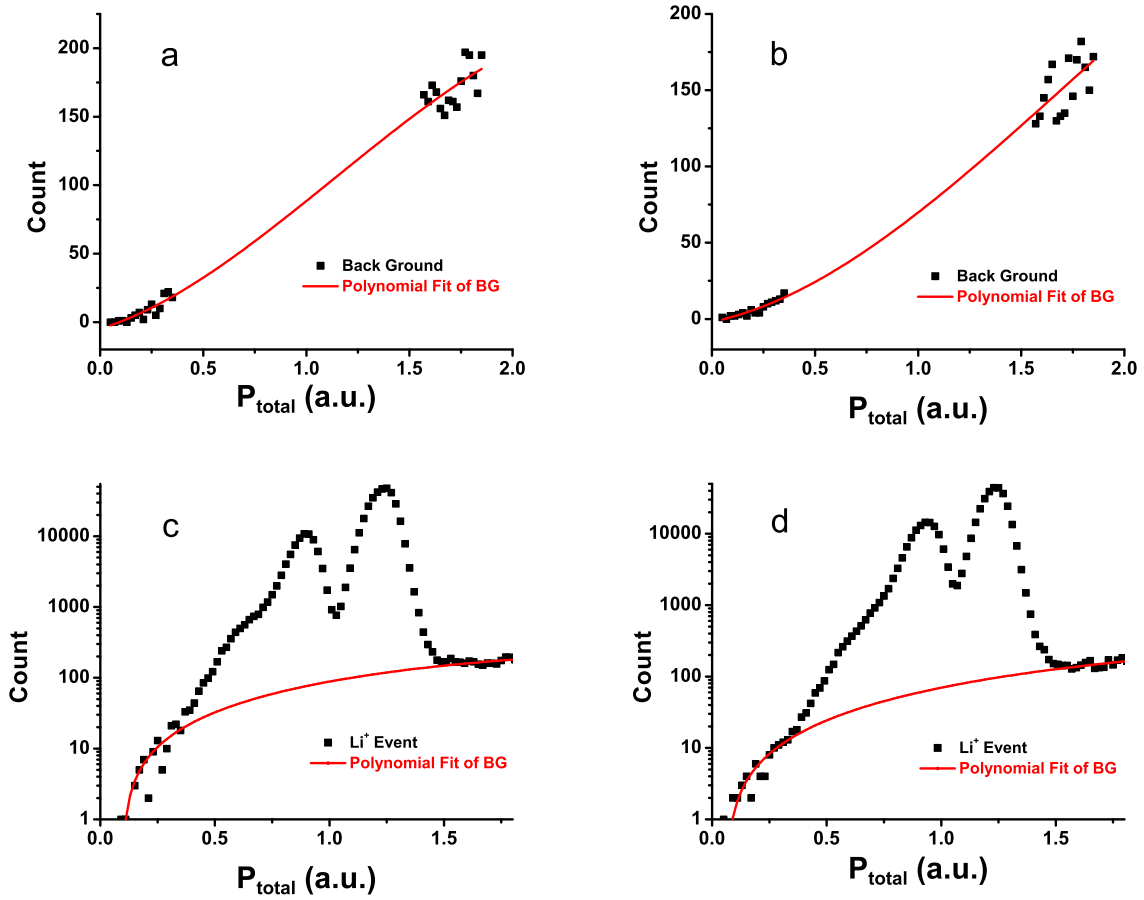


Figure 6.12: Procedure of $\text{Li}^+(1snl)$ yield determination. Plot a: based on the chosen background segments, a polynomial fit (up to the third order) has been made to retrieve the background tendency as a function of the recoil ion's momentum, in a momentum region where $\text{Li}^+(1snl)$ from the ionization of $\text{Li}(1s^22s)$ ground state emerges. Plot c: both the recoil $\text{Li}^+(1snl)$ events (with background not subtracted) and the polynomial fit on background are presented, as a function of the recoil ion's momentum, with the ordinate in a logarithmic scale. Applying integral on both the interested recoil ion plot and the background fitting curve via choosing same physical boundaries, following by a direct subtraction of these integrations, the true $\text{Li}^+(1snl)$ yield could be obtained. Plot b and d are specially for the ionization of $\text{Li}(1s^22p)$ excited state to estimate $\text{Li}^+(1snl)$ counts, which resemble Plot a and c.

here $A(\alpha\mathbf{J})$ describes an atomic system, \mathbf{J} denotes the total angular momentum of the electronic shell, and α characterizes all the other quantum numbers that necessarily specify the atomic state.

If the detector is not sensitive to the photon polarization, the angular distribution of

photons in the dipole approximation takes the following form [Bal00]:

$$I_{\alpha_f \mathbf{J}_f}(\vartheta, \varphi) = \frac{I_0}{4\pi} \left[1 + \alpha_2^\gamma \sqrt{\frac{4\pi}{5}} \sum_{q=-2}^2 \mathcal{A}_{2q}(\alpha \mathbf{J}) Y_{2q}(\vartheta, \varphi) \right] \quad (6.8)$$

where $Y_{2q}(\vartheta, \varphi)$ denotes the spherical harmonic function of degree 2 and order q , the intrinsic anisotropy parameter for photoemission is given by

$$\alpha_k^\gamma = \sqrt{\frac{3}{2}} \hat{J} (-1)^{J+J_f+k+1} \begin{Bmatrix} J & J & k \\ 1 & 1 & J_f \end{Bmatrix}, \quad \hat{J} \equiv \sqrt{2J+1} \quad (6.9)$$

In the dipole approximation, the angular distribution can't be affected by statistical tensors \mathcal{A}_{kq} ($k > 2$) of the decaying atom, which is the main qualitative difference between the angular distributions in the radiative and non-radiative decays. For polarization-insensitive detectors, an anisotropy of the angular distribution can occur only if the decaying state is aligned, *i.e.* if it is characterized by non-zero statistical tensors with $k = 2$. Therefore, the angular distribution presented by Eq. (6.8) is always isotropic for $J < 1$. An orientation of the decaying state, that is the tensors with odd ranks, does not affect the angular distribution.

If the decaying state is aligned along some direction (chosen as z -axis of the reference frame), the angular distribution of the dipole emission can be simplified as

$$I_{\alpha_f \mathbf{J}_f}(\vartheta) = \frac{I_0}{4\pi} [1 + \alpha_2^\gamma \mathcal{A}_{20}(\alpha \mathbf{J}) P_2(\cos \vartheta)] \quad (6.10)$$

where $P_2(\cos \vartheta)$ is the 2nd-degree Legendre polynomial, the product of $\alpha_2^\gamma \mathcal{A}_{20}(\alpha \mathbf{J})$ is also termed as the β_2 asymmetry parameter. For the decaying state with axial symmetry, the angular distribution exhibits the type of $I \sim a + b \cos^2 \vartheta$, which is axially symmetric with respect to the symmetry axis of the initial state and which is also symmetric with respect to reflection in the plane perpendicular to this axis.

The linear polarization of the emitted radiation depends on the alignment parameter $\mathcal{A}_{2q}(\alpha \mathbf{J})$ of the decaying state, not the orientation parameter $\mathcal{A}_{1q}(\alpha \mathbf{J})$. In particular, only the $q = 0$ component of the alignment tensor is non-zero, if this state is aligned along the z -axis. The degree of linear polarization P_L in a definite direction (φ, ϑ) is determined by measuring the intensities for two specified orientations of the polarizer axis, *i.e.* parallel (I_{\parallel}) and perpendicular (I_{\perp}) to the alignment axis ($\psi = 0$). Thus, the degree of linear polarization can be derived as [Bal00]:

$$P_L \equiv \frac{I_{\parallel} - I_{\perp}}{I_{\parallel} + I_{\perp}} = - \frac{\sqrt{\frac{3}{2}} \alpha_2^\gamma \sum_{q=-2}^2 \mathcal{A}_{2q}(\alpha \mathbf{J}) [D_{q2}^{2*}(\varphi, \vartheta, 0) + D_{q-2}^{2*}(\varphi, \vartheta, 0)]}{1 + \alpha_2^\gamma \sqrt{\frac{4\pi}{5}} \sum_{q=-2}^2 \mathcal{A}_{2q}(\alpha \mathbf{J}) Y_{2q}(\vartheta, \varphi)} \quad (6.11)$$

It follows immediately from the explicit form of the Wigner D-functions as shown in Eq. (E.4).

Typically, the axis of the detector system is oriented within the specific plane ($\varphi = 0$) under an Euler angle ϑ with respect to the photon beam direction, as illustrated in Fig. (6.13). The corresponding equation for the linear polarization degree now reads [Sch92, Sch03]:

$$P_L \equiv \frac{I_{\parallel} - I_{\perp}}{I_{\parallel} + I_{\perp}} = -\frac{3\alpha_2^{\gamma} \mathcal{A}_{20}(\alpha\mathbf{J}) \sin^2 \vartheta}{2\alpha_2^{\gamma} \mathcal{A}_{20}(\alpha\mathbf{J}) P_2(\cos \vartheta) + 2} \quad (6.12)$$

Obviously, the anisotropy and the linear polarization of the emitted photon, are both determined by the same asymmetry parameter $\beta_2 = \alpha_2^{\gamma} \mathcal{A}_{20}(\alpha\mathbf{J})$, via checking Eq. (6.10) and Eq. (6.12). Therefore, we conclude that the measurement of the linear polarization of the emitted radiation is equivalent to the measurement of the angular distribution.

Concerning the $|2^2S_{1/2}\rangle \xrightarrow{h\nu} |2^2P_{3/2}\rangle$ transition in our experiment, an alignment parameter with its maximum value $\mathcal{A}_{20}(2P_{3/2}) = 1$ provides that the magnetic sub-states with $M = \pm 1/2$ are occupied, while the $M = \pm 3/2$ ones are vacant, which is an ideal case — the so-called ‘perfect alignment’. However, due to the hyperfine interactions (for isotopes with non-vanishing nuclear spin) mainly [Fan73, Gre82b], the mechanism of depolarization unavoidably leads to the reduction of the resulting alignment in practice¹. Therefore, the reduced alignment/orientation parameter has the form via introducing a depolarization factor $G_k(\mathbf{J})$:

$$\mathcal{A}_{k0}^h(\alpha\mathbf{J}) = G_k(\mathbf{J}) \mathcal{A}_{k0}(\alpha\mathbf{J}) \quad (6.13)$$

Here $\mathcal{A}_{k0}^h(\alpha\mathbf{J})$ is the alignment ($k = 2$) or orientation ($k = 1$) reduced by the hyperfine interactions, $\mathcal{A}_{k0}(\alpha\mathbf{J})$ is the value without the depolarization effect considered. The $G_k(\mathbf{J})$ are generally expressed in terms of the hyperfine level separations a_{HFS} and natural linewidth Γ of the hyperfine levels. Within the limit of $\Gamma \ll a_{HFS}$, the depolarization factor takes the simple form

$$G_k(\mathbf{J}) = (2I + 1)^{-1} \sum_F (2F + 1)^2 \left\{ \begin{matrix} F & F & k \\ J & J & I \end{matrix} \right\} \quad (6.14)$$

Apparently, the depolarization effect becomes stronger (*i.e.* the $G_k(\mathbf{J})$ factors decrease) as the J quantum number decreases.

Experimental Arrangement

To assist the PDI study @ FLASH, a measurement of the degree of anisotropy of the excited state generated by a linearly polarized pump laser was performed by observing the linear polarization degree P_L of the emitted fluorescence radiation. Thus, the alignment parameter \mathcal{A}_{20} and the resulting magnetic sublevel populations can be deduced in the chosen experimental frame.

The schematic representation for this measurement is shown in Fig. (6.13), while, the experimental setup for PDI experiment is illustrated in Fig. (6.2) for comparison. The

¹Another two effects may also contribute to this depolarization phenomenon: the fluorescence cascades, and spurious magnetic fields and collisions in the interaction volume, which are neglected here.

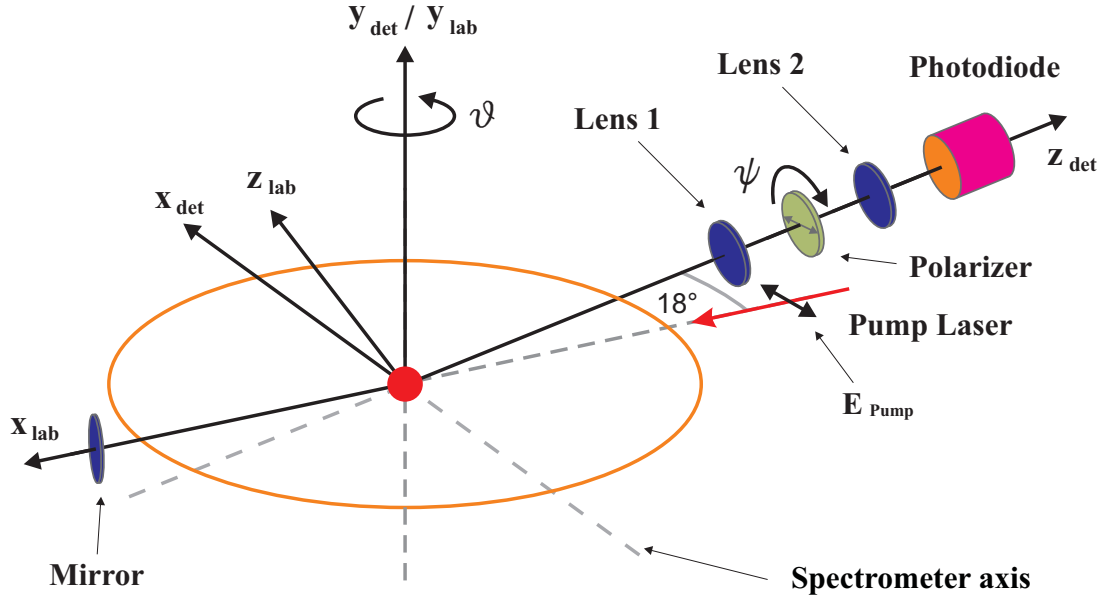


Figure 6.13: Fluorescence

detector (z_{det} -axis) is rotated by an Euler angle of $\vartheta = 288^\circ$ around the y_{lab} -axis with respect to the laboratory (z_{det} -axis). The linearly polarized pumping beam shoots along the x_{lab} -axis, and its polarization E_{Pump} is oriented along z_{lab} -axis, which defines the quantization axis thereby. A set of lenses (2 inches in diameter) are implemented to collect the emitted fluorescence, Lens 1 with a focal length of 400 mm collimates the divergent light, while Lens 2 with a focal length of 50 mm focuses the beam onto the photodiode. A polarizer is inserted to specify the chosen angles for the analysis of the fluorescence polarization.

The alignment parameter \mathcal{A}_{20} is determined, via following the measurement procedure as described by *O'Keeffe et al.* for instance, which records the angle-dependent intensity of the resonance fluorescence [OKe04]. However, in our measurement the fluorescence is detected under a small angle with respect to the direction of pumping beam (an angle of 18° between the z_{det} -axis and the x_{lab} -axis). It should be pointed out that, this geometric arrangement does not spoil the \mathcal{A}_{20} measurement, since the influence by the twisting of two coordinate systems against the Euler's angle ϑ can be separated and treated, as indicated in Eq. (6.12).

By rotating the polarizer axis, the measured fluorescence intensity reaches its maximum value (I_{\parallel}) as the transmission axis of the polarizer is parallel to the E vector of the (linearly polarized) pumping laser, and its minimum value (I_{\perp}) as the transmission axis is perpendicular to the E vector of the pumping laser. In consequence, these experimental results yield the degree of linear polarization for the fluorescence

$$P_L = \frac{I_{\parallel} - I_{\perp}}{I_{\parallel} + I_{\perp}} \quad (6.15)$$

Thus, the alignment parameter can be calculated through the following relation derived from Eq. (6.12)

$$\mathcal{A}_{20}(\alpha\mathbf{J}) = -\frac{2P_L}{[2P_L \cdot P_2(\cos\vartheta) + 3\sin^2\vartheta] \cdot \alpha_2^\gamma} \quad (6.16)$$

In order to construct meaningful value for the alignment parameter (as accurate as possible) in terms of a description of the PDI experiment @ FLASH, the determination of the alignment parameter was also performed in pulsed operation, which resembled the FLASH measurement condition. Especially, the same experimental duty-cycle (temporal structure) as described in Sec. 5.3 was applied, *i.e.* once the same amount of lithium was accumulated in the MOT, a MOT-field-free time of 1 ms was provided as the ‘MOT shut-down time’ $T_{shut-down}$, followed by a data acquisition (DAQ) period of 250 μs for fluorescence spectroscopy, in the meanwhile, a 15-pulse pumping laser train was delivered, with a pulse duration of 315 ns and a time interval of about 10 μs . Assuming the target density and excitation efficiency kept constant during the pulse train, it was expected that the alignments of the atoms remained the same for all pump pulses, which was also verified [Alb08].

In practice, the alignment parameter may exhibit a target-density-dependent behaviour, through the ‘radiation trapping’ mechanism, *i.e.* the re-absorption of fluorescence radiation emitted by other atoms at high target densities, which reduces the alignment (and/or orientation) parameters [Mol98]. To investigate this effect, two more measurements with shorter MOT shut-down time of 0.5 ms and 2 ms (a shorter shutdown time implies a higher density, and vice versa) were carried out, while the pump duration remained constant at 315 ns.

Measurement of the Alignment Parameter \mathcal{A}_{20}

Fig. (6.14) shows the measured fluorescence intensities as a function of the linear polarization’s orientation, with the maximum intensity value (I_{\parallel}) and the minimum intensity value (I_{\perp}) encompassed. The data in red represents the same experiment conditions as in our FLASH measurement ($T_{shut-down} = 1$ ms), while data in blue and black indicate different $T_{shut-down}$ of 0.5 ms and 2 ms for comparison.

A shorter shut-down time results in a shorter period for thermal expansion of the released atom cloud, and thus, means a larger number of atoms stimulated by pumping beam. As a consequence, the fluorescence intensity increases for decreasing shut-down time, as seen in the plots.

The intensity ratios between maximum and minimum values (thus, the degree of linear polarization P_L related), especially for $T_{shut-down}$ of 0.5 ms and 1 ms, are nearly the same within the error bars. This shows that the measurements were all performed in a low target density regime, where the effect of radiation trapping can be neglected. The deviation for $T_{shut-down} = 2$ ms case compared to the other two situations, is probably due to a worse signal-to-noise ratio of the photodiode for a smaller signal [Alb08], and may also origin from the larger fluctuation in the number of remaining atoms [Ste07].

Following the treatment procedure displayed in Eq. (6.15) and Eq. (6.16), the alignment

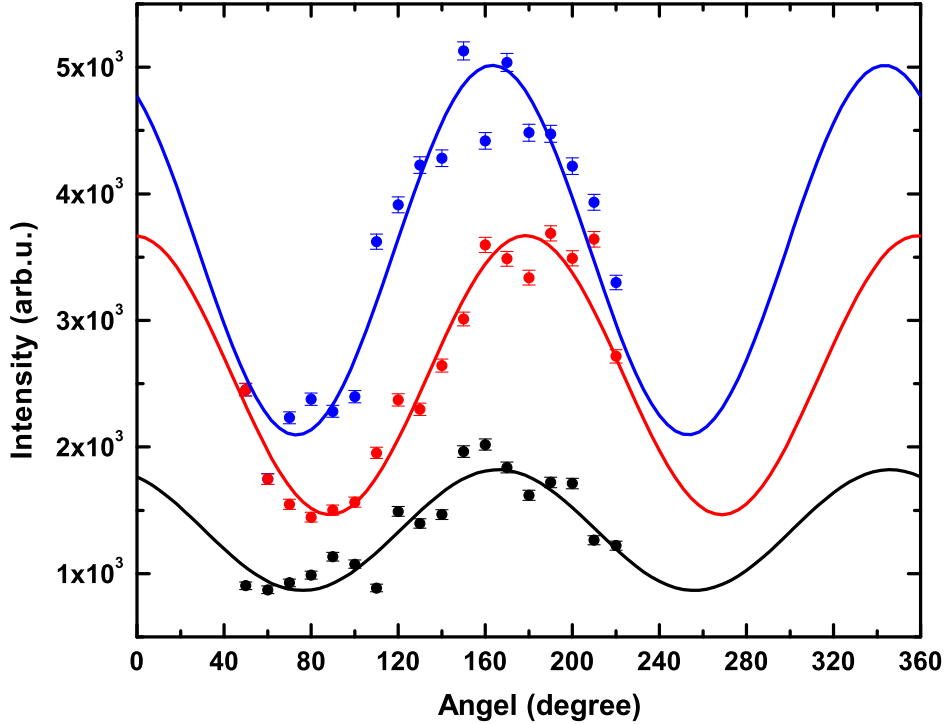


Figure 6.14: Angular distribution of the polarization of the emitted resonance fluorescence. It was measured with the polarizer's axis rotated from 50° and 220° with respect to a random set optical axis, covering the maximum and minimum intensity values. Three MOT shut-down times are labeled by different colours, blue for 0.5 ms, red for 1 ms and black for 2 ms. The lines here are the fitted curves to guide the reader's eyes.

parameter $\mathcal{A}_{20}(^2P_{3/2})$ for three $T_{shut-down}$ cases are calculated, and listed in Tab. (6.3). Except for observation with the longest $T_{shut-down}$ of 2 ms, the measurement results agree with the theoretical prediction of $\mathcal{A}_{20}^{theo}(^2P_{3/2}) = -0.72$ very well.

Transformation of the Occupation Distribution

The alignment parameter \mathcal{A}_{20} contains the complete information about the relative occupation probabilities for an atomic state $|\alpha\mathbf{J}\rangle$. Thus, for a given magnetic sub-state $|J, M\rangle$, its population can be calculated once the \mathcal{A}_{20} is known. If all sub-states with different M projections are equally occupied, then the state $|\alpha\mathbf{J}\rangle$ is isotropic, which corresponds to $\mathcal{A}_{20} = 0$. On the contrary, if the sub-states with different M are selectively populated, which obey the following relations

$$\begin{aligned} P(J, M) &\neq P(J, M') \\ P(J, +M) &= P(J, -M) \end{aligned} \quad (6.17)$$

then these state are called aligned, which corresponds to $\mathcal{A}_{20} \neq 0$.

Table 6.3: The alignment parameter $\mathcal{A}_{20}(^2P_{3/2})$ dependent on the MOT shut-down time.

MOT shut-down time [ms]	Alignment parameter $\mathcal{A}_{20}(^2P_{3/2})$
0.5	-0.68 ± 0.06
1.0	-0.71 ± 0.05
2.0	-0.58 ± 0.07

In the optical alignment case here, we consider the atom, being initially in $^2S_{1/2}$ state, is excited to $^2P_{3/2}$ state (since an alignment only occur for $J \geq 1$), the alignment parameter $\mathcal{A}_{20}(^2P_{3/2})$ is defined by [Cle74, Meh94]

$$\begin{aligned} \mathcal{A}_{20}(^2P_{3/2}) &= \frac{P(\frac{3}{2}, \frac{3}{2}) - P(\frac{3}{2}, \frac{1}{2})}{P(\frac{3}{2}, \frac{3}{2}) + P(\frac{3}{2}, \frac{1}{2})} \\ &= \frac{P(1, 1) - P(1, 0)}{2P(1, 1) + P(1, 0)} \end{aligned} \quad (6.18)$$

where the population probabilities of ionic states are given either by $P(J, M)$ or $P(L, M_L)$ in the first or the second part of Eq. (6.18), respectively. By applying the relationship

$$2P(1, 1) + P(1, 0) = 1 \quad (6.19)$$

$P(1, 0)$ can be resolved:

$$P(1, 0) = \frac{2}{3} \left[\frac{1}{2} - \mathcal{A}_{20}(^2P_{3/2}) \right] \quad (6.20)$$

For instance, as the determined alignment parameter $\mathcal{A}_{20}(^2P_{3/2})$ equals to -0.70, the magnetic sublevel populations are $P(1, 0) = 0.8$ and $P(1, 1) = P(1, -1) = 0.1$.

Because of the spatial orientation of the polarization of the pump laser is different with respect to the polarization of the FEL radiation, a projection operation is needed to calculate the populations of the magnetic sub-states defined by the new quantization axis in the FLASH experiment. The rotation of the reference system induces a unitary transformation of the occupation distribution the states (see Appendix E). The transformation is explicitly executed under the guidance of Eq. (E.3). More details on the matrix elements $D_{m'm}^{3/2}(\varphi, \vartheta, \psi)$ are contained in a book by Varshalovich *et al.* for details [Var88].

For the photoionization in polarization-‘parallel’ configuration, laser polarization \mathbf{E}_{Pump} and \mathbf{E}_{FEL} are coplanar, enclosing an angle of 18° . A rotation transformation with the Euler angles set $(\varphi, \vartheta, \psi) = (0^\circ, 342^\circ, 0^\circ)$ is applied. While, for the photoionization in polarization-‘perpendicular’ configuration, the two laser polarizations are in mutually orthogonal planes. Thus, it leads to a rotation transformation with the Euler angles set of $(\varphi, \vartheta, \psi) = (342^\circ, 90^\circ, 0^\circ)$, based on the experimental arrangement ($z_{lab} \rightarrow x_{lab}$, $x_{lab} \rightarrow y_{lab}$, $y_{lab} \rightarrow z_{lab}$). Fig. (6.15) shows the probability distribution of atomic states with the projection quantum number M in the laboratory system of fluorescence spectroscopy, and the subsequent values in the coordinate systems of the FLASH experiments.

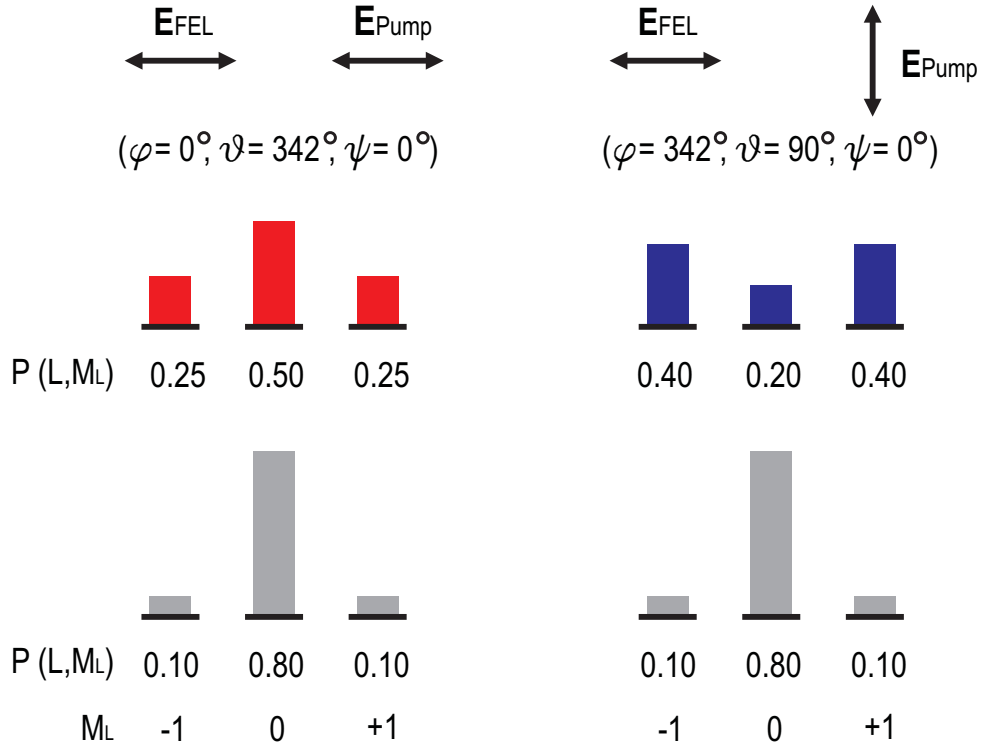


Figure 6.15: Schematic representation of the magnetic sub-state populations for the $|^2P_{3/2}\rangle$ state in the laboratory frame of \mathcal{A}_{20} determination (bottom row), and in the coordinate of the FLASH experiment (top row) for the ‘parallel’ (in red) and ‘perpendicular’ (in blue) polarization configurations separately.

For further reading on theoretical descriptions, please refer to a review paper by Kabachnik *et al.* [Kab07] and a book by Balashov *et al.* [Bal00] as well. And for more measurement details, please refer to a group thesis [Alb08].

Chapter 7

Experimental Results

In the present chapter, we will present in detail the experimental results on PDI depending on the alignment of valence electron and on the impact photon energy, and results on the PIE process as well. Issues as the fragmentation dynamics based on Wannier threshold law, the PDI mechanisms of ‘Two-step-1’ and ‘Shake-off’, and the symmetry-dependent selection rules will be discussed.

7.1 Photo Double Ionization

To study the influence of the initial target state $Li\{L M_L S \pi\}$ on PDI close to threshold, the target was prepared in the desired state through optical pumping. The experimental schematics is illustrated in Fig. (6.1). Lithium atoms prepared in either the $2s$ ground state or the $2p$ excited state are fragmented by the FEL photons, both ending in the Li^{2+} final ionic state, where one of the two inner-shell electrons and the valence-shell one get ionized.

Obviously, the symmetry of the initial state varies due to the change of electron configuration, therefore, the symmetry of the final two-electron state ends as an ‘unfavoured’ or ‘favoured’ one, according to the selection rules elucidated by Maulbetsch and Briggs [Mau95], which is discussed in Subsection 2.1.3. Furthermore, the $2p$ orbital can be spatially either aligned along the direction of the linearly polarized VUV-electric field vector \mathbf{E} , or orthogonal to it. Thus, the influence of this alignment or more specifically the initial state magnetic sublevel M_L population on the PDI dynamics is revealed. We note that the threshold behavior of the individual sublevels has not been discussed in literature before since such experimental studies which allow switch from one to the other do not exist.

Fig. (6.1) also represents a facile picture elucidating the PDI process intuitively, where two electrons come from different shells. With the photon energy above the lowest PDI threshold merely, the primary photo-absorption process dominantly happens to the inner-shell electron, while the photoionization of the valence electron directly is suppressed by two orders of magnitude for the $2s$ orbital and another magnitude lower for the $2p$ orbital.

This phenomenon is based on the conservation of energy and momentum: the ejected electron takes the excess energy in the photon-absorption process, whereas its kinetic momentum after ionization originates from the inherent momentum in the initial bound state, since the impact photon contributes no momentum. Therefore, it favors ionization of inner orbitals which contain high momentum components. As depicted in these figures, once the $1s$ -electron absorbs the photon, it escapes from the atomic shell within a \cos^2 -double lobe pattern (red lobes) aligned along the field vector \mathbf{E} , and induces the emission of the outer-shell electron (blue lobes) via ‘two-step-one’ mechanism. This short-range electron-electron correlation should depend on the level of excitation and possibly also on the spatial alignment of the valence electron with respect to \mathbf{E} , as indicated in Fig. (6.1) (b and c), therefore, be sensitive on the mechanisms within the reaction zone. However, it should be pointed out that, in the first step, the $1s$ -photoionization cross section should be independent of the $2p$ -orbital alignment and independent of the pure geometrical coupling of both angular momenta ($M = 0$ and $M = \pm 1$) also, since the aligned $2p$ -electron being a pure spectator remains in its orbital, without participating in the initial photon absorption by $1s$ -electron, and without modifying the inner-shell electron’s binding energy.

The photons from the FLASH VUV source were set at 85 eV and 91 eV, based on two considerations: firstly, as discussed above, we want DI to occur due to the TS1 mechanism which is the case at low excess energy, whereas at higher energy the shake-off mechanism gets more important, which was exploited *e.g.*, by Knapp *et al.* [Kna02a]; secondly, approaching the threshold the long range Coulomb interaction in the continuum becomes dominant and, therefore, the two-electron Wannier threshold dynamics can be studied.

7.1.1 $(\gamma, 2e)$ on $\text{Li}\{L M_L S \pi\}$ at $E_\gamma = 85$ eV

We examine the case of $(\gamma, 2e)$ on Li with the photon energy of $E = 85$ eV, to see how the PDI process is influenced by the symmetry of the initial state, and how initial state preparation can modify the electron pair emission geometry.

Taking lithium atoms in the ground state, and the excited states, in which below the two different alignments are indicated by $2p_\parallel$ (the $2p$ -orbital is aligned parallel to the polarization of the VUV radiation) and $2p_\perp$ (the $2p$ -orbital is aligned perpendicular to the polarization of the VUV radiation), the transitions are described by the following equations respectively:

$$\begin{aligned}
 & \text{Li}(1s^2 2s^2 S^e, M_S = 0) \xrightarrow{h\nu} \text{Li}^{2+}(1s^2 S) + 2e(1,^3P^o, M_P = 0) \\
 p_\parallel : & \text{Li}(1s^2 2p^2 P^o, M_P = 0) \xrightarrow{h\nu} \text{Li}^{2+}(1s^2 S) + 2e(1,^3S^e, ^1,^3D^e, M_{S,D} = 0) \\
 p_\perp : & \text{Li}(1s^2 2p^2 P^o, M_P = \pm 1) \xrightarrow{h\nu} \text{Li}^{2+}(1s^2 S) + 2e(1,^3D^e, M_D = \pm 1) \quad (7.1)
 \end{aligned}$$

where the total angular momentum L of atomic system is changed by ± 1 ; and the magnetic quantum number M_L is not changed, due to the dipole transition selection rules for linearly polarized light ($\Delta M = 0$). For the $2p_\parallel$ -configuration, the S - and D -partial waves are both permitted in the final states, while for $2p_\perp$ -configuration only two D -partial waves projections with $M = \pm 1$ are allowed, but the S -partial wave ($M_S \equiv 0$) is suppressed.

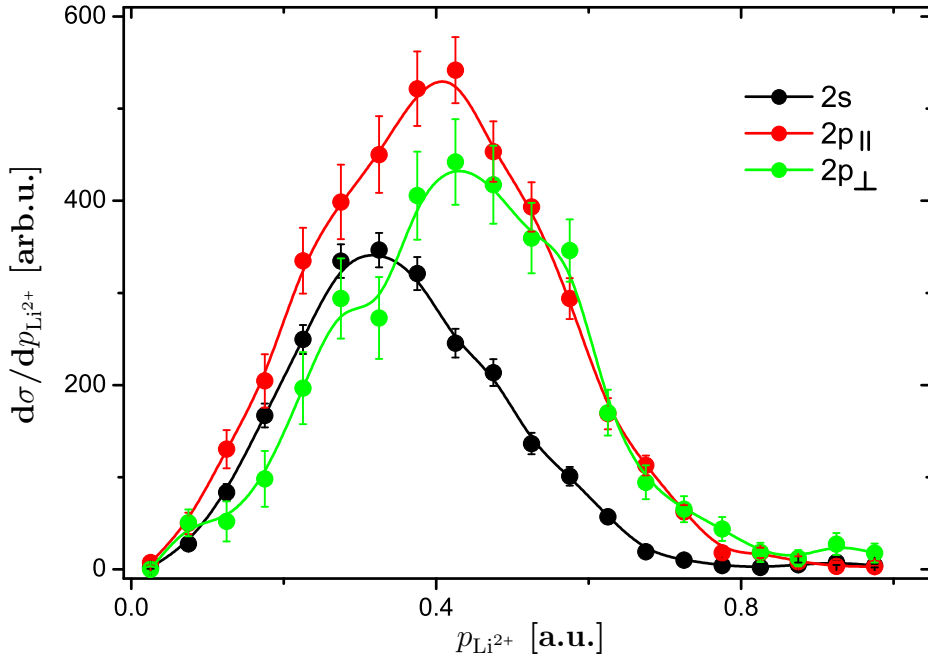


Figure 7.1: The PDI cross section differential in momentum for $\text{Li}(1s^2nl)$ by 85 ± 1 eV photons plotted as a function of the recoil ion momentum. The lithium target was initially prepared either in the ground state $2s$ (black curve) or with different spatial alignments of the laser excited orbital $2p_{||}$ (red curve), and $2p_{\perp}$ (green curve). Significantly, an alignment dependence effect could be seen directly via a comparison between $2p_{||}$ and $2p_{\perp}$ configurations. Here, the error bars are also displayed in each plot. Though the PDI from different states are measured under the same experimental condition, data deviation for $2p$ excited states is much larger than for $2s$ ground state, due to the fact that, the results for $2p$ are obtained indirectly, through a more complex way.

The corresponding single differential cross sections of Li^{2+} as function of the recoil ion's momentum $p_{\text{Li}^{2+}}$ are plotted in in Fig. (7.1), where the various initial states are indicated by different colors: the data points for the initial ground state $\text{Li}(2s)$ are black, the parallel alignment $\text{Li}(2p_{||})$ data are red and the perpendicular $\text{Li}(2p_{\perp})$ data are green. All cross sections presented in this chapter are normalized to 100% population of the respective initial state (for details see Sec. 6.3). From the diagrams, it is obvious that the Li^{2+} yields for the three initial states are different. The integrated doubly charged ion yield from the ground state is lower than from the $2p$ excited states no matter what kind of valence electron alignment they have. This can be easily explained by the Wannier threshold law: the lowest DI threshold for the $\text{Li}(2p)$ excited state is 79.15 eV instead of 81.03 eV for the $\text{Li}(2s)$ ground state due to the additional laser excitation. With the presupposition that for all the final states here, the total cross section behaves according to the relation $\sigma \propto \Delta E^{1.127}$, the excess energy difference leads to the fact that the mean DI cross section for the $2p$ -state (averaging over both alignment configurations) is 1.62

times larger than the initial $2s$ -state. Furthermore, due to the increased excess energy, the maximum momentum of the recoil ions increases for the excited state. Therefore also the momentum of the yield peak shifts to a higher value. With the focused interest on the investigation of M_L -substate-dependence of double ionization, distinct discrepancies are found in both the total counts and the curve behavior at $E_\gamma = 85 \text{ eV}$, by comparing the PDI cross sections of $2p_{\parallel}$ case with the $2p_{\perp}$ one in the plot: firstly, by utilizing the total PDI cross section for $2s$ as the reference, the integrated $2p_{\parallel}$ -cross section is enhanced by 1.82 ± 0.06 while the $2p_{\perp}$ -cross section is scaled only by a factor of 1.42 ± 0.06 ; secondly, the $2p_{\parallel}$ -curve is significantly higher than the $2p_{\perp}$ -curve in the low ion-momentum ($p_{\text{Li}^{2+}} \leq 0.6 \text{ a.u.}$), though the two curves overlap well in the high ion-momentum region ($p_{\text{Li}^{2+}} > 0.6 \text{ a.u.}$).

By recalling the discussion for the two reaction pathways with parallel ($2p_{\parallel}$) and perpendicular ($2p_{\perp}$) alignments respectively in Eq. (7.1), the displayed difference between the two curves roots in the difference of the projected final states in the two transition processes. Different from the $2p_{\parallel}$ case, where the two ejected electrons enable the S and D ($M = 0$), whereas the $2p_{\perp}$ configuration allows the D ($M = \pm 1$) partial waves in the final state. As a consequence of the selection rules by Maulbetsch and Briggs [Mau95], the former partial wave configuration favours a dominant back-to-back emission, while the later one prohibits the Wannier escape, therefore, resulting in a much larger cross section for $2p_{\parallel}$ case than for $2p_{\perp}$ case. In addition, it explains the discrepancy of PDI probability in the low ion-momentum region as well: once the final state exhibits the characteristic two-electron emission ('back-to-back' with close kinetic energy), the 'sum momentum taken' parent ion tends to end up with a low kinetic momentum.

Apart from this interpretation through the differences of the final states, the alignment-dependent double-ionization phenomenon could also be comprehended within the intuitive PDI picture at threshold, which is assumed to be dominated by TS1 other than SO. The primeval ejected $1s$ inner-shell electron is more likely to collide with the outer-shell electron in the $2p_{\parallel}$ configuration than the $2p_{\perp}$ one, simply based on a spatial overlap consideration.

In the following, we turn to the discussion how the two electron emission patterns depend on the symmetry of the final state, a more formal treatment in terms of angular momentum partial waves. According to the behaviour of the emitted two-electron wave function, we classify these symmetries as 'unfavoured' and 'favoured' Wannier configuration¹, following the notations by [Sta82, Gre82a].

Here we restrict to the discussion of the recoil ion momentum since electrons were not measured coincidentally. This was due to the rather high background signal at the electron spectrometer side. Nevertheless the recorded Li^{2+} gives detailed insight too, since it reflects the sum momentum of the emitted electrons, e.g., the Wannier geometry with two electrons ejected back-to-back with equal energies corresponds to vanishing Li^{2+} ion momentum.

According to the assertion made in Subsection 2.1.3, which declares 'the two escaping electrons in a PDI transition close to the threshold are more likely to have an antiparallel spin than a parallel spin', we would expect that for the accessible final states in Eq. (7.1),

¹These wave functions exhibit a node or an antinode for the Wannier configuration respectively.

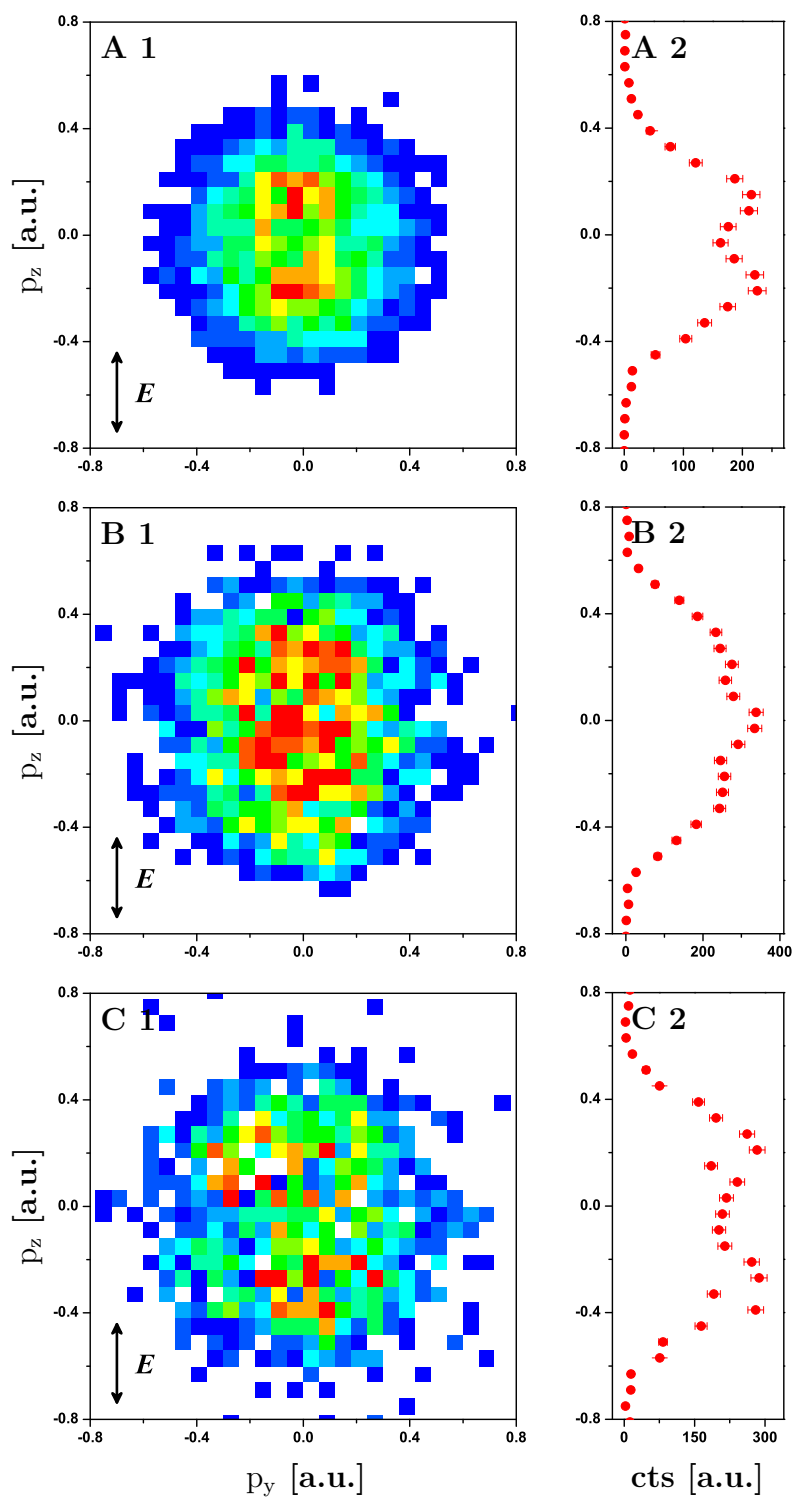


Figure 7.2: Left columns: Two-dimensional plots of the recoil-ion momentum distribution after PDI of $\text{Li}(1s^2 2s)$ (A1), $\text{Li}(1s^2 2p, \parallel)$ (B1) and $\text{Li}(1s^2 2p, \perp)$ (C1) at photon energy $E_\gamma = 85 \text{ eV}$. Right columns: Corresponding projection of the momentum distributions onto the vertical axis. The FLASH polarization is along the z -axis.

the $S = 1$ cases do not contribute significantly to the double ionization reaction. This phenomenon can be understood intuitively through the *Pauli Exclusion Principle*, where the total-symmetry $P_{total} \equiv -1$ (antisymmetric) is a direct product of the orbital-symmetry P_{orbit} and the spin-symmetry P_{spin} .

$$P_{total} = P_{orbit} \otimes P_{spin} \quad (7.2)$$

If the two electrons are chosen to be symmetric in spin, then the orbital-symmetry becomes antisymmetric naturally, meaning that the probability to find these two particles in one point is zero; *i.e.*, electrons with identical spin projection are prohibited from being close in position, originating from the requirement of an antisymmetric wave function for identical fermions. Thus with the precursor of PDI process via the TS1 mechanism, the triplet final states ($S = 1$) are largely suppressed due to the inhibition on the particles' approaching in space (as a hard collision), albeit the SO mechanism dose not restrict to this limitation where a direct electron-electron interaction is not a compulsory. Therefore, our discussion mainly concentrates on the singlet final states ($S = 0$), which dominates PDI close to the threshold, *i.e.*, the minor contribution by all $S = 1$ states [Har98, Weh02] is neglected, for simplicity.

Now, let's come to our PDI transitions shown in Eq. (7.1), where clearly defined examples are presented to elucidate the electron emission patterns influenced by the kinematical and dynamical factors, revealing that the prevailing node or antinode for the Wannier configuration results from their symmetries of the partial waves in the vicinity of threshold.

Firstly, for the double ionization starting from the initial ground state $2S^e$ of lithium, the outgoing electron pair will end in the symmetry of $1P^o$ under the assumption of vanishing triplet cross section made above. For this state the spatially symmetric emission is not allowed giving rise to the vanishing cross section for electron 'back-to-back' emission with equal energies [Mau95]. Thus, it is identified as an 'unfavoured' final state symmetry. As a result, we expect an emission pattern similar to the helium target [Kna02b]. Indeed, it is confirmed by the observed double-lobe pattern of the recoil ion momentum distribution displayed in Fig. (7.2) (A1), with a characteristic minimum at the origin, corresponding to the Wannier emission configuration with vanishing recoil ion momentum.

$$p_{rec} = \sum_{i=1}^2 p_e^i = 0 \quad (7.3)$$

We noticed that that in the modified momentum projection of Fig. (7.2) (A2), the dip at the position where $|p_{rec}| = 0$ is not diminished to zero. This maybe due to the $3P^o$ symmetry contribution, which assumed to be suppressed, enabling the 'back-to-back' emission². It should be pointed out that, the third component's projection p_x influences the visibility of the dip structure also, which reduces the contrast of these 2D-momentum plots as well.

²The triplet state contribution is generally small, except for the case from the $2s$ ground state, for one electrons is ejected along the photon polarization direction, where it is the same order as the fully differential cross section (FDCS) from the singlet state [Col09].

Now, let's switch to the excited initial states ${}^2P^o (M_P = 0, \text{ and } \pm 1)$, where, the populated initial magnetic sublevels differs according to the alignment configurations. By recalling the conclusions made in an earlier statement (the selection rule $\Delta M_L = 0$ for linearly polarized light; the suppression of triplet final states due to *Pauli Exclusion Principle*), we separate the partial wave of two continuum electrons into two cases: the ${}^2P^o (M_P = 0)$ initial state may have the outgoing ${}^1S^e (M_S = 0)$ and ${}^1D^e (M_D = 0)$ partial waves, and the ${}^2P^o (M_P = \pm 1)$ initial state reaches the ${}^1D^e (M_D = \pm 1)$, after absorbing one single photon.

For the 'favoured' symmetries of ${}^1S^e (M_S = 0)$ and ${}^1D^e (M_D = 0)$, the ionization dynamics evolves rather freely compared with other symmetry configurations, since none of the selection rules for the two-electron escaping [Mau95] would identify these two cases (and only these two), which are unique exceptions listed in Tab. (2.1). In a consequence, in the recoil Li^{2+} 2D-momentum plot of Fig. (7.2) (B 1), the feature at the $|p_{rec}| = 0$ changes to a hump other than a dip, indicating that the cross section is converted from a minimum to a maximum as the target's initial symmetry changes from ${}^2S^e$ to ${}^2P^o (M_P = 0)$. This is despite the fact that for the initial excited state the excess energy increases by 2 eV and, therefore, more phase space off the Wannier configuration is accessible.

While for the 'unfavoured' symmetries ${}^1D^e (M_D = \pm 1)$ from $2p_{\perp}$ configuration, an expected minimum in the cross section around $|p_{rec}| = 0$ gets confirmed through the observation displayed in Fig. (7.2) (C 1).

We notice that the double ionization starting from the initial states ${}^2S^e (M_S = 0)$ and ${}^2P^o (M_P = \pm 1)$ both have dip structures at the origin, although, different selection rules apply in the two cases. For lithium in ${}^2S^e (M_S = 0)$, selection rule C forbids the ' $\mathbf{k}=-\mathbf{k}$ ' emission thoroughly; while for lithium in ${}^2P^o (M_P = \pm 1)$, selection rule B1 eliminates the two-electron 'back-to-back' behavior only along the quantization axis. Since selection rule C is more drastic than selection rule B1, especially close to threshold where electron correlation favors this configuration, the minimum at $|p_{rec}| = 0$ for ${}^2S^e (M_S = 0)$ should be deeper than the one for ${}^2P^o (M_P = \pm 1)$, without other mechanisms participating [Mau95].

As result clear differences can be found in the electrons emission configurations by comparing the (representing) recoil Li^{2+} momentum distribution for PDI in $2p_{\parallel}$ and $2p_{\perp}$ alignment, though both initial states have the same quantum numbers $\{L S \pi\}$. Thus, for the first time a PDI dynamics/kinematics depending on the M_L quantum number is demonstrated through varying the $2p$ -orbit alignment.

7.1.2 $(\gamma, 2e)$ on $\text{Li}\{L M_L S \pi\}$ at $E_{\gamma} = 91$ eV

In addition to the measurements at photon energy $E_{\gamma} = 85$ eV, a second $(\gamma, 2e)$ measurement was performed at $E_{\gamma} = 91$ eV, which is 6 eV further away from the lowest PDI threshold for target atoms in both the ground state and the first excited states.

Again, the single differential cross sections of Li^{2+} as function of the recoil ion's momentum, for photoionization from different initial states are plotted respectively in Fig. (7.3), where the color denotations are the same as for $E_{\gamma} = 85$ eV: black for ground state $\text{Li}(2s)$, red for excited $\text{Li}(2p_{\parallel})$ (parallel alignment) and green for $\text{Li}(2p_{\perp})$ (perpendicular align-

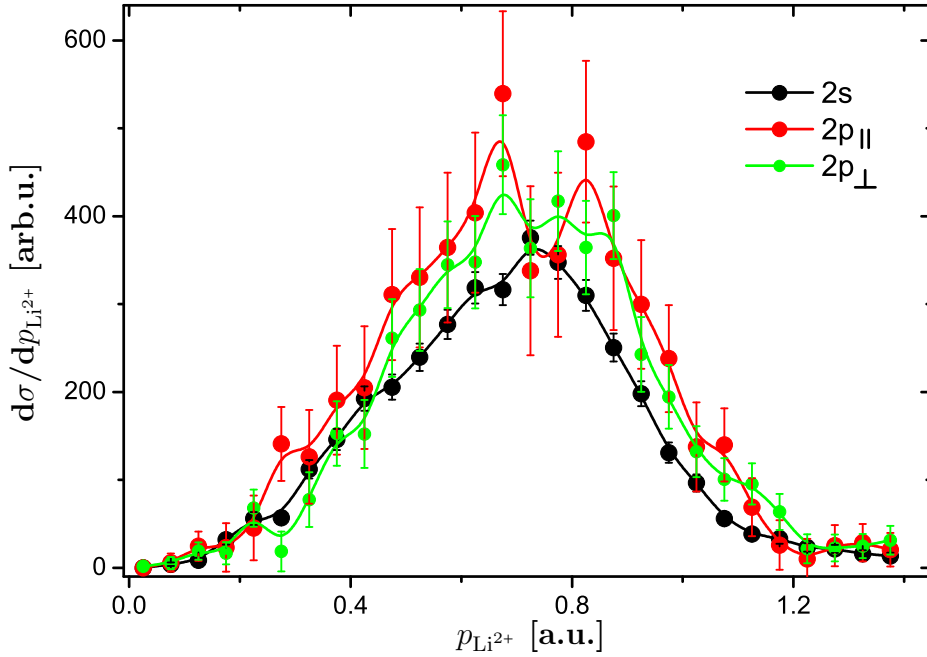


Figure 7.3: The PDI cross section differential in momentum for $\text{Li}(1s^2nl)$ by 91 ± 1 eV photons plotted as a function of the recoil ion momentum, with error bars displayed in each plot also. The lithium target was initially prepared either in the ground state $2s$ (black curve) or with different spatial alignments of the laser excited orbital $2p_{||}$ (red curve), and $2p_{\perp}$ (green curve). Interestingly, plots of different $2p$ alignment show less discrepancy than PDI at 85 eV photon energy, indicating that the alignment dependence effect becomes weaker as excess photon energy increases.

ment).

Comparing with the measurements for $(\gamma, 2e)$ at $E_{\gamma} = 85$ eV, the double ionization yields go up apparently³, as a direct result of the photon energy increasing. However, the cross section enhancement from $2s$ ground state to $2p$ excited states becomes smaller for higher photon energy, which is consistent with the Wannier threshold law $\sigma \propto \Delta E^{1.127}$ indeed. The excess energies are 10 eV for $2s$ state and 12 eV for $2p$ state at $E_{\gamma} = 91$ eV, leading to a yield increment of 29% (with respect to the theoretical prediction of 23%)⁴; in contrast, a yield increment of 62% (with respect to the theoretical prediction of 58%) is obtained at $E_{\gamma} = 85$ eV, as the excess energies are 4 eV and 6 eV respectively. Thus, these observations indicate once more again, that the threshold effects play a roll in the PDI dynamics.

Even more compelling is the observation, that the alignment sensitivity significantly decreases when the photon energy is increased to 91 eV. Here the integrated cross sections are $\sigma_{2p_{||}} = (1.39 \pm 0.07) \cdot \sigma_{2s}$ and $\sigma_{2p_{\perp}} = (1.19 \pm 0.05) \cdot \sigma_{2s}$. In principle, this observation

³This assertion is made by checking the Li^{2+} event rate during measurement, which is also hinted by the obtained double-to-single ionization cross section ratio $R = \sigma^{++}/\sigma^{+}$.

⁴Here we have the excited states pumped by different polarization configurations averaged to get the total count for a general case.

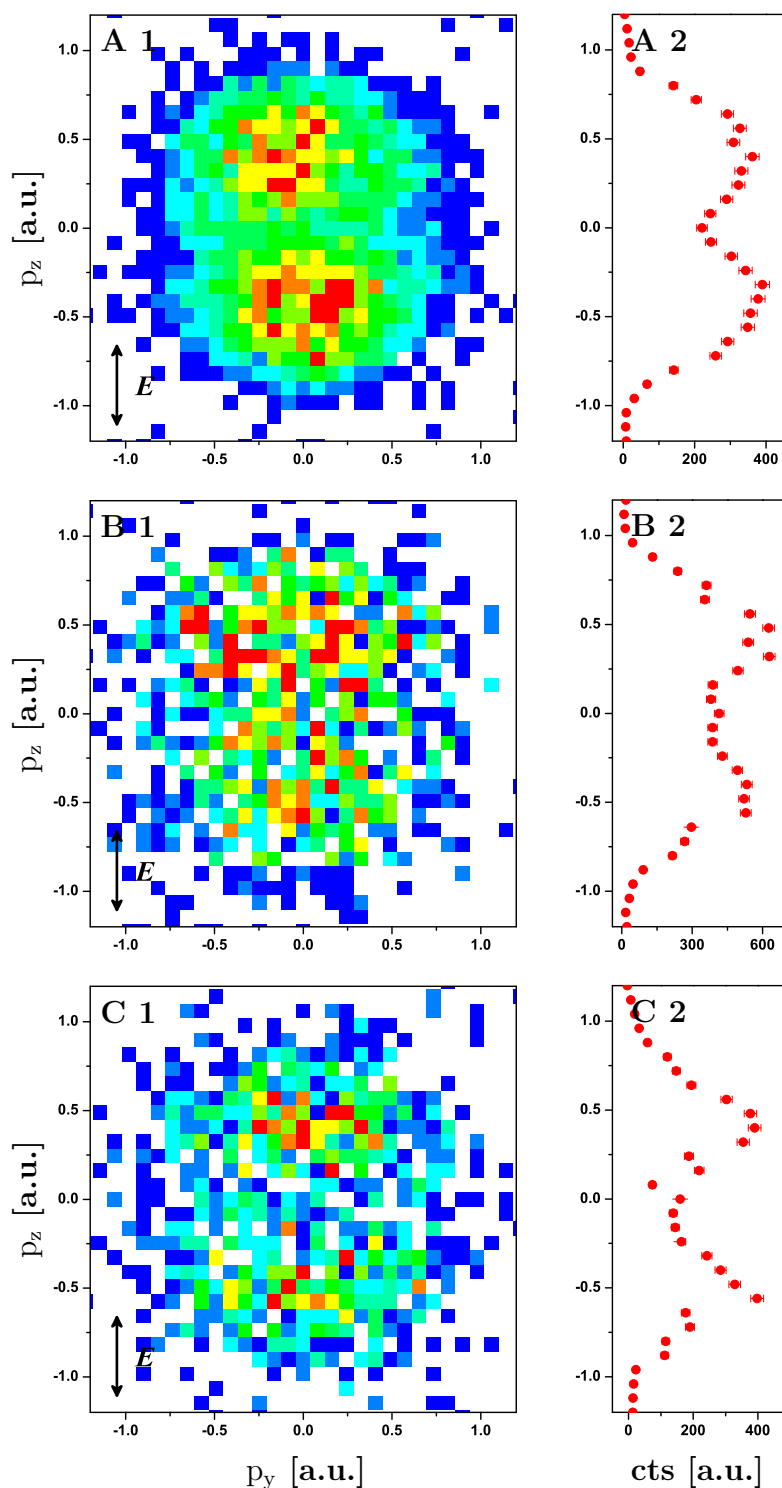


Figure 7.4: Left column: Two-dimensional plots of the recoil-ion momentum distribution after PDI of $\text{Li}(1s^2 2s)$ (A1), $\text{Li}(1s^2 2p, \parallel)$ (B1) and $\text{Li}(1s^2 2p, \perp)$ (C1) at photon energy $E_\gamma = 91 \text{ eV}$. Right column: Corresponding projection of the momentum distributions onto the vertical axis. The FLASH polarization is along the z -axis.

is consistent with the interpretation that the alignment dependence of DI is the result of the TS1 mechanism, which contains an electron-electron collision in the final stage. As the excess energy after ionization rises, the TS1 relative contribution (compared with the SO mechanism) to PDI total cross section reduces, therefore, the alignment dependence effects become weaker, intuitively. However, it should be pointed out that the alignment dependence effect is not present at all for IE process, *i.e.*, one of the electrons stays bound (other than the ‘two continuum electron’ situation), which will be discussed in the following section.

Further more, by checking the plots shown in Fig. (7.3), interestingly we find that in the low ion-momentum region, the discrepancy between the $2p_{\parallel}$ and $2p_{\perp}$ curves weakens, however, that the counts for $2p_{\parallel}$ still remains higher than those for $2p_{\perp}$, the same as in the 85 eV measurements. It reveals the fact that, the different amplitudes for the individual two-electron final states in PDI transitions illustrated in Eq. (7.1), enabling an alignment dependent cross section, vary as the photon energy changes. Taken the $2p_{\parallel}$ case for example, the portion of the *S*-partial wave diminishes for rising photon energy but not annihilate completely (which counts for the tiny variance between two curves at low momentum region), while the *D*-partial wave contribution dominates PDI total cross section (approaching to a *D*-wave emission trend exhibited by PDI in the $2p_{\perp}$ case). Therefore, it is demonstrated that the alignment dependence effect is not result of pure geometrical coupling but must be due to modified electron correlation.

As for completeness, the two-dimensional momentum spectra for recoil Li^{2+} measured at $E_{\gamma} = 91$ eV are shown in Fig. 7.4, which serve as the comparisons with the figures for PDI @ $E_{\gamma} = 85$ eV.

7.2 Single Ionization plus Simultaneous Excitation

Apart from the photo double ionization (PDI), the photo single ionization plus simultaneous excitation (PIE) of lithium atoms is also recorded in our measurements at FLASH, since the photon energy above the lowest double ionization threshold of $\text{Li}(2s)$ ($IP = 81.04$ eV) automatically fulfills the energy requirement for Li inner shell ionization plus valence shell excitation, listed in Tab. (6.1, 6.2). Though one electron (the one in the valence orbit) still remains bound after the ‘break up’ reaction via single photon absorption, in fact, the PIE transition is another dynamic process where two active electrons are involved.

The possible dynamic mechanisms that may lead to the PIE are illustrated in Fig. (2.1) (bottom) and Fig. (2.2) (bottom) in Chap. 2, namely ‘shake up’ and ‘knock up’, which resemble the ‘shake off’ and ‘knock out’ (also referred as ‘two-step-one’) in PDI respectively.

For the same technical reason as before in PDI observation, the ejected electron is not recorded in the PIE measurement. Nevertheless, in the case of single ionization, the registered recoil ion momentum balances the momentum of the ejected electron since the momenta of the absorbed VUV and visible photons are negligible in principle. Further

more, the MOTRIMS technique has a resolution of $\Delta p = 0.05$ a.u., which is comparable with the resolution of the electron momentum spectrometer.

A similar study on ‘intensity inversion between main and satellite lines in atomic photoionization’ was performed by Cubaynes *et al.*, with thermal lithium atoms, using the synchrotron radiation source BESSY [Cub07]. In this study, the simultaneous excitation and ionization by photo-absorption showed a strong dependence of cross section on the initial atomic state (nl) preparation. However, the authors did not investigate the dependence of PIE from the alignment of the initial state.

7.2.1 $(\gamma, e + e^b)$ on $\text{Li}\{L M_L S \pi\}$ at $E_\gamma = 85$ eV

Following the analyzing sequence from low photon energy to high value, at first, we look at PIE (denoted by $(\gamma, e + e^b)$ where e means the emitted electron and e^b is the excited electron which remains bound during and after the transition) at $E_\gamma = 85$ eV.

The two-dimensional momentum distributions of Li^+ projected onto a plane containing the \mathbf{E}_{FEL} and a transversal direction are shown in Fig. (7.5). Figure A is ionization from ground state lithium, and figure B and figure C are ionization of lithium from $2p$ excited state in $2p_{\parallel}$ and $2p_{\perp}$ configurations respectively.

In each individual 2D plot for single ionization, three circular shells are visible (although the outermost ring in the ionization for $2p$ states is relatively faint) and well separated, with a double lobe angular distribution aligned along the VUV polarization which is characteristic for dipole transitions from s -states. Going from large to small radii, they correspond to the final states of $|1s^2\rangle$, $|1s2l\rangle$ and $|1s nl\rangle$ ($n \geq 3$), which represent the ionization of the $2s$ or $2p$, one $1s$ electron and $1s$ ionization with simultaneous excitation of the valence electron $2s \rightarrow nl$, ($n > 2$), respectively (in the following abbreviated ionization-excitation, IE).

The bandwidth of the VUV FEL light @ $\lambda_{center} = 14.6$ nm is $\Delta\lambda = 0.2$ nm (corresponding to photon energy uncertainty ΔE about 1 eV) will lead to ± 0.03 a.u. momentum spread @ $E_{Exc} = 20$ eV (and ± 0.04 a.u. momentum spread @ $E_{Exc} = 10$ eV). Together with the MOTRIMS’s momentum resolution of 0.02 a.u., it leads to the width of the rings shown in this 2D recoil ion momentum spectrum, where the coalescence of individual ‘shake-up’ channels (also including ‘interchannel coupling’, IC, see Subsection 2.1.2) of PIE process is inevitable.

Through comparing these 2D recoil ions momentum distributions, we find that the registered total Li^+ events nearly remain the same, because the probability for the $1s$ electron to be ionized via primary photo-absorption should not depend on the nature of outer shell electrons, if their screening effect is negligible (which is the case for lithium atom). However, there is significant intensity change between main and satellite lines: the IE lobes get stronger, thus the $1s$ single-ionization lobes become weaker, as the target initial state switches from the $2s$ ground state to the $2p$ first excited state. To our surprise, no visible difference on the lines’ intensities between $2p_{\parallel}$ and $2p_{\perp}$ configurations is observed, which is different from the observation for the PDI processes. Additionally, we notice

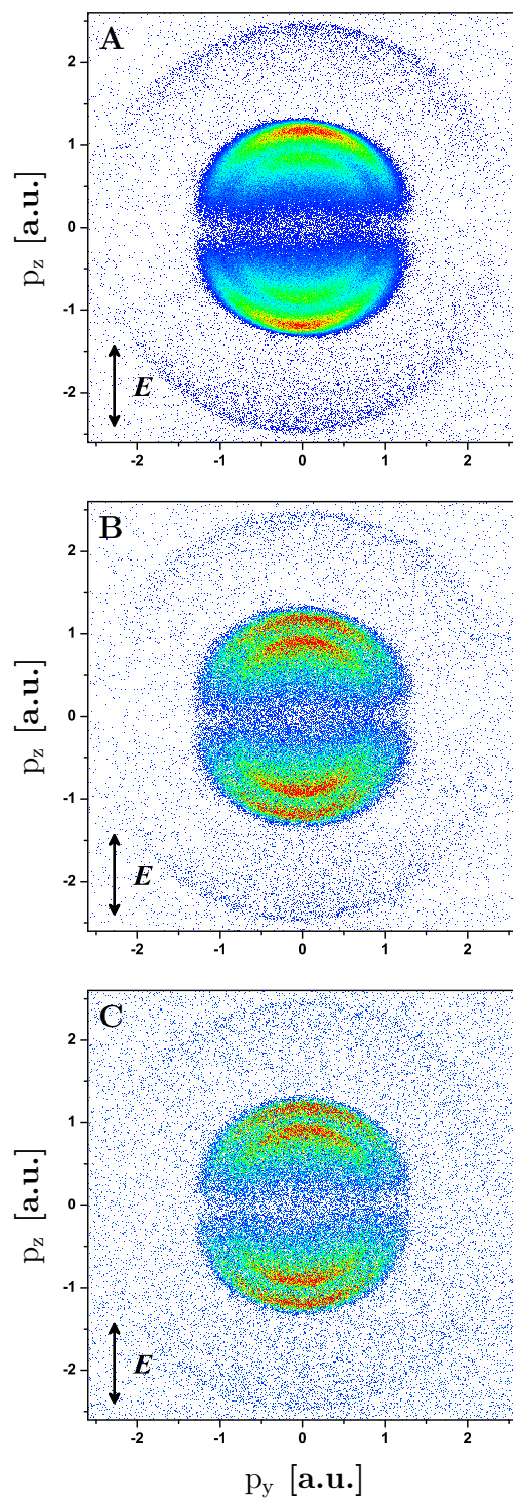


Figure 7.5: Two-dimensional plots of the recoil Li^+ momentum distribution after PIE of $\text{Li}(1s^2 2s)$ (A), $\text{Li}(1s^2 2p, \parallel)$ (B) and $\text{Li}(1s^2 2p, \perp)$ (C) at photon energy $E_\gamma = 85$ eV. The FLASH polarization is along the z -axis.

that the lobes for pure photoionization of the valence electron are reduced dramatically as the initial state changes from $2s$ to $2p$, fulfilling the predicted relation $\sigma_{2p}/\sigma_{2s} \approx 1/30$ approximately [Naj08].

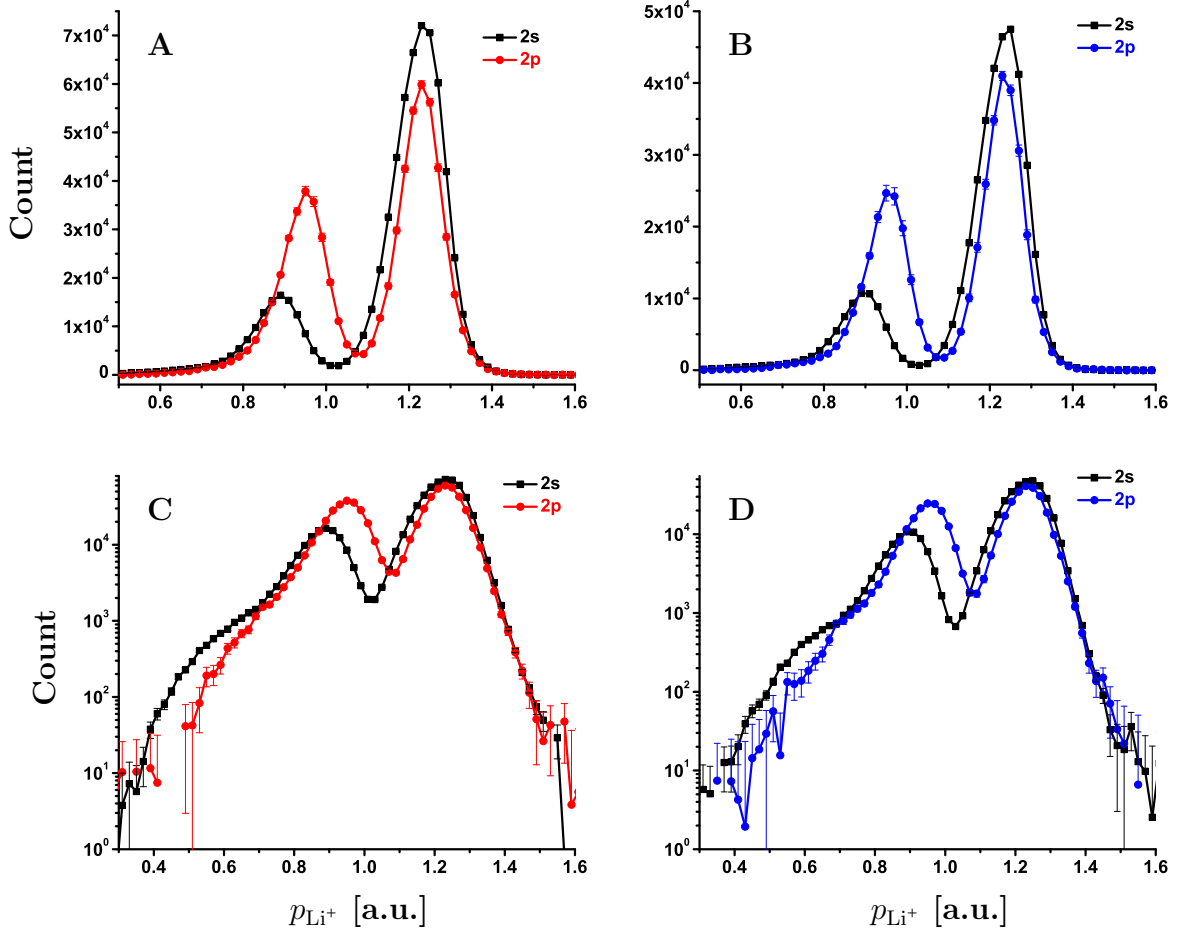
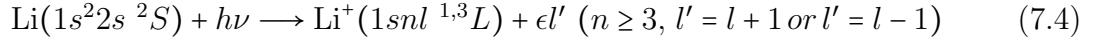


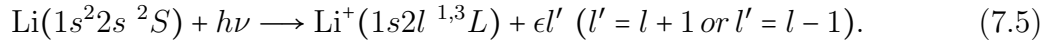
Figure 7.6: The PIE cross section for $\text{Li}(1s^2nl)$ by 85 eV photons as a function of the recoil ion momentum. Ionization result of configuration $2p_{\parallel}$ is plotted in figure A and C, which are in linear and logarithmic scale separately; while the result of configuration $2p_{\perp}$ is plotted in figure B and D. PIE from the ground state $\text{Li}(2s)$ is drawn in both cases, serving as a comparison.

With the goal to investigate the phenomenon of strong intensity change influenced by the initial atomic state quantitatively, at first, in Fig. (7.6), we plot the cross section of PIE on lithium as function of the Li^+ recoil momentum for parallel $\text{Li}(2p_{\parallel})$ (red curve, in figure A and figure C) and perpendicular $\text{Li}(2p_{\perp})$ (blue curve, in plots B and D) alignments separately. Both diagrams include a comparison to the ground state $\text{Li}(2s)$ (black curve). Again, the IE satellite, and the $1s$ -electron ionization main line (actually with the unresolved $2l$ IC satellites included) are referred by the peaks in Fig. (7.6) with rising recoil momentum p_{total} . Then, we integrate the different peaks to obtain the individual transition yields. Thus, via comparing these yields, the intensity change of main and satellite

lines can be studied. For single-ionization from the ground state $\text{Li}(2s)$, the so-defined cross section $\sigma_{n \geq 3} = \sum_{n=3}^{\infty} \sigma_n$ for all satellite lines with principal quantum number n higher than 2, corresponding to the following transitions:



is about $24.0 \pm 0.1\%$ of the cross section $\sigma_{n=2}$ for the transition, in which the principal quantum number n is not changed:



While for single-ionization from the excited state $\text{Li}(2p)$, the cross section for IE lines is enhanced significantly, leading to the branching ratio $\sigma_{n \geq 3}/\sigma_{n=2}$ increase to $71.5 \pm 1.5\%$ in $2p\parallel$ parallel alignment, and $68.4 \pm 2.4\%$ in $2p\perp$ perpendicular alignment respectively, which is about three times higher than the result for $\text{Li}(2s)$ case.

Therefore, our observation is consistent with the measurement by Cubaynes *et al.*, who concluded that the relative intensity of the satellites increases with the level of initial excitation of the Li atom. Via using a narrow bandwidth synchrotron source, their study on the $1s$ photoionization of Li by photoelectron spectroscopy could energetically discriminate between main lines and most satellites, especially the shake-up (SU) transitions $nl \longrightarrow n'l$ ($n' > n$) and interchannel coupling (IC) lines $nl \longrightarrow n'l'$ ($n' > n, l' = \pm 1$) were indentified precisely. According to the discussion in Subsection 2.1.2, the former lines can be explained in terms of the spatial overlap of the initial and final state wavefunctions for identical l , the latter transitions with changing l require an electron-electron collision in the final state as it occurs for the TS1 process. Since the initial-state alignment of their target was not determined, no conclusive result on the alignment dependence (AD) was obtained in a photon energy region between 85 and 140 eV for the excited configurations $\text{Li}^*(1s^2 np)$ ($n = 2, 3$).

In the present measurement, although the different ionic states reached for IE are not resolved, a tiny difference (though within error bars) between the $\sigma_{n \geq 3}/\sigma_{n=2}$ for different valence orbital alignment catches our eyesight, which is a weak hint on the AD effect in PIE process. On one hand this is expected, since the shake-up transitions, which have no alignment dependence, constitute at least 80% of the IE intensity at 85 eV photon energy (as displayed by Figure 4. of [Cub07]). On the other hand our observation shows that the interchannel coupling lines (given rise by the TS1 mechanism), which constitute up to 20% of the IE intensity, do not show a significant dependence on the target alignment. One possible reason is the poorly resolved transition line structure, which the coalescence of the IC satellites ($1s2s \ ^{1,3}S$) into the main lines ($1s2p \ ^{1,3}P$) conceals part of the AD effect.

Since the $2s$ photoionization contributes only marginally to the total photoionization cross section, and the $2p$ photoionization is even reduced by a factor of 27 further, the direct photoionization on valence electron is not considered within this text.

7.2.2 $(\gamma, e + e^b)$ on $\text{Li}\{L M_L S \pi\}$ at $E_\gamma = 91$ eV

The PIE of atomic Li in different initial states $\text{Li}\{L M_L S \pi\}$ is also explored at $E_\gamma = 91$ eV, where for the same final state $\text{Li}^+(1s n l \ ^1,^3L) + \epsilon l'$, the emitted electron carries a kinetic energy of 6 eV more, than for $E_\gamma = 85$ eV in Subsection 7.2.1.

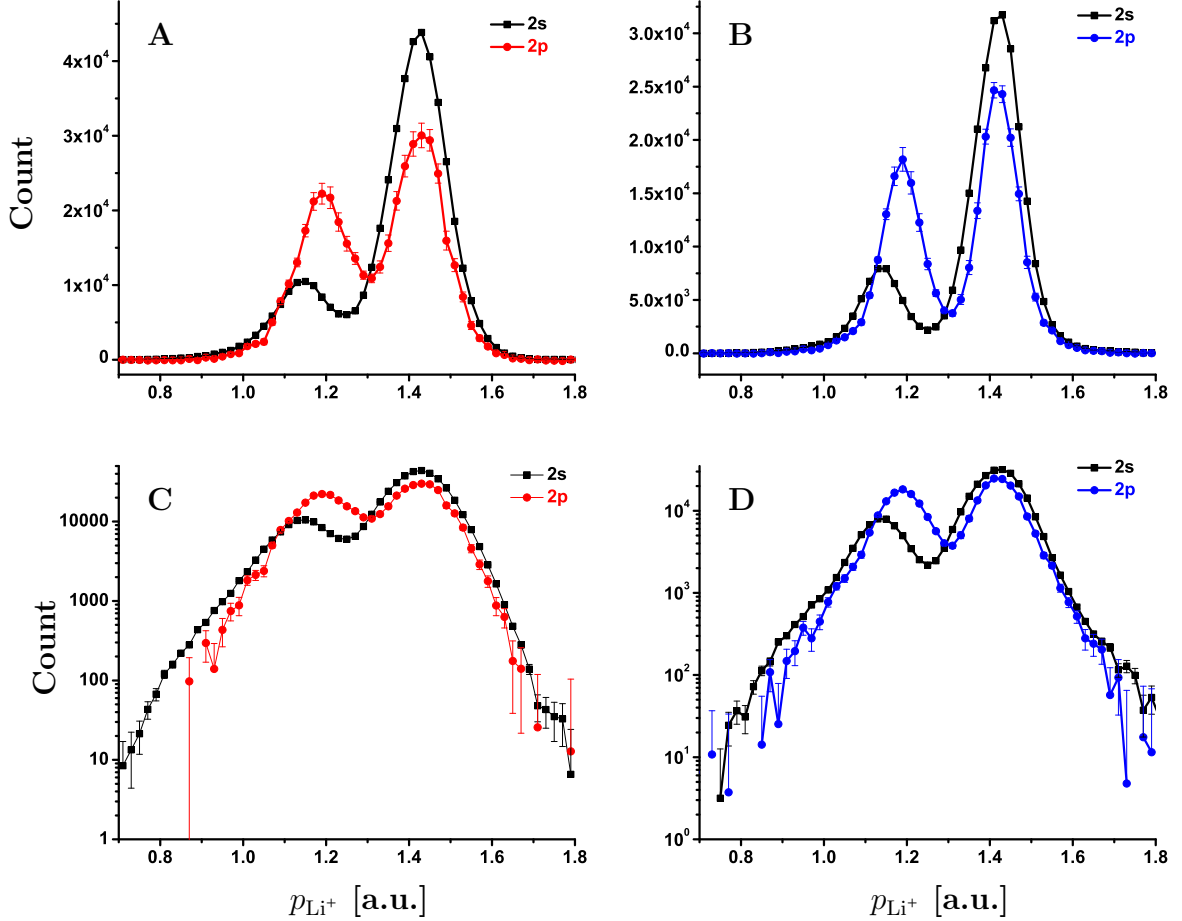


Figure 7.7: The PIE cross section for $\text{Li}(1s^2nl)$ by 91 eV photons as a function of the recoil ion momentum. Ionization result of configuration $2p_{\parallel}$ is plotted in figure A and C, which are in linear and logarithmic scale separately; while the result of configuration $2p_{\parallel}$ is plotted in figure B and D. PIE from the ground state $\text{Li}(2s)$ is drawn in both cases, serving as a comparison.

As for $E_\gamma = 85$ eV, we project the Li^+ momentum into a two-dimensional plane, containing the \mathbf{E}_{FEL} and a transversal direction shown in Fig. (7.8). The cross section of PIE on lithium is plotted as function of the Li^+ recoil momentum, for parallel $2p_{\parallel}$ and perpendicular $2p_{\perp}$ alignments compared with the ground state $2s$ (black), displayed respectively in Fig. (7.7).

The $\sigma_{n \geq 3} / \sigma_{n=2}$ ratio for photoionization from $2s$ initial state is $25.5 \pm 0.1\%$, and for pho-

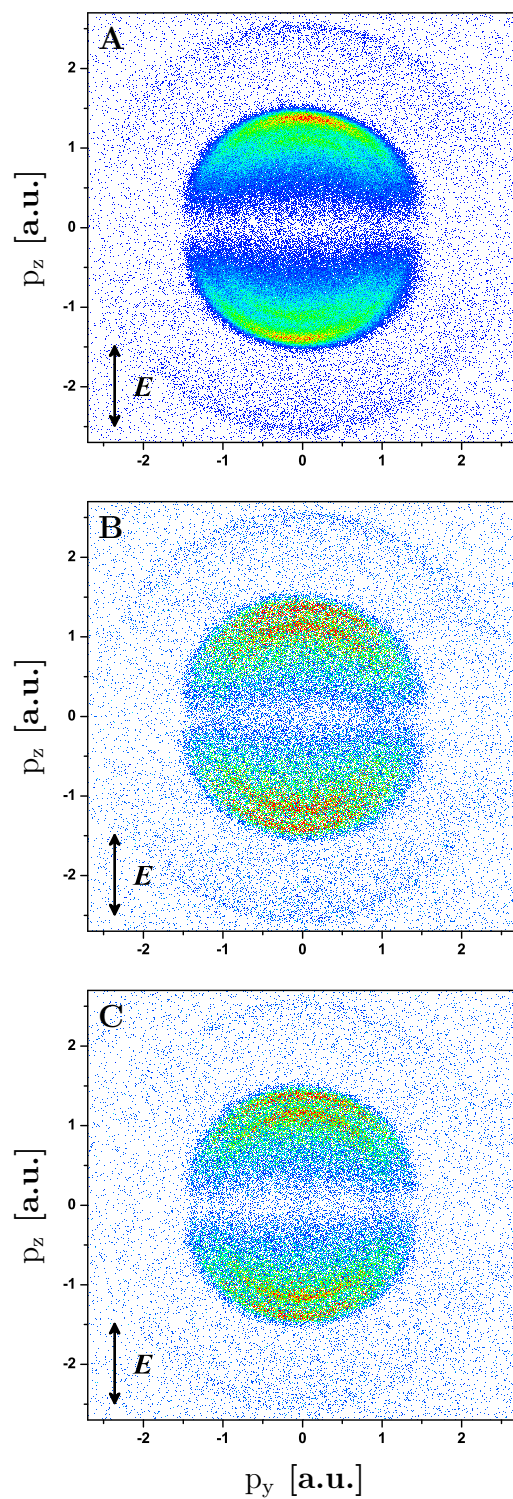


Figure 7.8: Two-dimensional plots of the recoil Li^+ momentum distribution after PIE of $\text{Li}(1s^22s)$ (A), $\text{Li}(1s^22p, \parallel)$ (B) and $\text{Li}(1s^22p, \perp)$ (C) at photon energy $E_\gamma = 91$ eV. The FLASH polarization is along the z -axis.

toionization from $2p$ initial state is $75.2 \pm 4.4\%$ for $2p_{\parallel}$ alignment configuration and $75.4 \pm 4.0\%$ for $2p_{\perp}$ alignment configuration, which are higher than the measured branching ratios for PIE at $E_{\gamma} = 91$ eV. Thus, the observations indicate an increasing intensity in the IE satellites as the photon energy goes up, which is also confirmed from both the theoretical [Zho99, Che00] and experimental sides [Cub07]⁵. Interestingly, the obtained branching ratios for the $2p$ state with different alignments are nearly identical within the statistical accuracy of $\leq 1\%$, showing a feature of convergence as the photon energy just increases by 6 eV, which imply that the alignment dependence effect already vanishes in PIE even when the photon energy is close to the threshold for PDI.

7.3 Comparison and Conclusion

In this section, we discuss our observations of photoionization on lithium atoms concerned in this chapter, via comparing the observations for PDI from different initial states $\text{Li}\{L M_L S \pi\}$ and at different photon energy, so for PIE process as well. Further more, we try extracting the mechanisms beneath the rich phenomena consisting two active electrons, which bridge all these dynamic processes and kinematic pictures. Additional, we examine our measurement with a time dependent close-coupling (TDCC) calculation by J. Colgan and M. Pindzola [Col09].

As being pointed out in Sec. 7.1, and being shown in Fig. (7.1, 7.3), interestingly, the PDI cross section for atomic Li depends on the electronic configuration ($1s2l$) and, especially demonstrates an alignment dependence effect upon the $2p$ valence electron, whose orbit (electron cloud) is not spherical symmetric with respect to the nucleus center. Additionally the PDI cross section adjusts its behaviour as the ionization excess energy changes.

Table 7.1: Experimental and theoretical total cross section ratios for double ionization from the aligned initial excited state and the initial ground state @ $E_{\gamma} = 85$ eV and 91 eV. Parallel alignments (polarizations of the optical pumping laser and the VUV-radiation) are marked by \parallel , perpendicular alignments by \perp .

Photon Energy (eV)	$\sigma_{2p_{\parallel}}/\sigma(2s)$		$\sigma_{2p_{\perp}}/\sigma(2s)$	
	Exp.	Theory	Exp.	Theory
85	1.82 ± 0.06	1.57	1.42 ± 0.06	1.22
91	1.39 ± 0.07	1.17	1.19 ± 0.05	1.90

The measured total cross section for PDI at different photon energies and from different states are collected in Tab. (7.1). The cross sections for the $2s$ initial state are taken as references and therefore the relative ratios σ_{2p}/σ_{2s} for the different spatial alignments (\parallel and \perp) are written down respectively. The calculated results by J. Colgan and M. Pindzola are listed also for comparison.

⁵These studies even extend the intensity change of main and satellite lines to the situation of ‘inversion’, *i.e.*, the shake-up process dominates for the initial excitation state of $\text{Li}(1s^2nl)$ ($n \geq 3$).

In the present experiment, with a photon energy of 85 eV the PDI cross section for $2p$ states is modified by 28.2%, just by modifying the geometry of the system without changing its internal energy. However, this difference drops to 16.8%, as the photon energy increases to 91 eV. This clearly demonstrates a strong sensitivity of the AD to the excess energy E_{exc} above threshold, which is not in favour of the TS1 mechanism to be dependent on the initial state alignment. An increase of E_{exc} from 6 eV to 11 eV results in the reduction of the AD by a factor of two, though the TS1 mechanism should be a major contribution to DI up to much higher energies [Khe01]. Furthermore, it is not clear why TS1 should be restricted to small recoil ion momentum where the AD is observed, since the momentum of the 1s-electron absorbing the primary photon is balanced by the ion in the first place and the subsequent electron-electron collision favours relative electron angles smaller than 180° .

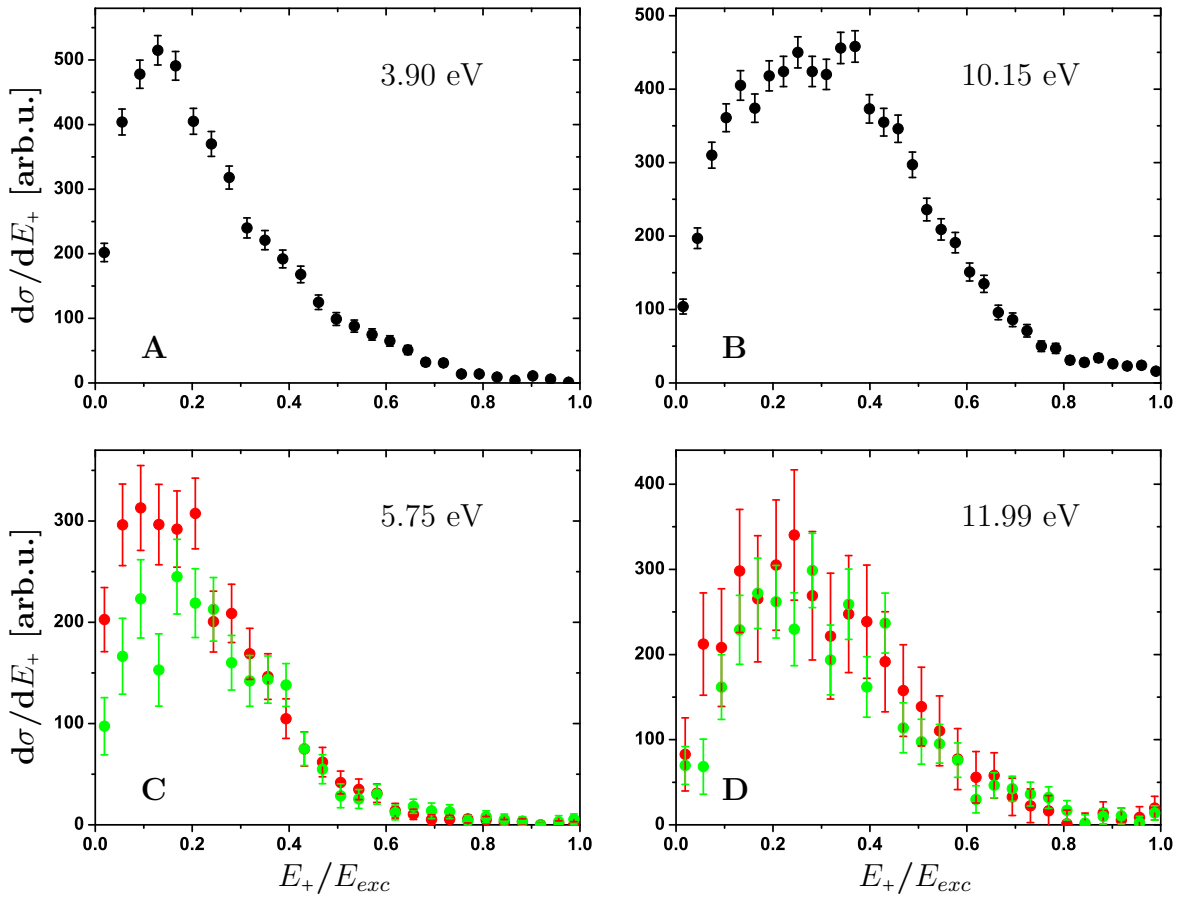


Figure 7.9: Single differential cross section $d\sigma/dE_+$ as a function of E_+/E_{exc} for PDI of Li from $2s$ (black dots in plots A and B) and $2p$ states (red dots and green dots in plots C and D are for $2p_{\parallel}$ and $2p_{\perp}$ alignment configurations respectively) at photon energies of 85 eV (left columns) and 91 eV (right columns). Where an energy conservation relation holds for $E_{Exc} = E_+ + E_-$, with $E_+ = k_+^2/4$ and $E_- = k_-^2$. The excess energies in different cases are labeled in each plot.

Inspired by the PDI studies of helium by Dörner *et al.* [Doer96b, Brae97, Kna02b], which explored the momentum configurations in Jacobi coordinates (please refer to Appendix F for a detailed description), we plot Li-PDI results in terms of the corresponding Jacobi coordinate energy, as shown in Fig. (7.9). With respect to the conventional momentum coordinates (\vec{k}_1 and \vec{k}_2 of the two electrons), the essence of the Jacobi coordinates ($\vec{k}_+ = \vec{k}_1 + \vec{k}_2$ and $\vec{k}_- = (\vec{k}_1 - \vec{k}_2)/2$) lies in the separation of the electron-pair center-of-mass (CM) motion and the electron-pair relative motion. Thus, the use of these relative coordinates, especially for PDI near threshold, reveals naturally certain simple characteristics of the strongly correlated motion of the electron pair, which is not easily seen in the \vec{k}_1, \vec{k}_2 description.

Fig. (7.9) (A) and (B) display cross sections differential in energy, for the photo double ionization from the $\text{Li}(1s^2 2s^2 S^e)$ initial state, plotted as a function of the fraction of the excess energy in the \vec{k}_+ motion, with excess energies of 3.90 eV and 10.15 eV respectively. It is apparent that, near threshold much more energy is carried in the relative motion of the two electrons than by their center of mass motion ($E_+ < E_- = E_{Exc} - E_+$), while as the excess energy increases, the energy sharing between the CM motion (E_+) and the relative motion (E_-) trends to be equal. These results are consistent with the experimental observations for He-PDI (see Figure 3. of [Doer96b]).

Next, we switch to the photo double ionization from the $\text{Li}(1s^2 2p^2 P^o)$ initial state (where different valence orbital alignments with respect to the FEL polarization, the $2p_{\parallel}$ and $2p_{\perp}$ configurations are denoted by the red and green dots), displayed in Fig. (7.9) (C) with $E_{Exc} = 5.75$ eV and (D) with $E_{Exc} = 11.99$ eV. In general, the relative partition of the excess energy between \vec{k}_+ and \vec{k}_- motions keeps the same ‘excess-energy-dependent’ trend as in PDI of He and Li in ground state. Furthermore, Fig. (7.9) (C) clearly demonstrates the alignment dependence effects: the $2p_{\parallel}$ configuration favours a ‘quiescent’ CM motion ($\vec{k}_+ = \vec{k}_1 + \vec{k}_2 \rightarrow 0$, which indicates the ‘back-to-back’ emission with equally shared kinetic energy between the two ionized electrons), while the $2p_{\perp}$ configuration prohibits such a behaviour⁶. Therefore, a significant discrepancy between two alignment configurations appears at small E_+ , though, two data sets agree well with each other at high E_+ value. As a consequence, the total cross section is much higher for $2p_{\parallel}$ configuration than for $2p_{\perp}$ configuration. However, for higher excess energy, the sensitivity of ‘alignment dependence’ decreases, as shown in Fig. (7.9) (D), where the discrepancy between two alignment configurations at small E_+ gets weak, and the difference in total cross section becomes small. These intriguing threshold dynamic/kinematic phenomena confirm the assertion that, *just above threshold the ionic motion tends to freeze out on the saddle* ($E_+ \ll E_-$) [Doer96b, Kna02b].

By checking the two-dimensional recoil Li^{2+} momentum distribution of PDI from different initial state with quantum numbers $\{L M_L S \pi\}$, shown in Fig. (7.2, 7.4), which are related with the ‘kinematic’ behaviour of emitted electrons, the underlying mechanism can be found in the threshold dynamics. According to the Wannier threshold theory, when PDI

⁶A simple explanation lies in the fact that, the momentum vector (momentum component perpendicular to the photon dipole axis) contributed by the ($2p, m_p = \pm 1$) electron in the initial state can not be annihilated during an optical-dipole-transition induced two-electron ejection. Thus, the E_+ can not be zero.

transition approaches threshold, only back-to-back emission of two electrons with equal energy is supported, resulting in vanishing sum momentum. Differences are found in the characteristic emission pattern, as well as in the total cross section, demonstrating that ‘the emitted two-electron wave function based on its symmetry $\{L M_L S \pi\}$ can exhibit nodes or antinodes at the Wannier configuration’. Thus, each final wave function can be classified as ‘unfavoured’ and ‘favoured’, respectively.

Before, such ‘favoured’ symmetries were observed only for PDI of Argon with the final state $Ar^{2+}(3s3p^5) + 2e(^1S^e, ^1D^e)$ with a dominant symmetric emission of the electron pair [Maz97]. However, in this and all other existing PDI studies on atoms, only spherically symmetric initial states were considered. In the present experiment the $2p$ -orbital is aligned along different spatial directions with respect to the VUV electric field vector \mathbf{E} allowing to investigate the M_L -substate dependence of double ionization.

It should be pointed out that, for perpendicular alignment of the $2p$ -orbital, there is a considerable momentum component transversal to the preferred emission axis of the inner shell electron along the polarization axis resulting in a finite sum momentum or centre of mass motion of the electron pair. While according to threshold theories [Ros91], this motion constitutes a stable oscillation on the Wannier potential saddle and, therefore, does not modify the Wannier threshold law, it contains energy which is not available for the radial escape of both electrons. Right at threshold the centre of mass motion of both electrons must vanish at all points of their escape trajectory. This intuitive picture represents the selection rule B1 of Maulbetsch and Briggs [Mau95] stating that states with $M_L \neq 0$ do not contribute to the cross section for emission of both electrons along (parallel or antiparallel with respect to each other) the quantization axis.

This is confirmed by the TDCC calculation of the fully differential cross section, which is presented in Appendix C. Here, for the exemplary case of equal energy sharing and one electron direction being fixed along the VUV electric field vector ($\theta_E = \theta_1 = 0^\circ$) the cross sections of the different emitted partial waves (L, M_L) are plotted as function of the second electrons’ emission angle. Both the $S(M_L = 0)$ and the $D(M_L = 0)$ cross sections show a pronounced maximum at $\theta_2 = 180^\circ$ with minor side maxima. The $D(M_L = 1)$ cross section on the other hand shows a minimum at 180° and two maxima close to 120° and 240° . While at 85 eV photon energy the $M_L = 0$ partial waves dominate at 91 eV photon energy the $D(M_L = 0)$ magnitude is strongly reduced with respect to the $D(M_L = 1)$ amplitude. For experiments with statistical population of the $M_L = 0, \pm 1$ initial state projections side lobes in addition to a strong 180° peak will appear for increasing excess energy as it has been observed by Mazeau *et al.* [Maz97] for Argon. In the present case pre-selection of the target magnetic substates allows to disentangle the individual contributions despite the fact that only the ion is detected since the symmetric electron emission configuration can be uniquely identified with vanishing recoil ion momentum $|p_{Li^{2+}}| = 0$.

The measured total cross section for PIE at different photon energies and from different states are listed in Tab. (7.2). The tremendous enhancement of the satellites (both the SU and the IC lines) is observed once the Li target initial state is switched from $2s$ to $2p$. This spectacular phenomenon can be attributed to the spatial overlap of the initial and final state wave functions [Zho99, Che00, Cub07]. Unlike in PDI, the alignment dependence is

nearly absent in the PIE process, where the observed tiny difference between $2p_{\parallel}$ and $2p_{\perp}$ configurations is within the error bars. The possible reason lies in the distinct dominated ionization mechanisms in the two different dynamic processes at present chosen photon energy: TS1 governs PDI, and SU prevails in PIE. The absence of AD in case of PIE can also be interpreted as that: since only one electron is emitted, only the short range ionization mechanisms may contribute to this process; while the long range Coulomb interaction is missing, in contrast to PDI at threshold where the dynamics is dominated by long range interaction.

Table 7.2: Branching ratios of the satellite ($n \geq 3$) and main line ($n = 2$) intensities for PIE from different initial states $2s$, $2p_{\parallel}$ and $2p_{\perp}$, measured @ $E_{\gamma} = 85$ eV and 91 eV.

Initial state	$2s$	$2p_{\parallel}$	$2p_{\perp}$
85 eV	$24.0 \pm 0.1\%$	$71.5 \pm 1.5\%$	$68.4 \pm 2.4\%$
91 eV	$25.5 \pm 0.1\%$	$75.2 \pm 4.4\%$	$75.4 \pm 4.0\%$

In summary, a new means to modify the dynamic electron correlation leading to double photoionization is demonstrated by laser preparing the target atoms in an excited state and with different spatial alignment. The observed alignment dependence was traced back to be result of long range correlation between the Coulomb interacting particles which dominates the dynamics close to threshold. The modifications of the recoil ion momentum distributions and the ratios of the total cross sections are consistent with results from time dependent close coupling calculations.

While in the present experiment the cross section could be modified by 34% for 6 eV excess energy a much higher contrast can be expected closer to threshold and with higher population of the $M = \pm 1$ magnetic substates as it can be reached by means of optical pumping with circularly polarized light. Thus, as result of a purely geometrical modification of the target initial state the dynamical electron correlation can be changed such that PDI is either enabled or largely suppressed.

In future the increased photon flux of the free electron laser FLASH as compared to 3rd generation synchrotrons in combination with the MOT reaction microscope will make kinematically complete studies of triple photoionization of lithium possible. Thus, one of the simplest four-body Coulomb break-up reactions will become accessible despite its small cross section in the order of a few 10^{-24} cm².

Chapter 8

Summary and Outlook

The present work is dedicated to study photo-fragmentation of lithium atoms by the advanced light facility of FLASH with the concept apparatus of MOTReMi. The study of the interested PDI threshold phenomena is benefited by the novel VUV photon machine (FEL as the 4th generation photon source), due to its unparalleled intensity/flux and the supreme temporal structure. The experimental realization is enabled by the unique platform of MOTReMi setup, which combines two state-of-the-art experimental techniques of contemporary atomic physics for the first time: the magneto-optical trap (MOT) as a modern target cooling and trapping method and the reaction microscope (ReMi) as a multi-particle imaging technology. Termed as the ‘bubble chamber of atomic and molecular physics’, ReMi is capable of measuring the full vector momenta of all charged fragments emerging from an ionization reaction in coincidence. With respect to the conventional ‘supersonic jet’, MOT, as an innovative target producer, creates a much colder target ‘in a real sense’ (quasi-stationary in a three-dimensional momentum space), therefore, it exploits the possible momentum resolution of the reaction microscope; furthermore, it provides target manipulation options, *e.g.*, optical-excitation, alignment and orientation.

In commissioning such a complex and novel apparatus, many experimental challenges have been overcome and several technical innovations have been applied to fight for a robust and versatile experimental platform, *e.g.*, the MOT fields are running in a switching mode to bypass the field incompatibility between the electron spectrometer’s requirement (homogeneity) and the MOT operation condition (strong gradient); the assembled recoil ion spectrometer with the 3D-focusing configuration option guarantees the fine resolution of ion momentum in all dimensions (longitudinally and transversally); a semiconductor laser device based optical system is selected for laser cooling and optical pumping, the technique of dual-frequency MOPA lies in the kernel of scheme. After numerous endeavors, a cold target ensemble at a minimum temperature of $400\ \mu\text{K}$ and with a peak density of $10^{10}/\text{cm}^3$ has been obtained within the MOT segment; together with the special designed the spectrometers, the finest momentum resolution ever about 0.05 a.u. has been achieved for the RIMS method.

In the year 2008, a campaign experiment for photo double ionization (PDI) was performed at the FLASH facility, DESY, which is the main course of this dissertation. Stressing on

probing the PDI threshold dynamics purely mediated by electron correlation, a sophisticated experiment method was designed and implemented. The trapped lithium target was carefully prepared in the $\text{Li}(1s^2 2s^2 S^e)$ ground state and the $\text{Li}^*(1s^2 2s^2 P^o)$ laser-excited state, in addition, the $2p$ valence orbit was spatially aligned parallel or perpendicular with respect to the linearly polarized VUV-electric field vector. By comparing the recorded recoil Li^{2+} ions from different initial states $\text{Li}\{L M_L S \pi\}$, the influence of this alignment or more specifically the initial state magnetic sublevel population on the PDI dynamics is revealed.

As shown, at the photon energy of $E_\gamma = 85 \text{ eV}$, the marked differences in the PDI yields and the recoil Li^{2+} momentum distributions (which reflect the characteristic two-electron emission patterns) for different initial states substantiate the PDI dynamic and kinematics mechanisms, determined by Wannier threshold law in a symmetry-favoured/unfavoured manner. More compelling this alignment sensitivity decreases strongly as the photon excess energy increases from 6 to 12 eV ($E_\gamma = 91 \text{ eV}$). Thus, this effect is not enforced by symmetry, but rather by a subtle dynamical correlation which is more effective closer to the double ionization threshold. Further more, these assertions are supported by time-dependent close-coupling calculations (TDCC) of the fully differential cross section, which are coded for computing the Li DPI after ‘freezing’ one of the 1s electrons.

In addition, the photoionization plus simultaneous excitation (PIE) processes of Li in different initial atomic states and by different photo energies were also observed. A cross section enhancement for IE channels was demonstrated, significantly increased by a factor of three as the initial state was switched from the $\text{Li}(2s)$ to $\text{Li}(2p)$. While in the present measurement the different residual ionic states for IE are not resolved the total IE cross section does not show any dependence on the alignment of the initial valence orbital within the statistical accuracy of 1%.

Though the accomplished MOTReMi setup has exhibited incomparable advantages and stable performance in the photo-fragmentation experiments carried out by far, it is a bit far from the consummate status still, leaving the room for technique improvements and scheme updates. Presently, the atom trapping scheme is being upgraded by implementing a dipole trap, a pure optical trap other than the hybrid MOT: the MOT method serves as the pre-cool stage, once a large number of atom at a reasonable low temperature are accumulated, they will be transported to a passive trap — dipole trap; then the MOT magnetic field is switched off, due to the ‘magnetic-field-independent’ feature of the dipole trap; the dipole trap acts as the experimental stage, where completely ‘field-free’ conditions are satisfied for high resolution coincident ion and electron momentum spectroscopy. Therefore, the MOTReMi can be operated in a semi-continuous mode instead of the fast-switching mode, increasing the efficiency of data acquisition and benefiting the measurement of electron momenta. Additionally, a transversal Doppler-cooling section (2D-MOT) is also proposed to be installed at the exit of the atomic beam source, enhancing the flux of slow atoms towards the MOT-region, thus, the trap loading rate can be boosted by a factor of hundred, which results in reducing the dead-time and speeding the experimental cycles up. Concerning the reaction microscope side, more modifications need to be executed in parallel, e.g., the refinements of the spectrometer electrodes can eliminate the lensing effect at RIMS which distorts the sensitive ion trajectory; the

amendments of the mechanical arrangement inside the housing chamber can reduce the photoelectrons generated by the stray light (of the projectile beams), and the induced secondary electrons as well, therefore, the background of the electron spectrum can be dramatically suppressed.

With respect to future perspectives, the advanced concept of MOTReMi opens a big field of further studies. The coming task will be the kinematically complete study of Li PDI, which requires the detection of the ejected electrons in coincidence with the recoiling target ion. In the near future, with the FLASH parameters being upgraded, the chased fully differential photo triple ionization (PTI) experiment can be performed, as the milestone for four-body time-dependent quantum studies. It will also supply a substantial proof for the surprising theoretical results by Emmanouilidou *et al.*, which predicts a nonsymmetric, T-shaped final configuration of the emerging electrons at threshold due to specific properties of the Li ground state [Emm08]. Beside the single-photon-induced multiple ionization and/or excitation of atoms, the combination of MOTReMi apparatus and FLASH facility also enables the ‘few-photon multiple ionization’¹ measurement in the VUV regime, which is of paramount scientific as well as practical importance for most experiments at FELs [Mos07, Rud08]. The proposed differential experiments on lithium target in this summer are under preparation, timely and urgently providing benchmark data to solve the puzzle — ‘How do two or three photons interact with three electrons in different shells?’. In addition, by implementing the electron gun as the projectile source, MOTReMi will also pave the way to a large number of unprecedented electron impact experiments, which probe the many-body Coulomb question in the $(e, 2e)$, $(e, 3e)$ methods.

As a versatile scientific machine, MOTReMi is not only limited in collision/fragmentation studies. It can be used as a generalized probe of AMO (atomic, molecular and optical physics) processes though the population dynamics analysis [Bre03], *e.g.*, MOT dynamics [Sha07], stimulated Raman adiabatic passage (STIRAP) process [Gea07], photo-association reaction [Tra07], efficient Rydberg atom formation [Kil01], and the creation and dynamics study of an ultra-cold neutral plasma as well [Kil99, Poh04, Kil07].

¹The interaction of two or three photons with two or more electrons, bridges the gap between the single- and multi-photon regimes.

Appendix A

Atomic Units

Quantity	Formula	SI units
Mass	m_e	$9.10938 \cdot 10^{-31}$ kg
Charge	e	$1.60218 \cdot 10^{-19}$ C
Length	a_0	$5.29177 \cdot 10^{-11}$ m
Velocity	v_0	$2.18769 \cdot 10^6$ m s ⁻¹
Time	a_0/v_0	$2.41888 \cdot 10^{-17}$ s
Momentum	$m_e v_0$	$1.99285 \cdot 10^{-24}$ kg m s ⁻¹
Angular momentum	$\hbar = a_0 m_e v_0$	$1.05457 \cdot 10^{-34}$ kg m ² s ⁻¹
Frequency	$v_0/(2\pi a_0)$	$6.57969 \cdot 10^{15}$ Hz
Angular frequency	v_0/a_0	$4.13414 \cdot 10^{16}$ s ⁻¹
Energy	$e^2/(4\pi\epsilon_0 a_0^2)$	27.2116 eV
Electric field	$e/(4\pi\epsilon_0 a_0^2)$	$5.14221 \cdot 10^{11}$ V m ⁻¹
Magnetic field	$\hbar/(e a_0^2)$	$2.35052 \cdot 10^5$ T
Intensity	$1/2 c \epsilon_0 (e/(4\pi\epsilon_0 a_0^2))^2$	$3.50953 \cdot 10^{16}$ W cm ⁻²

Quantity	Formula	SI units	Atomic units
Electron mass	m_e	$9.10938 \cdot 10^{-31}$ kg	1
Elementary charge	e	$1.60218 \cdot 10^{-19}$ C	1
Planck constant	\hbar	$1.05457 \cdot 10^{-34}$ kg m ² s ⁻¹	1
Proton mass	m_p	$1.67262 \cdot 10^{-27}$ kg	1836.15
Atomic mass unit	$\text{amu} = \frac{1}{12} m(^{12}\text{C})$	$1.66054 \cdot 10^{-27}$ kg	1822.89
Velocity of light	c	$2.99792 \cdot 10^8$ m s ⁻¹	137.04
Influence constant	ϵ_0	$8.85419 \cdot 10^{-12}$ A s V ⁻¹ m ⁻¹	$1/(4\pi)$
Induction constant	$\mu_0 = 1/(c^2 \epsilon_0)$	$e\pi \cdot 10^{-7}$ V s A ⁻¹ m ⁻¹	$4\pi/137.04^2$

Appendix B

Polarization Gradient Cooling Method

From the introduction in Sec. 3.1, we know that the reasonable cooling temperature is determined by the atomic property, within the concept of Doppler limit T_{Dopp} . However, a lower temperature could be achieved via implementing a different laser cooling mechanism — polarization gradient cooling [Dal89].

As illustrated in Fig. (B.1) (A), two circularly-polarized, counter-propagating laser beams serve as the cooling light, which their polarizations are opposite circularized along the Z-axis, in deed the helicities are the same, with respect to the k -vector (also referred as wave vector, indicating the light propagation direction). With such a configuration, a specific polarization is created, which is linear (polarized) and forms a helix with a period of $\lambda/2$ (λ is the wavelength). The laser intensity superposed keeps constantly. The energy levels of a multi level atom in this laser field will experience an energy shift, the so called light shift [Met99, Gri00], also noted as the AC-Stark shift,

$$\Delta \propto \frac{\Omega^2}{\delta}, \quad \Omega^2 = \frac{\Gamma^2}{2} \frac{I}{I_S} \quad (\text{B.1})$$

where δ is the laser detuning and Ω is the Rabi frequency. The populations in the ground level will depend on the Clebsh-Gordan coefficients. Take a transition $J = 1 \rightarrow J = 2$ for example: the π transition from the ground state $|g_0\rangle$ to the excited levels is 4/3 stronger than transitions from $|g_{\pm 1}\rangle$ to the excited levels, thus the light shifts are smaller for the $|g_{\pm 1}\rangle$ ground states than for the $|g_0\rangle$ state. Furthermore the transitions $|g_{\pm 1}\rangle \rightarrow |g_0\rangle$ is stronger than its inverse process transitions $|g_0\rangle \rightarrow |g_{\pm 1}\rangle$, i.e., a larger population would accumulated in the state of $|g_0\rangle$, which is shown in Fig. (B.1) (B). It should be noted that the above considerations are made for atoms at rest. However, as an atom travels in Z direction with a velocity $v > 0$, it will see a linear polarization, which rotates around the beam axis.

Via borrowing a novel rotating frame (where the linear polarization points always in the same direction) other than the normal atomic rest frame, a fictitious field will appear (Larmor's theorem), which looks like a magnetic field parallel to the Z axis. Different

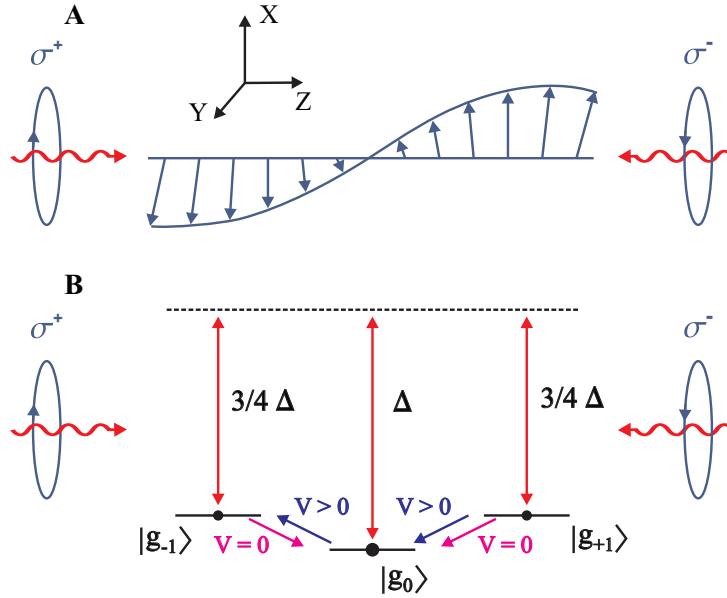


Figure B.1: A: Schematic of polarization gradient cooling, two counter-propagating laser beams with opposite circular polarization, forming a rotating linear polarization with a helix period of $\lambda/2$. In fact, such a polarization configuration is identical to a MOT beam arrangement. B: The situation of the shifted light levels. Due to the different Clebsch-Gordan coefficients, the $|g_0\rangle$ state is shifted further and populated more, compared with $|g_{\pm 1}\rangle$ states.

from the steady case, discussed above, we get a motion induced spin orientation in the atomic ground state, which means that we do not find the steady state population but we find more atoms in the $|g_{-1}\rangle$ state than in the $|g_{+1}\rangle$ state (for $v > 0$ and < 0). This unbalance in population will result in an unbalance of the radiation pressure of the σ^+ and σ^- light, thus the atom will absorb more counter-propagating σ^- photons than co-propagating σ^+ photons, which in turn slowed down the atom. As a result, the motion induced orientation of the atoms is reduced, so is the unbalanced population, and the damping gets smaller with reduced velocity.

The resulting force can be expressed as

$$\langle F \rangle \propto \hbar k^2 \frac{-\delta \Gamma}{5\Gamma^2 + 4\delta^2} \quad (\text{B.2})$$

Following the same argumentations for Doppler limit derivation in Sec. 3.1, a different minimum temperature is obtained again:

$$k_B T = \frac{\hbar \Omega^2}{|\delta|} \left[\frac{29}{300} + \frac{254}{75} \frac{\Gamma^2/4}{\delta^2 + \Gamma^2/4} \right] \quad (\text{B.3})$$

As we see, the temperature now depends on the laser detuning δ and on the Rabi frequency $\Omega = \Gamma \sqrt{I/2I_0}$, and therefore on the intensity of the laser. Both parameters can be experimentally tuned, which means, that with this method we are able to cool further

than the Doppler cooling limit. This cooling technique works well for small velocities, meaning that the $\Gamma' \ll \Gamma$, where Γ' is the mean scattering rate.

For the polarization gradient cooling exists also a limit, which is the so called recoil limit (that is the energy a single photon can transfer to the atom).

For completeness it should be mentioned, that a configuration consisting of two linear polarized laser beams (the polarizations are perpendicular to each other) can also be used.

Appendix C

TDCS Calculation for Li DPI Based on Parity

To assist the experimental studies of Li PDI @ FLASH, the triple differential cross sections (TDCS) for Li PDI from even parity state $\text{Li}(2s^2S^e)$ and odd parity state $\text{Li}(2p^2P^o)$ for photon energies of 85 eV and 91 eV were calculated by J. Colgan. A two-electron time-dependent close-coupling (TDCC) method was employed for these computations, where one of the $1s$ electrons were frozen for a quick but efficient examination (the final-state $1s$ electron does not have enough energy to be excited)¹. Singlet and triplet contributions from the coupling of the outgoing electron pair are included after appropriate recoupling.

C.1 Even parity state - $\text{Li}(1s^22s^2S^e)$

First, TDCS computations were performed for double ionization of lithium in the even parity state $\text{Li}(2s^2S^e)$. The two electron code does include some correlation effects between the two active electrons and the frozen $1s$ electron using a parameterized exchange potential. The two outgoing ionized electrons are fully correlated using 9 l_1, l_2 pairs to compute the initial ground state for $\text{Li}(1s^22s^2S^e)$ and 18 l_1, l_2 pair combinations to converge the final-state. Fig. C.1 (top two panels) shows the TDCS for equal energy sharing $E_1 = E_2$ at fixed $\theta_1 = 0^\circ$ (which is along the direction of VUV photon polarization) and θ_2 ranging from 0° to 360° , for Li PDI from even parity state at photon energies of 85 eV (left) and 91 eV (right) respectively. This choice to present only equal energy sharing was made to highlight the TDCS of interest, however, any energy sharing combinations can be calculated to suit the investigation needs. The TDCS shown in Fig. C.1 (top two panels) have similar structure to those found in He PDI from an excited initial state $\text{He}(1s2s^1S^e)$ [Col03].

¹Future calculations can include the correlation effects between all three electrons using a three electron TDCC code.

C.2 Odd parity state - Li($1s^22p\ ^2P^o$)

Double ionization of lithium from the odd parity state Li($2p^2P^o$) is rather complex. As depicted in Eq.7.1, the final state differs depending on the magnetic sublevel M_L of the initial state: PDI from Li($1s^22p\ ^2P^o, M_P = 0$) consist of both S and D ($M_{S,D} = 0$) components, while PDI from Li($1s^22p\ ^2P^o, M_P = \pm 1$) only allows D ($M_D = \pm 1$) waves. The number of l_1, l_2 channels needed to converge both the initial and final-states are larger than the even parity calculations. The initial odd parity state requires 24 l_1, l_2 pairs while the S final-state needed 8 l_1, l_2 pairs and the D final-state requires 34 l_1, l_2 pair combinations. Fig. C.1 (bottom two panels) shows the TDCS for equal energy sharing $E_1 = E_2$ at fixed $\theta_1 = 0^\circ$ and θ_2 ranging from 0° to 360° , for Li PDI from odd parity state at photon energies of 85 eV (left) and 91 eV (right) respectively. There are three calculations: black line for S partial wave, red line for D ($M = 0$) and blue line for D ($M = \pm 1$). Apparently, it demonstrates the two electrons emission pattern of double ionization from the $2p$ state: if the magnetic number of the initial state $M = 0$, the dominant emission is back-to-back, for ionization to either the S or D final states ²; if the magnetic number of the initial state $M = \pm 1$, back-to-back emission is forbidden and the distribution displays 2 nodes; at around 120° and 240° (rather like He, [Col03]). For $M = 0$, allowing the dominant back-to-back emission also results in a much larger cross section than for $M = \pm 1$ or from the ground state. These trends are found for both photon energies, which have similar behaviors, though, the transition amplitude for individual partial wave in the final state varies, which is expected as the result of the threshold dynamic effect.

²Note also that, for the $M = 0$ case, the contributions of S and D partial waves should be added coherently, which still gives the same dominant back-to-back emission.

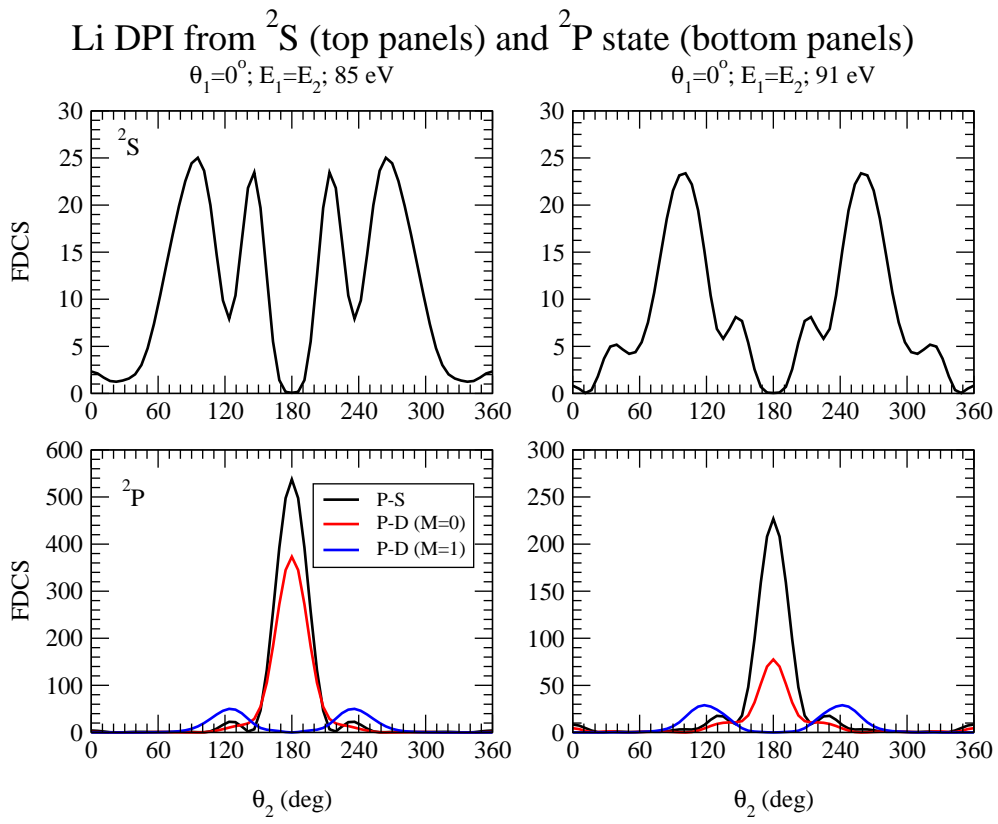


Figure C.1: Test Testing

Appendix D

C++ Code Segments in Data Analysis Program Agat32root

D.1 Agat32root Code for Cartesian Coordinate Transformation:

```
double Xraw(long index) {return pe → Xraw(index);}
double Yraw(long index) {return pe → Yraw(index);}

double XCorraw(long index) {return pe → Xraw(index)-xcorraw;} // translation
double YCorraw(long index) {return pe → Yraw(index)-ycorraw;} //

double XCorRotraw(long index) {return (cos(angle)*XCorraw(index)
                                     +sin(angle)* YCorraw(index));} // rotation
double YCorRotraw(long index) {return (-sin(angle)*XCorraw(index)
                                     +cos(angle)* YCorraw(index));} //

double Xmm(long index) {return XCorRotraw(index)*sfx;} // rescaling
double Ymm(long index) {return YCorRotraw(index)*sfy;}
```

D.2 Agat32root Code for ToF /position Signal Correction:

```
double CoX1; // CoX,CoY families are for Position-dependent ToF correction TofCns(index)
double CoX2; //
double CoY1; //
double CoY2; //
```

```
double CoXt0; // CoXt,CoYt families are for ToF-dependent Position correction XRmm(Index),
YRmm(Index)
double CoXt1; //
double CoXt2; //
double CoYt0; //
double CoYt1; //
double CoYt2; //

//Position-dependent ToF Correction
double MyParticle::TofRns(long index)
{
double tofR = pe → Tofns(index)-t0;
if ( (tofR > -800.) 'and' (tofR < 800.) )
return (tofR + CoX1*Xmm(index)+ CoX2*Xmm(index)*Xmm(index)+ CoY1*Ymm(index)+
CoY2*Ymm(index)*Ymm(index));
else
return tofR;
}

//ToF-dependent Position Correction
double MyParticle::XRmm(long index)
{
double xR = Xmm(index);
if( (xR > -40.) 'and' (xR < 40.) )
return (xR+CoXt0+CoXt1*TofRns(index)+CoXt2*TofRns(index)*TofRns(index));
else
return xR;
}

double MyParticle::YRmm(long index)
{
double yR = Ymm(index);
if( (yR > -40.) 'and' (yR < 40.) )
return(yR+CoYt0+CoYt1*TofRns(index)+CoYt2*TofRns(index)*TofRns(index));
else
return yR;
}
```

Appendix E

Rotations and Wigner D-Functions

E.1 Rotation Operator and Euler Angles

We use the right-handed coordinate system. An arbitrary rotation ω of the system of coordinates $S \{x, y, z\} \xrightarrow{\omega} S' \{x', y', z'\}$ can be executed by three successive rotations:

1. Rotation through the angle φ around the z -axis ($0 \leq \varphi \leq 2\pi$)
2. Rotation through the angle ϑ around the new y -axis ($0 \leq \vartheta \leq \pi$)
3. Rotation through the angle ψ around the new z -axis ($0 \leq \psi \leq 2\pi$)

Thus, a rotation operator can be written as

$$\mathcal{R}(\varphi, \vartheta, \psi) = \exp[-i\varphi J_z] \cdot \exp[-i\vartheta J_y] \cdot \exp[-i\psi J_z] \quad (\text{E.1})$$

where φ , ϑ and ψ are called the *Euler angles* (characterized by the keywords: z-y-z convention, right-handed frame, right-handed screw rule, active interpretation).

E.2 Definition of D-Function

Let $|jm\rangle$ be a state vector of a physical system with fixed angular momentum j and its projection m on the z -axis of the coordinate system S . Let $|\widetilde{j\widetilde{m}}\rangle$ be another state vector (of the same physical system) that is characterized by the same j and the same projection m , but on the z -axis of another (rotated) coordinate system S' . Operator $\mathcal{R}(\varphi, \vartheta, \psi)$ transforms the state vector $|jm\rangle$ into the state vector $|\widetilde{j\widetilde{m}}\rangle$:

$$|\widetilde{j\widetilde{m}}\rangle = \mathcal{R}(\varphi, \vartheta, \psi) |jm\rangle \quad (\text{E.2})$$

The *Euler angles* φ , ϑ and ψ characterize the rotation $S \xrightarrow{\omega} S'$. Then the state vector $|\widetilde{j\widetilde{m}}\rangle$ is expanded in terms of the state vectors $|jm\rangle$ ($m = -j, \dots, +j$) as follows:

$$|\widetilde{jm}\rangle = \sum_{m'} D_{m'm}^j(\varphi, \vartheta, \psi) |jm'\rangle \quad (\text{E.3})$$

where $D_{m'm}^j(\varphi, \vartheta, \psi)$ is the so-called *Wigner D-Functions*. It is defined as the matrix element of the rotation operator in the representation of the state vectors $|jm\rangle$:

$$\begin{aligned} D_{m'm}^j(\varphi, \vartheta, \psi) &\equiv \langle jm' | \mathcal{R}(\varphi, \vartheta, \psi) | jm \rangle \\ &= \exp[-im'\varphi] d_{m'm}^j(\vartheta) \exp[-im\psi] \end{aligned} \quad (\text{E.4})$$

The general element $d_{m'm}^j(\vartheta)$ is known as *Wigner d-matrix element*, which can be expressed in terms of polynomials in $\cos(\vartheta/2)$ and $\sin(\vartheta/2)$ (see examples in Tab. (E.1) as below).

 Table E.1: Functions $d_{m'm}^j(\vartheta)$

$d_{m'm}^{1/2}(\vartheta)$			
m →			
m'	1/2	-1/2	
↓			
1/2	$\cos \frac{\vartheta}{2}$	$-\sin \frac{\vartheta}{2}$	
-1/2	$\sin \frac{\vartheta}{2}$	$\cos \frac{\vartheta}{2}$	

$d_{m'm}^1(\vartheta)$			
m →			
m'	1	0	-1
↓			
1	$\frac{1}{2}(1 + \cos \vartheta)$	$-\frac{1}{\sqrt{2}} \sin \vartheta$	$\frac{1}{2}(1 - \cos \vartheta)$
0	$\frac{1}{\sqrt{2}} \sin \vartheta$	$\cos \vartheta$	$-\frac{1}{\sqrt{2}} \sin \vartheta$
-1	$\frac{1}{2}(1 - \cos \vartheta)$	$\frac{1}{\sqrt{2}} \sin \vartheta$	$\frac{1}{2}(1 + \cos \vartheta)$

$d_{m'm}^{3/2}(\vartheta)$				
m →				
m'	3/2	1/2	-1/2	-3/2
↓				
3/2	$\cos^3 \frac{\vartheta}{2}$	$-\sqrt{3} \sin \frac{\vartheta}{2} \cos^2 \frac{\vartheta}{2}$	$\sqrt{3} \sin^2 \frac{\vartheta}{2} \cos \frac{\vartheta}{2}$	$-\sin^3 \frac{\vartheta}{2}$
1/2	$\sqrt{3} \sin \frac{\vartheta}{2} \cos^2 \frac{\vartheta}{2}$	$\cos \frac{\vartheta}{2} (3 \cos^2 \frac{\vartheta}{2} - 2)$	$\sin \frac{\vartheta}{2} (3 \sin^2 \frac{\vartheta}{2} - 2)$	$\sqrt{3} \sin^2 \frac{\vartheta}{2} \cos \frac{\vartheta}{2}$
-1/2	$\sqrt{3} \sin^2 \frac{\vartheta}{2} \cos \frac{\vartheta}{2}$	$-\sin \frac{\vartheta}{2} (3 \sin^2 \frac{\vartheta}{2} - 2)$	$\cos \frac{\vartheta}{2} (3 \cos^2 \frac{\vartheta}{2} - 2)$	$-\sqrt{3} \sin \frac{\vartheta}{2} \cos^2 \frac{\vartheta}{2}$
-3/2	$\sin^3 \frac{\vartheta}{2}$	$\sqrt{3} \sin^2 \frac{\vartheta}{2} \cos \frac{\vartheta}{2}$	$\sqrt{3} \sin \frac{\vartheta}{2} \cos^2 \frac{\vartheta}{2}$	$\cos^3 \frac{\vartheta}{2}$

Appendix F

Single-Particle Coordinates and Jacobi Coordinates

To describe the momentum configurations of PDI fragments, two coordinate sets are widely used in the literature: (i) single-particle coordinates, which are spanned by the electron momenta $\vec{k}_{1,2}$ relative to the centre of mass of respective particles, with the excess energy given by $E_{Exc} = E_1 + E_2$ and $E_{1,2} = k_{1,2}^2/2$; (ii) Jacobi coordinates, which are spanned by the Jacobi momenta $\vec{k}_{+,-}$, where $\vec{k}_+ = \vec{k}_1 + \vec{k}_2$ is the momentum of the recoil ion, while $\vec{k}_- = (\vec{k}_1 + \vec{k}_2)/2$ is relative momentum of the electrons. Now, the excess energy shared in the corresponding energies reads as $E_{Exc} = E_+ + E_-$ with $E_+ = k_+^2/4$ and $E_- = k_-^2$. Atomic units are used throughout.

The two coordinate systems suggest two different perspectives on the double-ionization process: single-electron coordinates describe the escape of each electron from the nuclear potential. Therefore they would be most appropriate if the coupling between the electrons can be treated as perturbation while their motion is mainly governed by the nuclear field and the photon. This can be expected for example at very high photon energies, where one expects one electron to absorb the majority of the photon energy and angular momentum while the second electron is emitted with little energy either via a shake-off or is knocked out in a binary collision by the fast electron [Ten94, Kna02a]. In contrast, Jacobi coordinates are better suited to describe the motion of the ion (\vec{k}_+) in the potential of the electron pair and the breakup of the two electrons (\vec{k}_-). This is most useful if the saddle region of the potential surface governs the final state of the reaction, which is expected close to threshold [Wan53].

Appendix G

Deutsche Kurzfassung der Dissertation: Untersuchungen zur Photodoppelionisation von Lithium mit MOTRIMS

G.1 Einleitung

Das Verständnis der zeitlichen Entwicklung von korrelierten viel-Elektronen-Systemen und die Erarbeitung möglicher Verfahren zur Kontrolle ihrer Dynamik, gehören zu den großen Herausforderungen in der gegenwärtigen physikalischen Forschung. In der Atomphysik sind sehr fundamentale Mehrteilchensysteme z.B. als Aufbruchreaktionen von einfachen Atomen oder Molekülen realisierbar wobei die Zahl der beteiligten Teilchen festliegt und ihre Wechselwirkung exakt bekannt ist. Hochdifferentielle experimentelle Daten zu solchen Reaktionen sind für den kritischen Test von neu entwickelten Rechenverfahren zur Beschreibung von zeitabhängigen Mehrteilchen-Quantensystemen von großer Bedeutung. Besonders faszinierend und von grundsätzlichem Interesse ist das Verhalten solcher Systeme in extremen Situationen wie zum Beispiel bei der Annäherung an Schwellen. Hier wird die gesamte kinetische Energie im Endzustand sehr klein und es stellt sich ein subtiles Gleichgewicht und schließlich eine vollständige Korrelation zwischen allen beteiligten Teilchen ein. Diese Situation entzieht sich vollständig einer Beschreibung durch unabhängige Teilchen oder ‘selbstkonsistentes Feld’-Methoden.

Eines der saubersten und grundlegendsten Systeme für die Erforschung dieser Phänomene ist die Doppelphotoionisation (DPI) von Helium wo die Absorption eines Photons mit definierter Energie und festem Drehimpuls zur Emission von beiden zunächst gebundenen Elektronen führt. In der Vergangenheit wurden zahlreiche experimentelle und theoretische Untersuchungen dieser Reaktion durchgeführt [Ava05, Bol04] und es hat sich ein tiefes Verständnis der Helium DPI herausgebildet. Stimuliert durch theoretische

Ergebnisse ist in jüngerer Zeit die Rolle des atomaren Anfangszustandes bei Schwellenphänomenen wieder ins Zentrum der Aufmerksamkeit gerückt. Bisher war allgemein akzeptiert, dass mehrere emittierte Elektronen nahe der Ionisationsschwelle immer symmetrische Konfigurationen einnehmen. Zwei Elektronen werden z.B. in entgegengesetzte Richtungen emittiert, drei in einer gemeinsamen Ebene wobei ihre Trajektorien den Relativwinkel von 120° einschließen [Wan53, Kla76]. Im Gegensatz dazu sagen neue Rechnungen z.B. für die dreifach-Photoionisation von Lithium nahe an der Schwelle voraus, dass eine nicht-symmetrische T-Konfiguration der emittierten Elektronen auftritt [Emm08]. Grund seien die spezifischen Eigenschaften des Li-Grundzustands in dem die Elektronen in zwei Schalen mit stark unterschiedlichen klassischen Bahnradien vorliegen. In anderen Rechnungen wurde die Abhängigkeit der DPI vom Anfangszustand untersucht und Ergebnisse für den He($1s^2\ ^1S$) Grundzustand und des ($1s2s\ ^1,^3S$), angeregten Zustands bei hohen Energien [Ten94] sowie in der Nähe der Schwelle verglichen [Har98, Khe00a]. Signifikante Unterschiede der totalen Querschnitte, ihrer Energieabhängigkeit und der Elektronen Winkelverteilungen wurden vorhergesagt, aber nie experimentell untersucht.

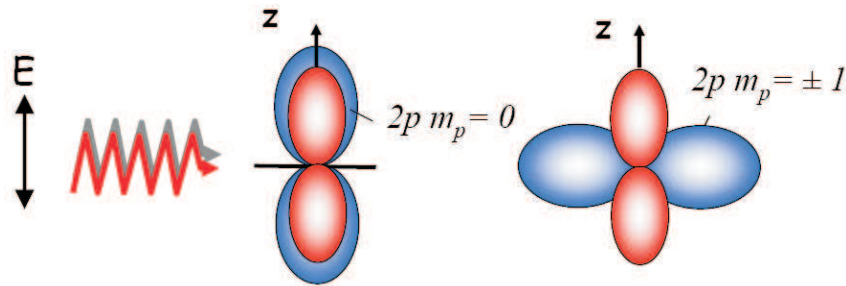


Figure G.1: Anschauliche Darstellung der Doppelionisation von präparierten Lithiumatomen durch vertikal polarisiertes UV-Licht. Dieses sorgt für eine Emission des Elektrons aus der $1s$ -Schale entlang einer Dipolverteilung die durch die roten Keulen angedeutet ist. Die Wahrscheinlichkeit für die Emission des zweiten Elektrons auf der $2p$ -Schale hängt davon ab, ob sein Orbital (blaue Keulen) parallel oder senkrecht zur Lichtpolarisation ausgerichtet.

All diesen Rechnungen zufolge eröffnet die Abhängigkeit der DPI Dynamik vom Anfangszustand die Tür zu ihrer Kontrolle. Dabei sind zwei zugrunde liegende Reaktionsmechanismen denkbar:

(i) die direkte Interaktion in der Frühphase der Ionisation bzw. in der ‘Reaktionszone’ wo alle Teilchen noch dicht beieinander sind wie in Abb. G.1 für Li DPI dargestellt: Ein $1s$ -Elektron absorbiert das linear polarisierte VUV Photon und wird gemäß einer Dipol-Winkelverteilung emittiert. Dieses Emissionsmuster ist durch die roten Keulen angedeutet. Nun ist anschaulich klar, dass die Wechselwirkung mit dem zweiten Elektron im $2p$ -Valenzorbital, die schließlich zur Emission oder Anregung dieses Elektrons führt, empfindlich von der Ausrichtung (dem Alignment) des $2p$ -Zustands abhängen kann. Z.B. bei einer Ausrichtung entlang der VUV-Polarisation, kann ein großer räumlicher Überlapp der Wellenfunktionen des auslaufenden $1s$ -Elektrons und des $2p\ (m_p = 0)$ Orbitals (blaue Keulen in Abb. G.1, Mitte) erwartet werden. Dieser Überlapp sollte stark reduziert sein

für die Ausrichtung senkrecht zur VUV-Polarisation (Abb. G.1, rechts) wie es für eine kohärente Überlagerung der $2p(m_p = \pm 1)$ magnetischen Unterzustände der Fall ist.

(ii) durch Elektron-Abstoßung, die die langsamen Elektronen in der Nähe der Schwelle über große Abstände beeinflusst. Hier erfordert das Streben des asymptotischen Zustands nach Stabilität die entgegen gesetzte Emission der Elektronen. Dementsprechend gibt es je nachdem, ob diese Konfiguration erlaubt ist bevorzugte (sog. ‘favoured’) oder unterdrückte (‘unfavoured’) Endzustands-Symmetrien [Sta82, Gre82a] mit stark unterschiedlichen DPI Wirkungsquerschnitten unabhängig von der Wechselwirkung bei kleinen Abständen im Atom.

Zur detaillierten Untersuchung der DPI-Dynamik von Lithiumatomen im Grundzustand und in angeregten Zuständen wurden in der vorliegenden Arbeit drei State-of-the-Art Technologien kombiniert: i. eine magneto-optische Falle (MOT) für die Herstellung eines Lithium-Gastargets bestehend aus ultra-kalten, zustandspräparierten sowie räumlich ausgerichteten Atomen. ii. ein Reaktionsmikroskop (REMI, [Ull03a]), das den impuls aufgelösten Nachweis aller entstehenden Fragmente bei Erfassung des vollen Raumwinkels ermöglicht. Und iii., die erste VUV-Lichtquelle der vierten Generation: der freie-Elektronen Laser in Hamburg (FLASH am DESY). Dieser erzeugt einen beispiellosen integralen Photonenfluss und eine günstige Pulsstruktur zur Messung schwelennaher differentieller Wirkungsquerschnitte für die Photodoppelionisation von Lithium im Grundzustand $\text{Li}(1s^2 2s^2 S^e)$ und im angeregten Zustand $\text{Li}^*(1s^2 2p^2 P^o)$.

Mit diesen experimentellen Möglichkeiten kann durch Präparation des Anfangszustands kontrolliert zwischen ‘favoured’ und ‘unfavoured’ Endzustands-Symmetrien umgeschaltet und verschiedene räumliche Ausrichtungen (Alignment) des angeregten p-Orbitals gewählt werden. Als Folge wurde eine starke Alignment-Abhängigkeit der Doppelionisation beobachtet. Andererseits war der totale Wirkungsquerschnitt für die Ionisation eines Innerschalenelektrons und die gleichzeitige Anregung des Valenzelektrons (simultane Ionisation und Anregung, IA) unabhängig von der anfänglichen Orbitalausrichtung. Diese Ergebnisse, die nahe der Schwelle besonders stark ausgeprägt sind, weisen auf die Möglichkeit hin, dass zwei-Elektronen-Übergänge durch dynamische Korrelation in der Nähe der Schwelle über obigen Mechanismus (ii) kontrolliert werden können. Obwohl die Anfangszustandspräparation offensichtlich einen Zugang zur Manipulation der zwei-Elektronendynamik bietet, wurden entsprechende Messungen bisher nicht durchgeführt. Es wurden nur Experimente zur IA-Reaktion publiziert (z.B. [Cub07]), wobei in neueren Messungen für angeregtes Lithium ‘spektakuläre Ergebnisse’ gefunden wurden.

G.2 Das Experiment

Innerhalb dieser Arbeit wurden verschiedene Teile der Apparatur entwickelt und zum Teil schon bestehende Teile verbessert. Sehr große Bedeutung wurde dem Aufbau eines zuverlässigen und stabilen Lasersystems zur Kühlung und zum Speichern der Lithium-Atome in der MOT beigemessen. Da bei der benötigten Wellenlänge von 671 nm keine leistungsstarken, Einmoden-Laserdioden kommerziell zu erhältlich sind wurden zunächst Multimoden-Laserdioden benutzt um einen schwachen Einmodenstrahl aus einer gitterst-

bilisierten Laserdiode zu verstärken. Da die Einkopplung des Einmodenlasers sehr kritisch und das Strahlprofil des erhaltenen Strahls schlecht war, wurde dieses System nicht weiter verfolgt. Im zweiten Schritt wurde ein Farbstofflasersystem benutzt. Dieses ermöglichte den Betrieb der MOT - es war jedoch sehr störungsanfällig und bedurfte sehr viel Justierarbeit. Als optimale Lösung stellte sich letztendlich die Verwendung eines ‘Tapered Amplifiers’ der Fa. Toptica zur Verstärkung des Einmoden-Laserstrahls heraus. Dadurch wurde der MOT-Betrieb über viele Stunden störungsfrei möglich. Der verstärkte Strahl mit ca. 400 mW Intensität wird mittels Sättigungsspektroskopie in einer Lithium-Dampfzelle und einer Regelungsschleife frequenzstabilisiert. Strahlteiler und akustooptische Modulatoren erzeugen dann die verschiedenen Einzelstrahlen und Frequenzen zum Laden der MOT mittels eines Zeeman-Abbremsers aus einem Lithium-Atomstrahl, zum Betrieb der MOT und zum optischen Pumpen der gespeicherten Atome.

Am Reaktionsmikroskop wurde die Impulsauflösung des Ionenspektrometers verbessert. Dazu wurde die Flugstrecke der Ionen deutlich, von 33 cm auf 77 cm erhöht und eine Linse zur Ortsfokussierung der Ionen eingebaut.

Unser auf einer MOT basierendes Li-Target enthielt etwa 10^7 Atome in einem Volumen von 0,5 mm Durchmesser bei einer Temperatur von etwa 1 mK. FLASH lieferte mit einer Wiederholfrequenz von 5 Hz Pulszüge bestehend aus 30 Einzelpulsen, jeweils mit 30 fs Dauer und mit bis zu 10^{13} Photonen. Dadurch wurde im Mittel in jedem Einzelpuls ein Doppelionisationsereignis induziert und nachgewiesen (Wirkungsquerschnitt $9 \cdot 10^{-21}$ cm² bei 85 eV Photonenenergie [Weh02]). Die Ionen wurden durch ein homogenes elektrisches Feld extrahiert und auf einen zeit- und 2D-positionsauflösenden Detektor projiziert. Aus dem Nachweisort und der Flugzeit wurde der Ionenimpuls berechnet. Um eine gute Impulsauflösung zu erzielen wurde das inhomogene Magnetfeld der MOT ungefähr eine Millisekunde vor Eintreffen jeder FLASH Pulsfolge von 150 μ m Dauer abgeschaltet. Die Impulsauflösung betrug 0,05 a.u. und praktisch alle Atome konnten nach Durchgang des Pulszuges wieder in der MOT gefangen werden. Besondere Sorgfalt wurde auf die Präparation des angeregten $\text{Li}^*(2p^2P_{3/2})$ Zustands verwendet durch Anwendung eines dezidierten, linear polarisierten Pumpplaserpulses auf der $2s_{1/2} \rightarrow 2p_{3/2}$ Resonanz. Der Anteil der angeregten Atome von $46 \pm 1\%$ wurde aus der Abnahme der Intensität der Photolinie aus der direkten Ionisation der Valenzelektron $\text{Li}(1s^22l) + \gamma \rightarrow \text{Li}^+(1s^2) + e^-$ bestimmt. Dieser Prozess ist um den Faktor 30 schwächer für den p -Zustand ($l = 1$) im Vergleich zum s -Zustand ($l = 0$). Der geringe Impulsunterschied der $2s$ - und $2p$ -Linien von 0,03 a.u. konnte nicht direkt aufgelöst werden.

Das Alignment des angeregten Zustands wurde aus dem Polarisationsgrad der emittierten Fluoreszenzstrahlung bestimmt. Die daraus resultierenden Besetzungszahlen der magnetischen Unterzustände in der l -Basis waren $P(m_p = 0) = 0,50$ und $P(m_p = \pm 1) = 0,25$ im parallelen Fall (\parallel), wo die zum optischen Pumpen verwendete Laserpolarisation parallel zur VUV-Polarisation ausgerichtet war. Entsprechend waren im senkrechten Fall (\perp) die Populationen $P(m_p = 0) = 0,20$ und $P(m_p = \pm 1) = 0,40$.

In den in dieser Arbeit diskutierten Experimenten wurden nur Rückstoionen-Impulse gemessen da die nach Abschalten des MOT-Magnetfeldes durch Wirbelströme verursachten Restfelder hochaufgelöste Elektronenspektroskopie unmöglich machten. Dieses

Problem wird in Zukunft durch Speicherung der Atome in einer optischen Dipolfalle vermieden. Dann werden durch den koinzidenten Elektronennachweis auch volldifferentielle Studien möglich sein.

G.3 Ergebnisse

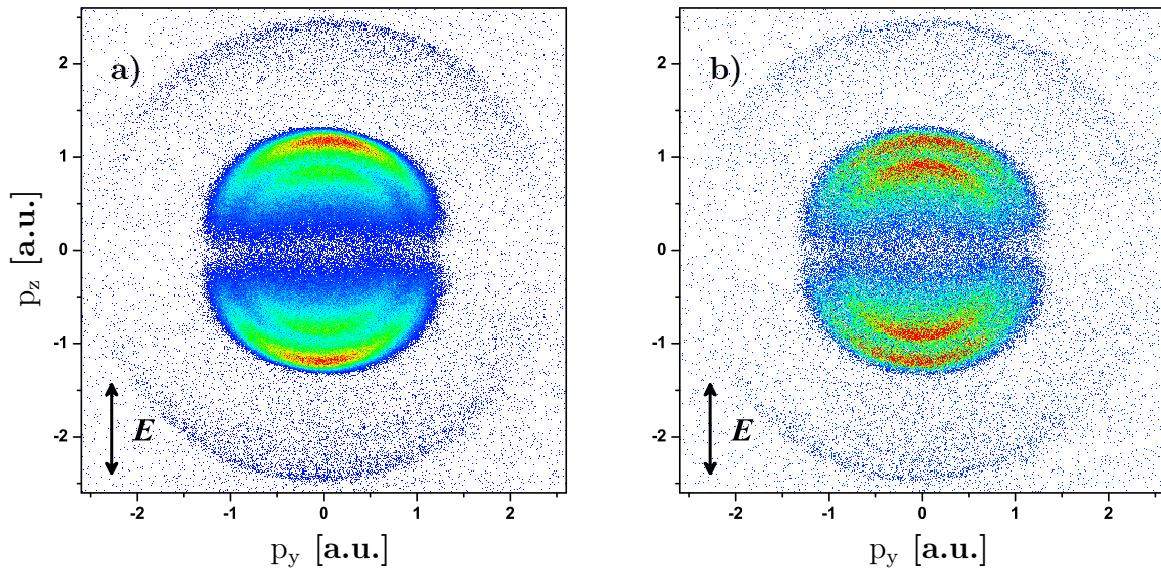


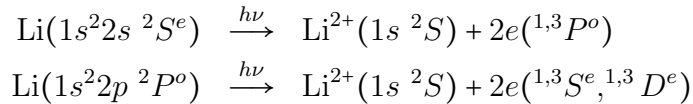
Figure G.2: Zweidimensionale Rückstoßionen Impulsverteilungen für die Einfachionisation durch 85 eV FEL Licht von (a) Li(2s) und (b) laserangeregtem Li(2p). Hier sind die Polarisationsrichtungen des VUV-Lichts und des zum optischen Pumpen benutzten Lasers parallel entlang der z -Achse ausgerichtet.

In Abb. G.2 sind zweidimensionale Li⁺-Impulsspektren projiziert auf eine Ebene, welche die E-Richtung enthält gezeigt. Da die Impulse der absorbierten Photonen unerheblich sind kompensiert der Ionenimpuls den Impuls des emittierten Elektrons. Daher sind die Ionen-Impulsspektren für die Einfachionisation äquivalent zu den Impulsverteilungen für die Elektronen. Die VUV-Photonenenergie beträgt $E_\gamma = 85$ eV, die DPI-Schwelle des Li-Grundzustands liegt bei 81 eV, die des laserangeregten Zustands bei 79 eV. Für die Ionisation vom Li-Grundzustand (Abb. G.2 a) sind drei kreisförmige Schalen sichtbar mit der für Dipolübergänge charakteristischen Winkelabhängigkeit der Intensität entsprechend einer \cos^2 -Verteilung, die entlang der VUV-Polarisation ausgerichtet ist. Von großen nach kleinen Radien entsprechen die Schalen der Ionisation eines 2s-, eines 1s-Elektrons und 1s-Ionisation bei gleichzeitiger Anregung (IA) des Valenzelektrons $2s \rightarrow nl$. Das Spektrum für den reinen Li*(2p)-Anfangszustand in Abb. G.2 b zeigt signifikante Veränderungen in den beobachteten Linienintensitäten. Wie bereits erwähnt ist die Photoionisation des Valenzelektrons um den Faktor 30 reduziert [Naj08]. Diese Tatsache

wurde dazu benutzt den Anteil der laserangeregten Targetatome im Experiment zu bestimmen. Mit dieser Zahl konnten anschließend Spektren für 100% Besetzung von $\text{Li}^*(2p)$ durch Abzug des entsprechend gewichteten Grundzustandsspektrums und anschließendem Renormieren gewonnen werden. Weiterhin steigt der Querschnitt für IA von 23% des reinen $1s$ -Ionisationsquerschnitts für den ursprünglichen Grundzustand auf 70% für den anfänglichen $2p$ -Zustand. Cubaynes *et al.* [Cub07] beobachteten dieses Verhalten noch stärker für höher aufgeregte Anfangszustände nl . Da jedoch die räumliche Ausrichtung des Anfangszustands nicht festgelegt war, konnten die Autoren kein schlüssiges Ergebnis über eine eventuelle Alignmentabhängigkeit erhalten.

Während in den vorliegenden Messungen die verschiedenen ionischen Zustände für IA nicht aufgelöst sind zeigt der totale Wirkungsquerschnitt für diesen Prozess keine Abhängigkeit von der Ausrichtung vom Anfangszustand innerhalb der statischen Fehlergrenzen von einem Prozent. Einerseits erwartet man dies für ‘shake-up’-Übergänge $2p \rightarrow np$ ($n > 2$), die etwa 80% der IA Intensität ausmachen [Cub07], da sie in der ‘sudden-approximation’ durch eine reine Projektion des $2p$ -Orbitals auf die np -Orbitale des Ions und daher ohne explizite Elektronen-Wechselwirkung im Endzustand erklärt werden können. Auf der anderen Seite bedeutet dies, dass auch die ‘conjugate shake-up’-Übergänge $2p \rightarrow ns, nd$ die auf einer expliziten Wechselwirkung der beiden aktiven Elektronen im Endzustand beruhen, keine ausgeprägte Ausrichtungsabhängigkeit aufweisen. Dies zeigt, dass der oben diskutierte Mechanismus (i) für IA von untergeordneter Relevanz sein muss. Nun zur Doppelionisation, für die zunächst demonstriert werden soll, wie die Reaktion durch die Symmetrie des Anfangszustands beeinflusst wird und wie die Präparation des Anfangszustands die Emissionsgeometrie des Elektronenpaares beeinflussen kann.

Wir betrachten folgende Übergänge für den Lithium Grundzustand und den angeregten Zustand:



Die zugehörigen Rückstoßionen-Impulsspektren sind in Abb. G.3 gezeigt. Hier sind sowohl die VUV-Strahlung als auch das zum optischen Pumpen des Anfangszustandes benötigte Licht parallel zueinander polarisiert, so dass nur ($\Delta M = 0$)-Übergänge bezüglich dieser Quantisierungsachse induziert werden. Von den zugänglichen Endzuständen dominieren die Singulett-Zustände den totalen DPI-Wirkungsquerschnitt. Dies wurde z.B. in Rechnungen für angeregtes $\text{He}^*(1s2s^1,3 S^e)$ gezeigt wo das Verhältnis $\sigma(^1P)/\sigma(^3P) \approx 10$ im Bereich von 5 eV bis 10 eV über der Schwelle ist [Har98, Khe00a]. In der folgenden Analyse ist es daher gerechtfertigt nur die Singulett-Zustände zu betrachten.

Abb. G.3 a zeigt ein Doppelkeulen-Emissionsmuster mit einem Minimum bei $|p_{rec}| = 0$. Wie für die DPI von Helium im Grundzustand folgt dies aus der $^1P^o$ -Symmetrie der Partialwelle des emittierten Elektronenpaares, die einen Knoten bei der raumsymmetrischen Wannier-Konfiguration aufweist. Dementsprechend ist $^1P^o$ eine unterdrückte (‘unfavoured’) Symmetrie mit kleinem Wirkungsquerschnitt für die Elektronenpaar-Emission in entgegengesetzte Richtungen und mit gleicher Energie die dem Rückstoß-Ionenimpuls Null entspricht. Im Gegensatz dazu entsprechen die ausgehend vom angeregten Anfangszustand auslaufenden $^1S^e$ - und $^1D^e$ -Wellen ($M = 0$) bevorzugten (‘favoured’) Symmetrien,

für die die Wannier-Konfiguration möglich ist. Darüber hinaus sind diese Partialwellen die einzigen bis $L = 3$, für die Maulbetsch und Briggs [Mau95] keine einzige Auswahlregel, d.h. keine Emissionsgeometrie mit verschwindendem Querschnitt identifiziert haben. Dies erlaubt es der Ionisationsdynamik sich frei zu entfalten. Als Ergebnis ist das Minimum bei $|p_{rec}| = 0$ in Abb. G.3 b aufgefüllt und in ein Maximum des Wirkungsquerschnitts verwandelt. Solche ‘bevorzugten’ Symmetrien konnten in früheren Untersuchungen nur bei der DPI von kugelsymmetrischen Argonatomen mit dem Endzustand $\text{Ar}^{2+}(3s^{-1}3p^{-1}) + 2e(^1S^e, ^1D^e)$, $^1D^e$ erreicht werden [Maz97].

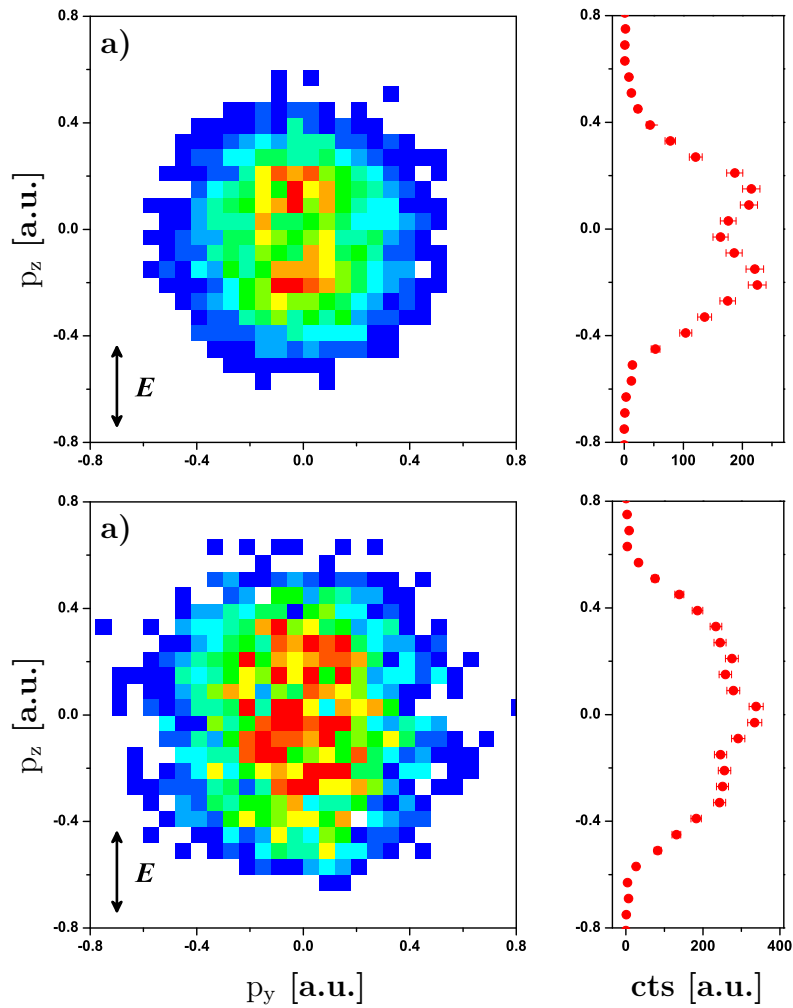


Figure G.3: Zweidimensionale Rückstoßionen Impulsverteilungen für die Doppelionisation durch 85 eV FEL Licht von (a) Li(2s) und (b) laserangeregtem Li(2p). Hier sind die Polarisationsrichtungen des VUV-Lichts und des zum optischen Pumpen benutzten Lasers parallel entlang der eingezeichneten Achse ausgerichtet.

Im nächsten Schritt drehen wir die Ausrichtung des $2p$ -Orbitals in Bezug auf den elektrischen Feldvektor \mathbf{E} der VUV-Strahlung von parallel ($2p_{\parallel}$) auf senkrecht ($2p_{\perp}$). Als Ergebnis sinkt die DPI-Rate signifikant für kleine Ionen-Impulse unter 0,6 a.u. wie in

Abb. G.4 a zu sehen ist. Wie in Abb. G.4 b zu sehen nimmt diese Alignment-Abhängigkeit deutlich ab für den Fall, dass die Photonen-Überschussenergie von 6 eV to 12 eV ($E_\gamma = 91$ eV) steigt.

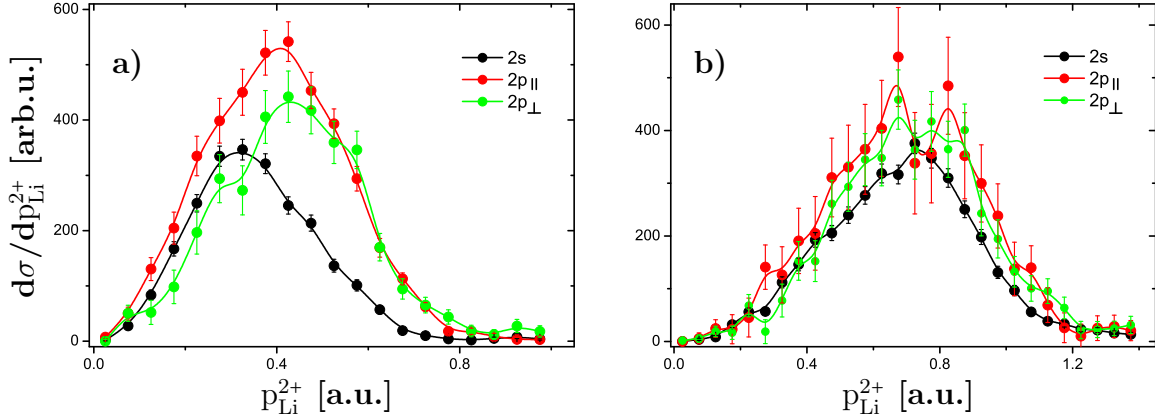


Figure G.4: Der Wirkungsquerschnitt als Funktion des Ionenimpulses nach Doppelionisation durch 85 eV (a) und 91 eV (b) Photonen. Die Ergebnisse für die verschiedenen Anfangszustände sind in schwarz ($2s$), grün ($2p_\perp$) und rot ($2p_\parallel$) gezeigt.

Dieser Effekt wird also nicht durch Symmetrie erzwungen, sondern folgt aus einer subtilen dynamischen Korrelation, die näher an der Doppel-Ionisationsschwelle effektiver ist. Diese Beobachtungen unterstützen den oben beschriebenen Mechanismus (ii), und weisen darauf hin, dass die weit reichende Korrelation nahe an der Schwelle zum Tragen kommt: DPI bei verschwindender Überschussenergie erfordert, dass alle verfügbare Energie zur Überwindung des attraktiven Ionenpotenzials verwendet wird. Für senkrechte Ausrichtung des $2p$ -Orbitals enthält der Anfangszustand erheblichen Impuls quer zur bevorzugten Abstrahlrichtung des ionisierten Innerschalen-Elektrons entlang der VUV-Polarisationsachse. Dies führt zu einem endlichen Netto-Impuls bzw. einer Bewegung des Schwerpunkts des emittierten Elektronenpaares. Während diese Bewegung nach Schwellentheorien ([Ros91] und Referenzen darin) eine stabile Schwingung auf dem Wannier-Sattelpotenzial darstellt und daher nicht das Wannier-Schwellengesetz ändert enthält sie Energie, die nicht für die radiale Flucht der beiden Elektronen zur Verfügung steht. Genau an der Schwelle muss die Schwerpunktsbewegung der beiden Elektronen auf allen Punkten von ihrer Flugbahn verschwinden. Dieses anschauliche Bild wird durch die Auswahlregel ‘B1’ vertreten, die Maulbetsch und Briggs zusammengestellt haben [Mau95]. Diese Regel besagt, dass Zwei-Elektronen-Symmetrien mit $M \neq 0$ nicht zum Wirkungsquerschnitt beitragen wenn beide Elektronen entlang der Quantisierungsachse, d.h. der VUV-Polarisationsachse emittiert werden (parallel oder antiparallel zueinander). Während beim anfänglichen $2p(m=0)$ Zustand für das emittierte Elektronenpaar zwei Partialwellensymmetrien $\epsilon S(M_S=0)$ und $\epsilon D(M_D=0)$ erreichbar sind, ist für senkrechte Ausrichtung mit $2p(m=\pm 1)$ Zuständen die S -Partialwelle nicht erlaubt, stattdessen tragen zwei D -Partialwellen mit ($M=\pm 1$) bei. In beiden Fällen sind also unterschiedliche Übergangsamplituden beteiligt. Dadurch wird die Alignment-Abhängigkeit des Wirkungs-

querschnitts grundsätzlich möglich. Diese nimmt aber für steigenden Photonenenergie und zunehmenden Energieabstand zur DPI Schwelle ab und ist vollkommen abwesend, wenn eines der beiden Elektronen gebunden bleibt, wie es für simultane Ionisation und Anregung der Fall ist.

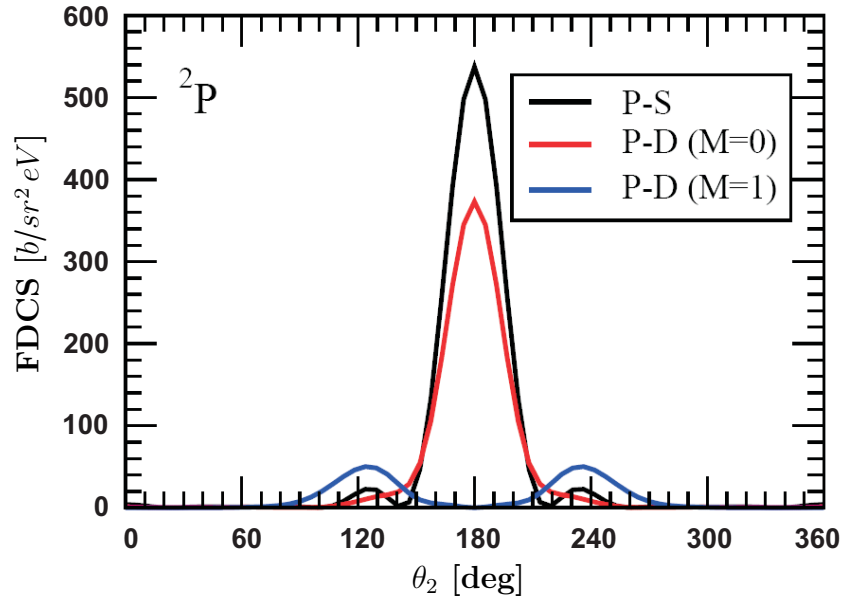


Figure G.5: TDCC-Rechnung des vollständig differentiellen Wirkungsquerschnittes für DPI aufgelöst nach den verschiedenen Partialwellen L , M_L und bei 85 eV. Die Aufteilung der Überschussenergie von 6 eV auf die beiden Elektronen ist symmetrisch ($E_1 = E_2 = 3$ eV) und der Emissionswinkel θ_1 eines der Elektronen ist entlang der VUV-Polarisationsachse.

Diese Argumente werden von Time Dependent Close Coupling (TDCC) Rechnungen, durchgeführt von James Colgan (Los Alamos National Laboratory, USA), gestützt. Mit der TDCC-Methode [Pin98a] wird die DPI von Lithium unter ‘Einfrieren’ eines 1s-Elektrons berechnet. Singulett- und Triplett-Beiträge des auslaufenden Elektronenpaars werden berücksichtigt. Bei 85 eV Photonenenergie ergibt die Rechnung beträchtlich höheren Wirkungsquerschnitt für die ‘favoured’ $\epsilon S (M_S = 0)$ und die $\epsilon D (M_D = 0)$ Partialwellen verglichen mit den $\epsilon D (M_D = \pm 1)$ Partialwellen. Für zunehmende Überschussenergie verringert sich dieser Unterschied. In Abb. G.5 sind beispielhaft völdifferentielle Wirkungsquerschnitte für symmetrische Energieaufteilung und für den Fall gezeigt, dass der Emissionswinkel eines Elektrons entlang der VUV Polarisation festgehalten wird ($\theta_{\mathbf{E}} = \theta_1 = 0^\circ$). Hier sind die Querschnitte der verschiedenen emittierten Teilwellen LML als Funktion der Emission des zweiten Elektronenwinkels aufgetragen. Sowohl die $S (M_S = 0)$ als auch die $D (M_D = 0)$ Wirkungsquerschnitte zeigen ein ausgeprägtes Maximum bei $\theta_2 = 180^\circ$ mit kleinen Nebenmaxima. Dies ist die bei niedriger Überschussenergie bevorzugte Wannier-Konfiguration. Im Gegensatz dazu hat der $D (M_D = 1)$ Querschnitt ein Minimum bei 180° und zwei Maxima bei 140° und 220° . Die Wannier-Konfiguration ist also unterdrückt. Während bei 85 eV Photonenenergie die $(M = 0)$ -Partialwellen dominieren, zeigt die Rechnung zunehmende relative Größe der $(M = 1)$ -Welle für steigenden Photonenenergie (hier

nicht gezeigt).

Table G.1: Experimentelle und theoretische totale DPI-Wirkungsquerschnitte für die verschieden ausgerichteten angeregten Zustände normalisiert auf DPI-Wirkungsquerschnitte des Grundzustands.

Photonen-energie (eV)	$\sigma_{2p\parallel}/\sigma(2s)$		$\sigma_{2p\perp}/\sigma(2s)$	
	Exp.	Theo.	Exp.	Theo.
85	1.82± 0.06	1.57	1.42± 0.06	1.22
91	1.39± 0.07	1.17	1.19± 0.05	1.90

In Tabelle G.1 sind die experimentellen und gerechneten Veränderungen des totalen Doppelionisationsquerschnitts für die verschieden ausgerichteten angeregten Zustände relativ zum Grundzustandswirkungsquerschnitt gezeigt. Die Werte stimmen innerhalb von 12% überein mit Ausnahme des p_{\perp} -Falles bei 91 eV Photonenenergie wo die Rechnung 30% unter dem Experiment liegt. In Experimenten mit statistischer Besetzung der $M = 0, \pm 1$ Projektionen im Anfangszustand, erscheinen neben dem 180° Maximum mit zunehmender Photonenenergie zwei Seitenmaxima wie es von Mazeau *et al.* [Maz97] bei Argon beobachtet wurde. Im vorliegenden Fall erlaubt die Besetzung ausgewählter Unterzustände die Trennung der einzelnen Beiträge schon über den Nachweis der Ionen, da die Wannier-Konfiguration eindeutig durch verschwindenden Ionenimpuls identifiziert werden kann $|p_{Li^{2+}}| = 0$.

G.4 Zusammenfassung

Zusammenfassend kann die beobachtete Alignment-Abhängigkeit für Doppel-Ionisation konsistent als Folge der bei Schwellenenergien über große Abstände wirkenden Coulomb-Wechselwirkung zwischen den freien Elektronen erklärt werden. Während der Querschnitt im vorliegenden Experiment um bis zu 34% für die verschiedenen Pumplaser-Polarisierungen variierte, kann ein deutlich höherer Kontrast erwartet werden, wenn die VUV-Energie näher an der Schwelle liegt oder für höhere Populationen der $M = \pm 1$ magnetischen Unterzustände wie sie z.B. durch optisches Pumpen mit zirkular polarisiertem Licht möglich sind. Bei dem beobachteten Effekt kann die dynamische Elektronenkorrelation durch eine reine Geometrievariation des Target-Anfangszustands kontrolliert werden ohne Änderung seiner inneren Energie. Damit kann die DPI entweder aktiviert oder im Wesentlichen unterdrückt werden.

In dieser Arbeit wurde demonstriert, dass die Präparation des Anfangszustandes (Anregung und gezielte räumliche Ausrichtung) ein effektives Mittel zur Kontrolle der Zwei-Elektronen Kontinuumsdynamik nahe der Schwelle ist. Die beobachtete Ausrichtungs-Abhängigkeit kann auf die große Reichweite der Elektronenkorrelation zurückgeführt werden. Die Rückstoßionen-Impulsspektren und das Verhältnis der totalen Querschnitte stehen mit den Ergebnissen der TDCC-Rechnungen in Einklang. Teile dieser Arbeit sind publiziert [Zhu09].

Bibliography

- [Abe70] T. Åberg, *Asymptotic Double-Photoexcitation Cross Sections of the Helium Atom*, Phys. Rev. A **2**, 1726 (1970).
- [Abe76] T. Åberg, *Photoionization and Other Probes of Many-Electron Interactions*, edited by F. J. Wuilleumier (Plenum Press, New York, 1976).
- [Ack07] W. Ackermann *et al.*, the supplementary information of *Operation of a free electron laser from the extreme ultraviolet to the water window*, Nat. Photonics **1**, 336 (2007).
- [Ago79] P. Agostini, F. Fabre, G. Mainfray, G. Petite and N. K. Rahman, *Free-Free Transitions Following Six-Photon Ionization of Xenon Atoms*, Phys. Rev. Lett. **42**, 1127 (1979).
- [Ago87] P. Agostini, J. Kupersztych, L. A. Lompré, G. Petite and F. Yergeau, *Direct evidence of ponderomotive effects via laser pulse duration in above-threshold ionization*, Phys. Rev. A **36**, 4111 (1987).
- [Aks88] H. Aksela, S. Aksela, H. Pulkkinen, G. M. Bancroft and K. H. Tan, *Anomalously strong shake-up processes in Auger decay of the resonantly excited $2p^5 3s^2 3p^6 nl$ states of Ar*, Phys. Rev. A **37**, 1798 (1988).
- [Alb08] J. Albrecht, *Experimente zur Laseranregung von Lithium*, Diploma thesis, Ruprecht-Karls-Universität, Heidelberg (2008).
- [Amu90] M. Y. Amusia, *Atomic Photoeffect*, edited by K. T. Taylo (Plenum Press, New York, 1990).
- [Amu93] M. Y. Amusia, *Vacuum Ultraviolet Radiation Physics*, VUV 10 Proceedings, edited by F. J. Wuilleumier, Y. Petroff, and I. Nenner (World Scientific, Singapore, 1993).
- [And95] M. H. Anderson, J. R. Ensher, M. R. Matthews, C. E. Wieman and E. A. Cornell, *Observation of Bose-Einstein Condensation in a Dilute Atomic Vapor*, Science **269**, 198 (1995).
- [Ava05] L. Avaldi and A. Huetz, *Photodouble ionization and the dynamics of electron pairs in the continuum*, J. Phys. B: At. Mol. Opt. Phys. **38**, S861 (2005).

BIBLIOGRAPHY

- [Bal79] V. I. Balykin, V. S. Lethokov and V. I. Mushin, *Observation of the cooling of free sodium atoms in a resonance laser field with a scanning frequency*, JETP Lett. **29**, 560 (1979).
- [Bal85] V. I. Balykin and A. I. Sidorov, *High-power two-frequency cw dye laser*, Sov. J. Quant. Elec. **14**, 1342 (1984).
- [Bal00] V. V. Balashov, A. N. Grum-Grzhimailo and N. M. Kabachnik, *Polarization and Correlation Phenomena in Atomic Collisions: A Practical Theory Course*, (Kluwer Academic/Plenum, NewYork, 2000).
- [Bec90] U. Becker and D. A. Shirley, *Threshold Behaviour and Resonances in the Photoionization of Atoms and Molecules*, Phys. Scr. T **31**, 56 (1990).
- [Beh09] J. A. Behr and G. Gwinner, *Standard model tests with trapped radioactive atoms*, J. Phys. G: Nucl. Part. Phys. **36** 033101 (2009).
- [Ber87] K. A. Berrington, P. G. Burke, K. Butler, M. J. Seaton, P. J. Storey, K. T. Taylor and Y. Yan, *Atomic data for opacity calculations: II. Computational methods*, J. Phys. B: At. Mol. Phys. **20**, 6379 (1987).
- [Bjo83] G. C. Bjorklund, M. D. Levenson, W. Lenth and C. Ortiz, *Frequency modulation (FM) spectroscopy*, Appl. Phys. B **32**, 145 (1983).
- [Bly99] R. R. Blyth, R. Delaunay, M. Zitnik, J. Krempasky, R. Krempaska, J. Slezak, K. C. Prince, R. Richter, M. Vondracek, R. Camilloni, L. Avaldi, M. Coreno, G. Stefani, C. Furlani, M. de Simone, S. Stranges and M.-Y. Adam, *The high resolution Gas Phase Photoemission beamline*, *Elettra*, J. Elect. Spect. Relat. Phenom. **101103**, 959 (1999).
- [Bol04] P. Bolognesi, G. C. King and L. Avaldi, *Photo-double-ionization of atoms*, Radiat. Phys. Chem. **70**, 207 (2004).
- [Bor79] B. W. Boreham and B. Luther-Davies, *High-energy electron acceleration by ponderomotive forces in tenuous plasmas*, J. Appl. Phys. **50**, 2533 (1979).
- [Bot85] C. Bottcher, *Numerical calculations on electron-impact ionization*, Adv. At. Mol. Phys. **20**, 241 (1985).
- [Bra90] C. A. Brau, *Free-Electron Lasers*, (Academic Press, Oxford, 1990).
- [Bra92] I. Bray and A. T. Stelbovics, *Convergent close-coupling calculations of electron-hydrogen scattering*, Phys. Rev. A **46**, 6995 (1992).
- [Bra93] I. Bray and A. T. Stelbovics, *Calculation of the total ionization cross section and spin asymmetry in electron-hydrogen scattering from threshold to 500eV*, Phys. Rev. Lett. **70**, 746 (1993).
- [Bra94] I. Bray and A. T. Stelbovics, *Convergent close-coupling method for the calculation of electron scattering on hydrogenlike targets*, Phys. Rev. A **49**, 1066 (1994).

-
- [Bra02] I. Bray, *Close Coupling Approach to Coulomb Three-Body Problems*, Phys. Rev. Lett. **89**, 273201 (2002).
- [Brae97] H. Bräuning, R. Dörner, C. L. Cocke, M. H. Prior, B. Krässig, A. Bräuning-Demian, K. Carnes, S. Dreuil, V. Mergel, P. Richard, J. Ullrich and H. Schmidt-Böcking, *Recoil ion and electronic angular asymmetry parameters for photo double ionization of helium at 99 eV*, J. Phys. B: At. Mol. Opt. Phys. **30** L649 (1997).
- [Bre03] R. Brédy, H. Nguyen, H. Camp, X. Flécharde and B. D. Paola, *MOTRIMS as a generalized probe of AMO processes*, Nucl. Instr. Meth. Phys. Res. B **205**, 191 (2003).
- [Bri00] J. S. Briggs and V. Schmidt, *Differential cross sections for photo-double-ionization of the helium atom*, J. Phys. B: At. Mol. Phys. **33**, R1 (2000).
- [Bro01] I. N. Bronstein, K. A. Semendajew, G. Musiol and H. Mühlig, *Taschenbuch der Mathematik*, (Verlag Harri Deutsch, Frankfurt am Main, 2001), 5th Edn.
- [Bru55] K. A. Brueckner, *Many-Body Problem for Strongly Interacting Particles. II. Linked Cluster Expansion*, Phys. Rev. **100**, 36 (1955).
- [Bur71] P. G. Burke, A. Hibbert and W. D. Robb, *Electron scattering by complex atoms*, J. Phys. B: At. Mol. Phys. **4**, 153 (1971).
- [Byr67] F. W. Byron and C. J. Joachain, *Multiple Ionization Processes in Helium*, Phys. Rev. **164**, 1 (1967).
- [Car67] T. A. Carlson, *Double Electron Ejection Resulting from Photo-Ionization in the Outermost Shell of He, Ne, and Ar, and Its Relationship to Electron Correlation*, Phys. Rev. **156**, 142 (1967).
- [Car68] T. A. Carlson, C. W. Nestor, Jr., T. C. Tucker and F. B. Malik, *Calculation of Electron Shake-Off for Elements from $Z=2$ to 92 with the Use of Self-Consistent-Field Wave Functions*, Phys. Rev. **169**, 27 (1968).
- [Car77] S. L. Carter and H. P. Kelly, *Double photoionization of neon and argon*, Phys. Rev. A **16**, 1525 (1977).
- [Car81] S. L. Carter and H. P. Kelly, *Double photoionization of helium*, Phys. Rev. A **24**, 170 (1981).
- [Cas82] D. T. Cassidy and J. Reid, *Harmonic detection with tunable diode lasers — two-tone modulation*, Appl. Phys. B **29**, 279 (1982).
- [Cha68] E. S. Chang and M. R. C. McDowell, *Photo-Ionization of Lithium: A Many-Body Calculation*, Phys. Rev. **176**, 126 (1968).
- [Cha71] T. N. Chang, T. Ishihara and R. T. Poe, *Correlation Effect and Double Electron Ejection in the Photoabsorption Process*, Phys. Rev. Lett. **27**, 838 (1971).

BIBLIOGRAPHY

- [Cha75b] T. N. Chang and R. T. Poe, *Double photoionization of neon*, Phys. Rev. A **12**, 1432 (1975).
- [Che00] W. T. Cheng, E. Kukk, D. Cubaynes, J.-C. Chang, G. Snell, J. D. Bozek, F. J. Wuilleumier and N. Berrah, *Measurements and calculations of high-angular-momentum satellite transitions in Li 1s photoionization*, Phys. Rev. A **62**, 062509 (2000).
- [Cho05] C. W. Chou, H. de Riedmatten, D. Felinto, S. V. Polyakov, S. J. van Enk and H. J. Kimble, *Measurement-induced entanglement for excitation stored in remote atomic ensembles*, Nature **438**, 828 (2005).
- [Chu86] S. Chu, J. E. Bjorkholm, A. Ashkin and A. Cable, *Experimental Observation of Optically Trapped Atoms*, Phys. Rev. Lett. **57**, 314 (1986).
- [Chu98] S. Chu, *The manipulation of neutral particles*, Rev. Mod. Phys. **70**, 685 (1998); Nobel lecture.
- [Cla95] A. Clairon, P. Laurent, G. Santarelli, S. Ghezali, S. N. Lea and M. Bahoura, *A Cesium Fountain Frequency Standard Preliminary-Results*, IEEE Trans. Instrum. Meas., **44**, 128 (1995).
- [Cla06] B. J. Claessens, J. P. Ashmore, R. T. Sang, W. R. MacGillivray, H. C. W. Beijerinck and E. J. D. Vredenbregt, *Measurement of the photoionization cross section of the $(2p)^5(3p)^3D_3$ state of neon*, Phys. Rev. A **73**, 012706 (2006).
- [Cle74] B. Cleff and W. Mehlhorn, *On the angular distribution of Auger electrons following impact ionization*, J. Phys. B: At. Mol. Opt. Phys. **7**, 593 (1974).
- [Coh98] C. Cohen-Tannoudji, *Manipulating atoms with photons*, Rev. Mod. Phys. **70**, 707 (1998); Nobel lecture.
- [Col77] W. B. Colson, Ph.D. thesis, *Free electron laser theory*, Stanford University, (1977).
- [Col02a] J. Colgan and M. S. Pindzola, *$(\gamma, 2e)$ total and differential cross-section calculations for helium at various excess energies*, Phys. Rev. A **65**, 032729 (2002).
- [Col02b] J. Colgan and M. S. Pindzola, *Core-Excited Resonance Enhancement in the Two-Photon Complete Fragmentation of Helium*, Phys. Rev. Lett. **88**, 173002 (2002).
- [Col03] J. Colgan and M. S. Pindzola, *Total and differential cross-section calculations for the double photoionization of the helium $1s2s^1,^3S$ states*, Phys. Rev. A **67**, 012711 (2003).
- [Col04] J. Colgan, M. S. Pindzola and F. Robicheaux, *Lattice Calculations of the Photoionization of Li*, Phys. Rev. Lett. **93**, 053201 (2004).
- [Col09] J. Colgan and M. S. Pindzola, *private communication* (2009).

-
- [Cou04] L. H. Coutinho, R. L. Cavasso-Filho, T. C. Rocha, M. G. Homem, D. S. Figueira, P. T. Fonseca, F. C. Cruz and A. Naves de Brito, *Relativistic and Interchannel Coupling Effects in Photoionization Angular Distributions By Synchrotron Spectroscopy of Laser Cooled Atoms*, Phys. Rev. Lett. **93**, 183001 (2004).
- [Cub07] D. Cubaynes, S. Diehl, F. J. Wuilleumier, M. Meyer, E. Heinecke, T. Richter and P. Zimmermann, *Intensity Inversion between Main and Satellite Lines in Atomic Photoionization*, Phys. Rev. Lett. **99**, 213004 (2007).
- [Dal89] J. Dalibard and C. Cohen-Tannoudji, *Laser cooling below the Doppler limit by polarization gradients: simple theoretical models*, J. Opt. Soc. Am. B **6**, 2023 (1989).
- [Dat95] G. Dattoli, A. Renieri and A. Torre, *Lectures in Free-Electron Laser theory and related topics* (World Scientific, Singapore, 1995).
- [Dav95] K. B. Davis, M.-O. Mewes, M. R. Andrews, N. J. van Druten, D. S. Durfee, D. M. Kurn and W. Ketterle, *Bose-Einstein Condensation in a Gas of Sodium Atoms*, Phys. Rev. Lett. **75**, 3969 (1995).
- [Dea77] D. A. G. Deacon, L. R. Elias, J. M. J. Madey, G. J. Ramian, H. A. Schwettman and T. I. Smith, *First Operation of a Free-Electron Laser*, Phys. Rev. Lett. **38**, 892 (1977).
- [Ded04] C. J. Dedman, J. Nes, T. M. Hanna, R. G. Dall, K. G. H. Baldwin and A. G. Truscott, *Optimum design and construction of a Zeeman slower for use with a magneto-optic trap*, Rev. Sci. Instrum. **75**, 5136 (2004).
- [Dem91] W. Demtröder, *Laser Spectroscopy* (Springer-Verlag, Heidelberg, 1991).
- [DeM99] D. DeMarco and D. Jin, *Onset of Fermi Degeneracy in a Trapped Atomic Gas*, Science **285**, 1705 (1999).
- [Din92] T. P. Dinneen, C. D. Wallace, K.-Y. N. Tan and P. L. Gould, *Use of trapped atoms to measure absolute photoionization cross sections*, Optics Letters **17**, 1706 (1992).
- [Doer96a] R. Dörner, T. Vogt, V. Mergel, H. Khemliche, S. Kravis, C. L. Cocke, J. Ullrich, M. Unverzagt, L. Spielberger, M. Damrau, O. Jagutzki, I. Ali, B. Weaver, K. Ullmann, C. C. Hsu, M. Jung, E. P. Kanter, B. Sonntag, M. H. Prior, E. Rotenberg, J. Denlinger, T. Warwick, S. T. Manson and H. Schmidt-Böcking, *Ratio of Cross Sections for Double to Single Ionization of He by 85 - 400 eV Photons*, Phys. Rev. Lett **76**, 2654 (1996).
- [Doer96b] R. Dörner, J. M. Feagin, C. L. Cocke, H. Bräuning, O. Jagutzki, M. Jung, E. P. Kanter, H. Khemliche, S. Kravis, V. Mergel, M. H. Prior, H. Schmidt-Böcking, L. Spielberger, J. Ullrich, M. Unverzagt and T. Vogt, *Fully Differential Cross Sections for Double Photoionization of He Measured by Recoil Ion Momentum Spectroscopy*, Phys. Rev. Lett. **77**, 1024 (1996).

BIBLIOGRAPHY

- [Doer97] R. Dörner, V. Mergel, L. Spielberger, M. Achler, K. Khayyat, T. Vogt, H. Bräuning, O. Jagutzki, T. Weber, J. Ullrich, R. Moshhammer, M. Unverzagt, W. Schmitt, H. Khemliche, M. H. Prior, C. L. Cocke, J. Feagin, R. E. Olson and H. Schmidt-Böcking, *Kinematically complete experiments using cold target recoil ion momentum spectroscopy*, Nucl. Instr. Meth. Phys. Res. B **124**, 225 (1997).
- [Doer98] R. Dörner, H. Bräuning, J. M. Feagin, V. Mergel, O. Jagutzki, L. Spielberger, T. Vogt, H. Khemliche, M. H. Prior, J. Ullrich, C. L. Cocke and H. Schmidt-Böcking, *Photo-double-ionization of He: Fully differential and absolute electronic and ionic momentum distributions*, Phys. Rev. A **57**, 1074 (1998).
- [Doer00] R. Dörner, V. Mergel, O. Jagutzki, L. Spielberger, J. Ullrich, R. Moshhammer and H. Schmidt-Böcking, *Cold Target Recoil Ion Momentum Spectroscopy: A ‘momentum microscope’ to view Atomic Collision Dynamics*, Phys. Rep. **330**, 95 (2000).
- [Don02] E. A. Donley, N. R. Claussen, S. T. Thompson and C. Wieman, *Atom-molecule coherence in a Bose-Einstein condensate*, Nature **417**, 529 (2002).
- [Don05] E. A. Donley, T. P. Heavner, F. Levi, M. O. Tataw and S. R. Jefferts, *Double-pass acousto-optic modulator system*, Rev. Sci. Instrum. **76**, 063112 (2005).
- [Dre83] R. W. P. Drever, J. L. Hall, F. V. Kowalski, J. Hough, G. M. Ford, A. J. Munley and H. Ward, *Laser phase and frequency stabilization using an optical resonator*, Appl. Phys. B, **31**, 97 (1983).
- [Dua90] F. J. Duarte and L. W. Hillman, *Dye laser principles: with applications*, (Academic Press, New York, 1990).
- [Ehr69] H. Ehrhardt, M. Schulz, T. Tekaas and K. Willmann, *Ionization of Helium: Angular Correlation of the Scattered and Ejected Electrons*, Phys. Rev. Lett. **22**, 89 (1969).
- [Ein05] A. Einstein, *Über einen die Erzeugung und Verwandlung des Lichtes betreffenden heuristischen Gesichtspunkt*, Ann. d. Phys. **17**, 132 (1905).
- [Eli76] L. R. Elias, W. M. Fairbank, J. M. J. Madey, H. A. Schwettman and T. I. Smith *Observation of Stimulated Emission of Radiation by Relativistic Electrons in a Spatially Periodic Transverse Magnetic Field*, Phys. Rev. Lett. **36**, 717 (1976).
- [Emm08] A. Emmanouilidou, P. Wang and J. M. Rost, *Initial State Dependence in Multielectron Threshold Ionization of Atoms*, Phys. Rev. Lett. **100**, 063002 (2008).
- [Ert85] W. Ertmer, R. Blatt, J. L. Hall and M. Zhu, *Laser Manipulation of Atomic Beam Velocities: Demonstration of Stopped Atoms and Velocity Reversal*, Phys. Rev. Lett. **54**, 996 (1985).
- [Fan73] U. Fano and J. H. Macek, *Impact Excitation and Polarization of the Emitted Light*, Rev. Mod. Phys. **45**, 553 (1973).

- [Fel92] Z. Felffi and S. T. Manson, *Photoionization of inner shells of excited atoms: Dominance of two-electron transitions*, Phys. Rev. Lett. **68**, 1687 (1992).
- [Fel05] J. Feldhaus, J. Arthur and J. B. Hastings, *X-ray free-electron lasers*, J. Phys. B: At. Mol. Phys. **38**, S799 (2005).
- [FEL09] The World Wide Web Virtual Library: Free Electron Laser research and applications (2009), http://sbfel3.ucsb.edu/www/vl_fel.html.
- [Fer87] T. A. Ferrett, D. W. Lindle, P. A. Heimann, W. D. Brewer, U. Becker, H. G. Kerkhoff and D. A. Shirley, *Lithium 1s main-line and satellite photoemission: Resonant and nonresonant behavior*, Phys. Rev. A **36**, 3172 (1987).
- [Fer99] G. Ferrari, M.-O. Mewes, F. Schreck and C. Salomon, *High-power multiple-frequency narrow-linewidth laser source based on a semiconductor tapered amplifier*, Opt. Lett. **24**, 151 (1999).
- [Fle01] X. Flechard, H. Nguyen, E. Wells, I. Ben-Itzhak and B. D. DePaola, *Kinematically Complete Charge Exchange Experiment in the $Cs^+ + Rb$ Collision System Using a MOT Target*, Phys. Rev. Lett. **87**, 123203 (2001).
- [Fit92] D. N. Fittinghoff, P. R. Bolton, B. Chang and K. C. Kulander, *Observation of nonsequential double ionization of helium with optical tunneling*, Phys. Rev. Lett. **69**, 2642 (1992).
- [For95] R. C. Forrey, H. R. Sadeghpour, J. D. Baker, J. D. Morgan and A. Dalgarno, *Double photoionization of two-electron atoms based on the explicit separation of dominant ionization mechanisms*, Phys. Rev. A **51**, 2112 (1995).
- [Fou08] L. M. Foucar, *Auslese von Delaylinedetektoren mit Hilfe von Transientenrekordern*, Ph.D. thesis, Johann-Wolfgang-Goethe-Universität, Frankfurt (2008).
- [Fur95] D. V. Fursa and I. Bray, *Calculation of electron-helium scattering*, Phys. Rev. A **52**, 1279 (1995).
- [Gea07] M. A. Gearba, H. A. Camp, M. L. Trachy, G. Veshapidze, M. H. Shah, H. U. Jang and B. D. DePaola, *Measurement of population dynamics in stimulated Raman adiabatic passage*, Phys. Rev. A **76**, 013406 (2007).
- [Gel74] U. Gelius, *Recent progress in ESCA studies of gases*, J. Elect. Spect. Relat. Phenom. **5**, 985 (1974).
- [Gib93] K. Gibble and S. Chu, *Laser-Cooled Cs Frequency Standard and a Measurement of the Frequency Shift due to Ultracold Collisions*, Phys. Rev. Lett. **70**, 1771 (1993).
- [Goep31] M. Göppert-Mayer, *Über Elementarakte mit zwei Quantensprüngen*, Ann. d. Phys. **401**, 273 (1931).
- [Goet06] J. R. Götze, M. Walter and J. S. Briggs, *Cross-sections for $(e, 3e)$ collisions on helium: the DS6C wavefunction*, J. Phys. B: At. Mol. Opt. Phys. **39**, 4365 (2006).

BIBLIOGRAPHY

- [Gol57] J. Goldstone, *Derivation of the Brueckner Many-Body Theory*, Proc. Phys. Soc. (London) **A239**, 267 (1957).
- [Gol88] L. Goldberg and M. K. Chun, *Injection locking characteristics of a 1 W broad stripe laser diode*, Appl. Phys. Lett. **53**, 1900 (1988).
- [Gre82a] C. H. Greene and A. R. Rau, *Double Escape of Two Electrons at Threshold: Dependence on L , S , and π* , Phys. Rev. Lett. **48**, 533 (1982).
- [Gre82b] C. H. Greene and R. N. Zare, *Photonization-produced alignment of Cd*, Phys. Rev. A **25**, 2031 (1982).
- [Gri00] R. Grimm, M. Weidemüller and Y. B. Ovchinnikov, *Optical dipole traps for neutral atoms*, Adv. At. Mol. Opt. Phys. **42**, 95 (2000).
- [Har98] H. W. van der Hart, K. W. Meyer and C. H. Greene, *Double photoionization and ionization excitation of the metastable helium S states*, Phys. Rev. A **57**, 3641 (1998).
- [Haen75] T. W. Hänsch, A. L. Schawlow, *Cooling of gases by laser radiation*, Optics Communications **13**, 68 (1975).
- [Hem04] O. Hemmers, R. Guillemin and D. W. Lindle, *Nondipole effects in soft X-ray photoemission*, Radiat. Phys. Chem. **70**, 123 (2004).
- [Her87] H. Hertz, *Ueber einen Einfluss des ultravioletten Lichtes auf die elektrische Entladung*, Ann. d. Phys. u. Chem. **31**, 983 (1887).
- [Her75] I. V. Hertel and A. S. Stamatović, *Spatial Hole Burning and Oligo-Mode Distance Control in CW Dye Lasers*, IEEE J. Quant. Elec. **11**, 210 (1975).
- [Hib75] A. Hibbert, *CIV3 - A general program to calculate configuration interaction wave functions and electric-dipole oscillator strengths*, Comput. Phys. Commun. **9**, 141 (1975).
- [Hof88] J. A. Hoffnagle, *Proposal for continuous white-light cooling of an atomic beam*, Opt. Lett. **13**, 102 (1988).
- [Hu05] S. X. Hu, J. Colgan and L. A. Collins, *Triple-differential cross-sections for two-photon double ionization of He near threshold*, J. Phys. B: At. Mol. Phys. **38**, L35 (2005).
- [Hua02] M.-T. Huang, L. Zhang, S. Hasegawa, S. H. Southworth and L. Young, *Measurements of the electron-impact double-to-single ionization ratio using trapped lithium*, Phys. Rev. A **66**, 012715 (2002).
- [Hua03] M.-T. Huang, W. W. Wong, M. Inokuti, S. H. Southworth and L. Young, *Triple Ionization of Lithium by Electron Impact*, Phys. Rev. Lett. **90**, 163201 (2003).

-
- [Hue91] A. Huetz, P. Selles, D. Waymel and J. Mazeau, *Wannier theory for double photoionization of noble gases*, J. Phys. B: At. Mol. Opt. Phys. **24**, 1917 (1991).
- [Hue94] A. Huetz, P. Lablanquie, L. Andric, P. Selles and J. Mazeau, *Multicoincidence measurements of double photoionization in helium*, J. Phys. B: At. Mol. Opt. Phys. **27**, L13 (1994).
- [Hue00] A. Huetz and J. Mazeau, *Double Photoionization of Helium Down to 100 meV above Threshold*, Phys. Rev. Lett. **85**, 530 (2000).
- [Ish91] T. Ishihara, K. Hino and J. H. McGuire, *Photoionization of two electrons in helium*, Phys. Rev. A **44**, R6980 (1991).
- [Ist02] A. Y. Istomin, N. L. Manakov and A. F. Starace, *Perturbative calculation of the triply differential cross section for photo-double-ionization of He*, J. Phys. B: At. Mol. Phys. **35**, L543 (2002).
- [Joc03] S. Jochim, M. Bartenstein, A. Altmeyer, G. Hendl, S. Riedl, C. Chin, J. H. Denschlag and R. Grimm, *Bose-Einstein Condensation of Molecules*, Science, **302**, 2101 (2003).
- [Jul91] P. S. Julienne and J. Vigue, *Cold collisions of Ground-State and Excited-State Alkali-Metal Atoms*, Phys. Rev. A **44**, 4464 (1991).
- [Kab07] N. Kabachnik, S. Fritzsche, A. Grum-Grzhimailo, M. Meyer, and K. Ueda, *Coherence and correlations in photoinduced Auger and fluorescence cascades in atoms*, Phys. Rep. **451**, 155 (2007).
- [Kai61] W. Kaiser and C. G. B. Garrett, *Two-Photon Excitation in $CaF_2: Eu^{2+}$* , Phys. Rev. Lett. **7**, 229 (1961).
- [Kas89] M. A. Kasevich, E. Riis, S. Chu and R. G. Devoe, *RF-spectroscopy in an Atomic Fountain*, Phys. Rev. Lett. **63**, 612 (1989).
- [Kee00] M. L. Keeler, L.W. Anderson and C. C. Lin, *Electron-Impact Ionization Cross Section Measurements Out of the 5^2P Excited State of Rubidium*, Phys. Rev. Lett. **85**, 3353 (2000).
- [Kel68] H. P. Kelly, *Correlation Structure in Atoms*, Adv. Theor. Phys. **2**, 75 (1968).
- [Khe96] A. S. Kheifets and I. Bray, *Calculation of double photoionization of helium using the convergent close-coupling method*, Phys. Rev. A **54**, R995 (1996).
- [Khe98a] A. S. Kheifets and I. Bray, *Application of the CCC method to the calculation of helium double-photoionization triply differential cross sections*, J. Phys. B: At. Mol. Opt. Phys. **31**, L447 (1998).
- [Khe98b] A. S. Kheifets and I. Bray, *Effect of the ground-state correlations on the helium double photoionization and ionization with excitation*, Phys. Rev. A **57**, 2590 (1998).

BIBLIOGRAPHY

- [Khe98c] A. S. Kheifets and I. Bray, *Photoionization with excitation and double photoionization of the helium isoelectronic sequence*, Phys. Rev. A **58**, 4501 (1998).
- [Khe00a] A. S. Kheifets, A. Ipatov, M. Arifin and I. Bray, *Double-photoionization calculations of the helium metastable $2^{1,3}S$ states*, Phys. Rev. A **62**, 052724 (2000).
- [Khe00b] A. S. Kheifets and I. Bray, *Equal energy-sharing double photoionization of helium from near-threshold to high energies*, Phys. Rev. A **62**, 065402 (2000).
- [Khe01] A. S. Kheifets, *On different mechanisms of the two-electron atomic photoionization*, J. Phys. B: At. Mol. Phys. **34**, L247 (2001).
- [Kil99] T. C. Killian, S. Kulin, S. D. Bergeson, L. A. Orozco, C. Orzel and S. L. Rolston, *Creation of an Ultracold Neutral Plasma*, Phys. Rev. Lett. **83**, 4776 (1999).
- [Kil01] T. C. Killian, M. J. Lim, S. Kulin, R. Dumke, S. D. Bergeson and S. L. Rolston, *Formation of Rydberg Atoms in an Expanding Ultracold Neutral Plasma*, Phys. Rev. Lett. **86**, 3759 (2001).
- [Kil07] T. C. Killian, *Ultracold Neutral Plasmas*, Science **316**, 705 (2007).
- [Kin93] E. S. Kintzer, J. N. Walpole, S. R. Chinn, C. A. Wang and L. J. Missaggia, *High-power, strained-layer amplifiers and lasers with tapered gain regions*, IEEE Photon. Technol. Lett. **5**, 605 (1993).
- [Kla76] H. Klar and W. Schlecht, *Threshold multiple ionization of atoms. Energy dependence for double and triple escape*, J. Phys. B: At. Mol. Phys. **9**, 1699 (1976).
- [Kla81] H. Klar, *Screening effects on Wannier's theory of atomic threshold ionisation*, J. Phys. B: At. Mol. Phys. **14**, 3255 (1981).
- [Kna02a] A. Knapp, A. Kheifets, I. Bray, T. Weber, A. L. Landers, S. Schössler, T. Jahnke, J. Nickles, S. Kammer, O. Jagutzki, L. P. H. Schmidt, T. Osipov, J. Rösch, M. H. Prior, H. Schmidt-Böcking, C. L. Cocke and R. Dörner, *Mechanisms of Photo Double Ionization of Helium by 530 eV Photons*, Phys. Rev. Lett. **89**, 033004 (2002).
- [Kna02b] A. Knapp, M. Walter, T. Weber, A. L. Landers, S. Schössler, T. Jahnke, M. Schoffler, J. Nickles, S. Kammer, O. Jagutzki, L. P. H. Schmidt, T. Osipov, J. Rösch, M. H. Prior, H. Schmidt-Böcking, C. L. Cocke, J. Feagin and R. Dörner, *Energy sharing and asymmetry parameters for photo double ionization of helium 100 eV above threshold in single-particle and Jacobi coordinates*, J. Phys. B: At. Mol. Phys. **35**, L521 (2002).
- [Kno03] S. Knoop, J. W. Turkstra, R. Morgenstern, R. E. Olson and R. Hoekstra, *Multi-electron processes in slow He^{2+} Na collisions measured with MOTRIMS*, Nucl. Instr. Meth. Phys. Res. B **205**, 560 (2003).
- [Kno05] S. Knoop, R. E. Olson, H. Ott, V. G. Hasan, R. Morgenstern and R. Hoekstra, *Single ionization and electron capture in $He^{2+} + Na$ collisions*, J. Phys. B: At. Mol. Phys. **38** 1987 (2005).

-
- [Kno06] S. Knoop, V. G. Hasan, H. Ott, R. Morgenstern and R. Hoekstra, *Single ionization of Na(3s) and Na*(3p) by low energy ion impact*, J. Phys. B: At. Mol. Opt. Phys. **39**, 2021 (2006).
- [Kon93] K. Kondo, A. Sagisaka, T. Tamida, Y. Nabekawa and S. Watanabe, *Wavelength dependence of nonsequential double ionization in He*, Phys. Rev. A **48**, R2531 (1993).
- [Kor91] U. Koren, R. M. Jopson, B. I. Miller, M. Chien, M. G. Young, C. A. Burrus, C. R. Giles, H. M. Presby, G. Raybon, J. D. Evankow, B. Tell and K. Brown-Goebeler, *High power laser-amplifier photonic integrated circuit for 1.48 μm wavelength operation*, Appl. Phys. Lett. **59**, 2351 (1991).
- [Kur07] M. Kurka, *Zwei- und Drei-Photonen Doppelionisation von Helium und Neon am Freie-Elektronen-Laser in Hamburg*, Diplomarbeit, Ruprecht-Karls-Universität, Heidelberg (2007).
- [Kuz03] A. Kuzmich, W. P. Bowen, A. D. Boozer, A. Boca, C. W. Chou, L.-M. Duan and H. J. Kimble, *Generation of nonclassical photon pairs for scalable quantum communication with atomic ensembles*, Nature **423**, 731 (2003).
- [Kos88] H. Kossmann, V. Schmidt and T. Andersen, *Test of Wannier threshold laws: Double-photoionization cross section in helium*, Phys. Rev. Lett. **60**, 1266 (1988).
- [Ky92] L. Vo Ky, H. E. Saraph, W. Eissner, Z. W. Liu and H. P. Kelly, *Inner-shell photoionization of beryllium*, Phys. Rev. A **46**, 3945 (1992).
- [Ky98] L. Vo Ky, P. Faucher, A. Hibbert, J.-M. Li, Y.-Z. Qu, J. Yan, J. C. Chang and F. Bely-Dubau, *Inner-shell photoionization of ground-state lithium: Theoretical calculation in the photon energy region below 130 eV including $1s\text{nl}n'l'$ Rydberg resonances series*, Phys. Rev. A **57**, 1045 (1998).
- [Lan91] B. Langer, J. Vieffhaus, O. Hemmers, A. Menzel, R. Wehlitz and U. Becker, *High-resolution photoelectron spectrometry study of conjugate shakeup processes in the Li 1s threshold region*, Phys. Rev. A **43**, 1652 (1991).
- [Las90] Laser Handbook Vol. 6, *Free-Electron Lasers*, ed. by W.B. Colson, C. Pellegrini and A. Renieri, North Holland, Amsterdam (1990).
- [Let88] P. D. Lett, R. N. Watts, C. I. Westbrook, W. D. Phillips, P. L. Gould and H. J. Metcalf, *Observation of Atoms Laser Cooled below the Doppler Limit*, Phys. Rev. Lett. **61**, 169 (1988).
- [Let89] P. Lett, W. Phillips, S. Rolston, C. Tanner, R. Watts and C. Westbrook, *Optical molasses*, J. Opt. Soc. Am. B **6**, 2084 (1989).
- [Lev91] J. C. Levin, D. W. Lindle, N. Keller, R. D. Miller, Y. Azuma, N. B. Mansour, H. G. Berry and I. A. Sellin, *Measurement of the ratio of double-to-single photoionization of helium at 2.8 keV using synchrotron radiation*, Phys. Rev. Lett. **67**, 968 (1991).

BIBLIOGRAPHY

- [Lin92] K. Lindquist, M. Stephens and C. Wieman, *Experimental and theoretical study of the vapor-cell Zeeman optical trap*, Phys. Rev. A **46**, 4082 (1992).
- [Lis90] A. Lisini, P. G. Burke, and A. Hibbert, *Theoretical study of the core photoionization of lithium*, J. Phys. B: At. Mol. Phys. **23**, 3767 (1990).
- [Lis99] F. Lison, P. Schuh, D. Haubrich and D. Meschede, *High-brilliance Zeeman-slowed cesium atomic beam*, Phys. Rev. A **61**, 013405 (1999).
- [Luk05] M. Lukomski, J. A. MacAskill, D. P. Seecombe, C. McGrath, S. Sutton, J. Teeuwen, W. Kedzierski, T. J. Reddish, J. W. McConkey and W. A. van Wijngaarden, *New measurements of absolute total cross sections for electron impact on caesium using a magneto-optical trap*, J. Phys. B: At. Mol. Opt. Phys. **38**, 3535 (2005).
- [Mac02] J. A. MacAskill, W. Kedzierski, J. W. McConkey, J. Domyslawska and I. Bray, *Measuring cesium electron impact cross-sections using a magneto-optical trap*, J. Elec. Spect. Relat. Phenom. **123**, 173 (2002).
- [Mad63] R. P. Madden and K. Codling, *New Autoionizing Atomic Energy Levels in He, Ne, and Ar*, Phys. Rev. Lett. **10**, 516 (1963).
- [Mad71] J. M. J. Madey, *Stimulated Emission of Bremsstrahlung in a Periodic Magnetic Field*, J. Appl. Phys. **42**, 1906 (1971).
- [Mad02] D. N. Madsen and J. W. Thomsen, *Measurement of absolute photo-ionization cross sections using magnesium magneto-optical traps*, J. Phys. B: At. Mol. Opt. Phys. **35**, 2173 (2002).
- [Mal97] A. W. Malcherek and J. S. Briggs, *The n -electron Coulomb continuum*, J. Phys. B: At. Mol. Opt. Phys. **30**, 4419 (1997).
- [Mal99] L. Malegat, P. Selles and A. K. Kazansky, *Double photoionization of helium: The hyperspherical R -matrix method with semiclassical outgoing waves*, Phys. Rev. A **60**, 3667 (1999).
- [Mal00] L. Malegat, P. Selles and A. K. Kazansky, *Absolute Differential Cross Sections for Photo Double Ionization of Helium from the Ab Initio Hyperspherical R -Matrix Method with Semiclassical Outgoing Waves*, Phys. Rev. Lett. **85**, 4450 (2000).
- [Man76] S. T. Manson, *Satellite lines in photoelectron spectra*, J. Elect. Spect. Relat. Phenom. **9**, 21 (1976).
- [Man96] N. L. Manakovy, S. I. Marmoyz and A. V. Meremianiny, *A new technique in the theory of angular distributions in atomic processes: the angular distribution of photoelectrons in single and double photoionization*, J. Phys. B: At. Mol. Opt. Phys. **29**, 2711 (1996).
- [Mar76a] R. L. Martin and D. A. Shirley, *Theory of the neon $1s$ correlation-peak intensities*, Phys. Rev. A **13**, 1475 (1976).

-
- [Mar76b] G. Marowsky and K. Kaufmann, *Influence of Spatial Hole Burning on the Output Power of a CW Dye Ring Laser*, IEEE J. Quant. Elec. **12**, 207 (1976).
- [Mar81] C. Martin, P. Jelinski, M. Lampton, R. F. Malina and H. O. Anger, *Wedge-and-strip anodes for centroid-finding position-sensitive photon and particle detectors*, Rev. Sci. Instrum. **52**, 1067 (1981).
- [Mar98] O. Maragò, D. Ciampini, F. Fuso, E. Arimondo, C. Gabbanini and S. T. Manson, *Photoionization cross sections for excited laser-cooled cesium atoms*, Phys. Rev. A **57**, R4110 (1998).
- [Mau95] F. Maulbetsch and J. S. Briggs, *Selection rules for transitions to two-electron continuum states*, J. Phys. B: At. Mol. Opt. Phys. **28**, 551 (1995).
- [Maz97] J. Mazeau, P. Lablanquie, P. Selles, L. Malegat and A. Huetz, *Symmetry-favoured double photoionization of argon*, J. Phys. B: At. Mol. Phys. **30**, L293 (1997).
- [McA96] W. I. McAlexander, E. R. I. Abraham and R. G. Hulet, *Radiative lifetime of the 2P state of lithium*, Phys. Rev. A **54**, R5 (1996).
- [McG95] J. McGuire, N. Berrah, R. Bartlett, J. Samson, J. Tanis, C. L. Cocke and A. S. Schlachter, *The ratio of cross sections for double to single ionization of helium by high energy photons and charged particles*, J. Phys. B: At. Mol. Phys. **28**, 913 (1995).
- [Meh94] W. Mehlhorn, *Alignment after inner-shell ionization by electron impact near and at threshold*, Nucl. Instr. Meth. Phys. Res. B **87**, 227 (1994).
- [Men98] G. Mentzely, K.-H. Schartnery, O. Wilhelmy, B. Magely, U. Staudey, F. Vollweiler, S. Lauerz, H. Liebelz, H. Schmoranz, V. L. Sukhorukov and B. M. Lagutin, *Photofragmentation analysis from fluorescence-radiation angular-asymmetry parameter measurements of $Ar^+(4p - 4s)$ fine-structure resolved transitions on resonances*, J. Phys. B: At. Mol. Opt. Phys. **31**, 227 (1998).
- [Men07] R. Menzel, *Photonics: linear and nonlinear interactions of laser light and matter*, (Springer-Verlag, Berlin, 2007), 2nd Edn.
- [Mer95] V. Mergel, R. Dörner, J. Ullrich, O. Jagutzki, S. Lencinas, S. Nüttgens, L. Spielberger, M. Unverzagt, C. L. Cocke, R. E. Olson, M. Schulz, U. Buck, E. Zanger, W. Theisinger, M. Isser, S. Geis and H. Schmidt-Böcking, *State Selective Scattering Angle Dependent Capture Cross Sections Measured by Cold Target Recoil Ion Momentum Spectroscopy*, Phys. Rev. Lett. **74**, 2200 (1995).
- [Mer96] V. Mergel, *Dynamische Elektronenkorrelationen in Helium*, Ph.D. thesis, Johann-Wolfgang-Goethe-Universität, Frankfurt (1996).
- [Met99] H. J. Metcalf and P. van der Straten, *Laser Cooling and Trapping* (Springer-Verlag, New York, 1999).

BIBLIOGRAPHY

- [Mey91] M. Meyer, E. v. Raven, B. Sonntag and J. E. Hansen, *Decay of the Ar $2p^5 nd$ core resonances: An autoionization spectrum dominated by shake processes*, Phys. Rev. A **43**, 177 (1991).
- [Mey94] K. W. Meyer and C. H. Greene, *Double photoionization of helium using R-matrix methods*, Phys. Rev. A **50**, R3573 (1994).
- [Mey97] K. W. Meyer, C. H. Greene and B. D. Esry, *Two-Electron Photoejection of He and H^-* , Phys. Rev. Lett. **78**, 4902 (1997).
- [Mol98] A. F. Molisch and B. P. Oehry, *Radiation Trapping In Atomic Vapours* (Oxford University Press, New York, 1999).
- [Mor76] J. Morellec, D. Normand and G. Petite, *Resonance shifts in the multiphoton ionization of cesium atoms*, Phys. Rev. A **14**, 300 (1976).
- [Mos94] R. Moshhammer, J. Ullrich, M. Unverzagt, W. Schmidt, P. Jardin, R. E. Olson, R. Mann, R. Dörner, V. Mergel, U. Buck and H. Schmidt-Böcking, *Low-Energy Electrons and Their Dynamical Correlation with Recoil Ions for Single Ionization of Helium by Fast, Heavy-Ion Impact*, Phys. Rev. Lett. **73**, 3371 (1994).
- [Mos96] R. Moshhammer, M. Unverzagt, W. Schmitt, J. Ullrich and H. Schmidt-Böcking, *A 4π recoil-ion electron momentum analyzer: a high resolution “microscope” for the investigation of the dynamics of atomic, molecular and nuclear reactions*, Nucl. Instr. Meth. Phys. Res. B **108**, 425 (1996).
- [Mos07] R. Moshhammer, Y. H. Jiang, L. Foucar, A. Rudenko, T. Ergler, C. D. Schröter, S. Lüdemann, K. Zrost, D. Fischer, J. Titze, T. Jahnke, M. Schöffler, T. Weber, R. Dörner, T. J. M. Zouros, A. Dorn, T. Fergner, K. U. Kihnel, S. Düsterer, R. Treusch, P. Radcliffe, E. Plönjes and J. Ullrich, *Few-Photon Multiple Ionization of Ne and Ar by Strong Free-Electron-Laser Pulses*, Phys. Rev. Lett. **98**, 203001 (2007).
- [Mot51] H. Motz, *Applications of the Radiation from Fast Electron Beams*, J. Appl. Phys. **22**, 527 (1951).
- [Naj08] B. Najjari, *private communication* (2008).
- [Nap94] R. Napolitano, J. Weiner, C. J. Williams and P. S. Julienne, *Line Shapes of High Resolution Photoassociation Spectra of Optically Cooled Atoms*, Phys. Rev. Lett. **73** 1352 (1994).
- [Nes63] A. N. Nesmeyanov, *Vapor Pressure of the Chemical Elements* (Elsevier Publishing Company, National Bureau of Standards, Washington D.C., 1963).
- [Nik01] L. A. A. Nikolopoulos and P. Lambropoulos, *Multichannel theory of two-photon single and double ionization of helium*, J. Phys. B: At. Mol. Opt. Phys. **34**, 545 (2001).
- [NIS09] NIST Atomic Spectra Database (2009),
<http://physics.nist.gov/PhysRefData/ASD/index.html>.

- [OKe04] P. O’Keeffe, S. Aloïse, S. Fritzsche, B. Lohmann, U. Kleiman, M. Meyer and A. N. Grum-Grzhimailo, *Resonant Auger decay of $Xe^* 4d_{5/2}^{-1}6p$: A contribution to the complete experiment from fluorescence polarization studies*, Phys. Rev. A **70**, 012705 (2004).
- [Pat01] T. Pattard and J. Burgdörfer, *Half-collision model for multiple ionization by photon impact*, Phys. Rev. A **64**, 042720 (2001).
- [Paw00] T. Pawletko, M. Houssin, M. Knoop, M. Vedel and F. Vedel, *High power broad-area diode laser at 794 nm injected by an external cavity laser*, Opt. Commun. **174**, 223 (2000).
- [Pet02] C. J. Pethick and H. Smith, *Bose-Einstein Condensation in dilute gases*, (Cambridge University Press, Cambridge, 2002).
- [Phi82] W. D. Phillips and H. Metcalf, *Laser Deceleration of an Atomic Beam*, Phys. Rev. Lett. **48**, 596 (1982).
- [Phi98] W. D. Phillips, *Laser cooling and trapping of neutral atoms*, Rev. Mod. Phys. **70**, 721 (1998); Nobel lecture.
- [Pin98a] M. S. Pindzola and F. Robicheaux, *Time-dependent close-coupling calculations of correlated photoionization processes in helium*, Phys. Rev. A **57**, 318 (1998).
- [Pin98b] M. S. Pindzola and F. Robicheaux, *Two-photon double ionization of He and H^-* , J. Phys. B: At. Mol. Opt. Phys. **31**, L823 (1998).
- [Poe01] M. van der Poel, C. V. Nielsen, M.-A. Gearba and N. Andersen, *Fraunhofer Diffraction of Atomic Matter Waves: Electron Transfer Studies with a Laser Cooled Target*, Phys. Rev. Lett. **87**, 123201 (2001).
- [Poh04] T. Pohl, T. Pattard and J.M. Rost, *Coulomb Crystallization in Expanding Laser-Cooled Neutral Plasmas*, Phys. Rev. Lett. **92**, 155003 (2004).
- [Pon95] M. Pont and R. Shakeshaft, *Theory of double photoionization of a two-electron atom: Circumventing the boundary conditions*, Phys. Rev. A **51**, 494 (1995).
- [Pon96] M. Pont, R. Shakeshaft, F. Maulbetsch and J. S. Briggs, *Angular distributions for double photoionization of helium: Discrepancies between theory and experiment*, Phys. Rev. A **53**, 3671 (1996).
- [Poo92] M. W. Poole, *FEL sources: Present status and future prospects*, Rev. Sci. Instrum. **63**, 1528 (1992).
- [Pra98] M. Praeger, V. Vuletic, T. Fischer, T. W. Hänsch and C. Zimmermann, *A broad emitter diode laser system for lithium spectroscopy*, Appl. Phys. B **67**, 163 (1998).
- [Pre92] W. H. Press, S. A. Teukolsky, W. T. Vetterling and B. P. Flannery, *Numerical Recipes* (Cambridge University Press, Cambridge, 1992).

BIBLIOGRAPHY

- [Pro93] D. Proulx and R. Shakeshaft, *Double ionization of helium by a single photon with energy 89140 eV*, Phys. Rev. A **48**, R875 (1993).
- [Qiu98] Y. Qiu, J.-Z. Tang, J. Burgdörfer and J. Wang, Phys. Rev. A **57**, *Double photoionization of helium from threshold to high energies*, R1489 (1998).
- [Raa87] E. L. Raab, M. Prentiss, A. Cable, S. Chu and D. E. Pritchard, *Trapping of Neutral Sodium Atoms with Radiation Pressure*, Phys. Rev. Lett. **59**, 2631 (1987).
- [Red97] T. J. Reddish, G. Richmond, G. W. Bagley, J. P. Wightman and S. Cvejanović, *Dual toroidal photoelectron spectrometer for investigating photodouble ionization in atoms and molecules*, Rev. Sci. Instrum. **68**, 2685 (1997).
- [Ren08] X. Ren, A. Dorn and J. Ullrich, *Coulomb Four-Body Problem: Electron-Impact Double Ionization of Helium in the Threshold Regime*, Phys. Rev. Lett. **101**, 093201 (2008).
- [Res99] T. N. Rescigno, M. Baertschy, W. A. Isaacs and C. W. McCurdy, *Collisional Breakup in a Quantum System of Three Charged Particles*, Science **286**, 2474 (1999).
- [Rio01] S. Rioual, B. Rouvellou, L. Avaldi, G. Battera, R. Camilloni, G. Stefani and G. Turri, *Experimental Observation of Post-Collision Interaction and Interference Effects in Resonant Double Photoionization Processes*, Phys. Rev. Lett. **86**, 1470 (2001).
- [Rob89] C. W. Roberson and P. Sprangle, *A review of free-electron lasers*, Phys. Fluids B **1**, 3 (1989).
- [Ros91] J. M. Rost and J. S. Briggs, *Mechanisms of electron impact ionization at threshold*, J. Phys. B: At. Mol. Phys. **24**, L393 (1991).
- [Rot72] T. Roth, *Threshold Law for Double Photoionization and Related Processes with $L=1$ Final States*, Phys. Rev. A **5**, 476 (1972).
- [Rud08] A. Rudenko, L. Foucar, M. Kurka, T. Ergler, K. U. Kühnel, Y. H. Jiang, A. Voitkiv, B. Najjari, A. Kheifets, S. Lüdemann, T. Havermeier, M. Smolarski, S. Schössler, K. Cole, M. Schöffler, R. Dörner, S. Düsterer, W. Li, B. Keitel, R. Treusch, M. Gensch, C. D. Schröter, R. Moshhammer and J. Ullrich, *Recoil-Ion Momentum Distributions for Two-Photon Double Ionization of He and Ne by 44 eV Free-Electron Laser Radiation*, Phys. Rev. Lett. **101**, 073003 (2008).
- [Sam90] J. A. R. Samson, *Proportionality of electron-impact ionization to double photoionization*, Phys. Rev. Lett. **65**, 2861 (1990).
- [Sam98] J. A. R. Samson, W. C. Stolte, Z.-X. He, J. N. Cutler and Y. Lu, *Double photoionization of helium*, Phys. Rev. A **57**, 1906 (1998).
- [Sch77] H. W. Schröder, L. Stein, D. Frölich, B. Fugger and H. Welling, *A High-Power Single-Mode cw Dye Ring Laser*, Appl. Phys. **14**, 377 (1977).

- [Sch92] V. Schmidt, *Photoionization of atoms using synchrotron radiation*, Rep. Prog. Phys. **55**, 1483 (1992).
- [Sch93] O. Schwarzkopf, B. Krässig, J. Elmiger and V. Schmidt, *Energy- and angle-resolved double photoionization in helium*, Phys. Rev. Lett. **70**, 3008 (1993).
- [Sch96] R. S. Schappe, T. Walker, L. W. Anderson and C. C. Lin, *Absolute Electron-Impact Ionization Cross Section Measurements Using a Magneto-Optical Trap*, Phys. Rev. Lett. **76**, 4328 (1996).
- [Sch98a] W. Schmitt, *Kinematisch vollständige Experimente zur Einfachionisation von Helium durch hochenergetische Schwerionen*, Ph.D. thesis, Johann-Wolfgang-Goethe-Universität, Frankfurt (1998).
- [Sch98b] V. Schyja, T. Lang and H. Helm, *Channel switching in above-threshold ionization of xenon*, Phys. Rev. A **57**, 3692 (1998).
- [Sch99] U. Schünemann, H. Engler, R. Grimm, M. Weidemüller and M. Zielonkowski, *Simple scheme for tunable frequency offset locking of two lasers*, Rev. Sci. Instrum. **70**, 242 (1990).
- [Sch02] T. Schneider, P. L. Chocian and J.-M. Rost, *Separation and Identification of Dominant Mechanisms in Double Photoionization*, Phys. Rev. Lett. **89**, 073002 (2002).
- [Sch03] R. H. Schill, D. Hasselkamp, S. Kammer, S. Mickat, B. Zimmermann, K.-H. Schartner, A. Ehresmann, H. Schmoranzler, M. Schlüter, Yu A. Schutov, B. M. Lagutin and V. L. Sukhorukov, *Partial wave analysis of the $Kr I 3d_{5/2}^9 5p_{3/2} \rightarrow Kr II 4p^4(^1D)5p^2F_{7/2}$ decay, based on orientation and alignment transfer*, J. Phys. B: At. Mol. Opt. Phys. **36**, L57 (2003).
- [Sch08] M. Schuricke, *Multiphoton Ionization of Lithium*, Diploma thesis, Ruprecht-Karls-Universität, Heidelberg (2008).
- [Sea87] M. J. Seaton, *Atomic data for opacity calculations: I. General description*, J. Phys. B: At. Mol. Phys. **20**, 6363 (1987).
- [Sel87] P. Selles, J. Mazeau and A. Huetz, *Wannier theory for P^o and D^e states of two electrons*, J. Phys. B: At. Mol. Phys. **20**, 5183 (1987).
- [Sel02] P. Selles, L. Malegat and A. K. Kazansky, *Ab initio calculation of the whole set of He double-photoionization cross sections*, Phys. Rev. A **65**, 032711 (2002).
- [Sha07] M. H. Shah, H. A. Camp, M. L. Trachy, G. Veshapidze, M. A. Gearba and B. D. DePaola, *Model-independent measurement of the excited fraction in a magneto-optical trap*, Phys. Rev. A **75**, 053418 (2007).
- [She94] J. Shertzer and J. Botero, *Finite-element analysis of electron-hydrogen scattering*, Phys. Rev. A **49**, 3673 (1994).

BIBLIOGRAPHY

- [Shv00] I. Shvarchuck, K. Dieckmann, M. Zielonkowski and J. T. M. Walraven, *Broad-area diode-laser system for a rubidium Bose-Einstein condensation experiment*, Appl. Phys. B **71**, 475 (2000).
- [Sny75] J. J. Snyder, *Paraxial ray analysis of a cat's-eye retroreflector*, Appl. Opt. **14**, 1825 (1975).
- [Spi05] F. Spiegelhalter, *Setting up a Lithium Magneto-Optical Trap as a Target for a Reaction Microscope*, Diploma thesis, Ruprecht-Karls-Universität, Heidelberg (2005).
- [Sta82] A. D. Stauffer, *The nodal structure of two-electron wave functions on the Wannier ridge*, Phys. Lett. A **91**, 114 (1982).
- [Ste07] J. Steinmann, *Multiphoton Ionization of Laser Cooled Lithium*, Ph.D. thesis, Ruprecht-Karls-Universität, Heidelberg (2007).
- [Tan95] J.-Z. Tang and I. Shimamura, *Double photoionization of helium at low photon energies*, Phys. Rev. A **52**, R3413 (1995).
- [Tem62] A. Temkin, *Nonadiabatic Theory of Electron-Hydrogen Scattering*, Phys. Rev. **126**, 130 (1962).
- [Ten94] Z.-J. Teng and R. Shakeshaft, *Double ionization of He($1s^2$) and He($1s2s^3S$) by a single high-energy photon*, Phys. Rev. A **49**, 3597 (1994).
- [Tow95] C. G. Townsend, N. H. Edwards, C. J. Cooper, K. P. Zetie, C. J. Foot, A. M. Steane, P. Szriftgiser, H. Perrin and J. Dalibard, *Phase-space density in the magneto-optical trap*, Phys. Rev. A **52**, 1423 (1995).
- [Tra07] M. L. Trachy, G. Veshapidze, M. H. Shah, H. U. Jang and B. D. DePaola, *Photoassociation in Cold Atoms via Ladder Excitation*, Phys. Rev. Lett. **99**, 043003 (2007).
- [Tru01] A. G. Truscott, K. E. Strecker, W. I. McAlexander, G. B. Partridge and R. G. Hulet, *Observation of Fermi Pressure in a Gas of Trapped Atoms*, Science **291**, 2570 (2001).
- [Tur01] J. W. Turkstra, R. Hoekstra, S. Knoop, D. Meyer, R. Morgenstern and R. E. Olson, *Recoil Momentum Spectroscopy of Highly Charged Ion Collisions on Magneto-Optically Trapped Na*, Phys. Rev. Lett. **87**, 123202 (2001).
- [Uhl05] L. J. Uhlmann, R. G. Dall, A. G. Truscott, M. D. Hoogerland, K. G. H. Baldwin and S. J. Buckman, *Electron Collisions with Laser Cooled and Trapped Metastable Helium Atoms: Total Scattering Cross Sections*, Phys. Rev. Lett. **94**, 173201 (2005).
- [Ull97] J. Ullrich, R. Moshhammer, R. Dörner, O. Jagutzki, V. Mergel, H. Schmidt-Böcking and L. Spielberger, *Recoil-ion momentum spectroscopy*, J. Phys. B: At. Mol. Phys. **30**, 2917 (1997).

- [Ull03a] J. Ullrich, R. Moshhammer, A. Dorn, R. Dörner, L. P. H. Schmidt and H. Schmidt-Böcking, *Recoil-ion and electron momentum spectroscopy: reaction-microscopes*, Rep. Prog. Phys. **66**, 1463 (2003).
- [Ull03b] J. Ullrich and V. P. Shevelko, *Many-Particle Quantum Dynamics in Atomic and Molecular Fragmentation* (Springer, Heidelberg, 2003).
- [Var88] D. A. Varshalovich, A. N. Moskalev and V. K. Chersonskii, *Quantum Theory of Angular Momentum* (World Scientific, Singapore, 1988).
- [Vol96] U. Volz, H. Schmoranzler, *Precision Lifetime Measurements on Alkali Atoms and on Helium by Beam-gas-laser spectroscopy*, Phys. Scr. T **65**, 48 (1996).
- [Vor66] G. S. Voronov and N. Delone, *Multiphoton ionization of xenon atoms by radiation from a ruby laser*, Sov. Phys. JETP **23**, 54 (1966).
- [Wal92] J. N. Walpole, E. S. Kintzer, S. R. Chinn, C. A. Wang and L. J. Missaggia, *High-power strained-layer InGaAs/AlGaAs tapered traveling wave amplifier*, Appl. Phys. Lett. **61**, 740 (1992).
- [Wal94a] B. Walker, B. Sheehy, L. F. DiMauro, P. Agostini, K. J. Schafer and K. C. Kulander, *Precision Measurement of Strong Field Double Ionization of Helium*, Phys. Rev. Lett. **73**, 1227 (1994).
- [Wal94b] T. Walker and P. Feng, *Measurement of collisions between laser-cooled atoms*, Adv. At. Mol. Opt. Phys. **34**, 125 (1994).
- [Wal96] J. N. Walpole, *Semiconductor amplifiers and lasers with tapered gain regions*, Opt. Quant. Elec. **28**, 623 (1996).
- [Wan53] G. H. Wannier, *The Treshold Law for Single Ionization of Atoms or Ions by Electrons*, Phys. Rev. **90** 817, (1953).
- [Wan55] G. H. Wannier, *Treshold Law for Multiple Ionization*, Phys. Rev. **100**, 1180 (1955).
- [Web04] T. Weber, A. O. Czasch, O. Jagutzki, A. K. Müller, V. Mergel, A. Kheifets, E. Rotenberg, G. Meigs, M. H. Prior, S. Daveau, A. Landers, C. L. Cocke, T. Osipov, R. Díez Muiño, H. Schmidt-Böcking and R. Dörner, *Complete photo-fragmentation of the deuterium molecule*, Nature **431**, 437 (2004).
- [Weh91] R. Wehlitz, F. Heiser, O. Hemmers, B. Langer, A. Menzel and U. Becker, *Electron-energy and -angular distributions in the double photoionization of helium*, Phys. Rev. Lett. **67**, 3764 (1991).
- [Weh95] R. Wehlitz, J. Viefhaus, K. Wieliczek, B. Langer, S. B. Whitfield and U. Becker, *Coincidence experiments following synchrotron radiation excitation*, Nucl. Instr. Meth. Phys. Res. B **99**, 257 (1995).

BIBLIOGRAPHY

- [Weh02] R. Wehlitz, J. B. Bluett and S. B. Whitfield, *Comparison of the double- to single-photoionization ratio of Li with He*, Phys. Rev. A **66**, 012701 (2002).
- [Wei99] J. Weiner, V. S. Bagnato, S. Zilio and P. S. Julienne, *Experiments and theory in cold and ultracold collisions*, Rev. Mod. Phys. **71**, 1 (1999).
- [Wel92] D. F. Welch, R. Parke, D. Mehuys, A. Hardy, R. Lang, S. O'Brien and S. Scifres, *1.1 W CW, diffraction-limited operation of a monolithically integrated flared-amplifier master oscillator power amplifier*, Elec. Lett. **28**, 2011 (1992).
- [Wil55] W. C. Wiley and I. H. McLaren, *Time-of-Flight Mass Spectrometer with Improved Resolution*, Rev. Sci. Instrum. **26**, 1150 (1955).
- [Win75] D. J. Wineland and H. G. Dehmelt, *Proposed $10^{14}\delta\nu/\nu$ laser fluorescence spectroscopy on Ti^+ mono ion oscillator*, Bull. Am. Phys. Soc. **20**, 637 (1975).
- [Wol97] S. Wolf and H. Helm, *Ion-recoil energy measurement in photoionization of laser-cooled rubidium*, Phys. Rev. A **56**, R4385 (1997).
- [Wol00] S. Wolf, H. Helm, *Ion-recoil momentum spectroscopy in a laser-cooled atomic sample*, Phys. Rev. A **62**, 043408 (2000).
- [Wui74] F. J. Wuilleumier and M. O. Krause, *Photoionization of neon between 100 and 2000 eV: Single and multiple processes, angular distributions, and subshell cross sections*, Phys. Rev. A **10**, 242 (1974).
- [Yaz91] P. A. Yazaki, K. Komori, G. Bendelli, S. Arai and Y. Suematsu, *A GaInAsP/InP tapered-waveguide semiconductor laser amplifier integrated with a $1.5\mu\text{m}$ distributed feedback laser*, IEEE Trans. Photon. Technol. Lett. **3**, 1060 (1991).
- [Yua08] Z.-S. Yuan, Y.-A. Chen, B. Zhao, S. Chen, J. Schmiedmayer and J.-W. Pan, *Experimental demonstration of a BDCZ quantum repeater node*, Nature **454**, 1098 (2008).
- [Zap05] M. Zapukhlyak, T. Kirchner, H. J. Lüdde, S. Knoop, R. Morgenstern and R. Hoekstra, *Inner- and outer-shell electron dynamics in proton collisions with sodium atoms*, J. Phys. B: At. Mol. Opt. Phys. **38**, 2353 (2005).
- [Zho99] H. L. Zhou, S. T. Manson, L. Vo Ky, P. Faucher, F. Bely-Dubau, A. Hibbert, S. Diehl, D. Cubaynes, J.-M. Bizau, L. Journel and F. J. Wuilleumier, *Inner-shell photoionization of excited lithium*, Phys. Rev. A **59**, 462 (1999).
- [Zhu91] M. Zhu, C. W. Oates and J. L. Hall, *Continuous high-flux monovelocity atomic beam based on a broadband laser-cooling technique*, Phys. Rev. Lett. **67**, 46 (1991).
- [Zhu09] G. Zhu, M. Schuricke, J. Steinmann, J. Albrecht, J. Ullrich, I. Ben-Itzhak, T. J. M. Zouros, J. Colgan, M. Pindzola and A. Dorn, *Controlling Two-Electron Threshold Dynamics in Double Photoionization of Lithium by Initial-State Preparation*, Phys. Rev. Lett. **103**, 103008 (2009).

Curriculum Vitae

Personal Information

Name	Ganjun Zhu
Gender	Male
Nationality	P. R. China
Date of Birth	23 Dec. 1977
Place of Birth	Huainan, P. R. China
Parents	Zhenyun Zhu and Yingying Xu
Marital Status	Married with Weiwei Xia since 22 Apr. 2004



Education

1984–1993	Compulsory education
1993–1996	High school education
1996–2001	University of Science and Technology of China, B. Sc. Chemistry
2002–2005	Ruprecht-Karls-Universität Heidelberg, M. Sc. Physics
2005–2009	Johann Wolfgang Goethe-Universität Frankfurt am Main, Ph.D Physics, promotion at Max-Planck-Institut für Kernphysik

Research and Teaching Experience

02.2000–07.2000	Teaching Assistant, University of Science and Technology of China, Department of Modern Physics, Hefei, P.R. China
04.2002–03.2005	Teaching and Research Assistant, Ruprecht-Karls-Universität Heidelberg, Department of Physics and Astronomy, Heidelberg, Germany
Since 08.2005	Research Assistant, Max-Planck-Institut für Kernphysik, Heidelberg, Germany

Conference / Presentations

03.2006	DPG-Frühjahrstagung, Frankfurt
07.2007	ICPEAC XXV, Freiburg
08.2007	($e, 2e$), Double Photoionization and related topics, Königstein
09.2008	ICOMP 2008, Heidelberg

- 10.2008 FLASH Symposium, Hamburg
- 03.2009 DPG-Frühjahrstagung, Hamburg
- 07.2009 ($e, 2e$), Double Photoionization and Related Topics, Lexington (USA)

Publication

- [1] Z. Yuan, Y. Chen, S. Chen, B. Zhao, M. Koch, T. Strassel, Y. Zhao, G. Zhu, J. Schmiedmayer, and J. Pan, *Synchronized Independent Narrow-Band Single Photons and Efficient Generation of Photonic Entanglement*, Phys. Rev. Lett. **98**, 180503 (2007)
- [2] G. Zhu, M. Schuricke, J. Steinmann, J. Albrecht, J. Ullrich, I. Ben-Itzhak, T. J. M. Zouros, J. Colgan, M. Pindzola, and A. Dorn, *Controlling Two-Electron Threshold Dynamics in Double Photoionization of Lithium by Initial-State Preparation*, Phys. Rev. Lett. **103**, 103008 (2009)

Heidelberg, February 2010

Acknowledgements

There is a long list of people, to whom I would like to express my gratitude here. Indeed, you all became part of my memory in the last four years.

- First, I would thank Prof. Joachim Ullrich for nicely offering me this PhD position. It is you who encouraged me to continue my scientific road, and re-stimulated my interest in the fantastic world of atom and photon. Thank you for supplying the excellent research conditions, and conducting us to march towards a forethoughtful perspective.
- I am indebted to Prof. Reinhard Dörner, for the promotion matter, along with the concern of Prof. Ullrich. And I am also grateful to your help in my thesis work truly. I can feel your care every time I met you, your lecture, your post presentation, your technical support and your comment on our project.
- Special regards and the deepest acknowledgments, no doubt, go to Priv.-Doz. Alexander Dorn (my Shifu), for the continuous supports and helpful hints. I am obligated to your patience and tolerance within the intensive supervision, so am I grateful to your trust in me. Alex, I did learn a lot from you, but words here is not enough at all.
- Jochen Steinmann, my best colleague in Germany, for the trust and support between you and me. I do really appreciate the time we were together. And I do remember one words from you forever ‘what has to be done is have-to-be-done’.
- I also thank Robert Moshhammer, Selim Jochim, Konstantin Simeonidis, and Benaceur Najjari for helpful discussions, inspiring suggestions and substantial backup. Without your invaluable collaboration and seasonable reinforcement, this work won’t run smoothly and successfully.
- I would also thank my colleagues Michael Schuricke, Johannes Albrecht, Xueguang Ren, Timo Ottenstein, Moritz Kurka *etc.* who contributed to this MOTRIMS project.

One more words, Alexander Dorn, Selim Jochim and Jochen Steinmann, you are the people came into my dream frequently in the past, definitely for Physics.

- The last, but not the least, I express my express my great gratitude to Prof. Horst Schmidt-Böcking for chairing my Ph.D. defense and for the correlated memories also!

‘Ein herzliches Dankeschön!’